

N66-14161

(ACCESSION NUMBER)

(THRU)

(PAGES)

(CODE)

(NASA CR OR TMX OR AD NUMBER)

(CATEGORY)

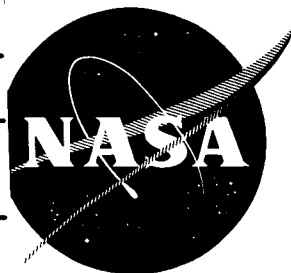
NASA CR-54323  
EOS REPORT 4920-Final

GPO PRICE \$

CFSTI PRICE(S) \$

Hard copy (HC) 6.00

Microfiche (MF) 1.50



ff 653 July 65

# ION ROCKET SYSTEM RESEARCH AND DEVELOPMENT

By

G. Sohl, G. C. Reid, F. A. Barcatta, S. Zafran,  
and R. C. Speiser

prepared for

NATIONAL AERONAUTICS AND SPACE ADMINISTRATION

CONTRACT NAS3-5250

**ELECTRO-OPTICAL SYSTEMS, INC.,** Pasadena, California  
A Subsidiary of Xerox Corporation

#### NOTICE

This report was prepared as an account of Government sponsored work. Neither the United States, nor the National Aeronautics and Space Administration (NASA), nor any person acting on behalf of NASA:

- A.) Makes any warranty or representation, expressed or implied, with respect to the accuracy, completeness, or usefulness of the information contained in this report, or that the use of any information, apparatus, method, or process disclosed in this report may not infringe privately owned rights; or
- B.) Assumes any liabilities with respect to the use of, or for damages resulting from the use of any information, apparatus, method or process disclosed in this report.

As used above, "person acting on behalf of NASA" includes any employee or contractor of NASA, or employee of such contractor, to the extent that such employee or contractor of NASA, or employee of such contractor prepares, disseminates, or provides access to, any information pursuant to his employment or contract with NASA, or his employment with such contractor.

Requests for copies of this report should be referred to  
National Aeronautics and Space Administration  
Office of Scientific and Technical Information  
Attention: AFSS-A  
Washington, D.C. 20546



FINAL REPORT

# ION ROCKET SYSTEM RESEARCH AND DEVELOPMENT

By

G. Sohl, G. C. Reid, F. A. Barcatta, S. Zafran,  
and R. C. Speiser

prepared for

NATIONAL AERONAUTICS AND SPACE ADMINISTRATION

30 December 1965

CONTRACT NAS3-5250

Technical Management  
NASA Lewis Research Center  
Cleveland, Ohio  
Spacecraft Technology Division  
James Wolters

ELECTRO-OPTICAL SYSTEMS, INC. — PASADENA, CALIFORNIA  
A Subsidiary of Xerox Corporation

# ABSTRACT

14161

A program of applied research; component development and extended testing on a 10 mlb thrust engine is reported. High performance was achieved with both electromagnet and permanent magnet versions of the engine. An electromagnet engine was operated for a total thrusting time of 2610 hours at the nominal design point of 7000 seconds specific impulse, 10 mlb thrust and a power-to-thrust ratio of 182 kw/lb. A 100 mlb engine design and results of tests of a new neutralizer concept are reported.

Author

## CONTENTS

1.	INTRODUCTION	1
1.1	Previous Work	1
1.2	Program Objectives	2
1.3	Organization of Report	3
2.	ENGINE COMPONENT DEVELOPMENT	4
2.1	Electrode Materials Tests	4
2.1.1	High Drain Current Mechanism	4
2.1.2	Heated Electrode Tests	11
2.1.3	Extended Electrode Tests	24
2.1.4	Sputtering Measurements	29
2.1.5	Emittance Measurements	37
2.2	Feed Systems	43
2.2.1	750-Hour Feed System	43
2.2.2	Feed System Improvements	43
2.2.3	Manually Operated Cesium Valve	43
2.3	Extended Tests of the DE Engines	46
2.3.1	Facility	48
2.3.2	281-Hour Test	48
2.3.3	Long Duration Test with Aluminum	71
2.4	DF Engine	78
2.4.1	Electrodes	78
2.4.2	Distributed Magnet Windings	79
2.4.3	Autocathode	79
2.4.4	Electrode Support System	81
2.4.5	Lightweight Engine	81

## CONTENTS (contd)

3.	DF ENGINE TESTS	90
3.1	Facility and Test Equipment	90
3.2	Performance Mapping	92
3.2.1	Measurements and Calculations	92
3.2.2	Results	96
3.3	Extended Duration Tests	96
3.3.1	Operating Level	101
3.3.2	878-Hour Test	101
3.3.3	880-Hour Test	108
3.3.4	838-Hour Test	114
3.4	Analysis of Components	118
3.4.1	Feed System	118
3.4.2	Engine Components	131
3.5	Conclusions	139
3.5.1	Performance	139
3.5.2	Engine Lifetime Limitations	140
4.	APPLIED RESEARCH	145
4.1	Plasma Distribution Studies	145
4.1.1	Ion and Neutral Efflux Distributions	145
4.1.2	Electrode Redesign	162
4.1.3	Inverted Engine	163
4.1.4	Magnetic Field Modification	165
4.2	Conceptual Design of Large Engine	173
4.2.1	Scaling Requirements	173
4.2.2	Supporting Tests	176
4.2.3	Conceptual Design	180
4.3	Autocathode Studies	186
4.3.1	Autocathode Starting Characteristics	186
4.3.2	Operating Characteristics	189
4.3.3	Improved Cathode	196

## CONTENTS (contd)

4.4	Permanent Magnet Engines	199
4.4.1	Magnetic Field Requirements	200
4.4.2	Permanent Magnet Modification of a DE Engine	204
4.4.3	Permanent Magnet Engine	209
4.4.4	Performance	215
4.5	Advanced Neutralizers	224
APPENDIX A - Quality Assurance		

## ILLUSTRATIONS

1	Residual Drain Current Versus Gap Voltage, Molybdenum Electrode	5
2	Residual Drain Current Versus Gap Voltage for Two Polarities, Molybdenum Electrode	5
3	Temperature and Oxygen Dependence of Drain Current	9
4	Cathode Mounting Plate After High Drain Test	9
5	Cooled-Copper Accelerator Electrode After 57-Hour Test	12
6	Heater Ring Clamped on Electrode Assembly	14
7	Drain Current and Accelerator Electrode Temperature Response Characteristics for Molybdenum Electrode	14
8	Electrode Temperature and Drain Current Versus Time for Molybdenum Electrode Heating Test	16
9	Electrode Temperature and Drain Current Versus Time for Aluminum Electrode Heating Test	16
10	Aluminum Electrode Current and Temperature at Time of Destruction	18
11	Destroyed Aluminum Electrode	18
12	Electrode Temperature and Drain Current Versus Time for Titanium	20
13	Electrode Temperature and Drain Current Versus Time for Titanium Electrode at Reduced Beam Level	20
14	Electrode Temperature and Drain Current Versus Time for Iron Electrode Heating Test	22
15	Electrode Temperature and Drain Current Versus Time for Continuous Test with Iron	22
16	Accelerator Temperature and Drain Current Versus Time for Tantalum Electrode Heating Test	25
17	Drain Current Versus Pressure for Various Electrode Materials	25
18	Extended Tests with Various Electrode Materials	26

# ILLUSTRATIONS (contd)

19	Accelerator Temperature and Drain Current Versus Time for Copper Accelerating Electrode	28
20	Sputtering Target Assembly with Secondary Electron Collector Removed	31
21	Assembled Sputtering Apparatus	32
22	Sputtering Yield of Aluminum Versus Bombarding Cesium Ion Energy	35
23	Schematic of Apparatus for Emittance Measurements by the Free Cooling Technique	38
24	Aluminum Emittance Measurements	40
25	Emittance Versus Temperature for Several Surface Conditions of Aluminum Samples	42
26	750-Hour Feed System and Solenoid-Operated Feed Valve	44
27	Manually-Operated Cesium Valve	45
28	Manual Valve	45
29	New Port Valve	47
30	Facility for Extended Tests of the DE Engine System	49
31	Vaporizer Power History for 281-Hour Test	50
32	Drain Current Versus Time for the Last 201 Hours of the 281-Hour Test	50
33	Accelerating Electrode Temperature and Drain Current After Test Termination	54
34	Accelerator Drain Current Versus Gap Voltage	54
35	Drain Current Versus Gap Voltage for Reversed Polarity Test	55
36	Schottky Plot for Reversed Voltage Test	55
37	DER-1 Engine System After 281-Hour Test	57
38	Orifice Plate and Cathode	58
39	Anode and Chamber Interior	58
40	Engine Shell with Electrodes Attached	60
41	Electrode Insulators	61
42	Screen Electrode	61
43	Accelerating Electrode - Downstream Side	62

## ILLUSTRATIONS (contd)

44	Cross Section of Deep Pit in Accelerating Electrode	62
45	Cross Section of Shallow Pit in Accelerating Electrode	64
46	Accelerating Electrode - Upstream Side	64
47	Solenoid Valve Components	68
48	End View of Vaporizer Surface	68
49	Porous Rod and Vaporizer Assembly	69
50	Location of Samples Taken for Analysis	69
51	Drain Current Versus Time Profile for 238-Hour Aluminum Electrode Test	75
52	Downstream Side of Aluminum Electrode After 238-Hour Test	76
53	Upstream Side of Aluminum Electrode After 238-Hour Test	76
54	Distributed Electromagnet Winding	80
55	DF Engine with 750-Hour Feed System	82
56	DF Engine System, Side View	83
57	End View of DF Engine System Showing DF Electrode	84
58	DF-S Lightweight Electromagnet Engine	85
59	DF-S and DF-1 Magnetic Field Plots	87
60	DF-S and DF-1 Overall Engine Efficiencies	88
61	DF-S and DF-1 Power-to-Thrust Ratios	89
62	Engine Test Chamber	91
63	DF-1 Engine Overall Efficiency Versus Specific Impulse	98
64	Power-to-Thrust Ratio Versus Specific Impulse for DF Engine	99
65	DF Engine Thrust Versus Specific Impulse	100
66	DF Engine and Feed System After 878-Hour Test	105
67	DF Engine and Feed System After 878-Hour Test	106
68	DF Engine and Feed System After 878-Hour Test	107
69	DF-1 Engine System After 1,772 Hours Cumulative Operation	111



# ILLUSTRATIONS (contd)

70	DF-1 Engine System After 1,772 Hours Cumulative Operation	112
71	DF-1 Engine System After 1,772 Hours Cumulative Operation	113
72	DF-1 Engine After 2,610 Hours Cumulative Operation with Feed System Removed	119
73	DF-1 Engine After 2,610 Hours Cumulative Operation with Feed System Removed	120
74	DF-1 Engine After 2,610 Hours Cumulative Operation with Feed System Removed	121
75	Time Dependent Functions from 2,610-Hour Test	122
76	Position of Samples Taken from Porous Rod	124
77	DF-1 Cathode After 2,610 Hours Cumulative Operation	132
78a	Cross Section of DF-1 Cathode Emitter	133
78b	Control Sample	133
79a	Cross Section of the Deepest Pit (X75)	137
79b	Cross Section of the Deepest Pit (X16)	137
80	Accelerator-Electrode Aperture Cross Section	138
81	Extrapolations of Erosion Pit Breakthrough	142
82	Extrapolations of Erosion Pit Breakthrough	142
83	Extrapolations of Erosion Pit Breakthrough	142
84	DF Accelerator Electrode with Holes Drilled Through at Erosion Pit Locations	143
85	Schematic of Scanning Neutral Detector Experiment	146
86	Variation of Neutral Efflux Distribution with Beam On, Beam Off, and Arc Off Conditions	148
87	Neutral Efflux Distribution with Varied Magnetic Field	148
88	Beam Density Distribution Variations with Magnetic Field	149
89	Neutral Efflux Distribution Variation with Magnetic Field	149
90	Neutral Efflux Distributions with Different Cathode Orifice Configurations	151

## ILLUSTRATIONS (contd)

91	Ion Beam Current Density Distributions	153
92	Variation of Ion Current Density Distribution with Source Potential	154
93	Variation of Ion Current Density Distribution with Accelerator Potential	155
94	Variation of Ion Current Density Distribution with Magnetic Field	156
95	Liquid-Nitrogen-Cooled Neutral Detector	158
96	Liquid-Nitrogen-Cooled Scanning Neutral Detector	160
97	Effect of Sweep Electrode Potential Variation	160
98	Neutral Efflux Distributions	161
99	Inverted Engine Design	164
100	PM Engine Field Configurations	167
101	Electromagnet Field Configurations	168
102	DE and Distributed Coil Fields Off-Axis	169
103	Distributed Coil Engine Efficiencies	170
104	Source Efficiency Variations with Magnetic Field Divergence	172
105	Axial Magnetic Field Components of DF and 20-cm Engine	177
106	Ion Current Distributions for 20-cm Engine	179
107	20-cm Source Electrode Systems	181
108	Schematic of Interelectrode Gap Spacer	182
109	30 KW Ion Engine	183
110	Internally-Heated DE Cathode with Orifice Plate Removed	187
111	Cold Cathode Start-Up Profile	188
112	Effect of Orifice Diameter on Source Efficiency	191
113	Externally Heated Cathode	192
114	External Heater Autocathode Design	197
115	External Heater Autocathode	198
116	Permanent Magnet Engine Configurations	203
117a	Axial Component of Magnetic Field of DE Engine with Electromagnets	205

## ILLUSTRATIONS (contd)

117b	Plot of Magnetic Field Lines for DE Engine with Electromagnets	205
118a	Axial Component of Magnetic Field of DE Engine with Permanent Magnets	207
118b	Plot of Magnetic Field Lines for DE Engine with Permanent Magnets	207
119	DE Engine with Permanent Magnet Modification	208
120	Permanent Magnet Engine Design	211
121	Permanent Magnet Engine	213
122	Permanent Magnet Engine Magnetic Field	214
123	Mass Utilization Efficiencies of PM-1 and DE Engines	218
124	PM-1, PM-2, and DE Engine Overall Efficiencies	222
125	PM-1, PM-2, and DE Engine Power-to-Thrust Ratios	222
126	Schematic of Plasma Bridge Neutralizer	225
127	Electrical Schematic for Neutralizer Tests	227
128	Beam Current versus Accelerator Bias	230

## LIST OF SYMBOLS

$\gamma$	Conductivity of loop
$\epsilon_t$	Total hemispherical emittance
$\eta_E$	Overall engine efficiency
$\eta_M$	Mass utilization efficiency
$\eta_p$	Power efficiency
$\rho$	Density
$\sigma$	Stefan Boltzmann constant
$\tau_m$	Monolayer time interval
$\frac{dT_a}{dt}$	Slope of cooling curve
$e$	Electronic charge
$g$	Acceleration due to gravity at earth's surface
$k$	Boltzmann's constant
$\ell$	Length of magnetic cylinder
$m$	Mass of molecule
$m_T$	Mass of target atom
$\dot{m}$	Total mass flowrate
$\dot{m}_+$	Flow rate of accelerated ions
$n_a$	Number of atoms sputtered from target material
$n_i$	Number of bombarding ions
$p$	Partial pressure
$q$	Charge per ion
$r$	Loop radius
$r/a$	Normalized radius
$t$	Exposure time
$v_M$	Volume of magnetic material

A	Cross-sectional area of loop
$A_g$	Cross-sectional area of engine
$A_s$	Surface area
B	Field strength of engine
$B_o$	Field at center
$B_R$	Maximum residual flux density
$\Delta B_z/B_{z_{max}}$	Linear field divergence
C	Specific heat
I	Loop current
$I_A$	Arc current
$I_B$	Beam current
$I_{Cs}$	Neutral particle current equivalent
$I_M$	Magnet current
$I_{NCD}$	Neutral cesium detector
$I_o$	Total flowrate (in current equivalent)
$I_{sp}$	Specific impulse
$I_+$	Ion current
$I_-$	Negative HV supply current (drain current)
K	Form factor
M	Mass
$M_{Cs}$	Mass of cesium ion
$N_+$	Number of ions leaving engine per second
P	Pressure
$P_A$	Arc power
$P_B$	Beam power
$P_D$	Drain power
$P_M$	Magnet power
$P_T$	Total power
$P_A/I_B$	Source power per ion
P/T	Power-to-thrust ratio
R	Loop resistance

S	Sputtering yield
T	Thrust
$T_a$	Absolute temperature
$T_A$	Accelerator electrode temperature
$T_C$	Cathode housing temperature
$V_A$	Arc voltage
$V_B$	Exhausted beam potential
$V_M$	Magnet voltage
$V_+$	Positive high voltage
$V_-$	Negative high voltage
W	Weight of loop
$\dot{W}$	Weight flowrate of propellant
X	Particle flux per unit pressure
Z	Number of molecules striking a unit surface in a unit time

## SUMMARY

This summary report of the period 24 February 1964 to 25 June 1965 describes the work performed under Contract NAS3-5250, "Ion Rocket System Research and Development." The objective of the program was to demonstrate reliability and long life through extended tests of an engine and zero-gravity feed system. Through life testing and development of improved engine components an engine with a projected minimum lifetime of 10,000 to 20,000 hours was obtained. Three consecutive tests of one such engine and feed system ran until the cesium supply was exhausted for an accumulated time of 2610 hours. Less than one percent of the initial cesium load remained in the feed system at the termination of each test.

Applied research programs led to the development of both electromagnet and permanent magnet engines with overall efficiencies ranging from 55 percent at 3000 seconds to 87 percent at 9000 seconds. The nominal operating level for both engines was 10 mlb of thrust at a specific impulse of 7000 seconds and a power-to-thrust ratio of 182 kw/lb.

A conceptual design study of a large engine, with supporting tests of new concepts, culminated in a design of an engine expected to have a thrust of 100 mlb at 5000 seconds specific impulse and a power-to-thrust ratio of 145 kw/lb.

Tests of an advanced neutralizer concept developed at EOS were conducted at the end of the program using a permanent magnet engine.

## 1. INTRODUCTION

The work described in this report was performed under Contract NAS3-5250 administered by the National Aeronautics and Space Administration's Lewis Research Center (NASA-LeRC). This program was a follow-on to completed contract NAS3-2516 and was based on continued development and testing of the 10 mlb thrust engine and feed system developed under that contract and applied research related to improvement of the 10 mlb engine. This report describes the development and testing of an improved engine which operated successfully for 2610 hours, research on autocathode, studies of the plasma distributions, and development of a lightweight permanent magnet engine. A conceptual design of a 100 mlb engine is presented.

### 1.1 Previous Work

The first demonstration that a low density plasma might make a satisfactory ion source for electric propulsion was made by H. Kaufman of NASA-LeRC in 1960.

The Kaufman source, using mercury as propellant, consists of a thermionic cathode placed inside a cylindrical anode with a magnetic field parallel to the axis of the system. A plasma is generated within the cylinder, and those ions which drift to one end are extracted through apertures in a screen by an accelerating electrode. This source differs from the Finkelstein oscillating-electron source primarily in the use of the gridded anticathode or screen electrode through which ions are withdrawn. The mercury ion engine has since been brought to a very high state of development by Kaufman and Reader at NASA-LeRC.

In 1961, following the Kaufman source, Forrester and Speiser of EOS proposed the use of cesium in an electron-bombardment ion engine to take advantage of several unique properties of



such a system. The source differs from the mercury source in that cesium is introduced through the cathode which is a cesiated thermionic emitter. In addition, the cathode is heated by ion bombardment from the plasma. This is feasible in the cesium source because the bombarding energy is below the sputtering threshold. Other advantages accruing from the use of cesium are lower arc voltage, lower magnetic field, the absence of doubly charged ions, and a very high percentage of ionization.

The cesium ion source was investigated at EOS under Contract NAS8-2511, "Study of a Gas Discharge Cesium Ion Source." Two engines, 6.5 and 10 cm in diameter, which were built and tested proved the feasibility of the use of cesium.

Under a follow-on contract from NASA-LeRC (Contract NAS3-2516) a 12.5 cm source was developed. Complete engine systems including zero-gravity feed systems and laboratory power supplies and control systems were developed. At the end of this program two complete engine systems were delivered to NASA-LeRC. A description of these systems may be found in Ref. 1. These systems were used extensively under the program herein reported.

### 1.2 Program Objectives

The objectives of this program were to continue development and testing of the engine system developed under Contract NAS3-2516 (engine system designated DE) to achieve demonstrated long life and reliability. It included elimination of short and long term failure modes and evaluation of lifetime limitations. A quality assurance and reliability program was followed on this task.

In addition to the long-life engine and feed system program, three research and development programs were conducted. They were:

1. Design, fabrication, and testing of a permanent magnet version of the DE engine.
2. Plasma distribution studies to investigate basic means of improving engine operation and lifetime.

3. Autocathode improvement studies to reduce the starting requirements of cesium election bombardment ion engines.

A preliminary study of engine scaling parameters based on existing engine characteristics and a conceptual design of a large engine was the last program objective.

### 1.3 Organization of Report

Development of components of the DE engine system conducted under the long-life engine and feed system program is described in Section 2. The DF engine system was developed with input from the applied research tasks. Section 3 describes the three long tests of the DF engine system in which 2610 hours of operation were accumulated on a single engine and feed system. The applied research tasks and conceptual design of a large engine are described in Section 4.

Appendix A describes the quality assurance plan used on the long life engine and feed system program. It includes a summary of the quality activities conducted during the program.

The authors wish to thank Mr. G. E. Trump for his assistance with the feed systems, Mr. K. G. Wood and Mr. V. V. Fosnight who worked on engine development and testing, and Mr. D. P. West, our designer. Special thanks are due Mr. D. L. Henderson who performed the emittance measurements and Dr. J. Perel and Mr. H. L. Daley who performed the sputtering measurements.

## 2. ENGINE COMPONENT DEVELOPMENT

This program began with the DE engine system which is described in detail in Ref. 1. Refinements of the DE engine design and some new components were required for extended testing. Electrode materials were studied and a feed system capable of operation for over 750 hours was developed. Tests of 281 hours and 231 hours were then conducted with a DE engine system. Improvements in engine design resulting from the applied research effort were incorporated and the system designated DF was developed.

### 2.1 Electrode Materials Tests

A test of the DE engine system conducted early in the program was terminated after 23 hours of operation when the accelerator electrode drain current rose to 25 mA or nearly six percent of the beam current.

These high drain conditions, occurring with a molybdenum accelerating electrode, were investigated. Selected electrode materials were evaluated on the bases of performance on an operating engine and sputtering yield. Emittance measurements were made on aluminum.

#### 2.1.1 High Drain Current Mechanism

After the 23-hour test was terminated, high voltage was turned back on and the drains were measured as a function of accelerator gap voltage as the engine cooled. The results are shown in Fig. 1. The temperatures were measured at the engine shell and are only roughly indicative of the screen electrode or accelerator electrode temperatures. The drain current - gap voltage relationship is highly nonlinear and suggests a field-enhanced emission effect, although the temperatures and magnitude of the field in the gap are much too low to give these phenomena for cesiated molybdenum.

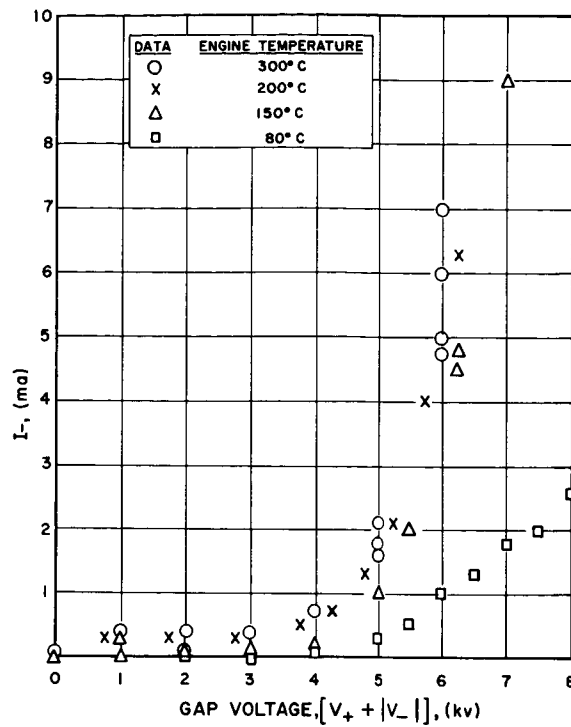


FIG. 1  
RESIDUAL DRAIN CURRENT  
VERSUS GAP VOLTAGE,  
MOLYBDENUM ELECTRODE

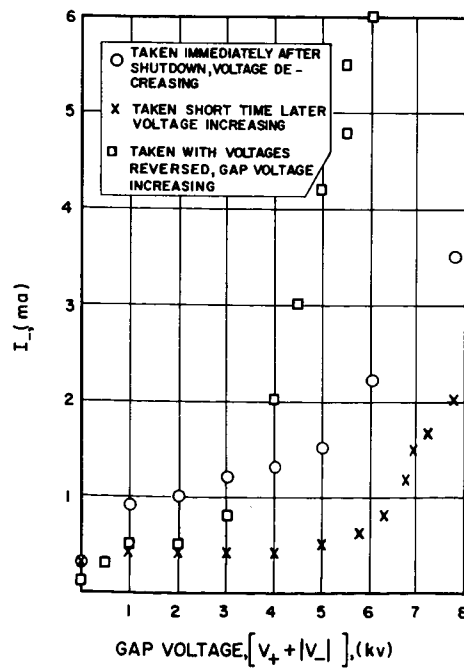


FIG. 2  
RESIDUAL DRAIN CURRENT  
VERSUS GAP VOLTAGE FOR  
TWO POLARITIES, MOLYB-  
DENUM ELECTRODE

After a long cooling period, the engine was restarted and after several hours high drains were again encountered. The feed system and arc power were removed and the data of Fig. 2 taken. For the two sets of data taken for normal polarity, the differences are partly due to cooling of the system but there was a significant hysteresis effect. The voltages applied to the electrodes were then reversed and the third set of data taken. The higher current for this case was significant as it indicated that the electrode surface effect giving rise to the drain current was more pronounced on the screen electrode than on the accelerating electrode. Since the screen electrode ran hotter and presumably stayed hotter than the accelerating electrode during the time both were cooling, the higher current with reversed polarity was consistent with an electron emission hypothesis.

Although not conclusive, these data and other information to be discussed led to the following hypothesis. With time, a composite Cs-O-Mo surface forms on the molybdenum accelerating electrode. The electrode temperature, surface conditions, and electric field are such that electron emission occurs. The electron current, accelerated across the gap, heats the screen electrode and engine. Subsequently, by conduction and radiation, the accelerating electrode is heated which increases the electron emission. The drains then continue to increase to a high value by this mechanism.

Although the Malter effect may play a role, the main mechanism is probably field-enhanced thermionic emission or the Schottky effect. Anomalies introduced by "patch effects" lead to the anomalous Schottky effect in which the current-voltage relationship may be such as that observed in Figs. 1 and 2.

Accelerating electrode temperatures were measured for operating engines. For typical operating conditions the temperature was determined to be about  $300^{\circ}\text{C}$  in the center and about  $270^{\circ}\text{C}$  at the periphery. At these temperatures, Schottky-enhanced thermionic emission from a Cs-Mo surface would be much too small to explain the

observed drain currents, but emission from a Cs-O-Mo surface would be about 1000 times higher and in the right range. Experiments investigating the drain currents in contact cesium ion engines are reported in EOS Report 3830-Final, "Applied Research on Contact Ionization Thrustor," (APL TDR 64-52)<sup>2</sup>, pages 329-367. In these experiments it was found that under conditions in which the accelerating electrode temperature was at about 300°C, the admission of oxygen into the vacuum system increased the drain current by a factor of 5. This test was made with a copper electrode but the drain mechanism is probably the same.

The Cs-O-Mo surface exhibits high electron emission in an intermediate temperature range (perhaps 300-700°C). At lower temperatures the composite surface exists but is too cool to give high emission. At higher temperatures, the composite surface is decomposed and the work function is too high to give high emission.

Other evidence exists that the drains are due to electron emission from the accelerating electrode. As the drains increase, the temperature of the cathode mounting plate at the rear of the engine is observed to increase. This is considered to be due to bombardment of the plate by some of the electrons accelerated across the accelerator gap. The high energy of these electrons (4-5 kev) is such that only a small fraction of the electrons need pass through the screen electrode apertures to provide the observed cathode plate heating.

#### Temperature Dependence

A series of measurements of the accelerator drain current as a function of accelerator temperature were made to determine the effect of temperature and oxygen on the drain current.

For these tests a heater was brazed around the periphery of the hole pattern of a molybdenum accelerator electrode and a thermocouple was attached to the support point of the accelerator. A bleed valve was connected to the vacuum system for admission of air or oxygen.

The engine was operated at approximately 8 millipounds thrust with a screen-to-accelerator potential difference of 5000 volts. The reduced thrust level was used to allow the accelerator to operate below its normal operating temperature. The neutral efflux was adjusted to be equivalent to 40-50 mA corresponding to the neutral efflux under full thrust conditions. With steady-state operation established the accelerator heater was turned on. Drain current was recorded as a function of temperature until the accelerator temperature reached 300°C. The heater was then turned off and drain current was recorded as a function of temperature until the initial operating conditions were regained.

The data obtained are shown by the circled data points in Fig. 3. The apparent hystereses in the data are probably due to slow changes in the equilibrium surface conditions on the accelerator and to a temperature difference between the emissive surface and the point at which the thermocouple was attached. The length of the support arm coupled with the heat capacity of the support insulator and shield should cause the measured temperature to lag the temperature of the electrode proper. A very strong temperature dependence is shown by the data of Fig. 3.

After returning to the original operating level, oxygen was admitted to the vacuum system until the pressure had risen from about  $10^{-6}$  torr to  $10^{-5}$  torr. A slight increase in drain current was noted as the pressure increased. When the pressure reached  $10^{-5}$  torr, the bleed valve was closed and a sharp rise in drain current was observed. The system was allowed to regain the initial conditions and the heating and cooling test was repeated. The data obtained are shown by the crossed data points (+) in Fig. 3. These data show a significant increase in the drain current during the early portion of the heating cycle with no hysteresis apparent in the higher temperature data. The oxygen admission had apparently increased the electron emission at the lower temperatures. The heating above 270°C, however, seems to have returned the electrode to its original surface condition.

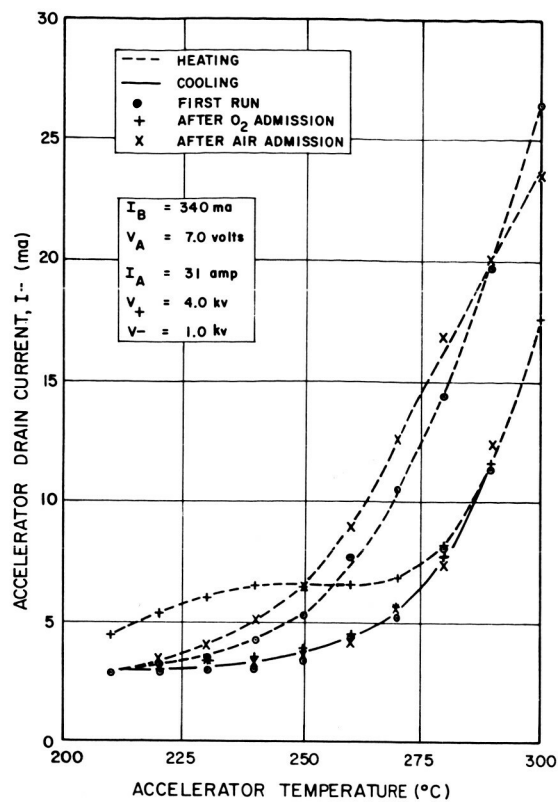


FIG. 3  
TEMPERATURE AND OXYGEN  
DEPENDENCE OF DRAIN  
CURRENT

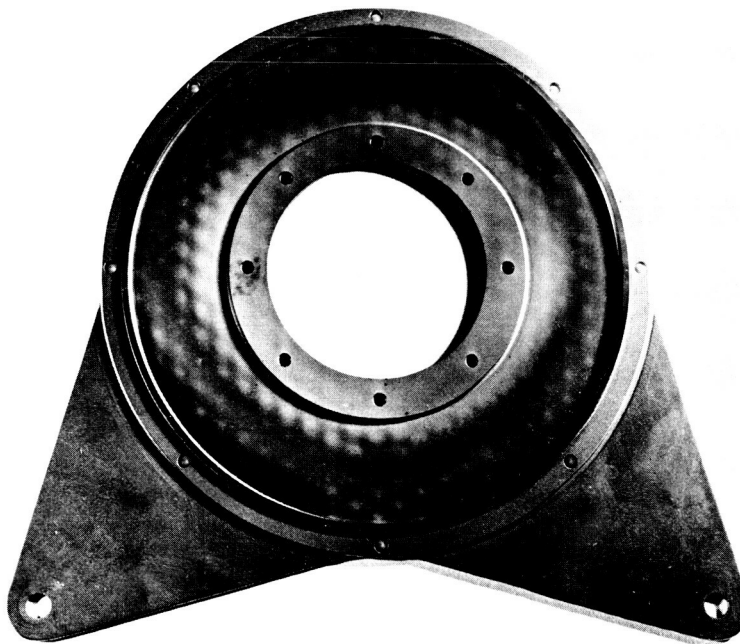


FIG. 4  
CATHODE MOUNTING PLATE  
AFTER HIGH DRAIN TEST



A third set of data was taken after air was admitted to the vacuum system in a manner similar to the previous admission of oxygen. These data are shown by the X's in Fig. 3. This curve is quite similar to the curve obtained during the first run and indicates that the electrode surface had indeed been returned to its initial condition.

During all three tests, significant increases in cathode temperatures were measured when the drain current was high. At times, drain currents higher than 50 mA were observed. Upon disassembly of the engine, a pattern of "clean" spots was observable on the cathode plate which closely matched the electrode pattern. A photograph of this cathode plate is shown in Fig. 4. These spots are considered to be due to electrons accelerated across the electrode gap and through the screen apertures.

Some sources of error in this experiment must be considered. As noted, the measured temperature is in error due to the location of the thermocouple. Secondly, the fact that these tests were performed sequentially may have had some effect not discussed above. Finally, variations in the heating rates used could have caused the observed results. This would not be a variable during the cooling portion of the tests. It must be concluded, since the cooling curves were identical, that either the original surface condition was regained after heating or the surface condition was not altered by the admission of pure oxygen. Finally, the conditions required to sustain the high drain currents at lower temperatures are elusive and even transient (high drain was encountered immediately after closing the oxygen valve) during short term testing.

The data do imply, however, that a molybdenum electrode designed to run at 230°C or less might not encounter the high drain conditions.

### Cooled Copper Electrode Tests

Since the drain current situation appears to be particularly unfavorable for a molybdenum electrode, it was decided to test the engine with a copper electrode and to run it cooler by providing a large radiating area.

The cooled copper electrode is shown in Fig. 5. It was fabricated by brazing a DE design copper accelerating electrode to a 13-inch-outer-diameter heavy copper fin. The large copper ring was grooved to enhance its emissivity.

With this electrode an extremely stable beam with little or no arcing was achieved. The engine was run for 56.9 hours but was interrupted several times by vacuum system and negative high voltage power supply malfunctions.

The engine was operated at a net accelerating potential of 4 kv and a beam current of 405 mA. During the run, the drain current was between 8.5 and 9.5 mA and showed no tendency to increase with time. The electrode temperature was 190°C compared with 270°C measured at the same point for a molybdenum electrode.

The run was terminated by an increase in pressure in the vacuum system resulting from the decomposition of an insert in a power plug used with the engines. This decomposition occurred due to the excessive heat generated by the arc current passing through terminals in the plug. For subsequent tests, both anode and cathode (large current) power leads were routed directly to the engine to bypass this plug.

#### 2.1.2 Heated Electrode Tests

Accelerating electrodes of molybdenum, aluminum, titanium, iron, tantalum, and copper were tested with DE engines. The molybdenum electrode had a sheathed heater (tantalum-magnesium oxide-tantalum) brazed to its peripheral area on the downstream side. Because of difficulty

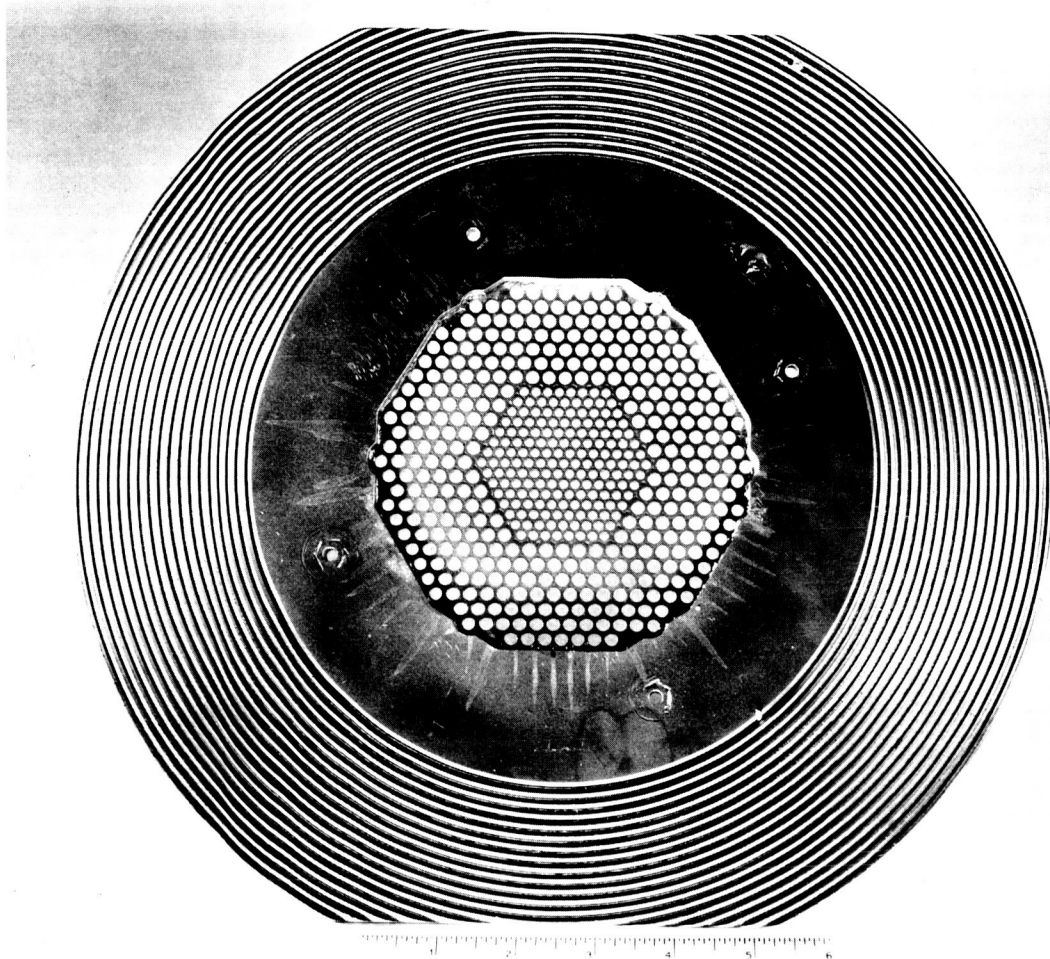


FIG. 5 COOLED-COPPER ACCELERATOR ELECTRODE AFTER 57-HOUR TEST

in brazing heaters to all of the materials tested, a separate heater ring was designed for use with the other electrodes. A stainless steel ring was fabricated and a heater brazed in a groove cut in the ring. This ring was used to heat the electrodes being tested for electron emission characteristics. Figure 6 shows an accelerator electrode assembly with the heater ring installed. The ring is clamped to the electrode with the brazed side facing downstream. This procedure was adequate for the testing undertaken. Electrode temperatures could be raised a hundred degrees centigrade or more over normal operating temperature.

#### Molybdenum Electrode Test

At the start of the molybdenum electrode test, with the engine in normal operation, some time constants associated with the temperature and drain current were investigated. Electrode temperature and drain current response to the application of 10 watts power to the accelerator electrode heater are shown in Fig. 7. For heating or cooling the electrode, the temperature changed by 1/e of the total change in about 5 minutes. The drain current exhibited a 12-minute time constant for heating and a time constant of only 4 minutes for the cooling portion of the curve. This explains why previous data (EOS Report 4920-Q-2; NASA CR-54026) taken for the drain current as a function of temperature exhibited hysteresis.

The engine system was then brought to the following steady-state operating conditions:

Positive High Voltage, $V_+$	4.2 kv
Negative High Voltage, $V_-$	-0.6 kv
Beam Current, $I_B$	410 mA
Negative HV Current, (drain current), $I_-$	4.7 mA
Accelerator Electrode Temperature, $T_A$	274°C
Arc Voltage, $V_A$	8.0 volts

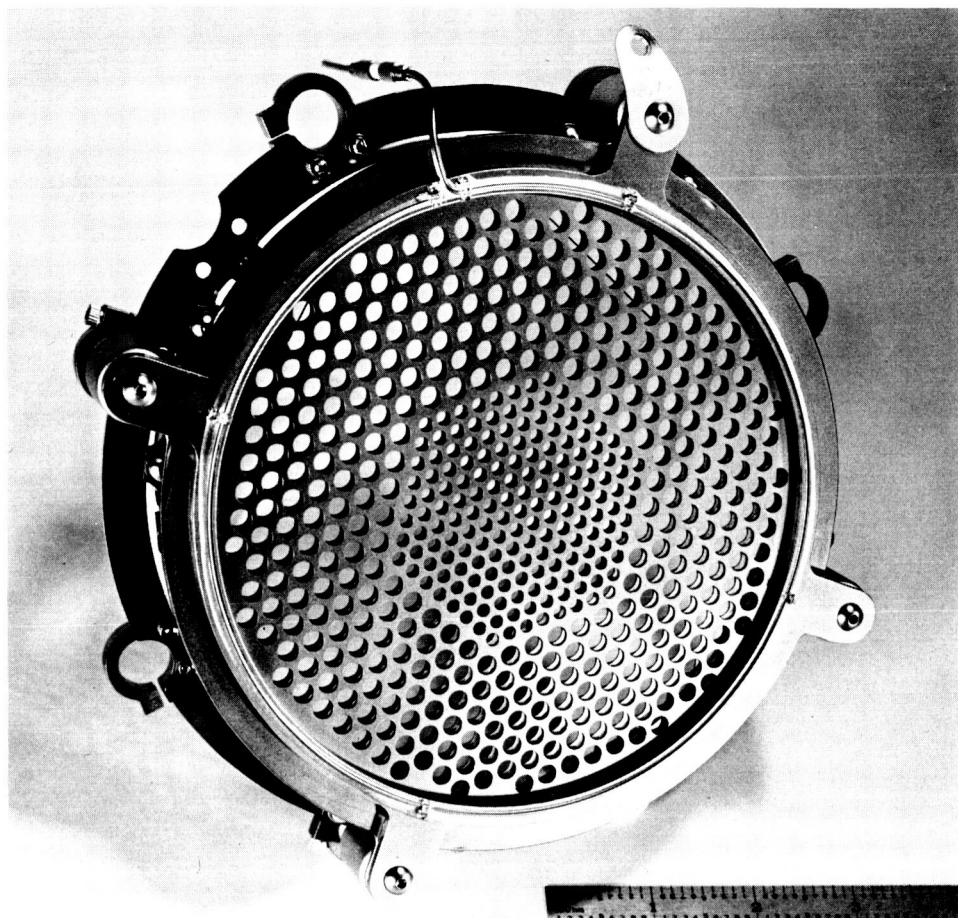


FIG. 6 HEATER RING CLAMPED ON ELECTRODE ASSEMBLY

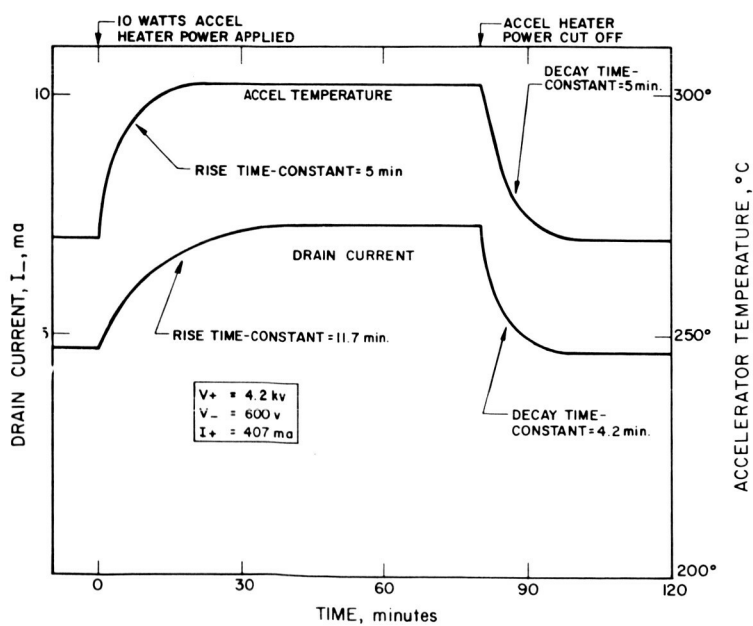


FIG. 7  
DRAIN CURRENT AND ACCELERATOR  
ELECTRODE TEMPERATURE  
RESPONSE CHARACTERISTICS FOR  
MOLYBDENUM ELECTRODE

Arc Current, $I_A$	40.5 amp
Cathode Housing Temperature, $T_C$	451°C
Chamber Pressure, P	$1.8 \times 10^{-7}$ mm Hg
Neutral Efflux (equivalent current)	~ 40 mA

Power was applied to the accelerating electrode heater in increments and the behavior of the accelerating electrode temperature and drain current was as exhibited in Fig. 8. With 12 watts applied to the accelerating electrode heater, the temperature was stabilized at about 312°C and the drain current at about 10 mA. The addition of one more watt accelerating electrode heater power started a slow runaway. The power was increased to 14 watts and the drain current and accelerating electrode temperature increased sharply.

When the drain current was up to 125 mA with accelerating electrode temperature at 360°C, the heater power was removed and conditions changed rapidly. The system recovered completely and returned to the initial steady-state operating conditions. Several tests were performed with the same results. The runaway appeared to be initiated at an accelerating electrode temperature of about 325°C and drain current of 12 mA. At the time of runaway, the cathode mounting plate temperature had increased by about 9°C.

#### Aluminum Electrode Test

An aluminum accelerating electrode was prepared and tested with a DE engine using the clamped heater system. The engine system was brought to the following steady-state operating conditions:

Positive High Voltage, $V_+$	3.8 kv
Negative High Voltage, $V_-$	-0.8 kv
Beam Current, $I_B$	412 mA
Negative HV Current, (drain current) $I_-$	8.0 mA
Accelerator Electrode Temperature, $T_A$	270°C
Arc Voltage, $V_A$	8.3 volts

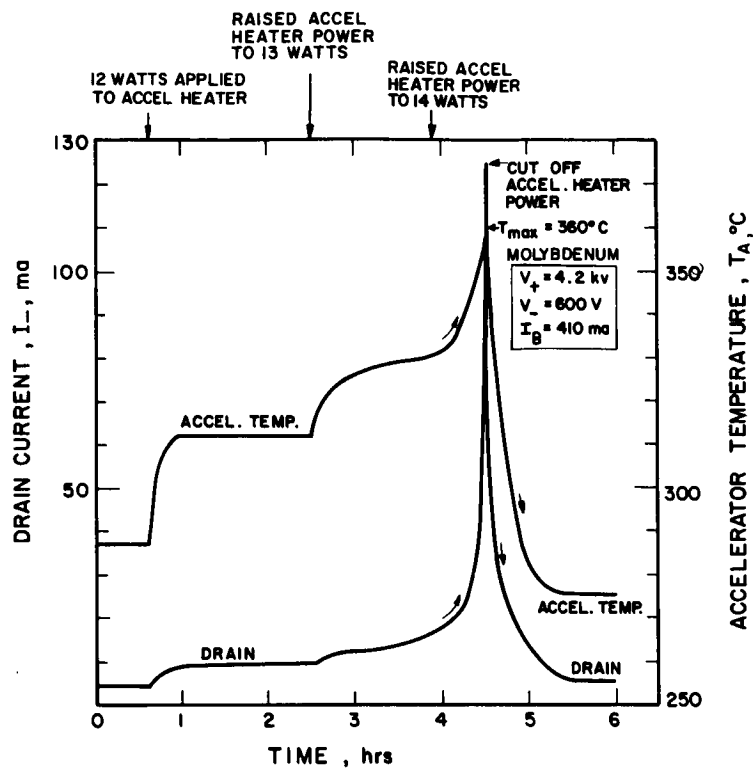


FIG. 8

ELECTRODE TEMPERATURE AND DRAIN CURRENT VERSUS TIME FOR MOLYBDENUM ELECTRODE HEATING TEST

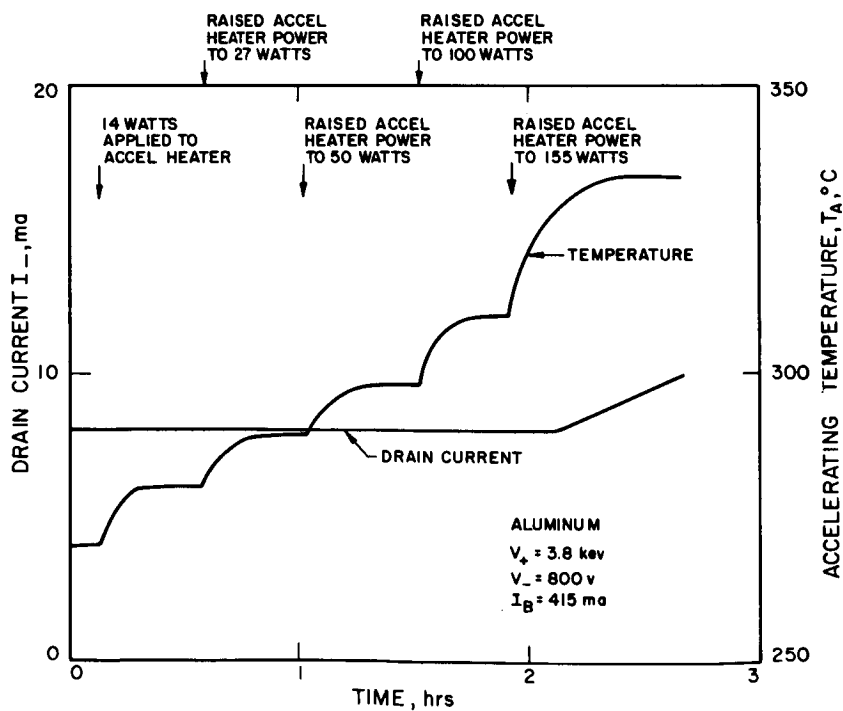


FIG. 9

ELECTRODE TEMPERATURE AND DRAIN CURRENT VERSUS TIME FOR ALUMINUM ELECTRODE HEATING TEST

Arc Current, $I_A$	42.0 amps
Cathode Housing Temperature, $T_c$	468°C
Chamber Pressure, P	$2 \times 10^{-6}$ mm Hg
Neutral Efflux (equivalent current)	~ 45 mA

Power was applied to the accelerating electrode heater in increments and the behavior of the electrode temperature and drain current was as shown in Fig. 9. With heater power inputs of 14, 27, 50, 100, and 155 watts, the electrode temperature stabilized at 280, 289, 298, and 334°C, respectively. The drain current remained constant at 8 mA until the accelerating electrode temperature reached about 330°C. At this point the drain current began to increase with time. This increase continued with the temperature stabilized at 334 degrees and was considered to be due to warping of the electrode. The drain current rose to 14 mA, at which point a malfunction of the arc power circuit necessitated the shutdown of the test. Throughout this test, the temperature of the cathode housing,  $T_c$ , remained constant, which indicated that the rising drain current was due to electrode warpage and not electron emission.

When the arc power circuit had been repaired, an attempt was made to restart the engine and repeat the test. The start went smoothly until a beam level of approximately 200 mA was reached. At this point severe arcing between electrodes occurred and the drain current began to rise. As viewed through a vacuum chamber window the electrode appeared to be severely bowed in the downstream direction. Heating power to the electrode (used in starting to provide smoother and more rapid starts) was immediately shut down. The electrode had by this time reached a temperature of approximately 270°C. The drain current continued to rise and it was impossible to obtain more than 250 mA of beam current. Electrode temperature rose steadily with the drain current (Fig. 10) until local heating melted a large hole in the aluminum grid. The test was terminated at this point.



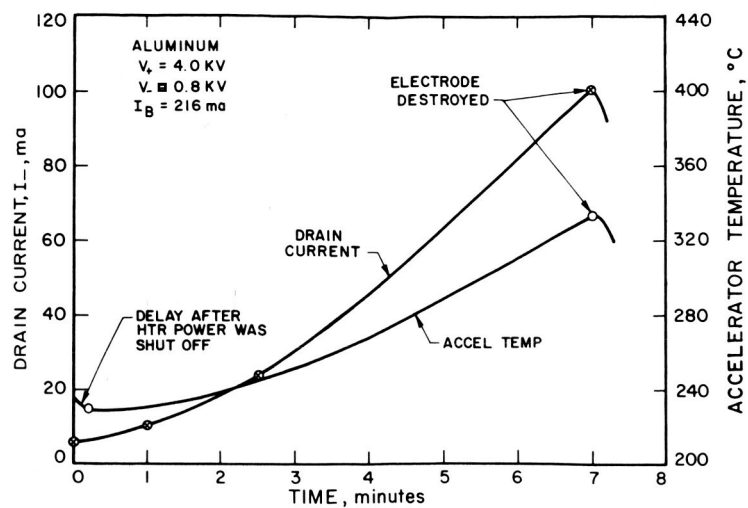


FIG. 10 ALUMINUM ELECTRODE CURRENT AND TEMPERATURE AT TIME OF DESTRUCTION

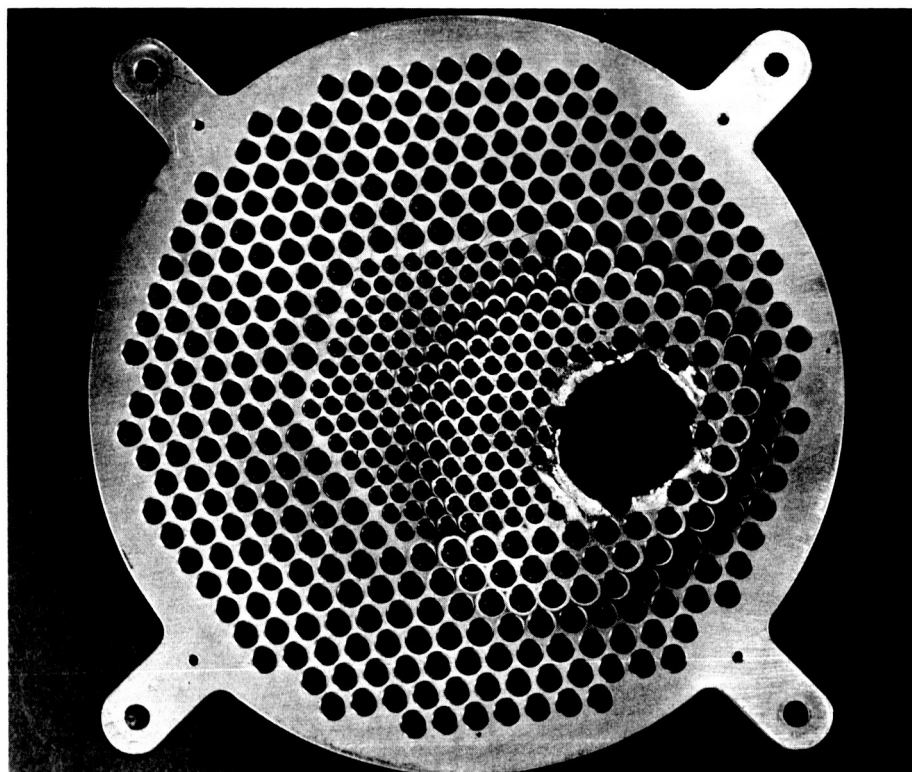


FIG. 11 DESTROYED ALUMINUM ELECTRODE

Inspection of the engine after it was removed from the facility revealed the accelerator electrode to be bowed approximately 1/2 inch in the downstream direction. The electrode had expanded and distorted in such a manner as to move webs between apertures in a portion of the accelerator electrode into the paths of beams from apertures of the screen electrode. A photograph of the accelerator electrode after the test is shown in Fig. 11. Although design problems are introduced because of the high coefficient of thermal expansion of aluminum, thermionic electron emission was undetectable.

#### Titanium Electrode Tests

A titanium electrode was then fabricated and tested with the DE engine. The clamped heater ring was again used. The engine was started automatically and brought to the following operating conditions:

Positive High Voltage, $V_+$	4.2 kv
Negative High Voltage, $V_-$	-0.7 kv
Beam Current, $I_B$	410 mA
Negative HV Current, (drain current), $I_-$	10 mA
Accelerator Electrode Temperature, $T_A$	200°C
Arc Voltage, $V_A$	8.0 volts
Arc Current, $I_A$	40.5 amps
Cathode Housing Temperature, $T_C$	479°C
Chamber Pressure, $P$	$1.5 \times 10^{-6}$ mm Hg
Neutral Efflux, (equivalent current)	~ 42 mA

The drain current was not stable at these conditions and immediately went into a runaway condition. A time profile of accelerator temperature and drain current variations during this runaway condition is shown in Fig. 12.

Since it was found to be difficult to obtain stable operation of the DE engine with a titanium electrode at the usual beam level (~ 400 mA), the beam was reduced to 240 mA to study drain current

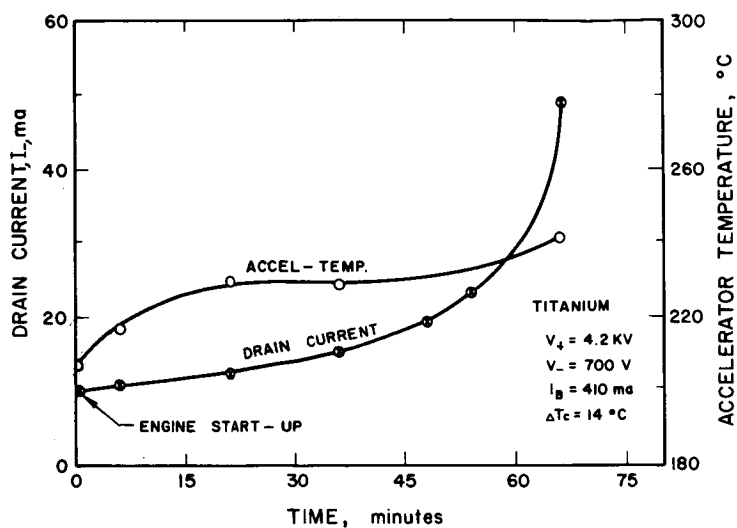


FIG. 12  
ELECTRODE TEMPERATURE AND  
DRAIN CURRENT VERSUS TIME  
FOR TITANIUM

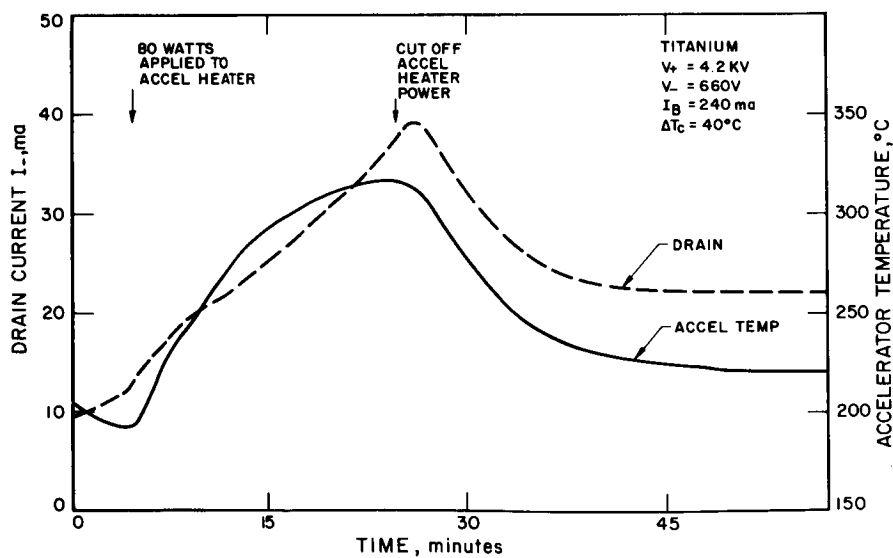


FIG. 13 ELECTRODE TEMPERATURE AND DRAIN  
CURRENT VERSUS TIME FOR TITANIUM  
ELECTRODE AT REDUCED BEAM LEVEL

as a function of accelerator temperature. Data from this test are shown in Fig. 13. It should be noted that although reducing the beam level lowered the drain current from the high level attained during runaway at full beam, the drain again began to increase immediately. When the accelerator temperature had dropped to  $191^{\circ}\text{C}$ , 80 watts of heater power were applied to the accelerating electrode. Both drain current and accelerator temperature rose steadily as shown. When it became obvious that the drain current was not going to stabilize, the accelerator heating power was turned off. The drain current leveled at 22 mA and the accelerator temperature at  $220^{\circ}\text{C}$ .

Because of its high drain current characteristics and its instability at normal operating conditions, titanium was not tested further.

#### Iron Electrode Tests

An iron electrode was also tested with the DE engine at about the same operating conditions as used with aluminum. Accelerator heater power was added in three steps, raising the electrode periphery temperature from  $238^{\circ}\text{C}$  to  $338^{\circ}\text{C}$ . Drain current increased in a like manner from approximately 7 mA to just over 44 mA. Figure 14 is a time profile of this test. At no time did a runaway condition ensue. Cathode temperature increased  $19^{\circ}\text{C}$  during the test indicating the presence of electron emission.

Although electron emission was present it was still not obvious that a runaway condition would result during a long duration test. A continuous run was started immediately following the heating tests. The operating conditions were as follows:

Positive High Voltage, $V_+$	4.2 kv
Negative High Voltage, $V_-$	0.55 kv
Beam Current, $I_B$	408 mA
Drain Current, $I_-$	8.1 mA
Accelerator Electrode Temperature, $T_A$	$232^{\circ}\text{C}$

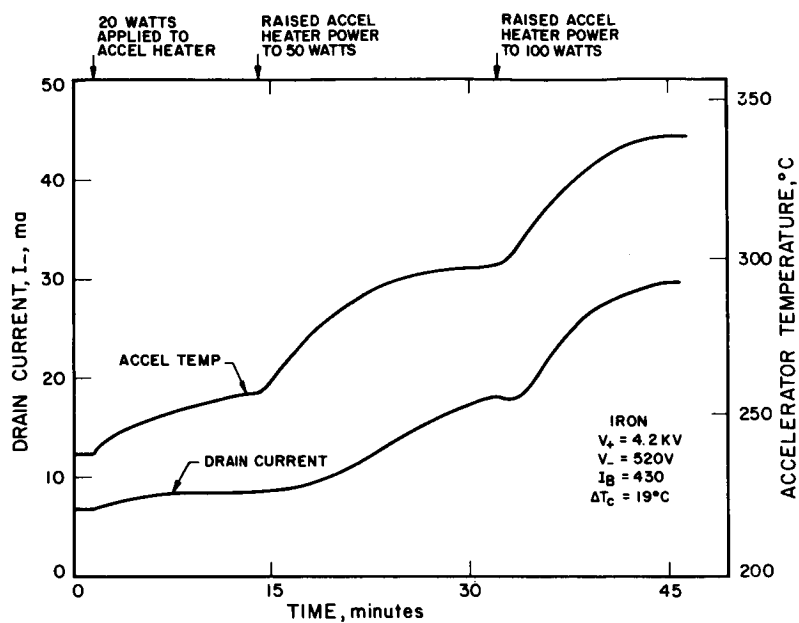


FIG. 14

ELECTRODE TEMPERATURE AND DRAIN CURRENT VERSUS TIME FOR IRON ELECTRODE HEATING TEST

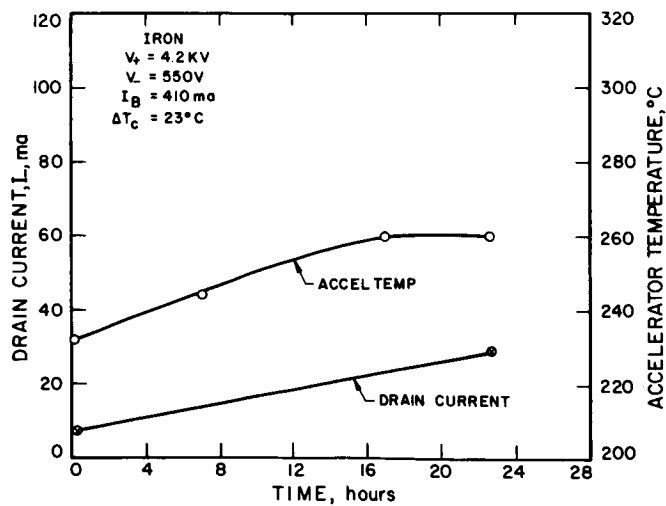


FIG. 15

ELECTRODE TEMPERATURE AND DRAIN CURRENT VERSUS TIME FOR CONTINUOUS TEST WITH IRON

Arc Voltage, $V_A$	8.0 volts
Arc Current, $I_A$	38.5 amps
Cathode Housing Temperature, $T_C$	455°C
Chamber Pressure, P	$3 \times 10^{-6}$ mm Hg
Neutral Efflux (equivalent current)	~ 48 mA

A time history of electrode temperature and drain for this run is presented in Fig. 15. An increasing drain condition was obtained at the start and the drain current increased by approximately 7 mA every 4 hours for over 20 hours. When the run was terminated, the cathode housing temperature had increased by about 20°C.

It was concluded that iron is not suitable for long-duration runs and that conditions similar to those encountered with molybdenum electrodes would result.

#### Tantalum Electrode Test

A tantalum accelerating electrode was then tested. The engine system was brought to the following steady-state operating conditions:

Positive High Voltage, $V_+$	4.2 kv
Negative High Voltage, $V_-$	-0.6 kv
Beam Current, $I_B$	405 mA
Negative HV Current, (drain current), $I_-$	4.9 mA
Accelerator Electrode Temperature, $T_A$	230°C
Arc Voltage, $V_A$	8.0 volts
Arc Current, $I_A$	40.0 amps
Cathode Housing Temperature, $T_C$	440°C
Chamber Pressure, P	$1.7 \times 10^{-7}$ mm Hg
Neutral Efflux (equivalent current)	~ 40 mA

After the engine operation had stabilized at these conditions, power was applied in increments to the accelerator heater, engine operation being allowed to stabilize between the addition of each heater power increment. The behavior of the accelerator temperature and the drain

current were as shown in Fig. 16. The drain current rose steadily with accelerator temperature throughout the run except for a sudden drop of about 0.3 mA after a high-voltage interelectrode arc which took place 20 minutes after the initial 5 watts of heater power were applied. The drop in drain current may have been due to a change in the composite surface on the accelerator due to the arc.

#### Pressure Dependence

Drain current versus pressure data, compiled from all of the electrode tests, are presented in Fig. 17. In general, the dependence is nonlinear. Doubling the ambient pressure raised the drain current from 10 percent to 50 percent for the various materials. Long tests are conducted at pressures of about  $2 \times 10^{-7}$  mm Hg where the effect of ambient pressure should be negligible.

#### 2.1.3 Extended Electrode Tests

In the course of the electrode material studies, the electrodes were also tested without the addition of electrode heater power. These tests were made at approximately the same engine operating levels as follows:

Positive High Voltage, $V_+$	$\sim 4$ kv
Negative High Voltage, $V_-$	$\sim -0.6$ kv
Beam Current, $I_B$	$\sim 400$ mA
Mass Utilization Efficiency	$\sim 90$ %

Drain current versus time data for all the materials are presented in Fig. 18. The copper data came from a 281-hour run described in paragraph 2.3 of this report. The aluminum data came from a 238-hour test also described in paragraph 2.3.

#### Copper Electrode Test

The copper electrode was prepared and tested with a DE engine using the clamped heater system (EOS Report 4920-ML-8)<sup>3</sup>. The engine system was brought to the following steady-state operating conditions:

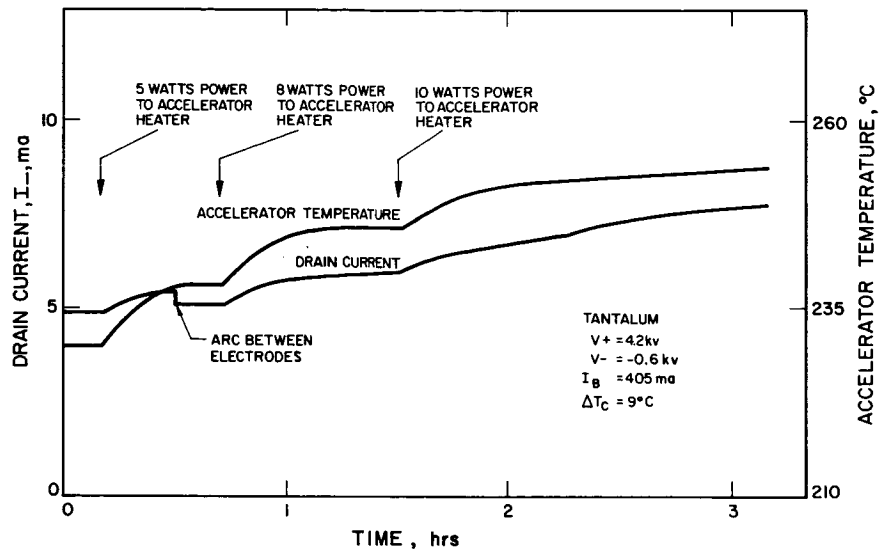


FIG. 16 ACCELERATOR TEMPERATURE AND DRAIN CURRENT VERSUS TIME FOR TANTALUM ELECTRODE HEATING TEST

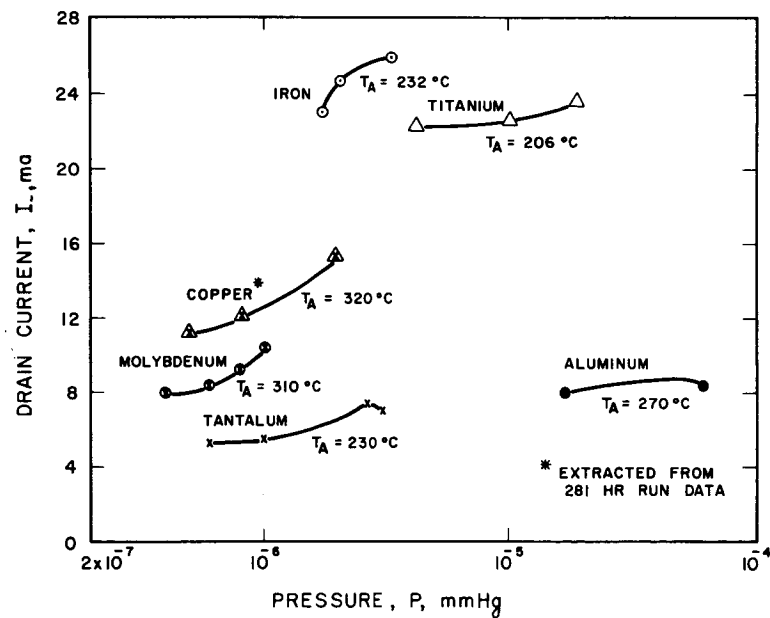


FIG. 17 DRAIN CURRENT VERSUS PRESSURE FOR VARIOUS ELECTRODE MATERIALS



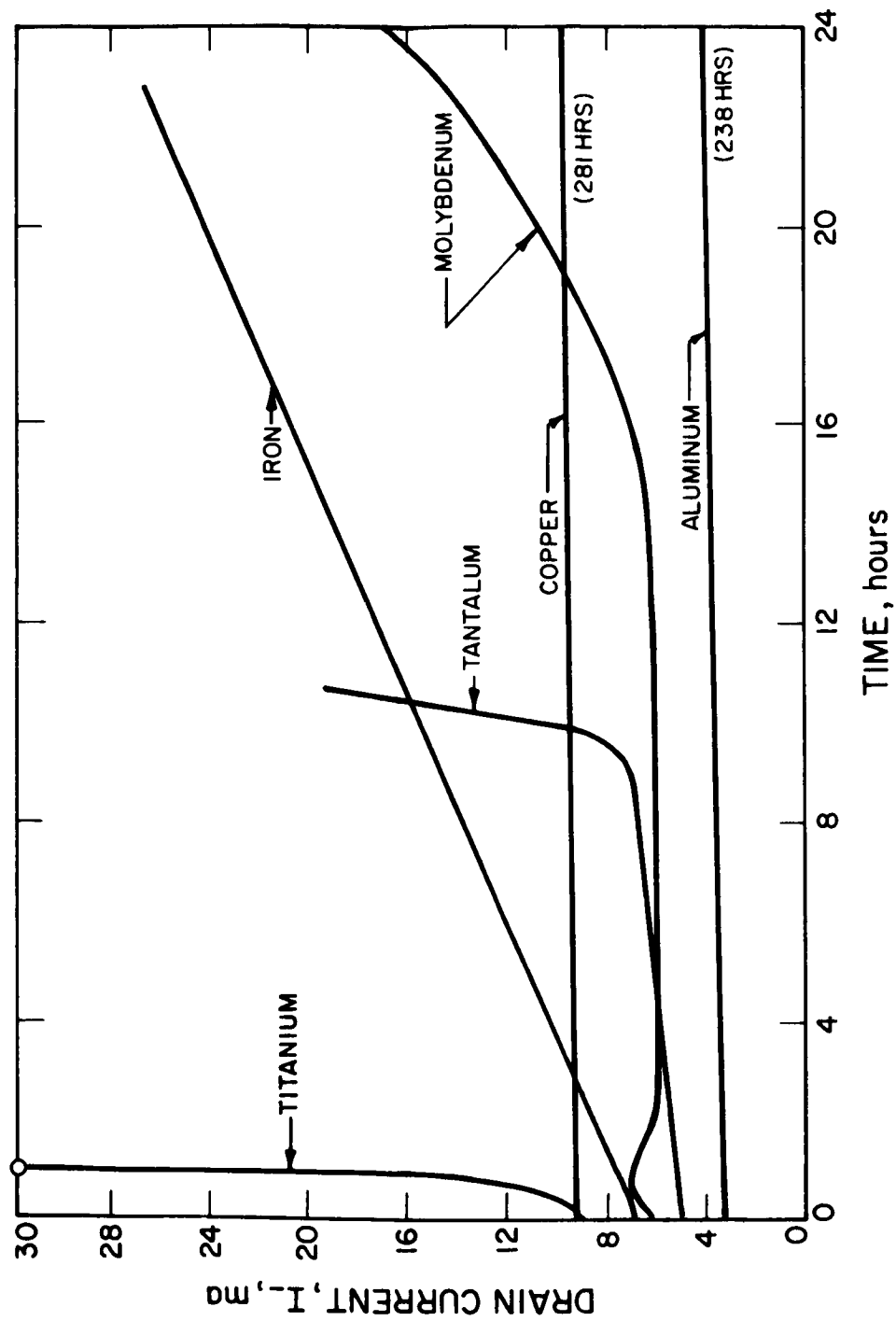


FIG. 18 EXTENDED TESTS WITH VARIOUS ELECTRODE MATERIALS

Positive High Voltage, $V_+$	4.2 kv
Negative High Voltage, $V_-$	-0.6 kv
Beam Current, $I_B$	380 mA
Negative HV Current (drain current), $I_-$	4.0 mA
Accelerator Electrode Temperature, $T_A$	240°C
Arc Voltage, $V_A$	7.8 volts
Arc Current, $I_A$	38.5 amps
Cathode Housing Temperature, $T_C$	490°C
Chamber Pressure, $P$	$5 \times 10^{-6}$ mm Hg
Neutral Efflux (equivalent current)	$\sim 33$ mA

Power was applied to the accelerating electrode heater in increments and the behavior of the electrode temperature and drain current was as shown in Fig. 19. The drain current was observed to increase with increasing accelerator temperature. At the maximum temperature attained, 322°C, the drain current was 13.9 mA. During the time these changes took place, the cathode housing temperature also increased by 10°C.

When the electrode heater power was removed, both drain current and electrode temperature began to fall immediately. Within 45 minutes after power turnoff, the drain current and accelerating electrode temperature had returned to their initial steady-state operating levels.

Although copper does exhibit increased electron emission at high temperatures, the absence of a runaway drain condition and the fairly low drain level for normal operating temperatures make copper suitable for use as an accelerating electrode, as demonstrated by the 281-hour test reported in paragraph 2.3.2. Copper and aluminum were the only materials tested which permitted long duration runs without occurrence of the high drain condition.

For the other materials, drain increases were encountered in relatively short times. The drain current for the iron electrodes increased from 7 mA to 27 mA in 23 hours. The tantalum

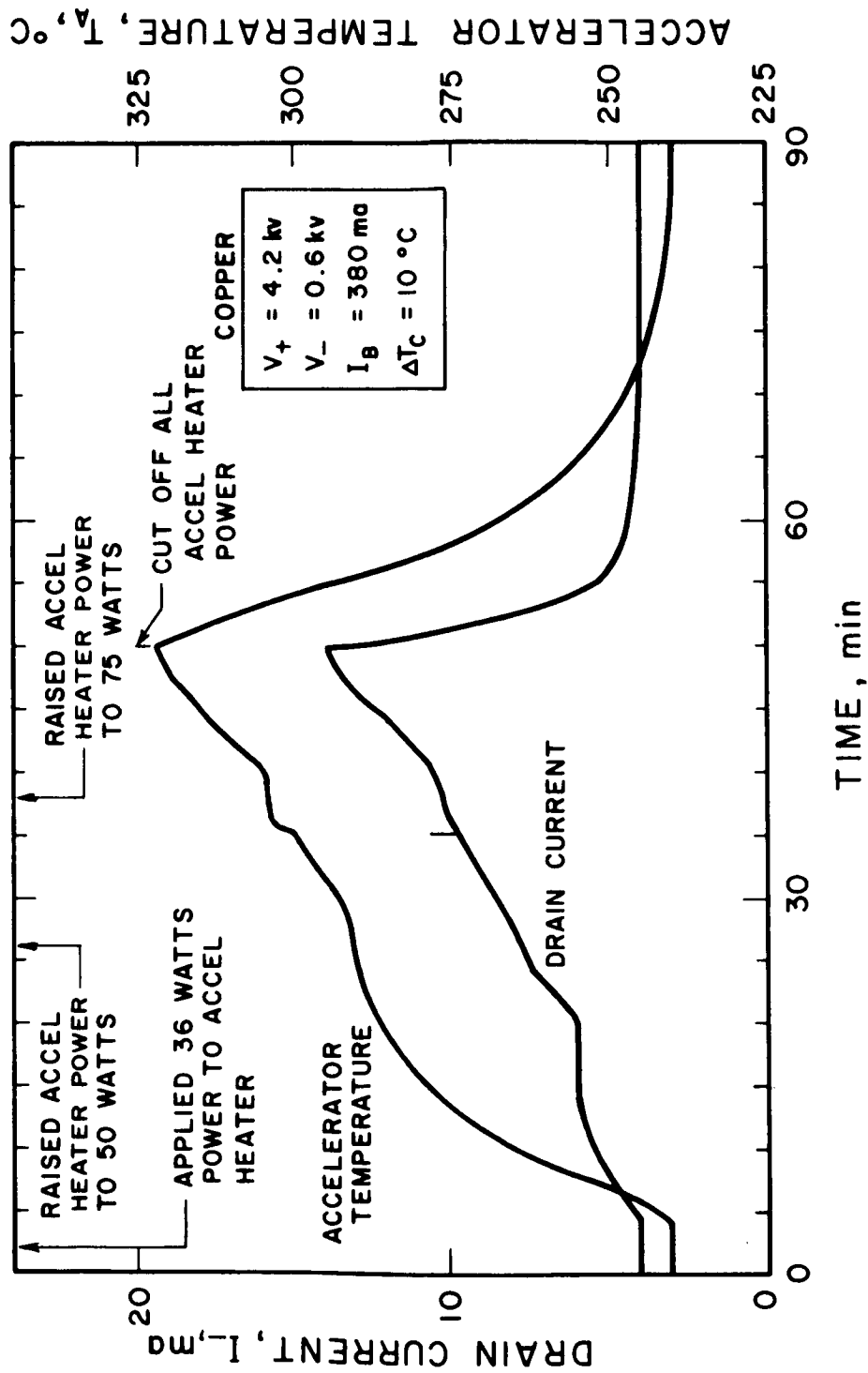


FIG. 19 ACCELERATOR TEMPERATURE AND DRAIN CURRENT VERSUS TIME FOR COPPER ACCELERATING ELECTRODE

electrode drain current increased from 5 mA to 7 mA in 9 hours after which a runaway condition occurred. The test was terminated at 10-3/4 hours with a drain of 20 mA. As mentioned in paragraph 2.1, the titanium electrode test had an immediate runaway, the drain current increasing from 9 mA to 30 mA in 1 hour.

The temperature increase of electrodes during the early hours of extended duration tests was determined to be caused by a change in emissivity of the downstream side of the electrode. The deposition of copper, sputtered from the collector and liner, onto this surface decreases the emissivity in all cases except that of the copper electrode. Since the engine power radiated to the upstream side of the electrode remains the same, the electrode temperature rises.

In those cases where a low work function composite surface exists, the drain current increases with time because the electrode temperature is increasing. The electrons accelerated across the electrode gap heat the engine. When this heating becomes significant in terms of the additional power radiated to the accelerating electrode, the runaway condition occurs.

Although the low work function composite surface is present in the case of copper, the emissivity did not change and the electrode temperature and drain current were fairly stable during the 281-hour run. In the 238-hour aluminum electrode test, the emissivity of the electrode changed and the electrode temperature increased by over 40°C in the first 50 hours of operation. The high drain current condition was not encountered because of the absence of a very low work function composite surface.

#### 2.1.4 Sputtering Measurements

Sputtering yield determinations for cesium ions incident on aluminum were made. The sputtering yield ( $S$ ) is defined as the ratio of the number of atoms sputtered from the target material ( $n_a$ ) to the number of bombarding ions ( $n_i$ ). In terms of experimental parameters, this ratio can be expressed as:

$$S = \frac{n_a}{n_i} = \frac{\frac{\Delta m_T}{m_T}}{\frac{I_+ t}{q}}$$

where  $\Delta m_T$  is the weight loss of the target in grams,  $m_T$  is the mass of a target atom in grams,  $I_+$  is the total ion current to the target in amperes,  $t$  is the exposure time in seconds, and  $q$  is the charge per ion in coulombs.

Measurements of the experimental parameters was made using the target assembly shown in Figs. 20 and 21. The triangular target block permits three separate sputtering determinations before breaking vacuum. The samples are mounted on the target block using a retainer ring attached to the block to insure good thermal conductivity. The target block is heated by a sheathed resistance heater and the temperature is monitored with an iron-constantan thermocouple. A cylindrical collector, used to determine secondary electron emission from the target, surrounds the target block. Two beam collimation plates are located in front of the collector. They are electrically isolated from ground potential so the first can be biased positive and the second negative to prevent electrons from entering the target region and causing errors in the ion current measurements. The aperture in the first plate defines the sputtering area since the apertures in the second plate and the collector are progressively larger. The shutter is manually operated and is used to protect the samples during the initial startup of the ion source.

The experimental procedure using this apparatus consists of preheating the target block to the desired operating temperature, stabilizing beam current from the ion source at the desired level, opening the shutter, and measuring the collector current, target current, and sample temperature. The power to the target block is adjusted to maintain constant temperature.

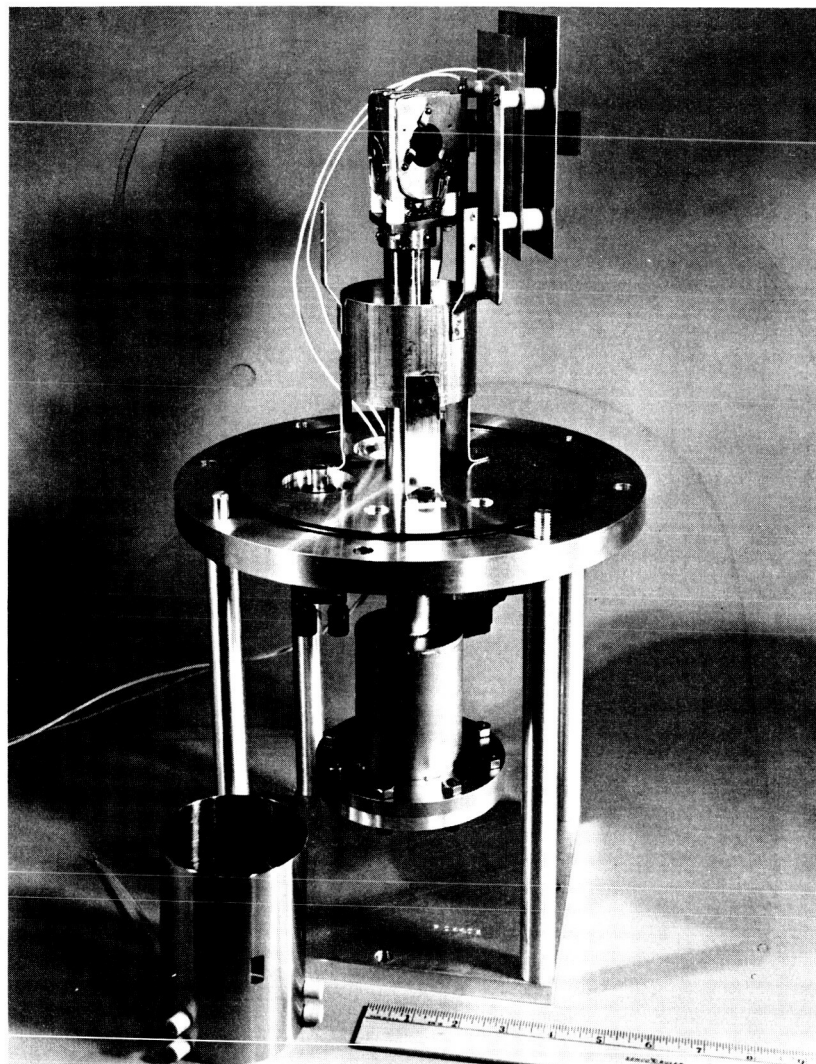


FIG. 20 SPUTTERING TARGET ASSEMBLY WITH SECONDARY ELECTRON COLLECTOR REMOVED

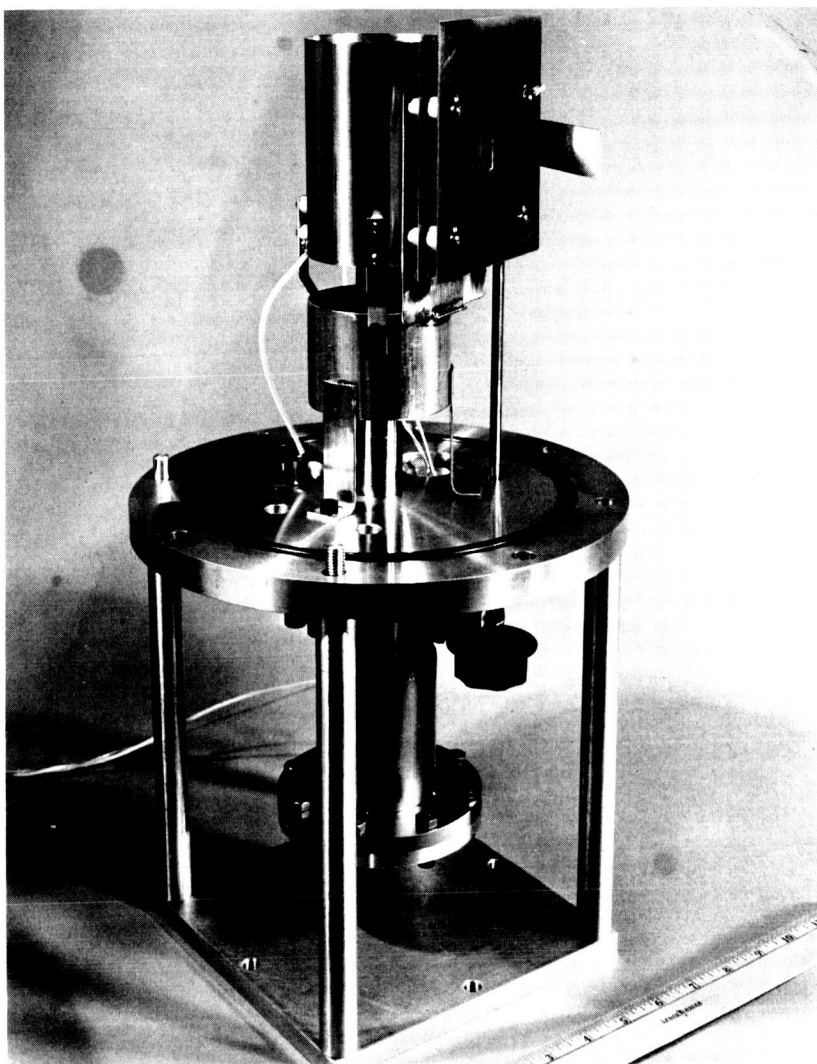


FIG. 21 ASSEMBLED SPUTTERING APPARATUS

A major problem encountered during sputtering experiments is the surface condition of the sample and the contamination of the surface by the vacuum environment. The partial pressures of reactive and soluble gases in the experimental chamber must be sufficiently low that surface contamination is negligible during the time expended in cleaning and experimentation. A useful measure of the vacuum conditions necessary to minimize contamination is the time interval,  $\tau_m$ , in which an initially clean surface will become completely covered by molecules from the surrounding gas if each molecule striking the surface remains on the surface. The number of molecules of mass  $m$  striking a unit area of surface in a unit time at a partial pressure  $p$  is given by

$$Z = p/(2\pi mkT_a)^{1/2}$$

where  $k$  is Boltzmann's constant, and  $T_a$  is the absolute temperature. If it is assumed that a monolayer consists of  $10^{14}$  molecules per square centimeter, then the monolayer time interval,  $\tau_m$ , can be approximated by

$$\begin{aligned}\tau_m &= 10^{14}/Z, \\ &= 10^{14}/Ap\end{aligned}$$

where

$$X = 1/(2\pi mKT)^{1/2}$$

Typical values of  $X$ , in molecules/cm<sup>2</sup> sec torr, and  $\tau_m$ , in seconds, at a pressure of  $10^{-6}$  torr for several gases and vapors normally present in vacuum systems are given in Table I for  $T_a = 273^\circ\text{K}$ .



TABLE I  
MONOLAYER TIME INTERVALS

Gas or Vapor	$A \times 10^{-20}$	$\tau_m$ (seconds) at $10^{-6}$ torr
	$\frac{\text{molecules}}{\text{cm}^2 \text{ sec torr}}$	
H <sub>2</sub>	15.0	0.067
H <sub>2</sub> O	5.01	0.20
CO	4.02	0.25
N <sub>2</sub>	4.02	0.25
O <sub>2</sub>	3.76	0.27
CO <sub>2</sub>	3.20	0.31

From Table I it is seen that an initially clean surface exposed to oxygen at a partial pressure of  $10^{-6}$  torr could be completely contaminated within one second after cleaning. The partial pressure of O<sub>2</sub> in EOS vacuum systems has been determined to be three to four orders of magnitude less than the operating pressure so that contamination should take longer than one minute. The arrival rate of O<sub>2</sub> is thus much less than the ion beam arrival rate for the lowest current density used in these tests. Since other contaminants, principally hydrogen, are less reactive with aluminum than oxygen, the surface should be free of contamination after absorbed gases have been removed by initial sputtering. After ion bombardment is terminated, the surface contamination should have the same general makeup as before sputtering.

A correction was made for the effect of sputtered copper deposits on the sample weight loss determinations. The target samples and a clean control sample were cleaned using nitric acid. New weight losses were within a few percent of the uncleaned weight losses. Figure 22 shows the yield obtained over the ion energy range from 0.5 to 4.0 kev.

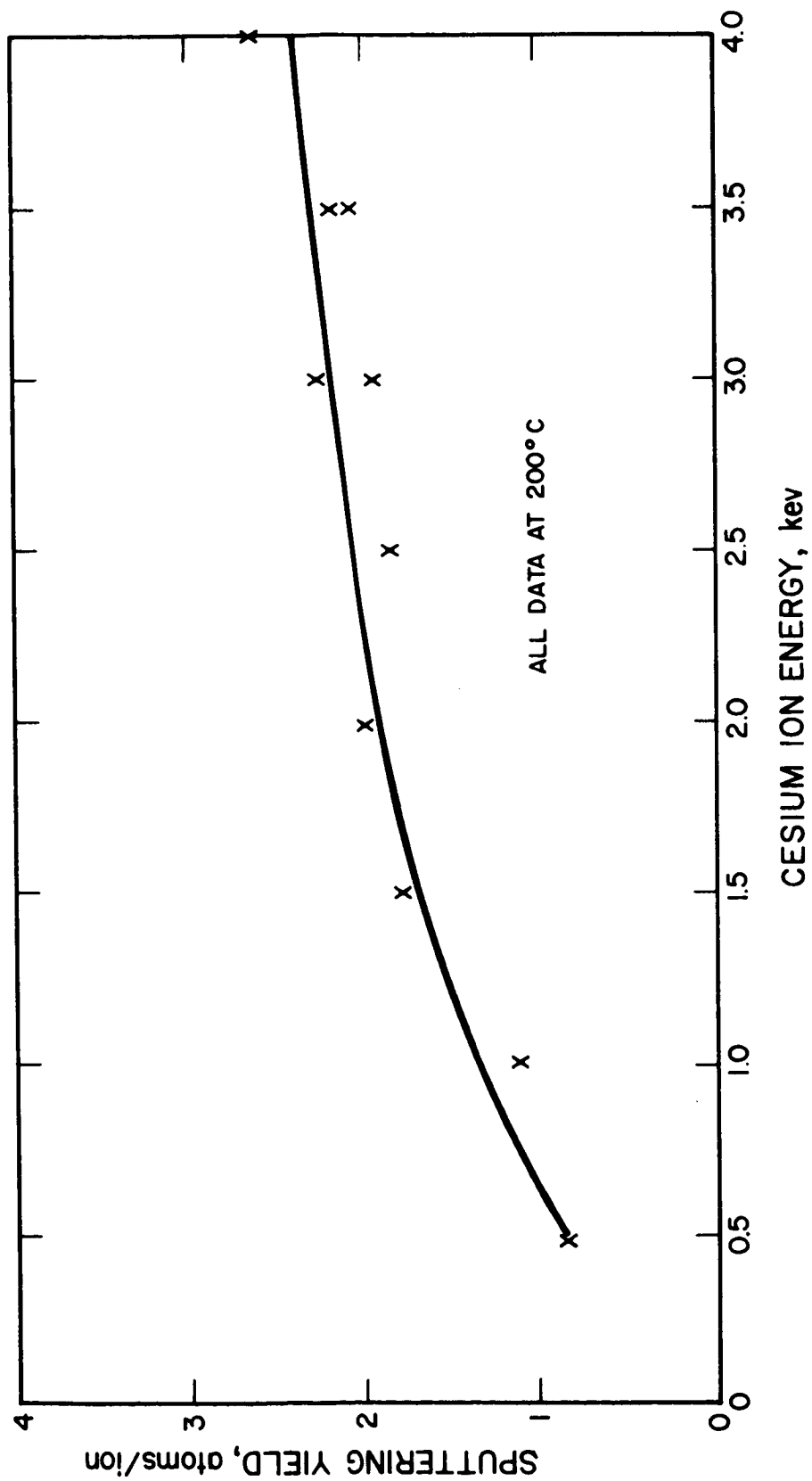


FIG. 22 SPUTTERING YIELD OF ALUMINUM VERSUS BOMBARDING CESIUM ION ENERGY

### Al/6 Percent $\text{Al}_2\text{O}_3$ Sputtering Measurement

A sample of Alcoa XAP001 alloy was provided by the LeRC for evaluation as a possible electrode material. This alloy is made by powder metallurgy techniques and is sintered from a mixture of 94 percent (by weight) aluminum powder and 6 percent  $\text{Al}_2\text{O}_3$  powder. It has significantly higher mechanical strength than other aluminum alloys but its sputtering yield was unknown.

The sputtering rate of the Al/6 percent  $\text{Al}_2\text{O}_3$  alloy was compared with that of the high purity 1100H14 alloy used for the DF electrode by sputtering samples of each with the same exposure. The samples were held at  $200^\circ\text{C}$  during the exposures and the pressure was maintained between  $7 \times 10^{-7}$  and  $1 \times 10^{-6}$  torr.

The yields obtained are listed in Table II together with a previously obtained yield for aluminum at the same energy.

TABLE II  
COMPARISON OF ALUMINUM AND  
ALUMINUM-ALUMINUM OXIDE SPUTTERING YIELDS

Sample Material	Ion Energy (kev)	Yield (atoms/ion)
Al/6% $\text{Al}_2\text{O}_3$	1	5.1
Aluminum	1	1.2
Aluminum	1	1.1*
Al/6% $\text{Al}_2\text{O}_3$	2	3.3**
Aluminum	2	2.0

\*Data from previous determination

\*\*Weight loss on this sample approached the accuracy of the balance used

There appeared to be no advantage to the use of the new aluminum alloy since low sputtering yield is far more important than physical strength for this application.

On the basis of the low sputtering yield of aluminum (about half that of copper), the low drain currents experienced with an aluminum accelerator electrode, and its low weight, aluminum was selected as the best material for further use for accelerator electrode fabrication.

#### 2.1.5 Emittance Measurements

To permit more realistic estimates of radiation power losses from the aluminum electrode, total hemispherical emittance values for aluminum with a coating of sputtered copper were necessary. The free cooling technique equipment in use on Air Force Contract AF 33(615)-1530 was modified to accommodate the lower temperatures necessary for the aluminum samples.

The free cooling rate technique was used to measure the total hemispherical emittance,  $\epsilon_t$ . When a heated sample suspended by thin thermocouple wires is suddenly removed from its heat source, the following relation is valid if conduction by the wires and wall radiation effects are negligible as they are for the results shown later:

$$\epsilon_t = \frac{MC}{A_s \sigma T_a^4} \left( \frac{dT_a}{dt} \right)$$

where M is the mass of the sample, C is the specific heat of the sample material,  $A_s$  is the surface area,  $\sigma$  is the Stefan-Boltzmann constant,  $T_a$  is the absolute temperature of the sample, and  $dT_a/dt$  is the slope of the cooling curve. Thus by measuring the slope of the cooling curve from a strip chart recorder, an emittance curve as a function of temperature can be determined.

Samples made from the same alloy as the electrodes (1100H14) were supported by swaging the thermocouple junction into the periphery.

The samples were then mounted in the emittance apparatus as shown in Fig. 23. The nominal sample size was 0.250-inch diameter by 0.040-inch thick. The chromel-constantan thermocouples were 0.003-inch

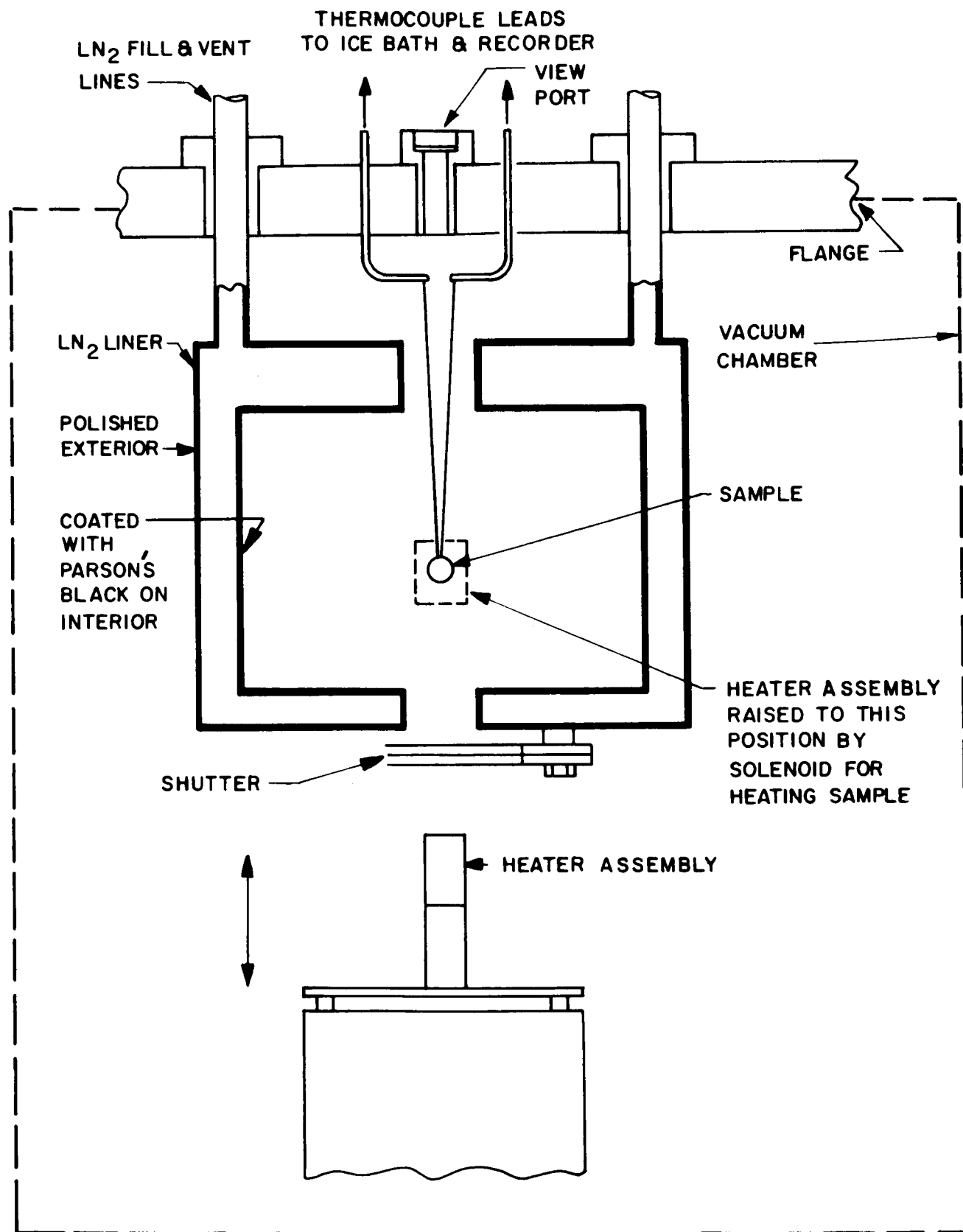


FIG. 23 SCHEMATIC OF APPARATUS FOR EMITTANCE MEASUREMENTS BY THE FREE COOLING TECHNIQUE

diameter. A brief outline of the measuring procedure will explain the apparatus in Fig. 23. The sample is mounted and the chamber evacuated to  $1 \times 10^{-6}$  torr or less. The liner is filled with  $\text{LN}_2$ . The heater is then brought up to temperature and elevated into the  $\text{LN}_2$  liner so that it surrounds the sample. When the maximum sample temperature is obtained, the heater is shut off and lowered out of the liner. The shutter closes automatically after the oven drops. This procedure is repeated as required to insure reproducibility between runs. The data from one representative run is then reduced.

Measurements were made on two samples of 1100H14 aluminum alloy. The resulting values of the total hemispherical emittance as a function of absolute temperature are shown in Fig. 24.

Samples were prepared from the same 0.125-inch-thick stock which is used for DF electrodes. The sample nominal dimensions were 0.250-inch diameter and 0.040-inch thick. Two samples were retained in the as-machined condition and the others were liquid-honed to a matte finish as in electrode preparation.

The adjective "uncorrected" is used on Fig. 24 since all the corrections were not included in the presented data. These corrections include the heat loss due to the thermocouples, the variation of specific heat and area with temperature, and the variation of the thermoelectric power of the thermocouple as a function of temperature. These corrections are less than 10 percent.

The lower curve in Fig. 24 represents three of the five runs made with sample No. 1. The other two were within the values shown. The upper curve was evaluated from only one of three runs since all runs were within a pen width on the recording potentiometer record.

Emittance measurements were made on one sample of copper-coated 1100H14 aluminum alloy. A machined and liquid-honed sample with the thermocouple mounted was packaged in such a manner that only the sample surface was exposed. This sample package was then mounted in a facility in which engine testing was being conducted.

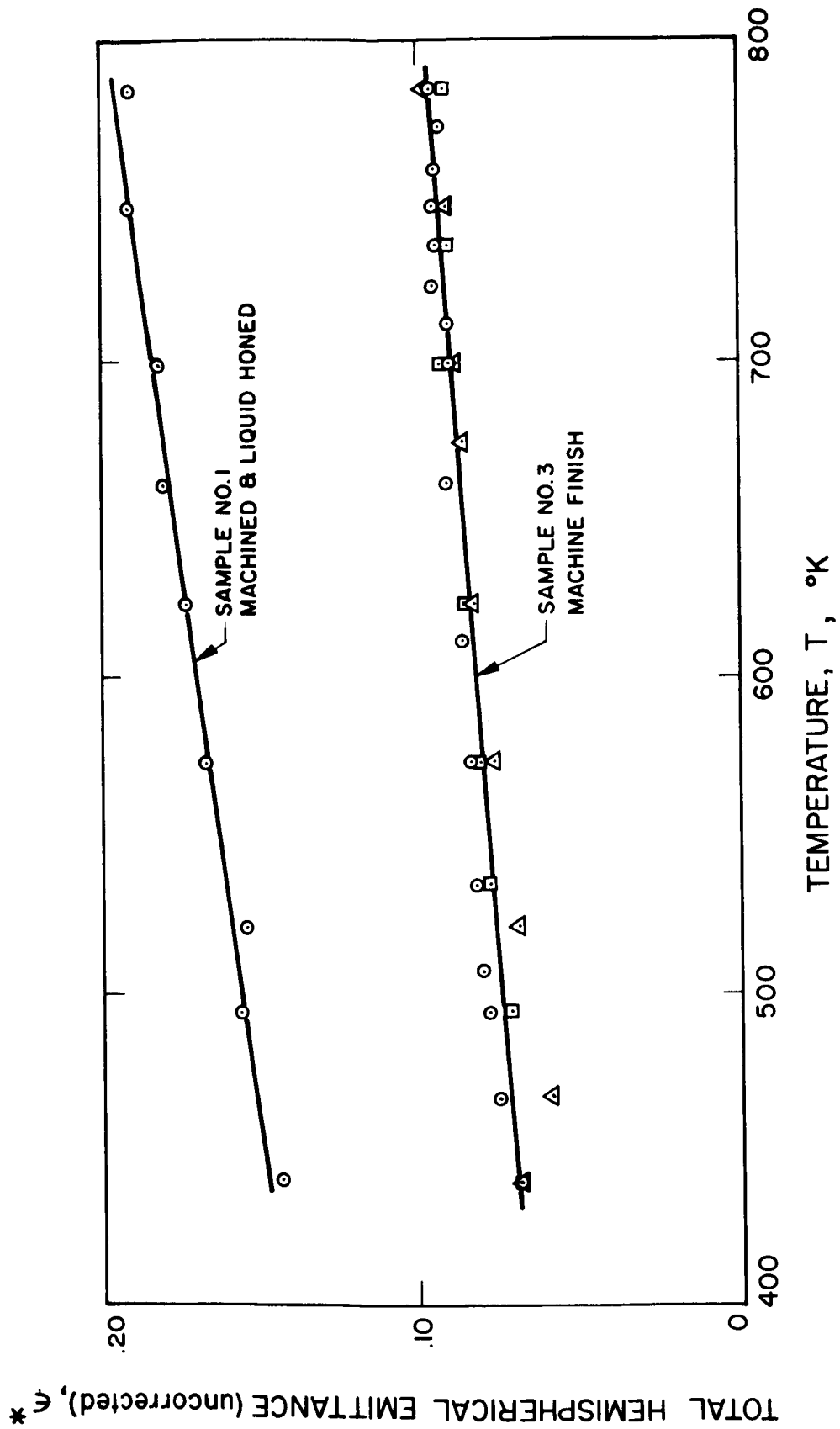


FIG. 24 ALUMINUM EMITTANCE MEASUREMENTS

Copper sputtered back from the collector was deposited on the sample. The sample was rotated periodically so that the copper would accumulate at a reasonably uniform rate on all sides.

The coating thickness was determined by weighing the sample with the thermocouple before and after exposure. Assuming simple geometry, uniform coating, and normal copper density, the coating thickness was calculated to be  $20 \times 10^{-6}$  inch or 0.5 micron.

During the emittance tests a gradual reduction of slope in the temperature-time charts was observed. Evidence of loss of copper by flaking was definitely visible when the sample was removed from the system. This could not be observed during the tests since only a small portion of the sample edge is visible through the  $\text{LN}_2$  chamber wall.

The emittance values from Fig. 24 corrected for thermocouple loss, thermal expansion of the surface area, and thermal variation of specific heat of the sample are shown by the extreme upper and lower curves of Fig. 25. The general effect was to reduce the values previously reported by 2 percent at  $750^\circ\text{K}$  and by approximately 5 percent at  $450^\circ\text{K}$ .

The results for the copper-coated sample are shown by the center curve in Fig. 25. This curve was based on several tests. Each test subjected the sample to  $800^\circ\text{K}$  for about 9 minutes. Total heating and cooling time was about 5.5 hours. The calculations did not include the added weight of the copper since it amounted to only 0.37 percent.

At  $500^\circ\text{K}$  ( $227^\circ\text{C}$ ) the emittance of the as-machined sample was 0.063 which increased to 0.143 when liquid-honed. The effect of the copper ( $\sim 0.5\mu$  thick) was to reduce the emittance to 0.084. Time at high temperature ( $800^\circ\text{K}$ ) caused spalling of the copper which increased the emittance to 0.089.

The general trends appear to be that liquid honing approximately doubles the emittance of as-machined 1100H14 aluminum alloy, and copper coating reduces it toward the original as-machined condition.



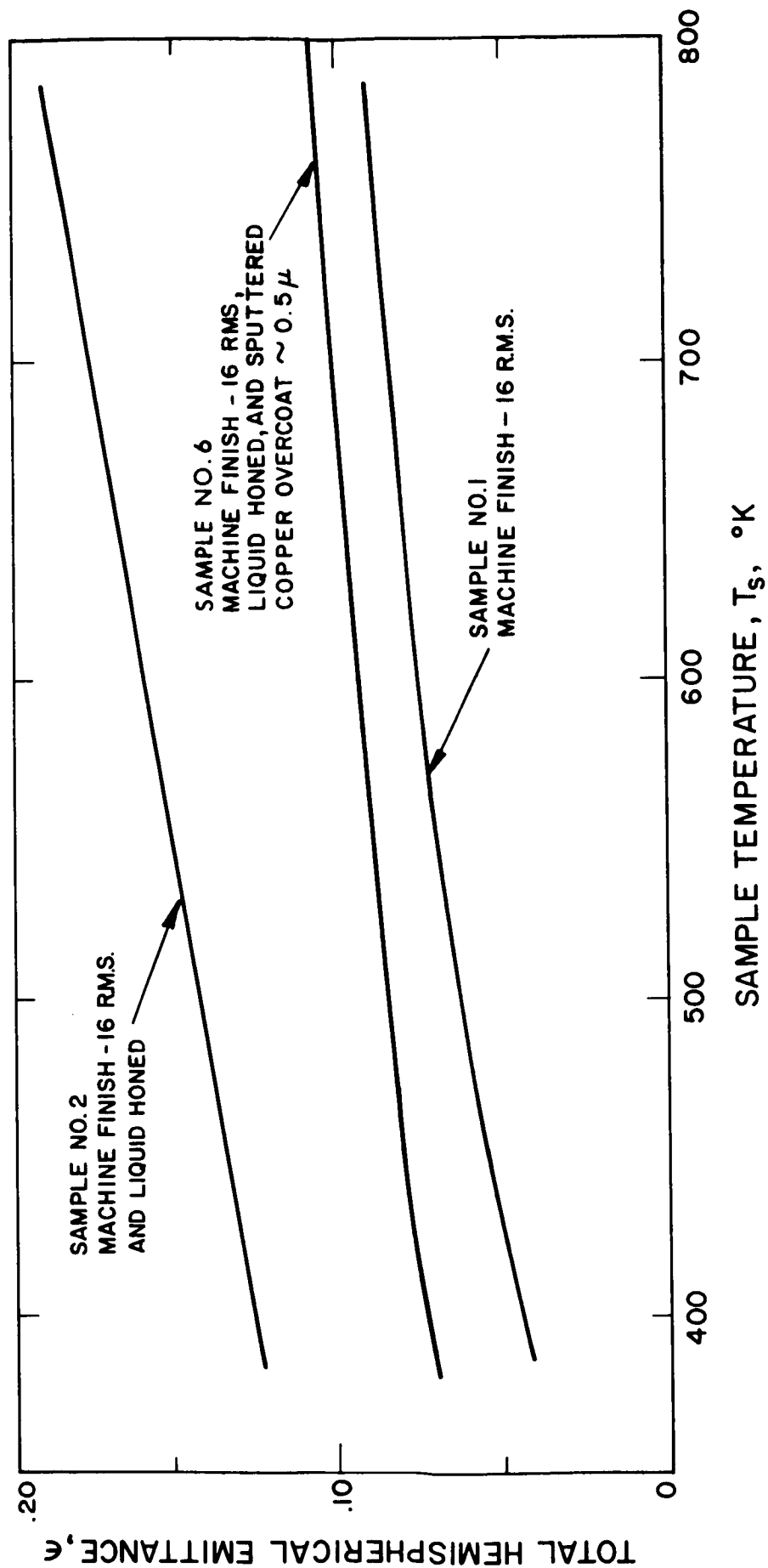


FIG. 25 EMISSANCE VERSUS TEMPERATURE FOR SEVERAL SURFACE CONDITIONS OF ALUMINUM SAMPLES

## 2.2 Feed Systems

Cesium feed systems capable of operation in both zero-g and 1-g environments were used for all extended tests on this program. A description of the principle of operation and associated hardware may be found in EOS Report 3670-Final (NASA CR-54067).

### 2.2.1 750-Hour Feed System

The 750-hour feed system used a solenoid-operated feed valve and a solenoid-operated pump-out port valve shown on the assembled system in Figure 26 (3670-Final 3-24, page 111)<sup>1</sup>. This system has a capacity of about 5 pounds of cesium, an amount sufficient for a minimum of 750 hours operation of the DE engine. Performance of this system with the DE engine is described in Subsection 2.3 of this report.

### 2.2.2 Feed System Improvements

After the tests with the DE engine two modifications were made to the 750-hour feed system to enhance reliability for long term operation. These included a manually-operated cesium flow valve and improved solenoid port valve for pump-out.

### 2.2.3 Manually Operated Cesium Valve

The zero-g feed system has had response characteristics sufficiently fast to accommodate all of the engine control requirements. A valve was required only to provide a barrier to protect the cesium when the feed system was not in the vacuum environment of the test chamber. Consequently, the solenoid valve was replaced with a manual valve which could be opened prior to engine start and closed prior to engine removal from the vacuum chamber.

The valve (Figs. 27 and 28) consists of three sub-assemblies; the valve body, the poppet assembly, and the actuating mechanism. The valve body is fabricated of type 347 stainless steel and is heated with a sheathed heater. Its mass is considerably less than the mass of the solenoid valve it replaced.

The poppet assembly consists of the valve poppet which is welded to a metal diaphragm similar to that used on the solenoid valve.

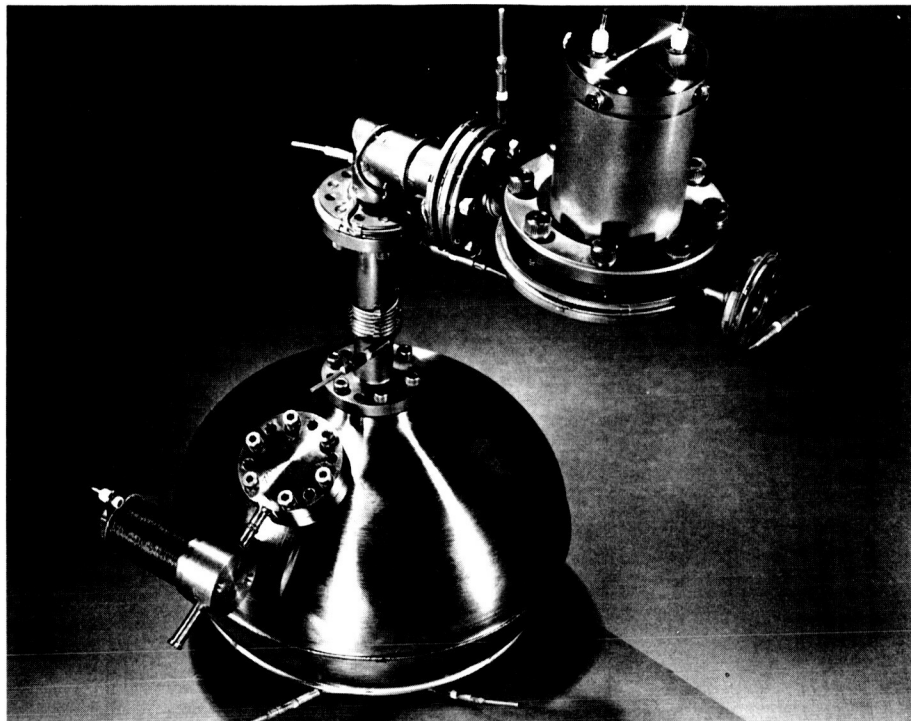


FIG. 26 750-HOUR FEED SYSTEM AND SOLENOID-OPERATED  
FEED VALVE

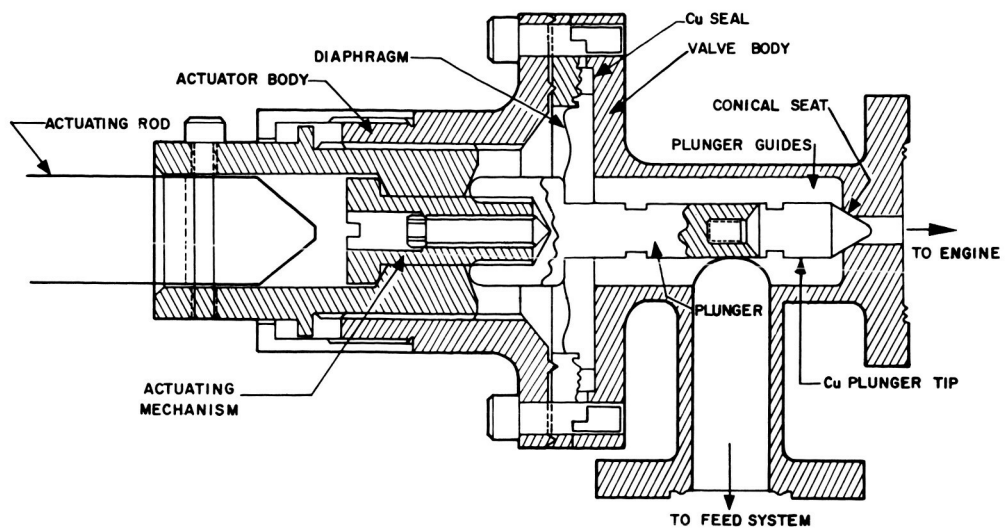


FIG. 27 MANUALLY-OPERATED CESIUM VALVE

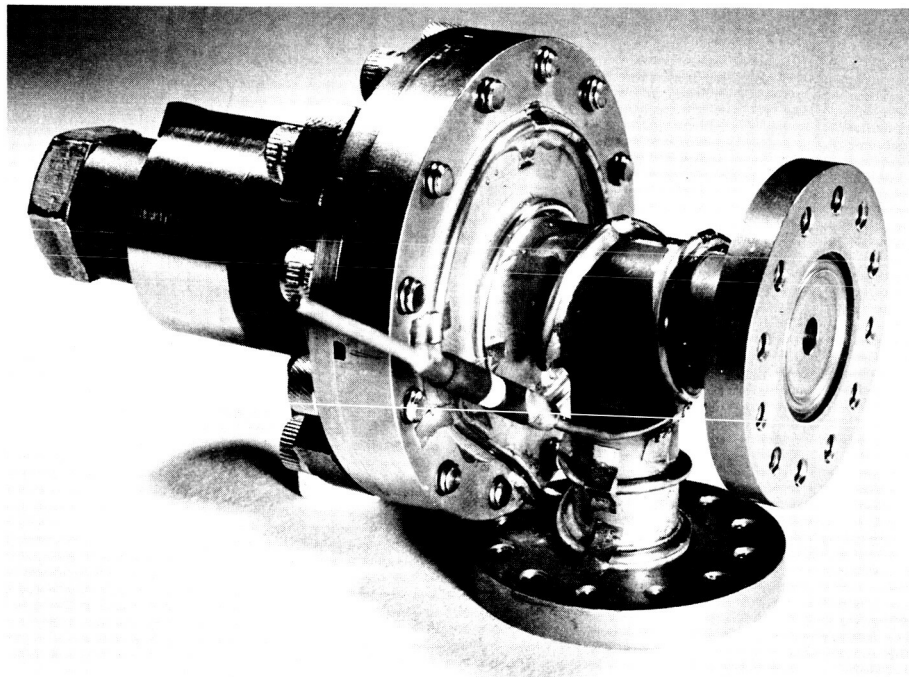


FIG. 28 MANUAL VALVE

The only seal used in the valve is between the body and poppet assembly. The actuating mechanism is of hardened type 17-4 stainless steel. The screw mechanism is overcoated with a high-temperature, solid-film lubricant to minimize friction. Thermal isolation is provided between the actuating assembly and the valve body to minimize heat conduction to the actuating assembly.

Actuation of the valve is provided by a retractable rod which is introduced through the vacuum flange. An O-ring assembly on the flange prevents leakage at the flange. Since the rod is retracted when high voltage is applied to the engine, there is no need for electrical isolation of the rod.

Testing of this valve included helium mass spectrometer leak-checking and room-temperature cycling. Twenty successive actuations were made with no detectable leak across the valve. The detector used had a sensitivity of  $10^{-10}$  std cc He/sec. Actuating torque during this test was held constant at 25 inch-pounds. The valve was assembled to a feed system and cesium flow tested at valve body temperatures up to 400°C. All tests were satisfactory.

#### Pump-Out Valve

The rear pump-out valve on the cesium reservoir was redesigned to provide a larger orifice. The old pump-out valve had a port orifice diameter of only 1/16 inch. This small orifice was easily obstructed by cesium deposits which might result from distillation or handling. The new design used a 1/4-inch-diameter orifice. A drawing of the new valve is shown in Fig. 29.

### 2.3 Extended Tests of the DE Engines

Two extended tests were made during the course of accelerator electrode material selection. A DE engine with a copper electrode was operated for 281 hours and an engine with an aluminum electrode was operated for 231 hours.

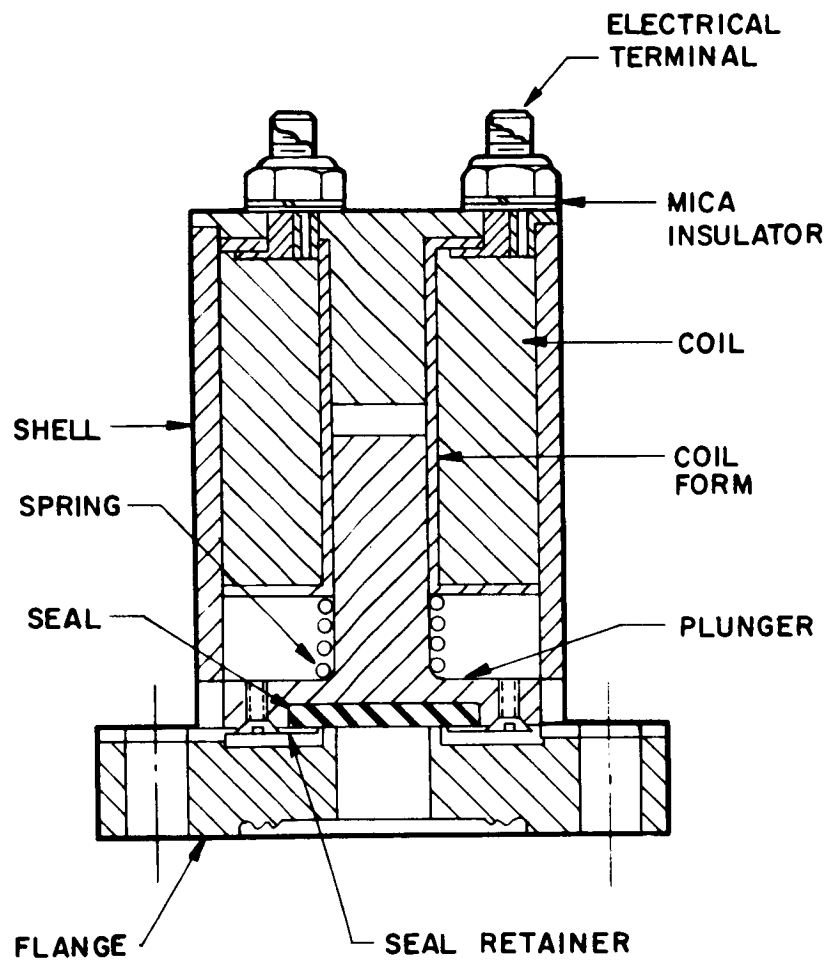


FIG. 29 NEW PORT VALVE

### 2.3.1 Facility

The test chamber which was used for extended testing of the DE engine and feed system is represented schematically in Fig. 30. The engine was mounted in a tank section 28 inches in diameter and 42 inches long. This section had a 24-inch diameter liquid nitrogen-cooled liner and was pumped by a 10-inch diffusion pump with a 6-inch standby diffusion pump. Both pumps had liquid nitrogen-cooled baffles. A neutral cesium detector with a housing which was cooled by conduction to the liner was incorporated. The detector had a mechanically-operated shutter for determining background levels.

The collector section of the facility was 28 inches in diameter and 60 inches long. It had a 24-inch diameter liquid nitrogen-cooled liner with conduction-cooled baffles. The collector was made of thick stacked copper plates and was water-cooled at 22°C. Liquid nitrogen was run through the diffusion pump baffle, the collector section liner and the engine section liner. Flow was controlled to regulate the outlet temperature of the engine section liner at -100°C. The collector and both liner sections could be floated for neutralization tests.

The engine and feed system were operated by a control system of the type discussed in EOS Report 3670-Final (NASA CR-54067)<sup>1</sup>. Vacuum, power, and high-voltage functions were interlocked to provide alarm signals or shut the system down in the event of engine system or test equipment malfunctions.

### 2.3.2 281-Hour Test

The first test required a total of 297 hours, during which time the engine was operated 281 hours. The test was interrupted five times during the first 86 hours.

Three malfunctions occurred as a result of a high-voltage cycling relay sticking in a mode that kept high voltage turned off and provided a full beam demand signal to the feed control system. The vaporizer power (Fig. 31) was full on during these delays. The test was interrupted two other times in an attempt to repair the circuit components.

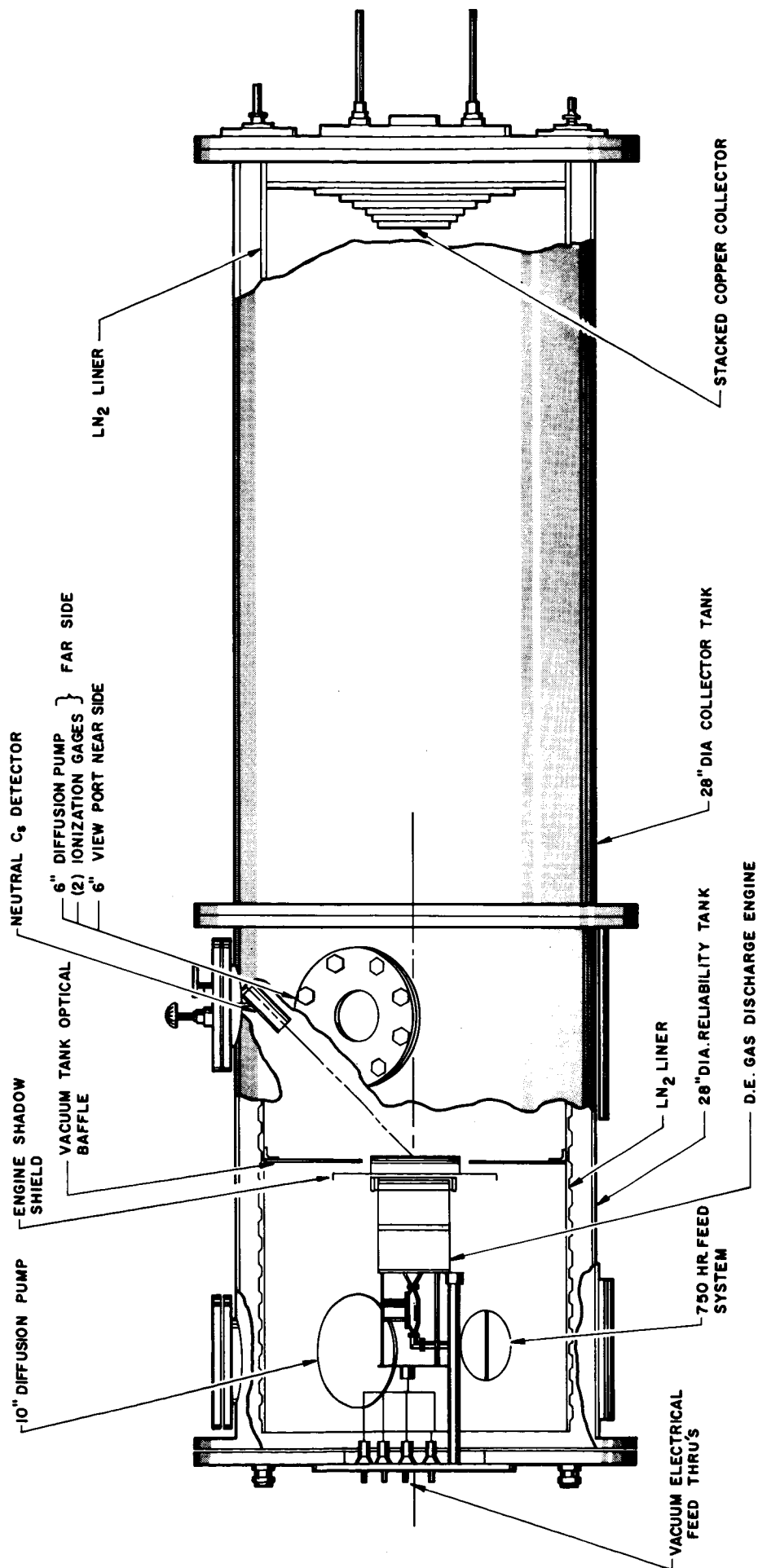


FIG. 30 FACILITY FOR EXTENDED TESTS OF THE DE ENGINE SYSTEM



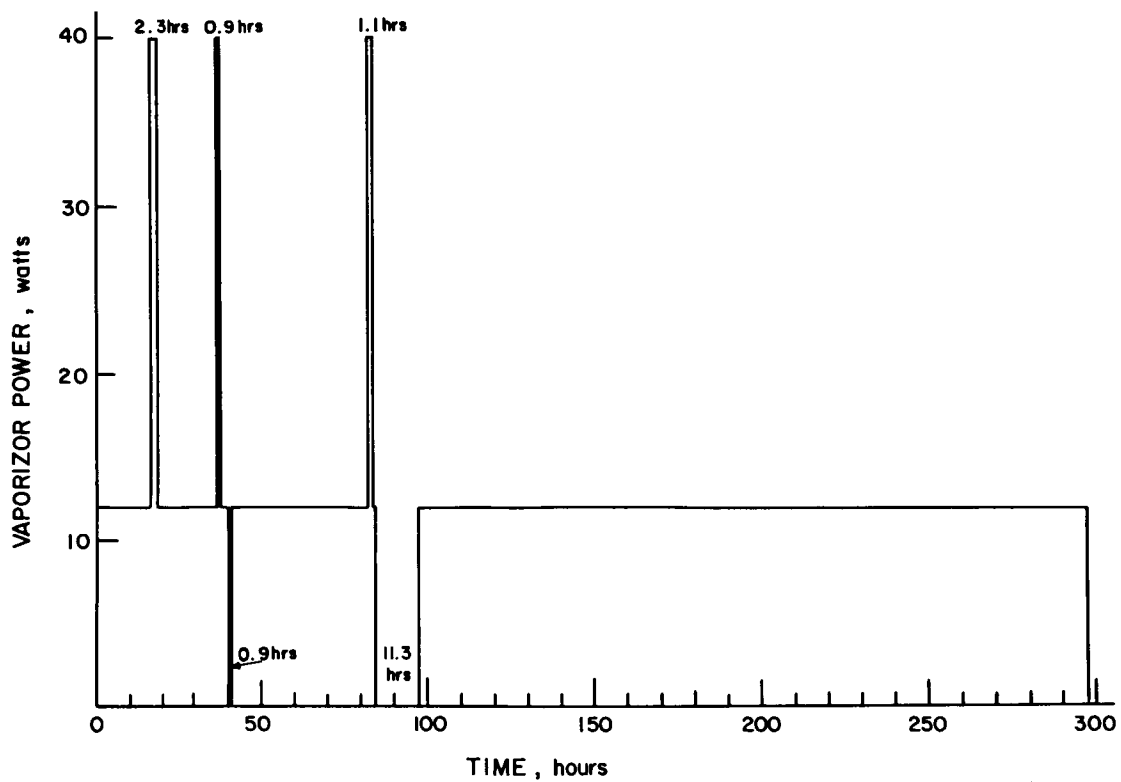


FIG. 31 VAPORIZER POWER HISTORY FOR 281-HOUR TEST

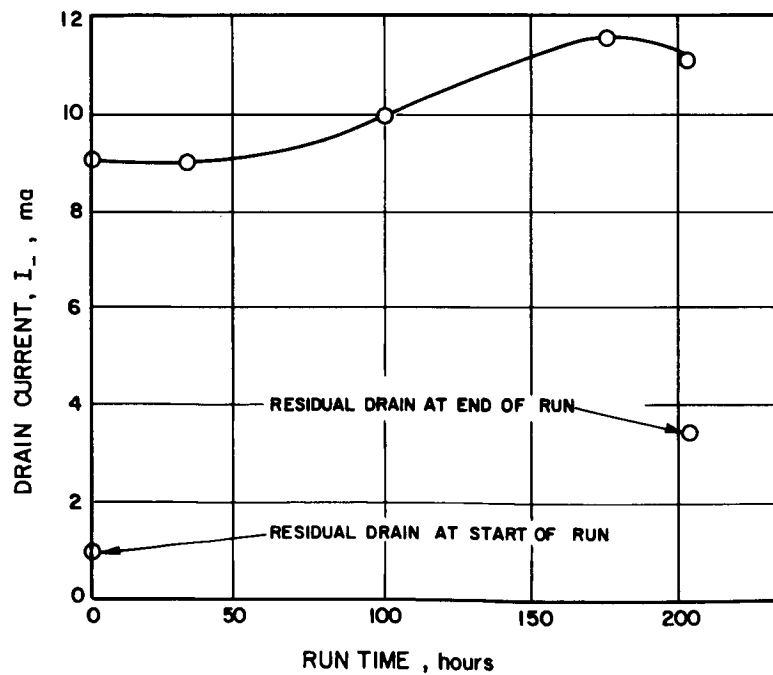


FIG. 32 DRAIN CURRENT VERSUS TIME FOR THE LAST 201 HOURS OF THE 281-HOUR TEST

During this initial 86 hours, the longest uninterrupted period of operation was 42.1 hours. A total operating time of 80 hours was accumulated.

The test then continued for 201 hours without incident, and was terminated on 7 August 1964, with the engine functioning normally. A total operating time of 281 hours was accumulated. Although the drain current fluctuated about 2.5 mA, there was no significant increase other than in the residual insulator leakage current.

The engine operating parameters during the 201-hour continuous segment of the test are presented in Table III. Three points are shown indicating the trend with time. Small changes were made in the high voltage and arc power settings to minimize drain during the course of the run. The drain current increased from 9 to 11.5 mA during the 201-hour period while accelerator electrode and cathode temperatures were on a downward trend. Downward adjustment of arc power from time to time would explain the decrease in the above temperatures. Figure 32 shows the gradual drain increase with time; it also shows the residual drains taken immediately before and after the continuous run. With the arc extinguished and the electrodes cool, the residual drain at the start was approximately 2.5 mA below the drain at the finish (1.0 mA versus 3.5 mA). This indicated that the increase in drain current was due to insulator leakage and not electron emission.

It was assumed that the high operating level of the drain current (over 2 percent of beam) was due to misalignment of the accelerator electrode as a jig was not used in assembly of the electrode structure. Inspection after the test did reveal a nonconcentric erosion pattern on the outer holes of the accelerator electrode.

Vaporizer power ran at 12.1 watts throughout the run with vaporizer temperature at 250°C; variations in these values were less than 3 percent. The test can be summarized as one characterized by little or no unexplainable drift in the measured parameters and by very stable operation.

A liquid nitrogen-cooled, neutral cesium detector, used at the start of the run, gave a mass utilization efficiency of 90 percent.

TABLE III

Engine Operating Parameters  
During 201-Hour Continuous Test Period

<u>Operating Parameters</u>	<u>Run Time (hours)</u>		
	<u>34</u>	<u>100</u>	<u>175</u>
Positive High Voltage, $V_+$ (kv)	4.2	4.2	4.2
Negative High Voltage, $V_-$ (kv)	0.75	0.60	0.55
Negative HV Current, $I_-$ (amp)	0.009	0.010	0.0115
Beam Current, $I_B$ (amp)	0.405	0.402	0.402
Arc Voltage, $V_A$ (volt)	7.7	7.6	7.5
Arc Current, $I_A$ (amp)	41.0	40.5	40.5
Beam Power, $P_B$ (kw)	1.701	1.689	1.688
Drain Power, $P_D$ (kw)	0.045	0.048	0.055
Magnet Power, $P_M$ (kw)	0.008	0.008	0.008
Arc Power, $P_A$ (kw)	0.316	0.308	0.304
Total Power, $P_T$ (kw)	2.070	2.053	2.055
Thrust, T (mlb)	9.89	9.81	9.81
Power-to-Thrust, P/T (kw/lb)	209	209	210
Power Efficiency, $\eta_p$	82.2%	82.5%	82.2%
Mass Efficiency, $\eta_M \sim$	90%	90%	90%
Overall Engine Efficiency, $\eta_E$	74.0%	74.2%	74.0%
Specific Impulse, $I_{sp}$ (sec)	7160	7160	7160
$I_-/I_B$	2.2%	2.5%	2.9%
$P_A/I_B$ (kev/ion)	0.780	0.766	0.756
Pressure (mm Hg)	$2.2 \times 10^{-7}$	$2.4 \times 10^{-7}$	$1.8 \times 10^{-7}$
Operating Temperatures ( $^{\circ}\text{C}$ )			
Accelerating Electrode	306	305	304
Engine Shell	306	301	309
Cathode Housing	440	425	428
Vaporizer	251	243	250

At the end of the run a mass utilization efficiency of 90.6 percent was obtained. During the full 297.5 hours of the test, 776.2 gms of cesium were expelled. In the 4.3 hours during which the high voltage was off and the vaporizer power was full on, it was estimated that the cesium flowrate was equivalent to 6 to 9 amperes of cesium ions. This was based on flowrate versus vaporizer power tests conducted under previous programs. It is therefore estimated that about 150 grams of cesium were lost to the system during these periods and that about 620 grams were consumed during engine operating periods. This gives a mass utilization efficiency of 90.55 percent, in agreement with the mass utilization measurements made using the neutral cesium detector.

#### Residual Drains

At the termination of the 281-hour test, the accelerating electrode temperature and the drain current were monitored. Figure 33 presents these parameters as a function of time after termination of the run. The high voltages were maintained during the procedure. A residual drain of 3.5 mA remained after the electrode was quite cool ( $185^{\circ}\text{C}$ ). This is considered to be an insulator drain current.

The residual drain current was then measured as a function of voltage across the accelerating gap. The temperature of the electrode was about  $185^{\circ}\text{C}$  at this time. The data are presented in Fig. 34. Each time the original voltages were applied (as indicated by the squares) the drain returned to 3.5 mA.

The voltages applied to the arc chamber and the accelerating electrode were then reversed and reversed polarity data were taken. These data are presented in Fig. 35. The test indicates the existence of electron emission from the molybdenum screen electrode which was at about  $200^{\circ}\text{C}$  when the data were taken. The data indicated by X's, for the decreasing gap voltage, were plotted as a Schottky plot shown in Fig. 36. As can be seen from the figure, a definite linear relation exists between the logarithm of the current and the square root of the voltage (or field intensity).

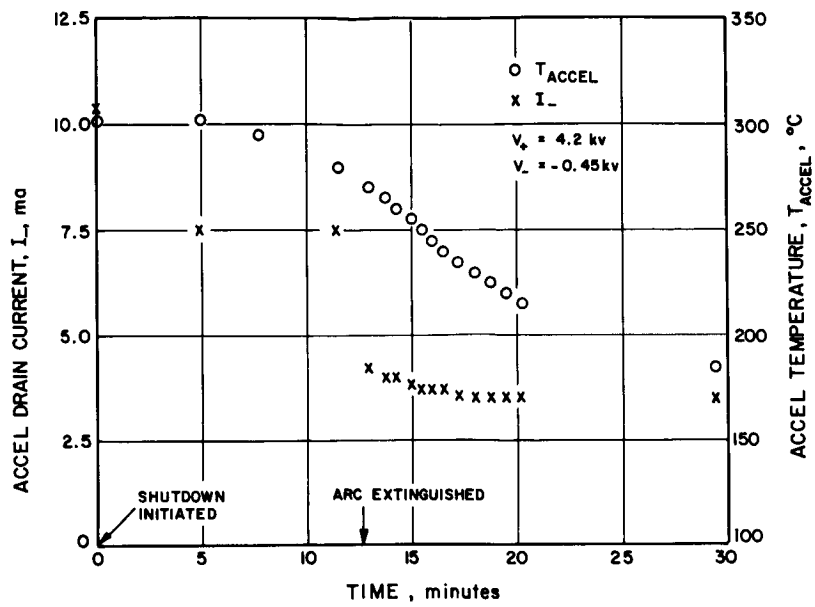


FIG. 33 ACCELERATING ELECTRODE TEMPERATURE AND DRAIN CURRENT AFTER TEST TERMINATION

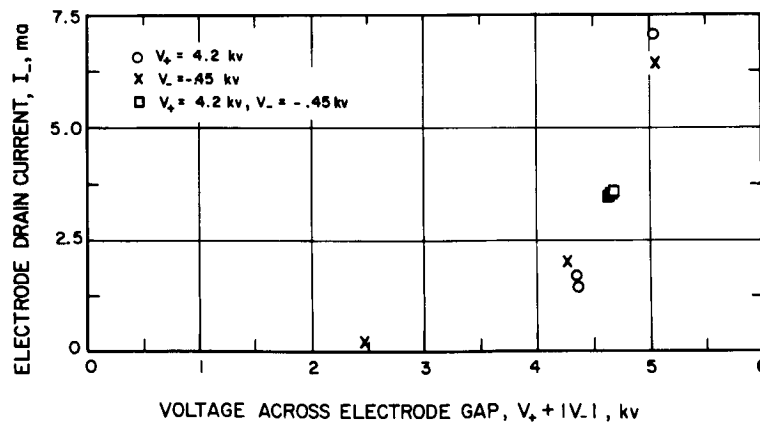


FIG. 34 ACCELERATOR DRAIN CURRENT VERSUS GAP VOLTAGE

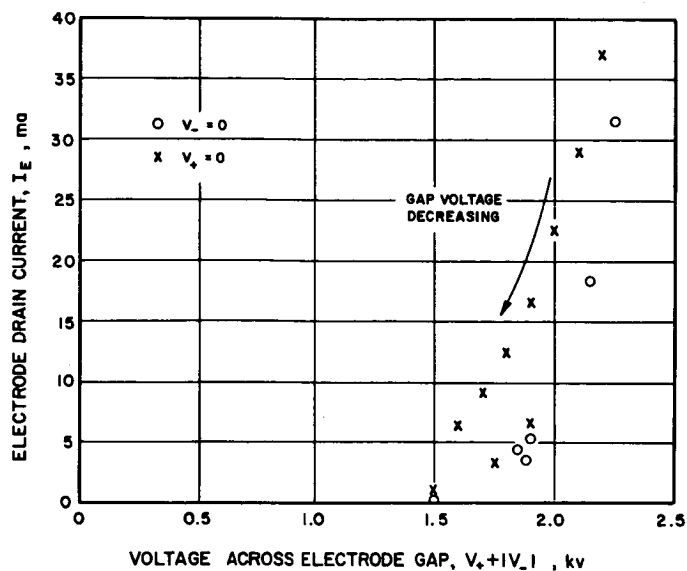


FIG. 35 DRAIN CURRENT VERSUS GAP VOLTAGE FOR REVERSED POLARITY TEST

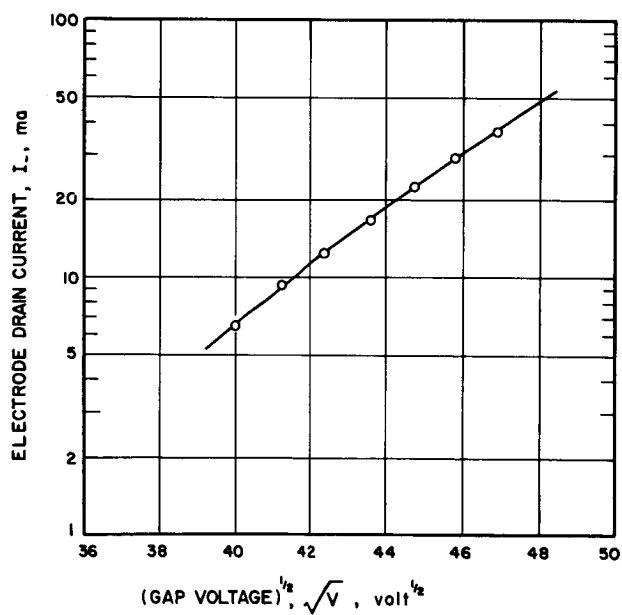


FIG. 36 SCHOTTKY PLOT FOR REVERSED VOLTAGE TEST

Extrapolation of the Schottky plot indicates a thermionic current requiring a work function of less than 1.2 ev. The Cs-O-Mo composite surface appears to exist on the molybdenum screen electrode.

The field between flat parts of the screen and accelerating electrodes is on the order of 10,000 volts/cm at 2.2 kv across the gap. The slope of the Schottky plot requires a field over 100 times more intense. The field at the sharp edges of the apertures in the screen electrode may be high enough to account for the large Schottky enhanced emission.

#### Condition of Engine After Test

A pictorial record of the system and components immediately after the run is shown in Figs. 37 through 44. The engine system, shown in Fig. 37, was quite clean. Only backspattered copper (on areas facing the collector) was visible upon inspection. Figure 38 is a view of the inside of the cathode and orifice plate. They both appeared in excellent condition. A light deposit was found on the first two coils of the cathode emitter next to the baffle (see photo) which appeared to be either residue from impurities in the propellant or from the braze compound. Not enough of this substance could be obtained for an analysis.

There was a nonuniform heating pattern on the orifice plate. A similar off-center, light area was found on the upstream side of the accelerator electrode. This condition has been noted before. The clean area at the cathode is due to electron heating. Since the clean areas on both parts are in line with each other it would appear that the emission was occurring from the clean spot on the electrode.

Figure 39 shows the inside of the arc chamber. The chamber and cathode plates were copper coated to thicknesses up to 0.001 inch. Note the distorted electrode hole pattern on the front portion of the anode. This is due to copper, sputtered back from the liner and collector, passing through the electrode system.

The most severe damage to the engine occurred on the outer shell (magnet cover) where electron bombardment had worn through the 0.003-inch-

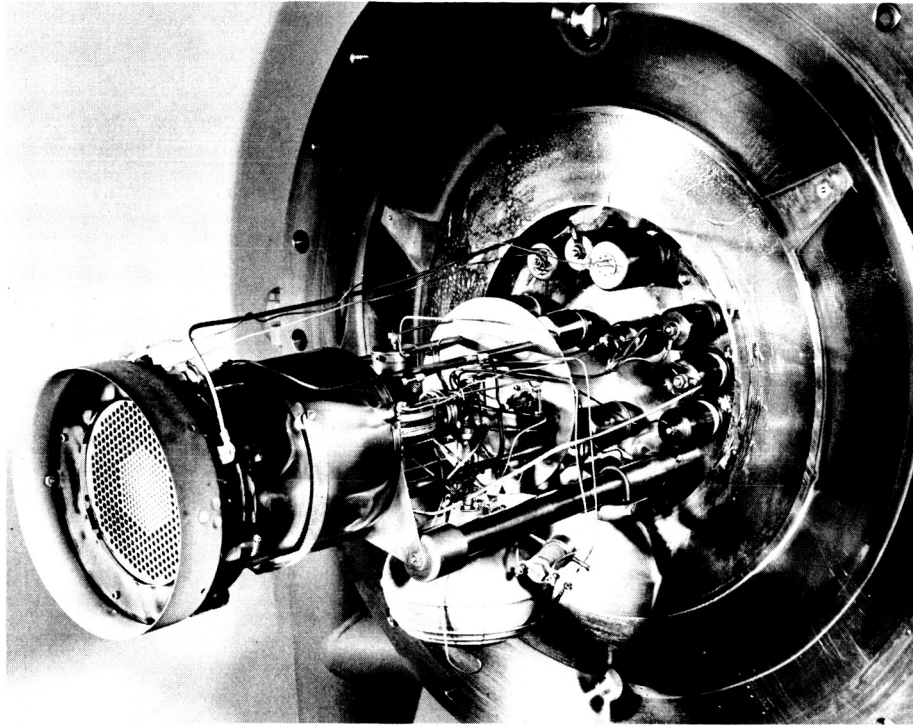


FIG. 37 DER-1 ENGINE SYSTEM AFTER 281-HOUR TEST



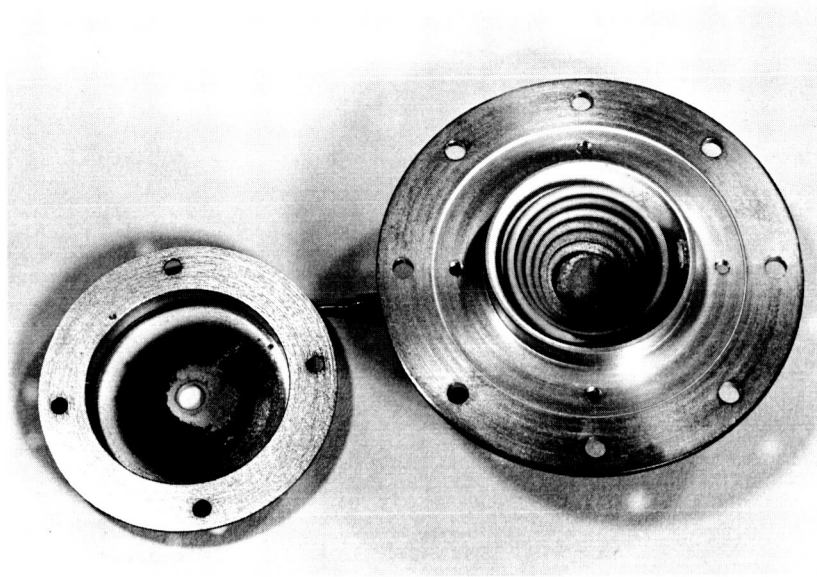


FIG. 38 ORIFICE PLATE AND CATHODE

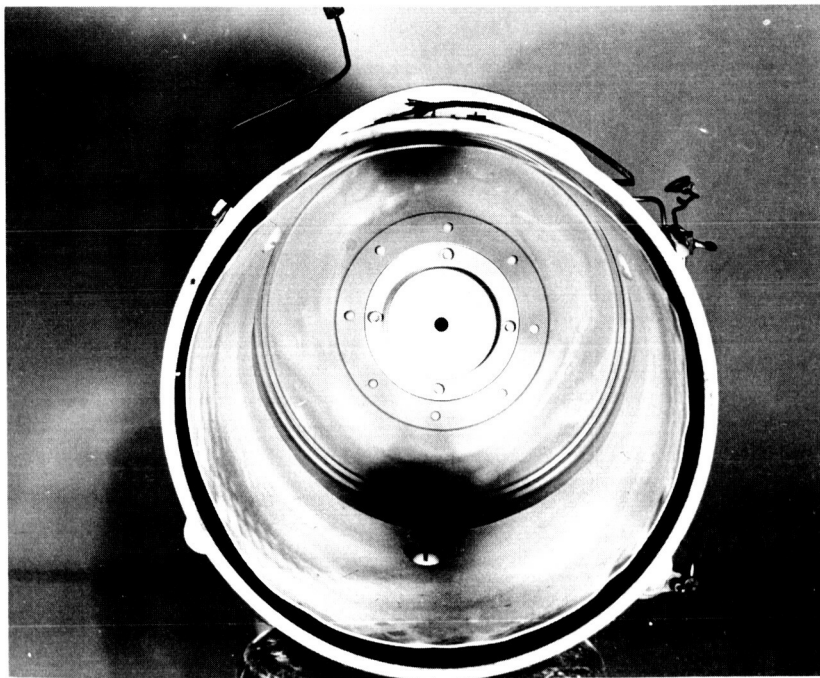


FIG. 39 ANODE AND CHAMBER INTERIOR

thick titanium sheet. This might have damaged the magnet coils had the run continued. Careful inspection of Fig. 40 reveals one of these thin spots on the lower front cover. It would appear that some electrons from the beam plasma were focused on these spots.

There was a 2-to 3-inch wide annular gap between the engine and the front of the ground cage. The placement of the negative high-voltage lead was such as to focus backstreaming electrons to spots on the shell on both sides of the negative lead. The damage by backstreaming electrons can be easily eliminated by removing these negative leads from the area between the engine and ground shield and by reducing the radial gap between the accelerator electrode and the ground shield.

Figure 41 indicates the condition of insulators after the run. They appeared relatively clean under the shielded area although localized dark rings could be found in the troughs of the convoluted surfaces. In general, the hotter the running temperature, the cleaner the surface. Unshielded parts of the insulators were contaminated.

The screen electrode was discolored but no visible erosion was noted. Figure 42 is a view of the electrode assembly showing the upstream side of the screen. Note the discoloring in the grid portion and the metallic appearance of the outer edge of this plate. The small lip machined on these plates is successfully preventing cesium from escaping through this joint.

All wiring and connectors including Deutsch plugs seemed in excellent condition with no observable loosening of the joints.

#### Accelerating Electrode

Figure 43 is a photograph of the downstream side of the accelerating electrode. The major erosion occurred on the webbing between large and small holes. Depth of the pits at this interface and at positions along six equally spaced radial lines from the electrode center were measured. The deepest pits were in twelve locations, where a large web area results from the change in hole patterns. The depth of these pits ranged from 0.0184 to 0.0238 inches. A photomicrograph of a sample section through one of these pits appears in Fig. 44.

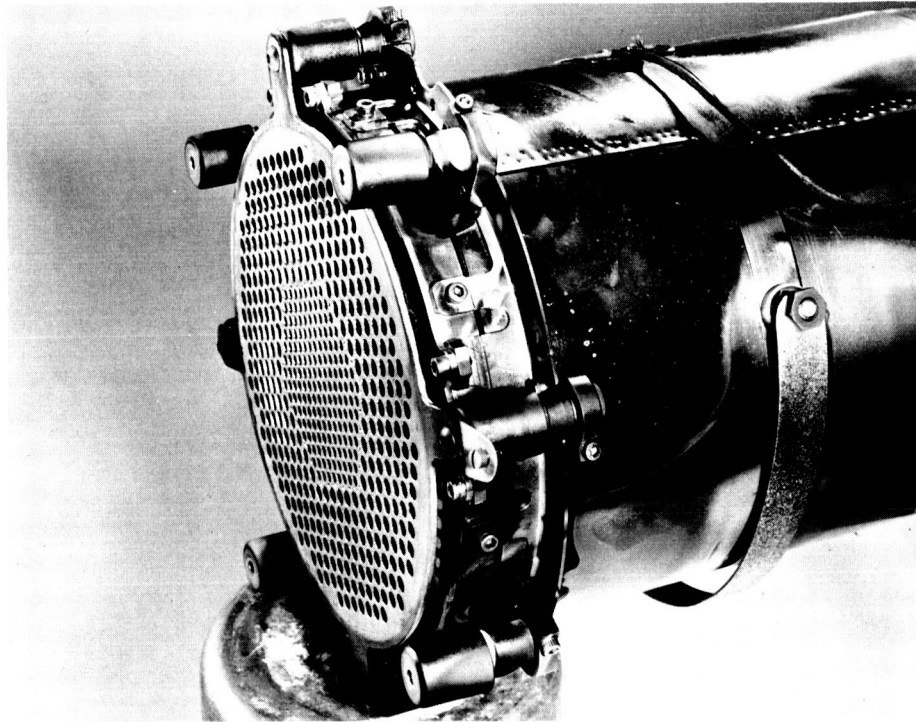


FIG. 40 ENGINE SHELL WITH ELECTRODES ATTACHED

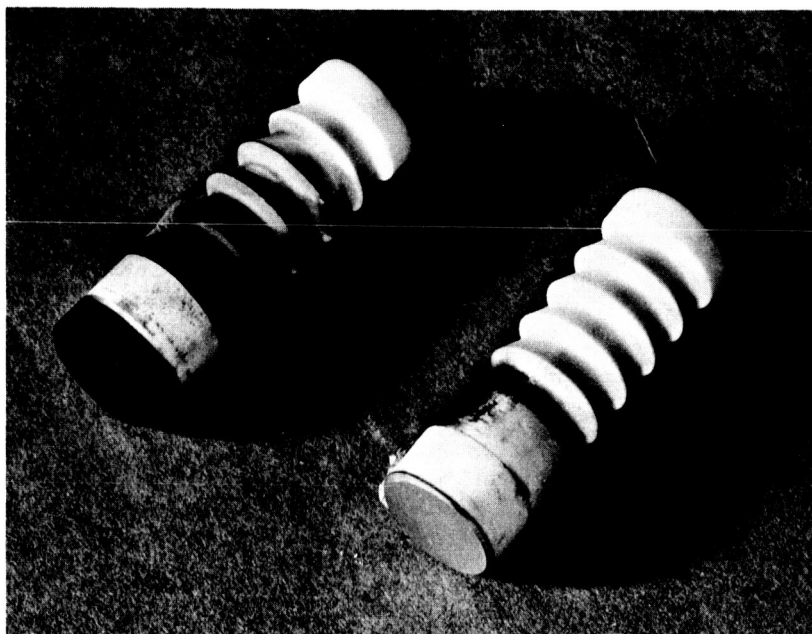


FIG. 41 ELECTRODE INSULATORS

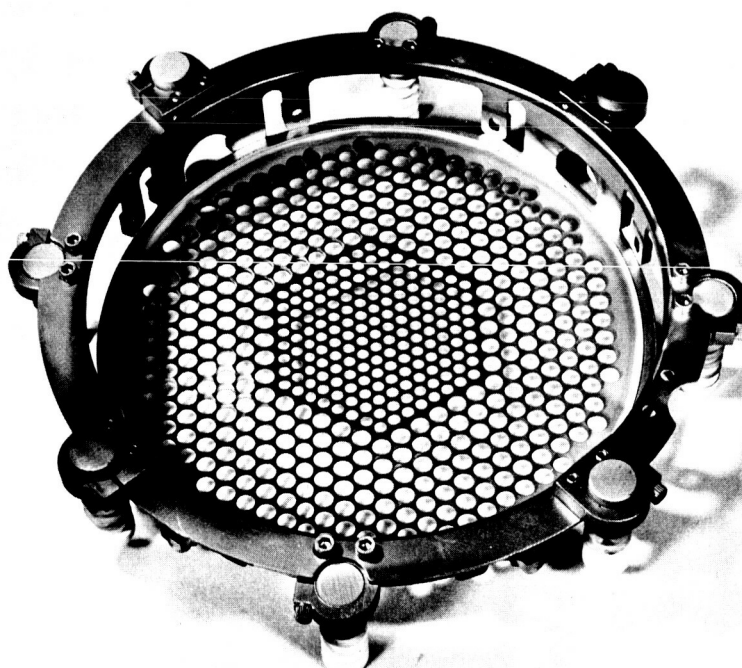


FIG. 42 SCREEN ELECTRODE

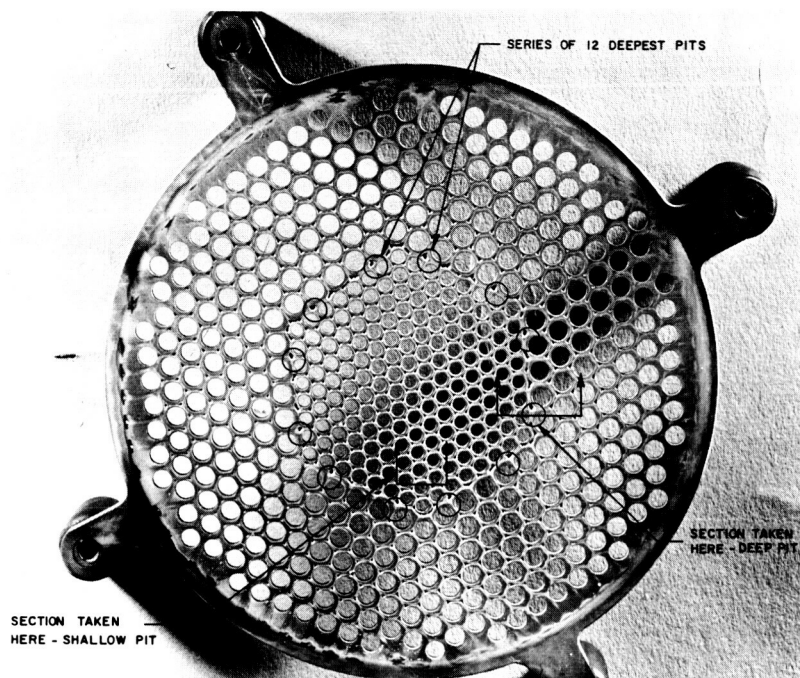


FIG. 43 ACCELERATING ELECTRODE - DOWNSTREAM SIDE

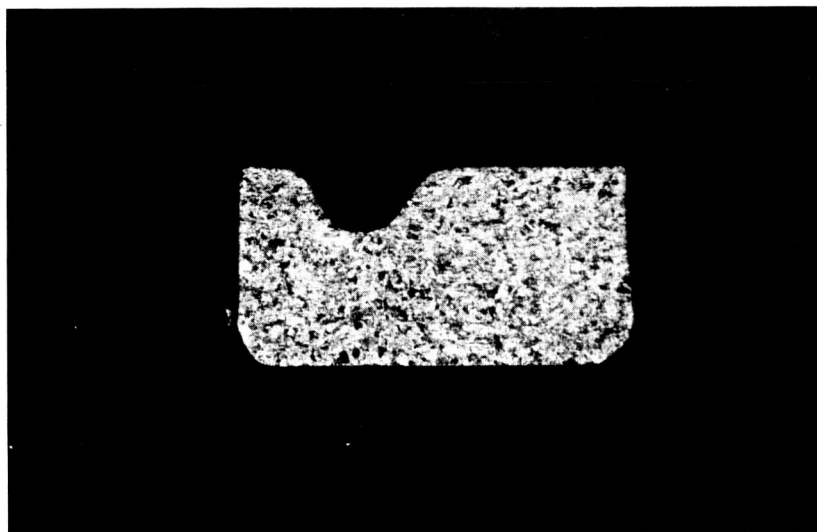


FIG. 44 CROSS SECTION OF DEEP PIT IN ACCELERATING ELECTRODE

Depth of pits in the central hole pattern ran from 0.0048 to 0.0139 inch with the deepest holes nearer the outer part of the pattern. Pits in the outer hole pattern ran from 0.0099 inch at the inside of the pattern to no pits at the outer edge. A photomicrograph of one of the shallow pits appears in Fig. 45. Figure 46 shows the upstream side of the accelerator electrode. There was no visible erosion.

Copper deposited on the downstream side of the electrode was 0.00062-inch thick. The estimated weight of this layer is 1.1 gm. Adding this to the weight loss of the electrode after the run indicates a total weight loss, during 281 hours of operation, of 2.25 gm.

Several holes were eroded on one side indicating the misalignment due to visual adjustment; as mentioned earlier this was a contributing factor to high drain.

It is possible that this electrode could be run for a few thousand hours. Even when the twelve deep pits had eroded through, the structural rigidity would have remained.

#### Sample Analysis

Scrapings were taken from various components for chemical analysis. A summary of the results is presented in Table IV. Only a qualitative analysis is meaningful due to the lack of knowledge regarding the amount of base material taken into the sample.

Small amounts of silicon appeared in all the samples and this is attributed to diffusion pump oil which contains this element. Similarly, copper was found on all components and as mentioned earlier this material was sputtered back to surfaces facing the collector. The upstream side of the screen electrode which does not face the collector, apparently collected copper evaporated off the cathode plate and orifice.

The molybdenum on the anode and on the upstream side of the accelerator electrode probably came from the molybdenum orifice plate as this part had lost weight during the run. Gold was located on both the anode and screen. The only gold in the system is found in the braze material used to fasten cathode parts.

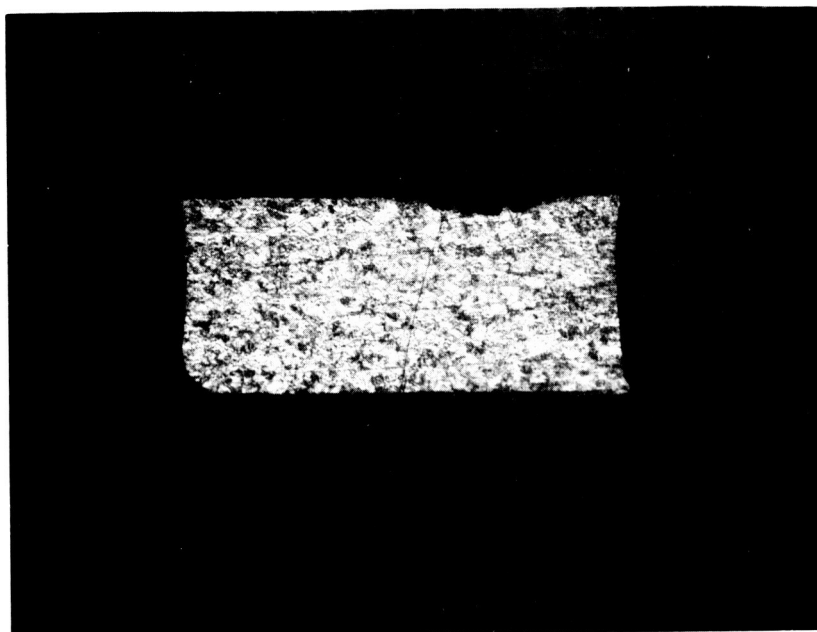


FIG. 45 CROSS SECTION OF SHALLOW PIT IN ACCELERATING ELECTRODE

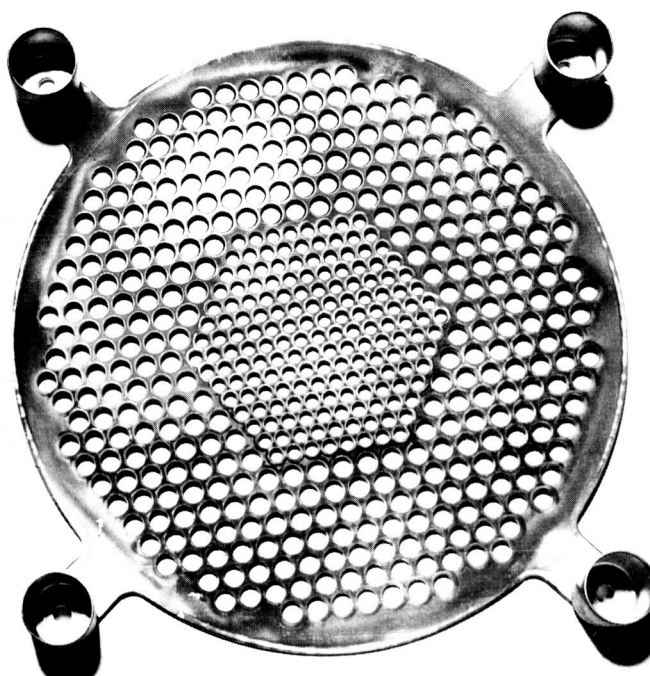


FIG. 46 ACCELERATING ELECTRODE - UPSTREAM SIDE

TABLE IV

Analyses of Deposits on Components

<u>Component</u>	<u>Base Material</u>	<u>Major Contaminant</u>	<u>Other Significant Contaminants</u>
Accelerating Electrode (Downstream)	Copper	Molybdenum (small amount)	Silicon
Accelerating Electrode (Upstream)	Copper	Molybdenum	Silicon
Screen Electrode (Downstream)	Molybdenum	Copper	Silicon
Screen Electrode (Upstream)	Molybdenum	Copper	Gold Silicon
Anode (Inside Front)	Copper	Molybdenum	Gold Silicon
Cathode Orifice Plate (Downstream)	Molybdenum	Copper	Silicon

Very small traces (<0.01%) of iron, titanium, and aluminum were detected for all samples.



The single result that is difficult to explain is the presence of molybdenum on the downstream side of the accelerator electrode. Since molybdenum was leaving the cathode orifice plate and probably the cathode, part of it must have reached the collector. This may have been sputtered back to the engine.

#### Weight Changes

Weight of the critical parts before and after the run are presented in Table V.

It is difficult to say how much error is introduced into the determination of these net weight changes by the cleaning processes. Care was exercised to remove only coatings but base material was found in most samples.

Since the anode is made of copper and since no photomicrographs were taken the added weight due to plating was not determined. The cleaning process did not remove all of the plating; thus the gain in anode weight.

#### Analysis of Feed System After Test

Following the 281-hour duration test, the zero-g feed system was completely dismantled and an analysis made on many of the components. The feed system was disassembled in the dry box. The photographs of Figs. 47, 48 and 49 show the components of the system while still in the dry box. It was observed that the cesium, both in the reservoir and the porous rod, was clean and bright. Slight discolorations were noted in the vaporizer tube and on the valve body. The valve ball contained a small deposit of material. Analysis of this deposit disclosed copper, gold, and silicon as the contaminants. Sectioning of the reservoir showed it to be exceptionally clean inside with no evidence of cesium corrosion or attack at weld joints or on the fin assembly.

The porous rod was sectioned while still in the dry box. Five samples were removed for analysis. Figure 50 indicates the location on the porous rod where samples were removed. Table VI lists the results of the quantitative spectrographic analysis that was performed on these

TABLE V

Component Weight Changes

Component	Weight Before Run (gms)	Weight After Run (gms)	Weight After Cleaning (gms)	Net Change (gms)	%Change
Accelerating Electrode	141.9354	140.7920		-1.1434	-0.80%
Screen Electrode	119.2758	119.6846	118.8092	-0.4666	-0.04%
Anode	349.6603	350.7488	350.2770	+0.6167	+0.02%
Cathode Orifice Plate	26.4270	26.4854	26.3614	-0.0656	-0.25%
Cathode Mounting Plate	135.4051		135.3540	-0.0511	-0.04%

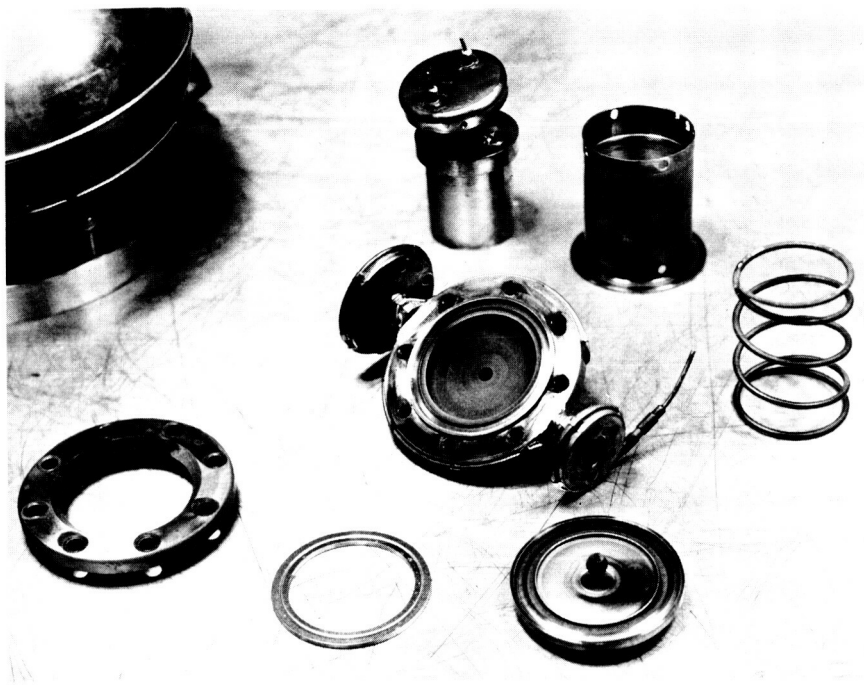


FIG. 47 SOLENOID VALVE COMPONENTS

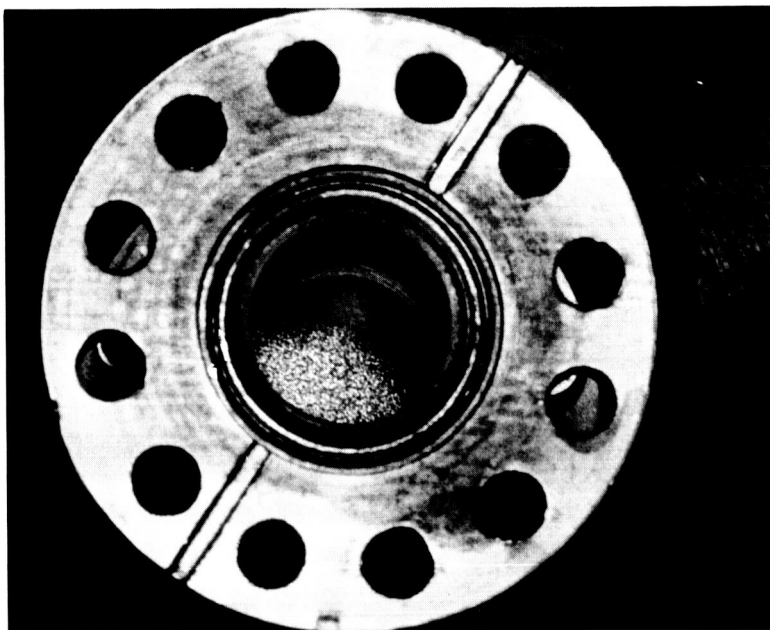


FIG. 48 END VIEW OF VAPORIZER SURFACE

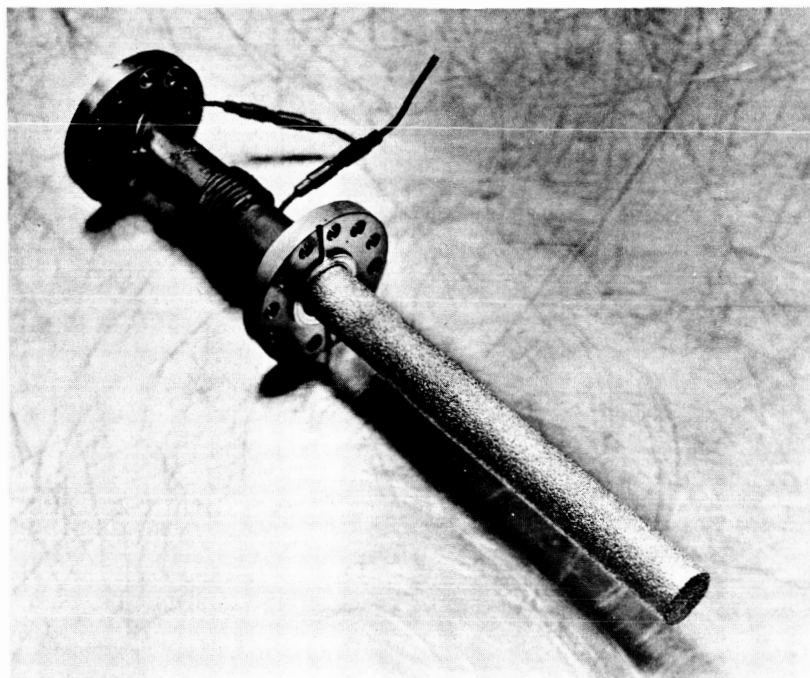


FIG. 49 POROUS ROD AND VAPORIZER ASSEMBLY

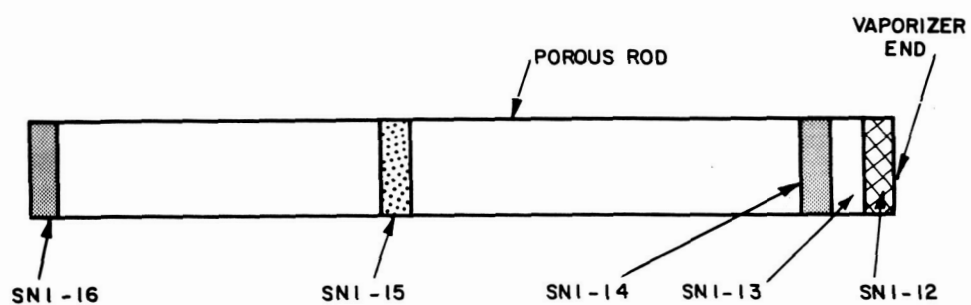


FIG. 50 LOCATION OF SAMPLES TAKEN FOR ANALYSIS

TABLE VI  
Analysis of Porous Rod

<u>Element</u>	<u>Control Sample SN1-11</u>	<u>SN1-12</u>	<u>SN1-13</u>	<u>SN1-14</u>	<u>SN1-15</u>	<u>SN1-16</u>
Manganese	0.09%	0.01%*	0.01%*	0.01%*	0.01%*	0.02%*
Iron	0.38%	0.09%	0.03%	0.12%	0.10%	0.11%
Silicon	0.10%	0.17%	0.13%	0.12%	0.11%	0.18%
Copper	0.03%	0.15%	0.08%	0.10%	0.13%	0.09%
Cobalt	0.16%	0.11%	0.09%	0.12%	0.15%	0.13%
Titanium	0.03%	0.01%*	0.01%*	0.01%	0.02%	0.03%
Magnesium	0.06%	0.12%	0.05%	0.06%	0.02%	0.11%
Nickel	Rem.	Rem.	Rem.	Rem.	Rem.	Rem.

\*Less than

samples. Included in this table is the analysis of a control sample which was removed from the same porous rod prior to the engine run.

A sample of the remaining cesium was also obtained during the disassembly. An analysis of this sample is compared with a sample that was obtained during the initial filling operation and is shown in Table VII.

After removal from the dry box, the reservoir was sectioned. Photomicrographs showed no attack of either the base material (type 347 stainless) or the weld joints. No change in composition of the fin material could be detected by spectrographic analysis. The largest weight loss detected was a loss of 0.8 percent from the fin assembly of the reservoir. This was not considered significant in terms of its effect on feed system lifetime. It appeared that the system could easily meet its design lifetime of 750 hours.

#### 2.3.3 Long Duration Test with Aluminum

On the basis of the electrode material studies reported in Subsection 2.1, aluminum was chosen for a second long duration engine test.

##### Operating Conditions and Time History

The DE engine was used with a zero-g feed system loaded with about 1 pound of cesium. The aluminum electrode was 1/16 inch thick and had a DE electrode aperture pattern with hole locations matching those of the molybdenum screen electrode. The usual DE configuration was altered slightly by bringing the three anode leads from the anode posts to the rear of the engine before joining them. The DE configuration used previously had the three posts joined by a strap at the middle of the engine with a single lead brought back to the rear of the engine.

Average engine operation during the test was at the parameters presented in Table VIII. The engine ran at full beam for 238 hours. The run was terminated when the cesium was nearly exhausted and the feedrate could no longer be maintained.

TABLE VII  
Analysis of Cesium Samples

Element	Sample	
	Before Run	After Run
Cesium -----	Remainder	Remainder
Aluminum -----	1 PPM*	1 PPM*
Barium -----	20 PPM*	20 PPM*
Boron -----	10 PPM*	10 PPM*
Calcium -----	10 PPM	1 PPM*
Chromium -----	1 PPM*	1 PPM*
Iron -----	13 PPM	1 PPM*
Magnesium -----	1 PPM	0.5 PPM
Manganese -----	1 PPM*	1 PPM*
Nickel -----	1 PPM*	1 PPM*
Lead -----	25 PPM	7 PPM*
Tin -----	35 PPM	15 PPM*
Strontium -----	2 PPM*	1 PPM*
Lithium -----	20 PPM*	20 PPM*
Titanium -----	3 PPM*	3 PPM*
Thallium -----	3 PPM*	3 PPM*
Sodium -----	5 PPM*	5 PPM
Potassium -----	10 PPM*	10 PPM*
Columbium -----	20 PPM*	-
Molybdenum -----	3 PPM*	-
Silicon -----	8 PPM	1 PPM*
Copper -----	1 PPM	1 PPM

\* less than  
- not detected

TABLE VIII

Engine Operating Parameters  
During 238-Hour Aluminum Electrode Test

<u>Run Time (hours)</u>	
Positive High Voltage, $V_+$	3.8 kv
Negative High Voltage, $V_-$	-0.6 kv
Negative HV Current (drain current) $I_-$	4.5 mA
Beam Current, $I_B$	389 mA
Arc Voltage, $V_A$	7.7 volts
Arc Current, $I_A$	38.5 amps
Beam Power, $P_B$	1.479 kw
Drain Power, $P_D$	0.020 kw
Magnet Power, $P_M$	0.007 kw
Arc Power, $P_A$	0.298 kw
Total Power, $P_T$	1.804 kw
Thrust, T	9.03 mlb
Power to Thrust, P/T	200 kw/lb
Power Efficiency, $\eta_p$	82%
Mass Efficiency, $\eta_M$	91.5%
Overall Engine Efficiency, $\eta_E$	75%
Specific Impulse, $I_{sp}$	6930 sec
$I_-/I_B$	1.2%
$P_A/I_B$	0.766 kev/ion
Accel Electrode Temperature, $T_A$	282°C
Cathode Housing Temperature, $T_c$	462°C
Chamber Pressure, P	$1.0 \times 10^{-7}$ mm Hg



The rate of cesium consumption, as determined by weighing the reservoir before and after the run, was determined to be 2.12 gm/hr with an average beam current of 389 mA. This gives an absolute mass utilization determination of 91.5 percent at 766 ev/ion. This is in excellent agreement with previous determinations made with a neutral efflux detector (EOS Report 3670-Final, NASA CR-54067). Neutral efflux determinations made in the facility being used for extended duration tests have indicated slightly lower mass utilization efficiencies (87.5 percent in the case of the 238-hour test).

Figure 51 presents a time profile of the accelerating electrode temperature and the drain current during the 238-hour run. The lowest drain current toward the beginning of the run was 3 mA of which 0.5 mA was residual. Toward the end of the run the drain current was 4.8 mA of which 1 mA was determined to be residual. The net increase during the 238 hours was about 1.3 mA while the net increase in accelerating electrode temperature was over 40°C.

The highest temperatures and drain currents encountered around the middle of the test are believed to be due to direct interception caused by thermal expansion of the aluminum electrode. The coefficient of thermal expansion of aluminum is 1-1/2 times that of copper and 3-1/2 times that of molybdenum. At 2-inch radius, and 280°C, the apertures would be misaligned by 0.011 inch, sufficient to introduce some direct interception. Apparently, after about 150 hours, changes in the edges of the outer apertures caused by sputtering had proceeded to the point where the direct interception was reduced.

#### Condition of Engine After Test

After the run the engine was in excellent condition. A more complete ground cage enclosure prevented backstreaming electrons from the beam plasma from striking the magnet covers as had been the case in the 281-hour run with a copper electrode.

Figures 52 and 53 are photographs of the accelerating electrode after the run. Damage was minimal; the deepest pits, at the

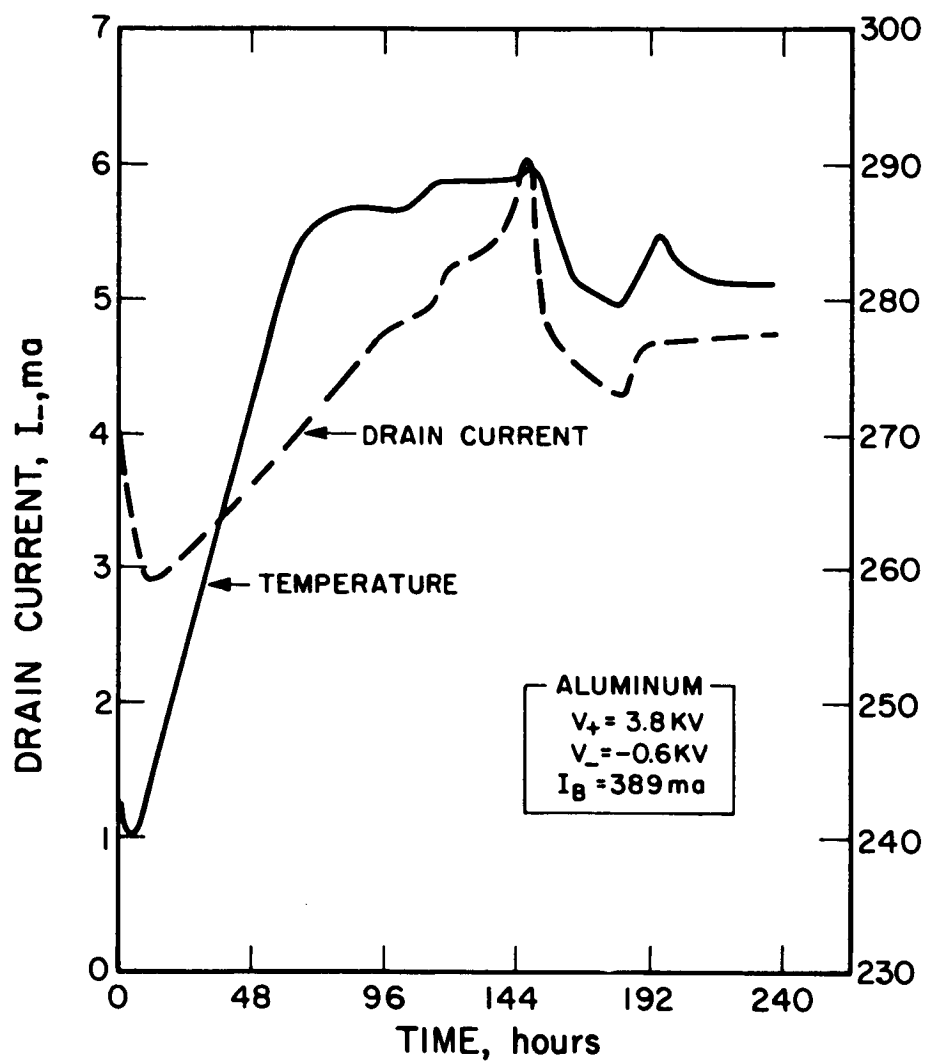


FIG. 51 DRAIN CURRENT VERSUS TIME PROFILE FOR 238-HOUR ALUMINUM ELECTRODE TEST



FIG. 52 DOWNSTREAM SIDE OF ALUMINUM ELECTRODE AFTER  
238-HOUR TEST

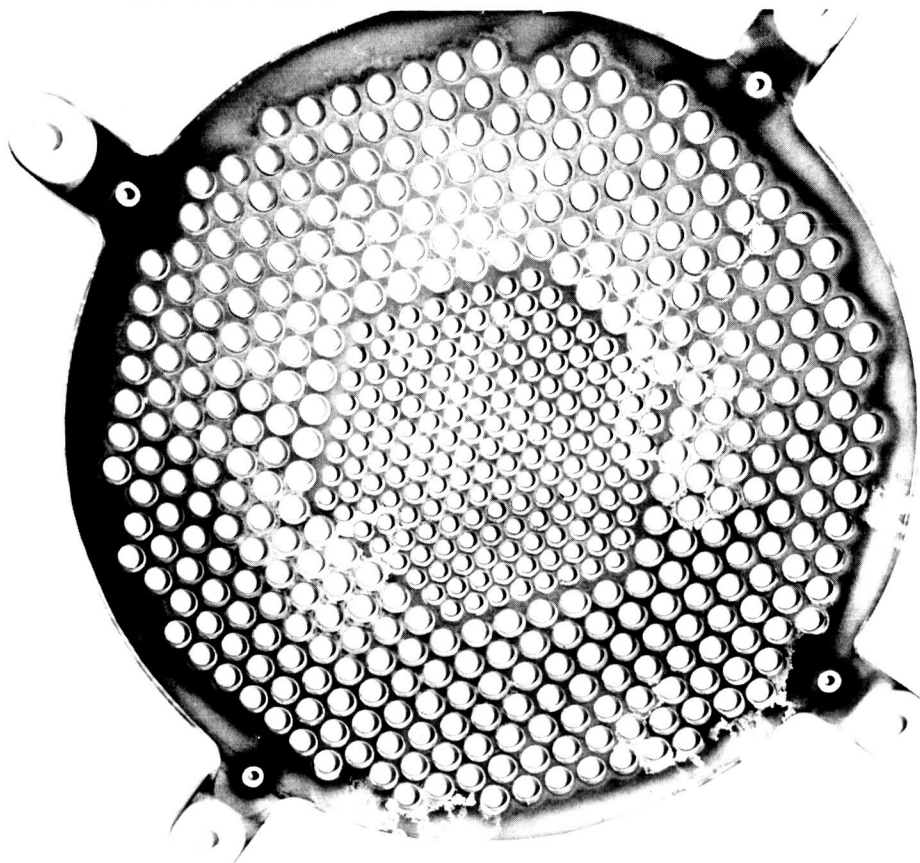


FIG. 53 UPSTREAM SIDE OF ALUMINUM ELECTRODE AFTER  
238-HOUR TEST

region between the large and small hole patterns were 0.003 to 0.004 inch. During the 238 hours the electrode lost 0.323 gms of aluminum, 0.8 percent of its original weight.

The 0.003 to 0.004-inch deep pits for the 238-hour aluminum electrode test may be compared with the corresponding 0.018 to 0.024-inch pits for the 281-hour run with the copper electrode. The volume erosion rate of the aluminum electrode appears to be about 1/5 that of the copper electrode. On the basis of the 238-hour run and the electrode material studies, aluminum was chosen as the electrode material for the 750-hour tests described in Section 3.

#### Feed System Performance

During the 238-hour run, no feed system malfunctions were encountered. Near the beginning of the run, the vaporizer power was 17 watts which decreased to 15 watts as the reservoir reached its steady-state temperature range of 130 to 140°C. In the last hour of the run, vaporizer power increased to the imposed limit of 30 watts but the beam current could not be maintained due to lack of cesium.

Weighing of the reservoir disclosed that 18.4 gm of cesium remained in the feed system. A calculation based on the porosity and volume of the porous vaporizer rod indicates that it holds about 19 gm cesium. The only cesium remaining in the feed system would therefore be that trapped in the porous wick. Since the feed system used in these tests can be filled with about 2.13 kg cesium, 99 percent of a full load can be utilized with the 5-pound feed system.

## 2.4 DF Engine

The engine designated DF was developed from the DE engine using components and modifications as suggested by the results of the two long tests of the DE engine and, where possible, as suggested by results obtained on the applied research portion of the program described in Section 4 of this report.

An electrode system developed under the applied research effort for the permanent magnet engine was adopted for the DF engine. A modification was made to the magnet windings on the engine to generate a divergent magnetic field toward the screen electrode. This also was a direct result of the applied research program and resulted in an increase in overall engine efficiency of approximately 10 percent over the entire operating range of specific impulse. The cathode for the DF engine was fabricated entirely of molybdenum rather than titanium alloy to prevent contamination of the electrodes. Finally, a new electrode support insulator and shield system was designed to prevent insulator contamination and to allow free radial expansion of the accelerating electrode.

### 2.4.1 Electrodes

The electrodes designed for the DF engine were of the distributed geometry type developed under the previous program and described in Ref. 1. This design was modified by the addition of a third aperture size pattern between the inner and outer aperture areas to reduce the discontinuity in focusing characteristics observed during the course of the plasma distribution studies. For the DF engine, the screen electrode aperture diameters were reduced slightly from the corresponding dimensions of the DE electrodes. The counter-sink angle on the back side of the screen electrode apertures was increased from  $72^{\circ}$  to  $90^{\circ}$  to more closely approximate a thin screen. The apertures' diameters on the accelerating electrode were reduced to approximately 80 percent of the diameters of the screen electrode.

The accelerating electrode was increased in thickness from 0.062 inch to 0.125 inch and was fabricated from aluminum. On the basis of a linear extrapolation of the results of the 238-hour test, it was estimated that only 8 percent of the electrode weight would be lost in 5000 hours. Since the accelerating electrode and screen electrode operate at 250°C, the matched drilling previously employed to obtain close alignment between matching apertures was abandoned in favor of drilling the apertures on different hole patterns. This allowed a reduction in the radial distance to a given accelerator electrode aperture as compared with the radial distance to the matching screen electrode aperture at room temperature. With this process it is possible to correct for the difference in thermal expansion of the two electrode materials and achieve better alignment of the apertures at operating temperature.

#### 2.4.2 Distributed Magnet Windings

The high efficiency of the permanent magnet engine reported in Subsection 4.4 of this report was the result of the new electrode aperture pattern and a divergence in the magnetic field toward the screen electrode. The divergence of the magnetic field caused a displacement of the electrons toward the screen electrode, a resultant potential gradient within the discharge, and acceleration of ions within the discharge toward the screen electrode. This increased the ratio of ions to neutral cesium atoms arriving at the screen electrode for a given ionization percentage within the chamber. As a result, the same high mass efficiency (90 to 93 percent) was obtainable with much less arc power. Mass utilization of 93 percent was obtainable at 400 ev per ion as compared with 750 ev per ion for the DE engine.

Since the PM engine had not been run extensively and the DF engine was being designed for a 750-hour run, the magnet winding on the DF engine was redistributed to create a magnetic field divergence toward the screen electrode similar to that of the PM engine as shown in Fig. 54.

#### 2.4.3 Autocathode

To avoid the possibility of titanium contamination, the housing of the autocathode used on the DF engine was made of molybdenum. The orifice plate had previously been changed to molybdenum as a result of titanium contamination of the DE engine electrodes.

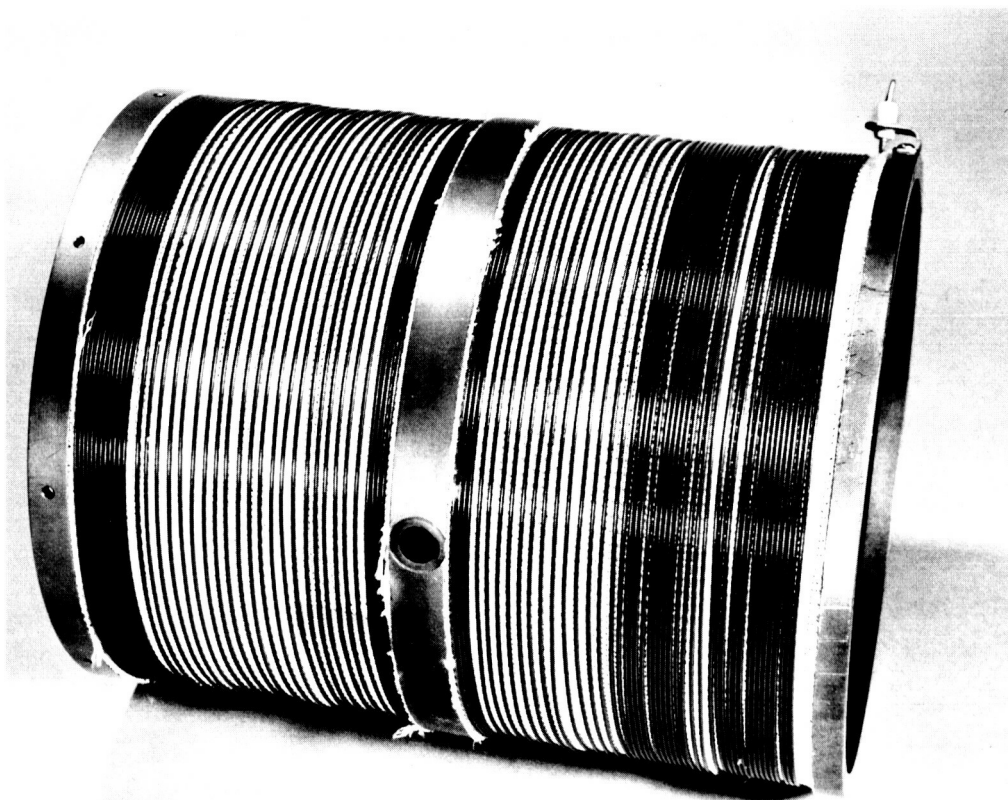


FIG. 54 DISTRIBUTED ELECTROMAGNET WINDING

#### 2.4.4 Electrode Support System

Modifications and redesign of the accelerator electrode supporting insulators, the insulator shields, and the electrode support ring were accomplished. The convolutions on the insulator were reversed to increase their effectiveness. Contamination of the insulators was decreased by reducing the diameter of the shields. Redesign of the support ring resulted in a weight reduction and better flexibility to accommodate expansion of the accelerator electrode.

The DF engine with the 750-hour cesium feed system and manual valve is shown in Figs. 55, 56, and 57 prior to the start of the long tests described in the next section.

#### 2.4.5 Lightweight Engine

A lightweight version of the DF engine was fabricated and tested. The major change from the DF engine used for the long duration test was in the design of the engine body. The body of the lightweight engine consists of two nested shells of spun stainless steel 0.010 inch thick. Circular grooves were spun into the inner shell at four positions along its axis to provide structural rigidity.

A stainless steel end ring was electron-beam welded to the inner shell. After the magnet windings had been installed, the outer shell was slipped over the inner shell and fixed to the end ring with screws. The end ring and ridges spun into the inner shell maintained clearance between the two shells. Bosses were then fitted into holes in the shells to accept the insulators for the anode supports. The inner and outer shells were then bolted to the cathode plate. The assembled body weighs 598.5 grams, approximately 150 grams less than the standard DF body. Figure 58 is a photograph of a complete engine, designated the DF-S, utilizing the lightweight shell. The holes in the outer shell permit outgassing when the engine is in the vacuum facility.



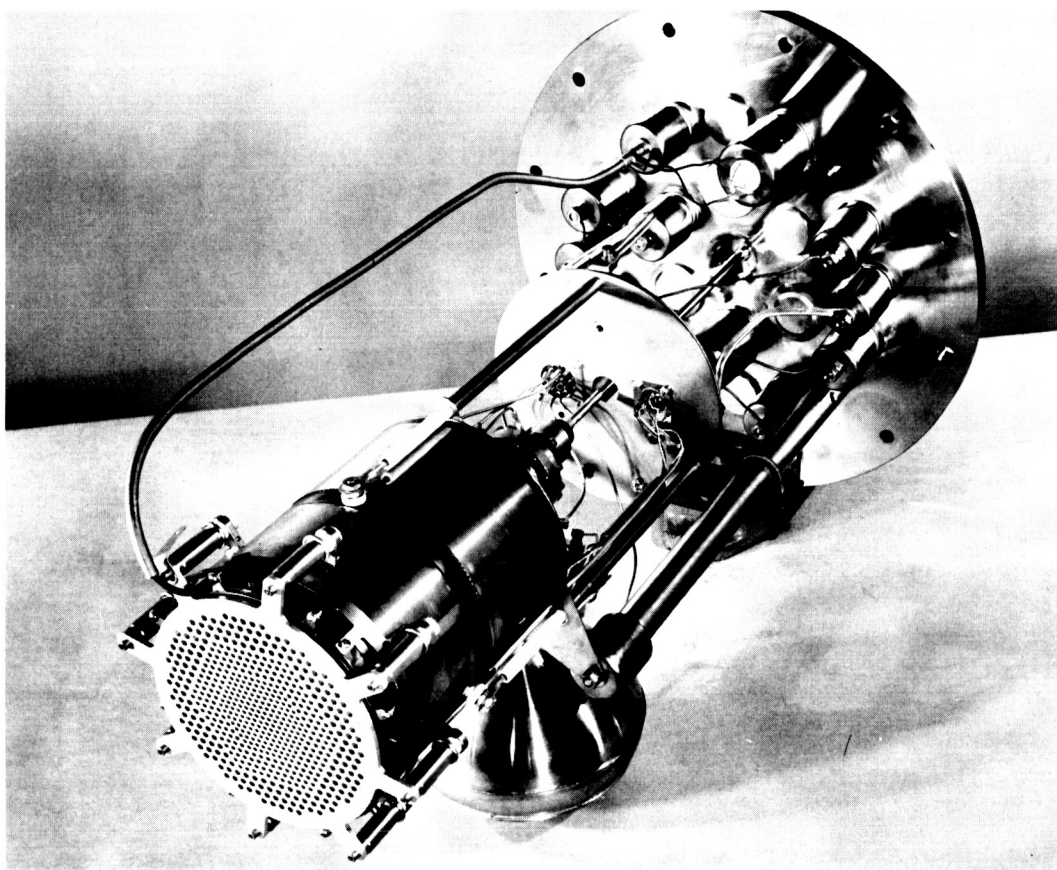


FIG. 55 DF ENGINE WITH 750-HOUR FEED SYSTEM

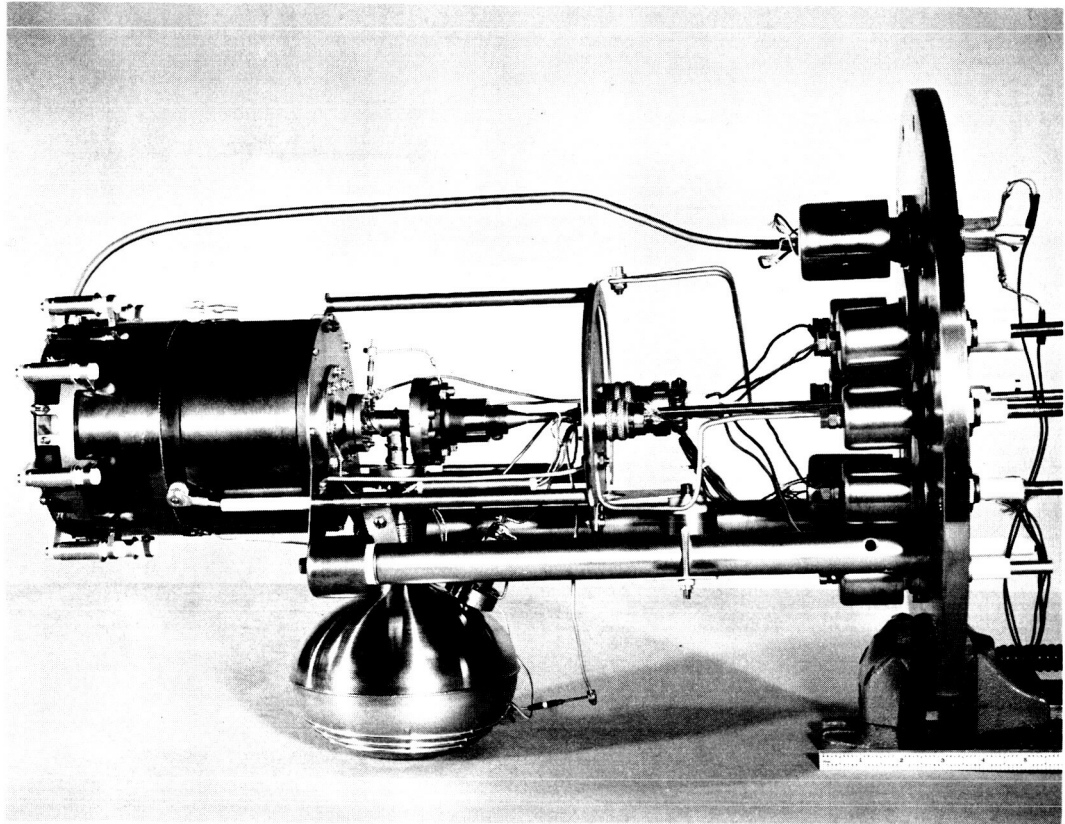


FIG. 56 DF ENGINE SYSTEM, SIDE VIEW

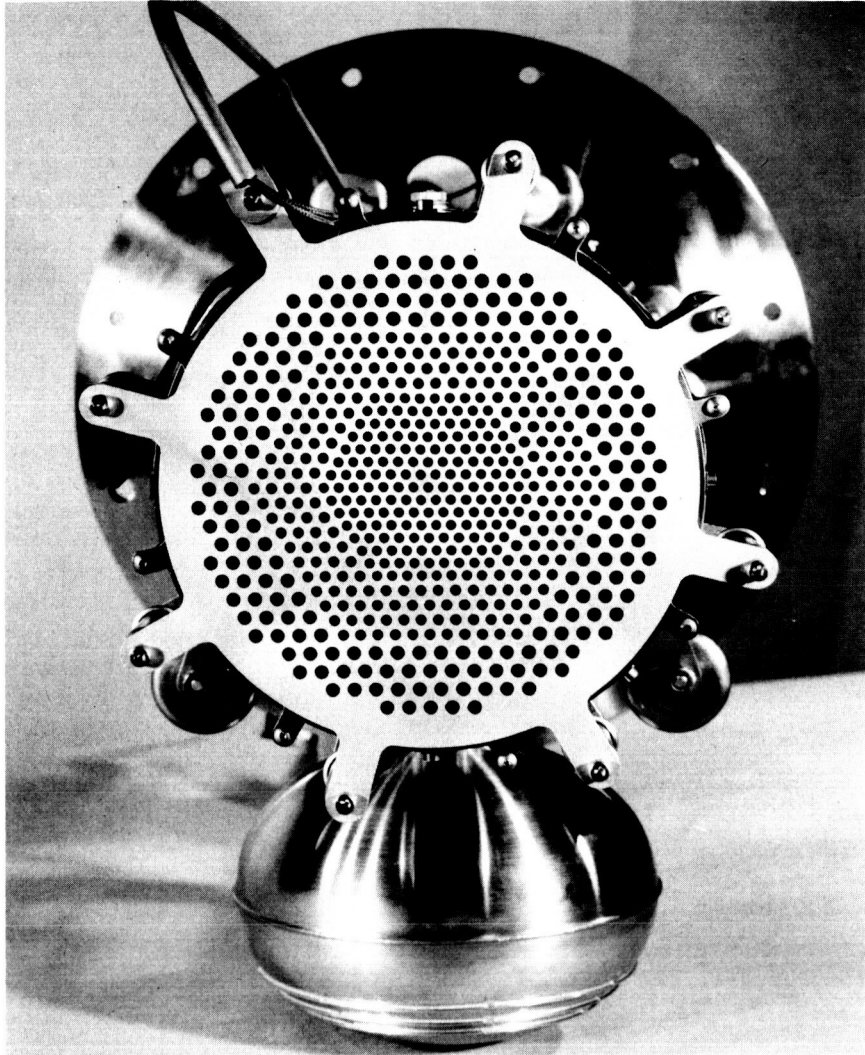


FIG. 57 END VIEW OF DF ENGINE SYSTEM SHOWING  
DF ELECTRODE

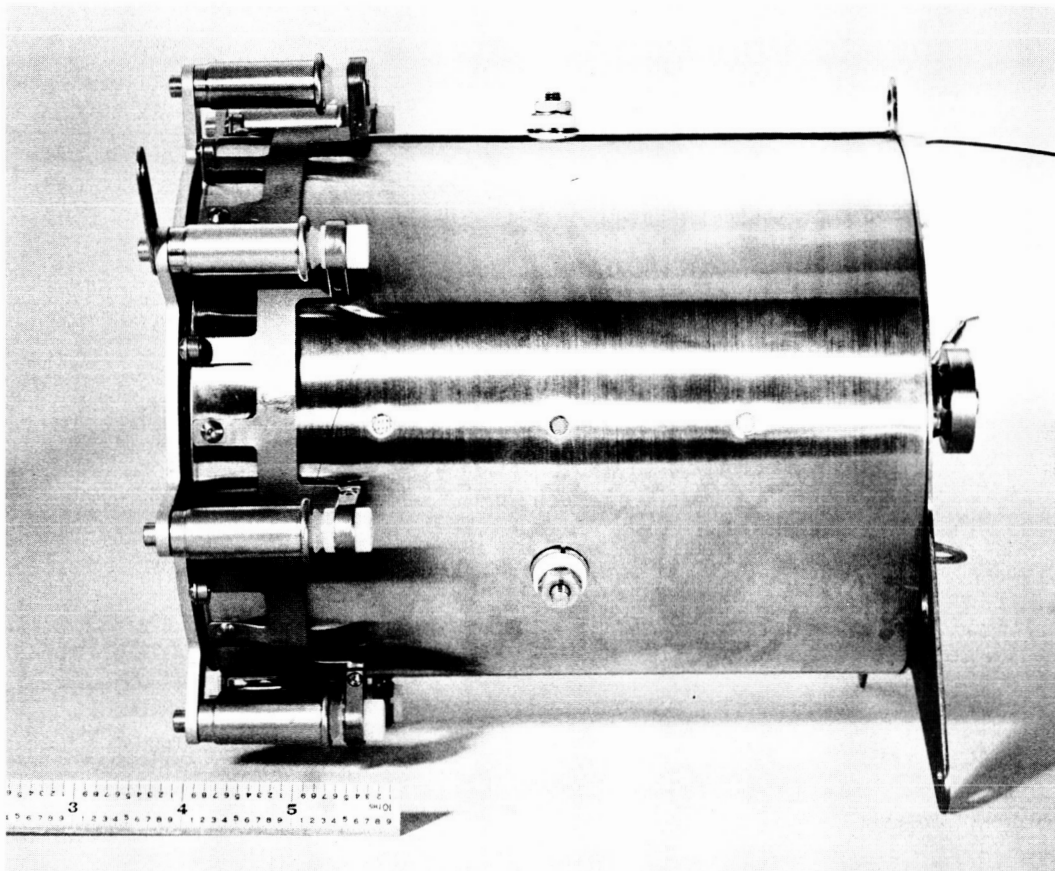


FIG. 58 DF-S LIGHTWEIGHT ELECTROMAGNET ENGINE

Plots of the axial magnetic field along the axis and 1.25 inches off the axis are shown in Fig. 59. Corresponding points for the DF engine used in the long duration test are shown for comparison. The fields are seen to be similar. Design differences between the DF-S body and the standard DF body prevented exact duplication of the field windings.

The DF-S engine was operated for approximately 20 hours. Its performance was thoroughly mapped and found to be similar to that of the standard DF engine. Overall engine efficiency versus specific impulse and power-to-thrust ratio versus specific impulse curves for these points are displayed in Figs. 60 and 61. Corresponding curves for the standard DF engine are also shown. The curves mesh at 7000 seconds with the standard DF engine performing better at the lower specific impulses. This is due to the fact that the electrode gap was slightly larger for the DF-S engine tests.

While minor problems were encountered during fabrication, it was possible to reduce the engine weight by 10 percent through the use of this type of construction.

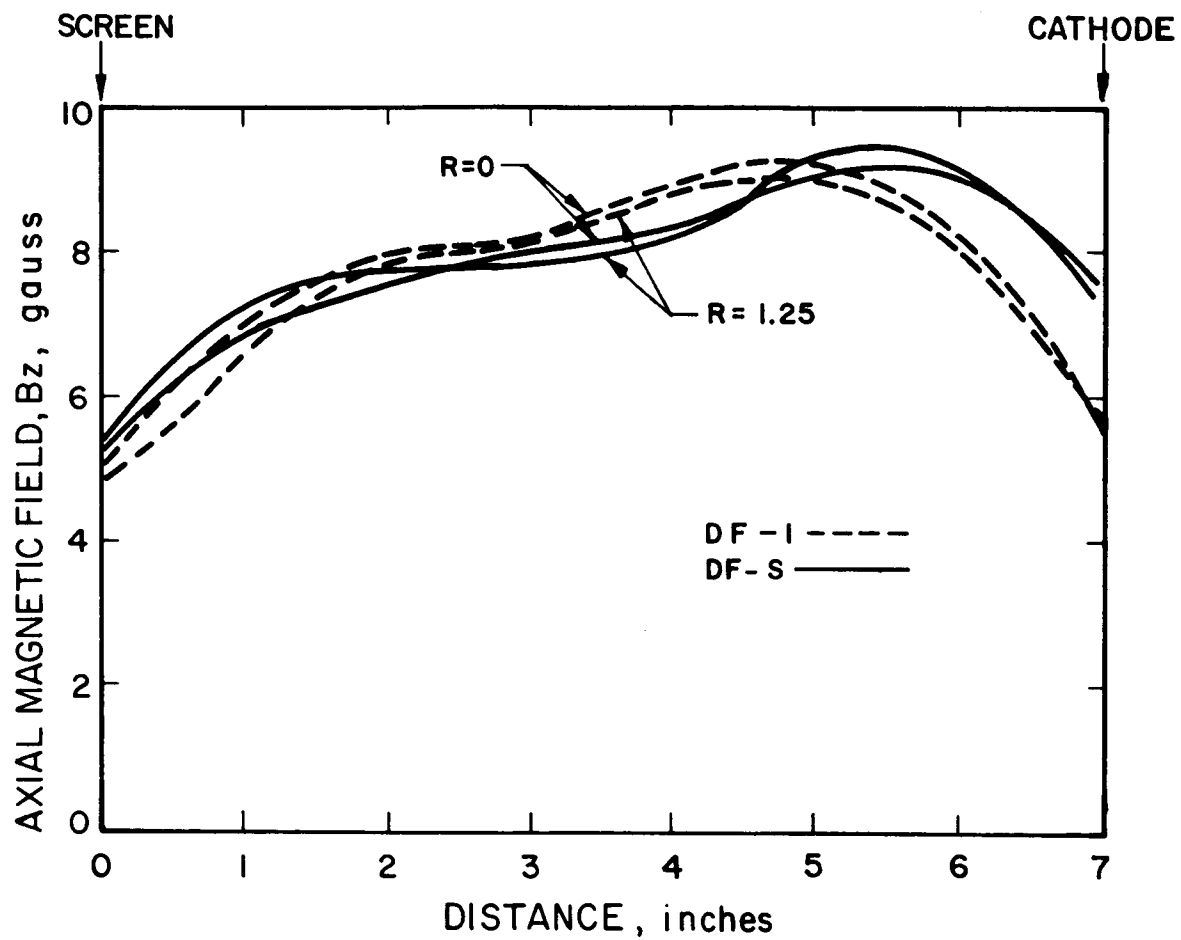


FIG. 59 DF-S AND DF-1 MAGNETIC FIELD PLOTS

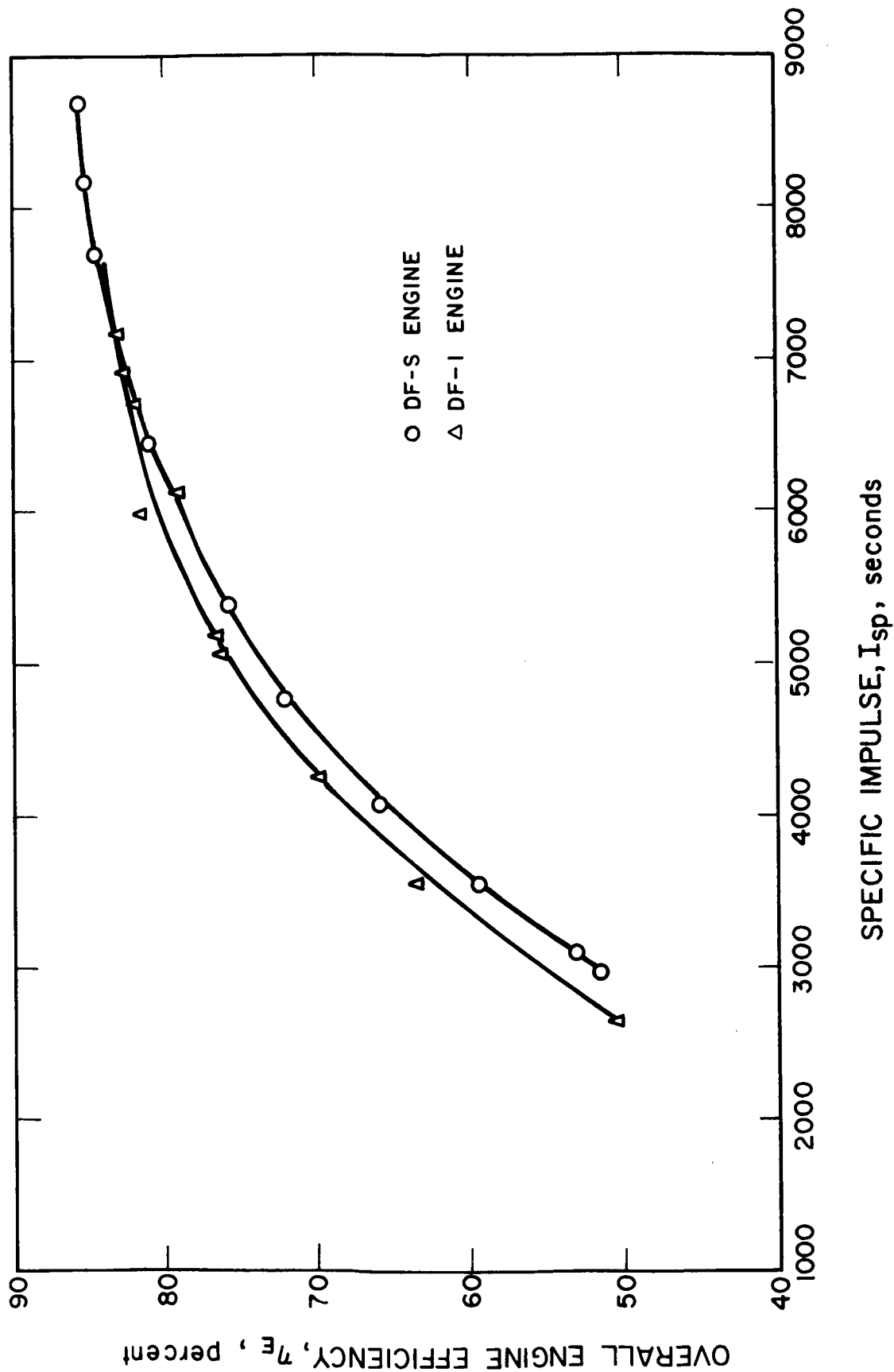


FIG. 60 DF-S AND DF-1 OVERALL ENGINE EFFICIENCIES

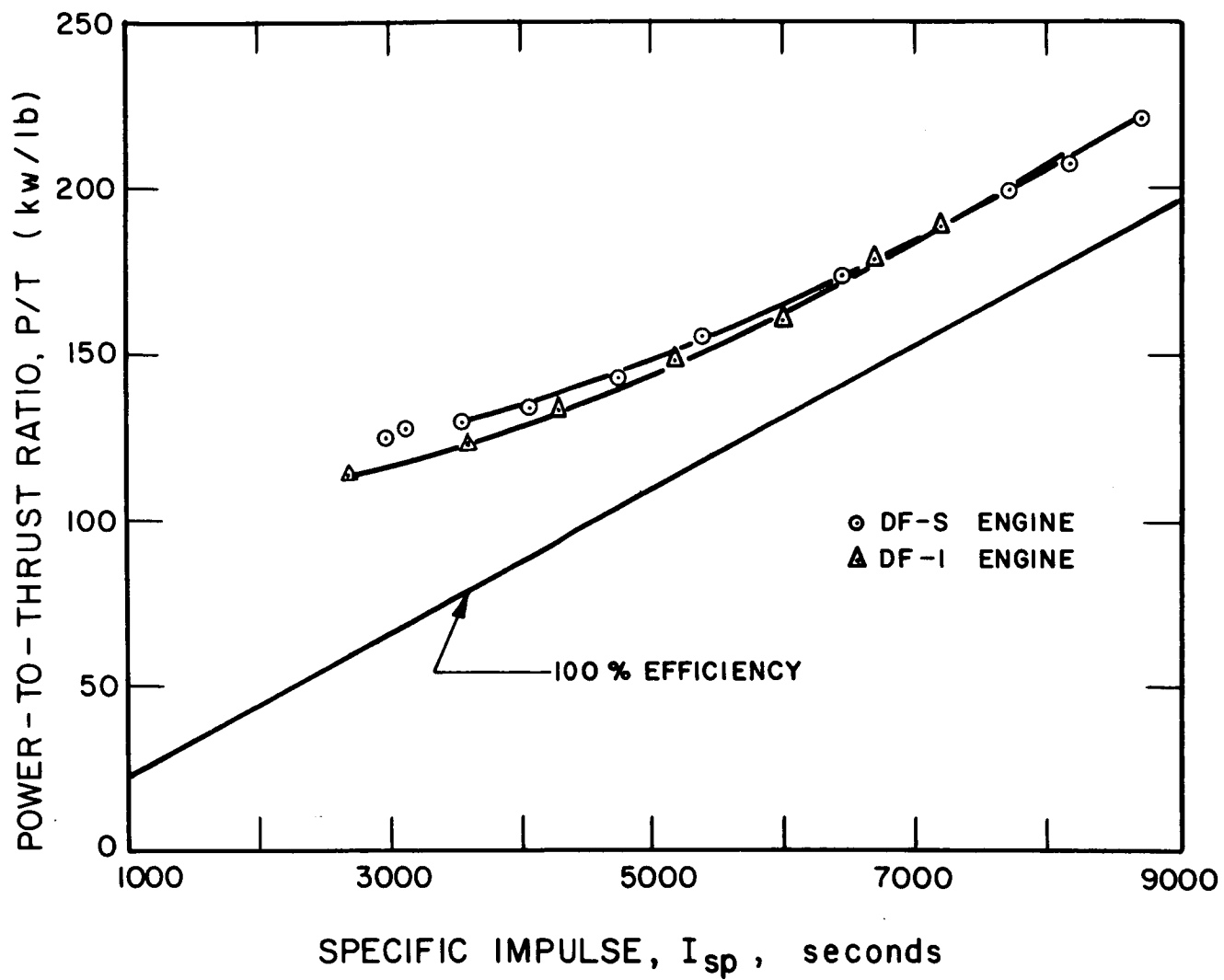


FIG. 61 DF-S AND DF-1 POWER-TO-THRUST RATIOS



### 3. DF ENGINE TESTS

Engine performance and lifetime were evaluated through performance mapping and extended tests of a DF engine. Engine efficiency over 80 percent at a specific impulse of 7000 seconds was achieved in three consecutive tests of a DF engine during which 2610 hours of operation were accumulated. Lifetime estimates based on the results of these long tests exceed 10,000 hours.

#### 3.1 Facility and Test Equipment

For the DF engine tests, the collector and liner designs of the facility described in Subsection 2.3.1 were changed to reduce back sputtering of copper to the engine system. The modified facility is shown in Fig. 62.

The inside diameter of the liner baffles was increased to allow more of the engine exhaust to pass to the collector and thus reduce sputtering from the liner. To shield the exposed liner surfaces from ion beam impingement, more baffles (with the large inside diameter) were added. A new collector consisting of long square tubes stacked parallel to the tank axis was designed and fabricated. Because the tube length is 5 times its width, trapping of material sputtered within the tube is very effective. The walls of the tubes represent only 15 percent of the frontal area of the collector.

The facility maintained pressures below  $1 \times 10^{-6}$  mm Hg with an operating engine system.

The engine and feed system were operated by a DE control system of the type discussed in EOS Report 3670-Final (NASA CR-54067)<sup>1</sup>. Vacuum, power, and high-voltage functions were interlocked to provide alarm signals or shut the system down in the event of engine system or test equipment malfunctions. Modifications were made to the system to allow recording of the beam current, arc current, vaporizer heater

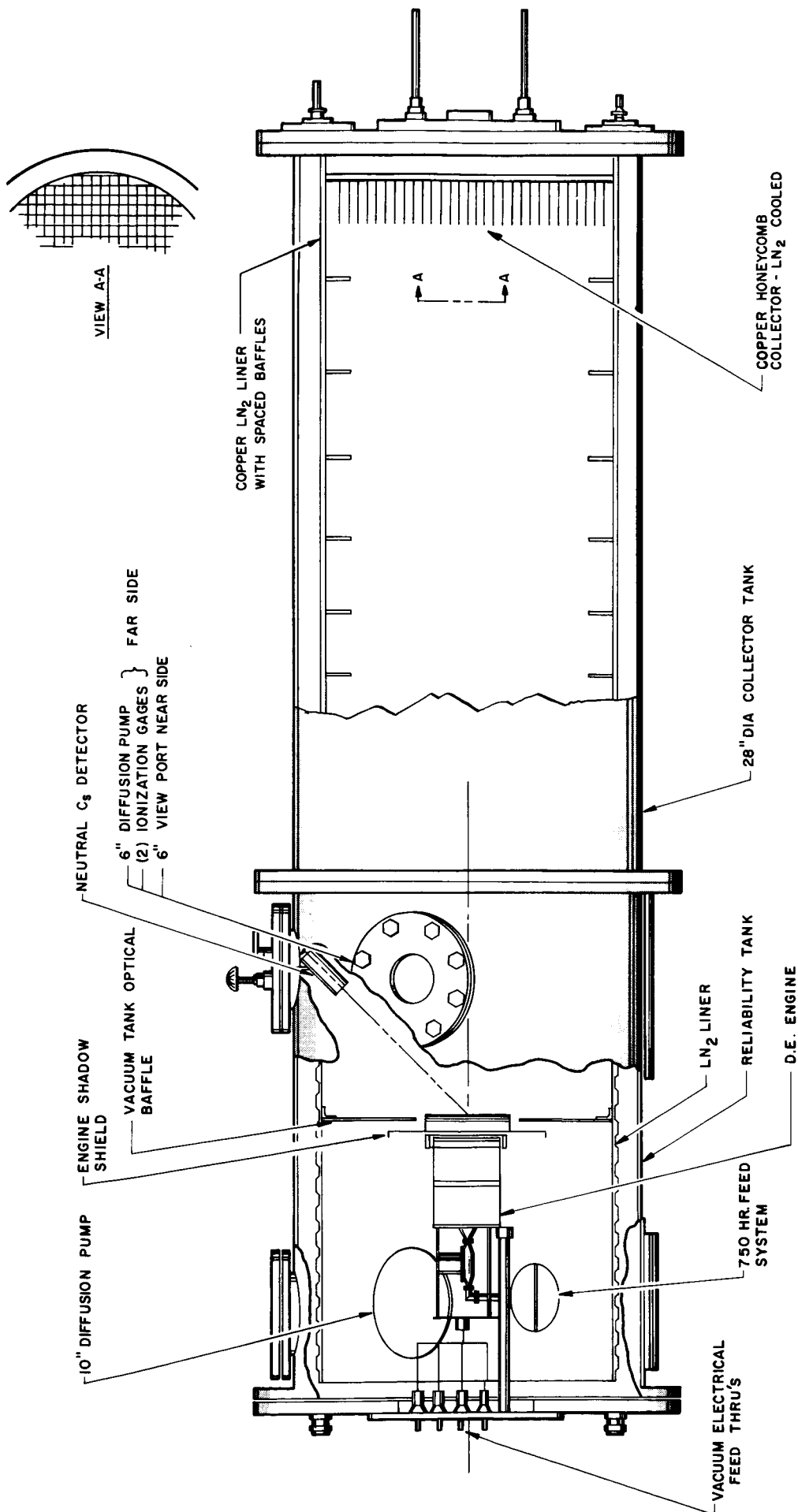


FIG. 62 ENGINE TEST CHAMBER

current, and run time. A new, more reliable high voltage cycling circuit was incorporated into the system and provision for automatic removal of vaporizer heater power in the event of any high-voltage malfunction was added.

### 3.2 Performance Mapping

The DF engine was placed in the above described facility and its performance evaluated over a wide range of operating levels.

#### 3.2.1 Measurements and Calculations

The directly measured engine operating parameters are the positive and negative high voltages, the beam current, the negative high voltage supply drain current, the arc current, the arc voltage, the magnet current, and the magnet supply voltage. The total flowrate is measured indirectly by a method which will be discussed later in this section.

#### Voltages and Currents

The arc current, arc voltage, magnet current, and magnet voltage are read off dc meters between the power supplies (which are isolated at high positive potential) and the power feedthroughs on the engine mounting flange. The positive and negative high voltages are read from meters mounted in the control panels of the HV power supplies. The signals are measured near ground by means of voltage dividers. The negative supply drain is also metered at the control panel.

The low sides (near ground potential) of both high voltage supplies are joined together and go through a current meter to ground. This meter thus reads the difference between the positive and negative supply currents, which is the net positive current leaving the engine, and is taken to be the beam current. This measurement of the beam current should be lower, if anything, than the actual energetic particle flow out of the engine since fast neutrals, formed by charge exchange, are not counted in the beam current and electrons going from

the accelerating electrode to ground are subtracted from the beam current. Electrons going from the accelerating electrode to  $V_+$  or ions going from the ion source to  $V_-$  (the accelerating electrode) do not affect the beam current measurement.

#### Total Flowrate

The total flowrate is determined by means of a neutral cesium detector. This detector has an entrance portion in which electric fields sweep away ions and prevent them from entering the detector. Neutral cesium atoms entering the detector are ionized at a hot tungsten filament and these ions are collected and measured. A mechanical shutter prevents any particles from entering the detector and allows determination of the background signal level which is subtracted from the detector reading.

The angular acceptance entrance area, and distance of the detector from the engine are such that about  $4 \times 10^{-7}$  of the neutral particles are sampled. The angular acceptance is wide enough so that the efflux over most of the engine frontal area is sampled.

The total flowrate is determined for each performance point by calibrating the neutral detector signal in terms of a total equivalent neutral efflux current. The vaporizer power is set manually and when steady-state conditions are reached, the beam current  $I_B$ , and the neutral cesium detector signal,  $I_{NCD}$ , are recorded. Keeping the vaporizer power (and the feedrate) unchanged, the arc power is then reduced and a lower beam current,  $I'_B$ , and a higher neutral detector signal,  $I'_{NCD}$ , are measured.

The change in the neutral detector signal,  $\Delta I_{NCD} = I'_{NCD} - I_{NCD}$ , corresponds to an increase of the total neutral efflux of  $\Delta I_B = I_B - I'_B$  since the flowrate was held constant. The neutral particle current equivalent of the neutral detector signal  $I_{NCD}$  is therefore

$$I_{Cs} = I_{NCD} \left( \Delta I_B / \Delta I_{NCD} \right)$$

and the total flowrate (in current equivalent) is

$$I_o = I_B + I_{Cs}$$

### Calculations

The total power into the engine is defined to be the sum of the beam power, the drain power, the arc power, and the magnet power. The currents and voltages are designated as:

<u>Symbol</u>	<u>Meaning</u>
$V_+$	positive high voltage
$V_-$	negative high voltage
$I_B$	beam current
$I_-$	negative HV supply current (drain current)
$V_A$	arc voltage
$I_A$	arc current
$V_M$	magnet voltage
$I_M$	magnet current

The associated powers are:

<u>Power</u>	<u>Symbol</u>	<u>How Calculated</u>
Beam Power	$P_B$	$I_B V_+$
Drain Power	$P_D$	$I_- (V_+ +  V_- )$
Arc Power	$P_A$	$I_A V_A$
Magnet Power	$P_M$	$I_M V_M$

The total power into the engine,  $P_T$ , is therefore:

$$P_T = P_B + P_D + P_A + P_M$$

The power efficiency,  $\eta_p$ , is defined to be the ratio of the power in the beam to the total power being fed into the engine or:

$$\eta_p = P_B / P_T$$

The mass utilization efficiency,  $\eta_M$ , is defined to be the ratio of the ion efflux to the total efflux (ions plus neutral particles) or:

$$\eta_M = I_B / I_o$$

The overall engine efficiency,  $\eta_E$ , is defined as the product of the power efficiency and the mass utilization efficiency or:

$$\eta_E = \eta_p \eta_M$$

The thrust,  $T$ , is calculated from the beam current ( $I_B$  and the net accelerating voltage  $V_+$ ). The ions leave the engine with a velocity  $v_+ = (2eV_+/M_{Cs})^{1/2}$  where  $e$  is the electronic charge and  $M_{Cs}$  is the mass of a cesium ion. The number of ions leaving the engine per second is  $\dot{N}_+ = I_B/e$  and since each ion has the mass  $M_{Cs}$  the flowrate of accelerated ions is

$$\dot{m}_+ = M_{Cs} I_B / e$$

The thrust is then given by

$$T = \dot{m}_+ v_+ = I_B \left( \frac{2M_{Cs} V_+}{e} \right)^{1/2}$$

For  $I_B$  in amps and  $V_+$  in kilovolts this is

$$T = 11.9 I_B V_+^{1/2} \text{ mlb}$$

To calculate the specific impulse,  $I_{sp}$ , the neutral efflux is assumed to have negligible velocity. The specific impulse is defined to be the thrust, in pounds divided by the total flowrate of propellant in lbs/sec, or:

$$I_{sp} = T/\dot{W} = T/\dot{m}g = \dot{m}_+ v_+ / \dot{m}g$$

where  $\dot{m}$  is the total mass flowrate and  $g$  is the acceleration due to gravity at the earth's surface.

The specific impulse is then

$$I_{sp} = (\eta_M/g) (2eV_+/M_{Cs})^{1/2}$$

For  $V_+$  in kv, the specific impulse is given by:

$$I_{sp} = 3.88 \times 10^3 \eta_M (V_+)^{1/2} \text{ seconds}$$

The power-to-thrust ratio is calculated simply as the total power into the engine divided by the thrust. The usual units are kilowatts per pound thrust.

### 3.2.2 Results

The DF-1 engine was performance mapped over a wide range of optimum and nonoptimum operating conditions. The measurements with the reduced data are presented in Table IX. All data were taken after a minimum of 10 minutes steady operation and at a pressure less than  $1 \times 10^{-6}$  mm Hg.

Figure 63 presents the optimum overall engine efficiency as a function of specific impulse. The minimum power-to-thrust ratio as a function of specific impulse is given in Fig. 64. Figure 65 presents some data for thrust versus specific impulse. The high thrust data do not always correspond to optimum operating parameters for high efficiency. The maximum thrust curve represents a limit imposed by the perveance and optics of the electrode system and perveance matching of the plasma density distribution. The dotted line represents the thrust as calculated from the best performance data of Figs. 63 and 64 corrected to 2.4 kw total engine power level.

### 3.3 Extended Duration Tests

A single test with the operational requirements shown below was originally planned. The excellent condition of the DF-1 engine after the first and second tests prompted the second and third tests, respectively.

TABLE IX

## DF ENGINE PERFORMANCE MAPPING DATA

	Positive High Voltage, V <sub>+</sub> (kv)	Negative High Voltage, V <sub>-</sub> (kv)	Beam Current, I <sub>b</sub> (amp)	Arc Voltage, V <sub>a</sub> (volt)	Arc Current, I <sub>a</sub> (amp)	Magnet Voltage, V <sub>m</sub> (volt)	Magnet Current, I <sub>m</sub> (amp)	Beam Power, P <sub>b</sub> (kw)	Drain Power, P <sub>d</sub> (kw)	Magnet Power, P <sub>m</sub> (kw)	Arc Power, P <sub>a</sub> (kw)	Total Power, P <sub>t</sub> (kw)	Thrust, T (mlb)	P/T (kw/lb)	Power Efficiency, $\eta$ (%)	Mass Efficiency, $\eta$ (%)	Overall Engine Efficiency, $\eta$ (%)	Specific Impulse, I <sub>sp</sub> (sec)	Ratio of Drain Current to Beam Current, I <sub>d/Ib</sub> (%)	Source Energy per Ion, P <sub>a/Ib</sub> (kev/ion)	Neutral Detector Current, I <sub>ND</sub> (10 <sup>-9</sup> amp)	Neutral Detector Current at I <sub>b</sub> WDN (10 <sup>-9</sup> amp)	Reduced Beam Current, I <sub>r</sub> (amp)	Total Cesium Flowrate, I <sub>o</sub> (amp)	
1	4.00	0.78	0.0050	0.425	7.1	23.5	5.0	2.0	1.700	0.024	0.010	0.167	1.901	10.11	188.0	89.4	93.0	83.1	7198	1.18	0.393	14.0	64.0	0.310	0.457
2	4.00	0.78	0.0060	0.408	7.5	26.5	5.8	2.35	1.632	0.029	0.014	0.199	1.874	9.71	193.0	87.1	94.0	81.9	7276	1.47	0.488	12.0	45.0	0.335	0.434
3	4.00	0.78	0.0059	0.411	7.2	23.5	5.8	2.35	1.644	0.028	0.014	0.169	1.855	9.78	189.7	88.6	93.0	82.4	7198	1.44	0.411	13.0	47.0	0.335	0.440
4	4.00	1.25	0.0075	0.408	7.2	23.5	5.8	2.35	1.632	0.039	0.014	0.169	1.854	9.71	190.9	88.0	91.9	80.9	7113	1.84	0.414	13.5	35.0	0.350	0.444
5	3.50	0.60	0.0050	0.439	7.0	24.5	5.8	2.35	1.537	0.021	0.014	0.172	1.744	9.77	178.5	88.1	92.6	81.6	6705	1.14	0.392	15.0	60.0	0.335	0.474
6	3.50	0.60	0.0059	0.471	6.8	25.5	5.8	2.35	1.649	0.024	0.014	0.173	1.860	10.49	177.3	88.7	92.7	82.2	6712	1.25	0.367	15.0	70.0	0.335	0.508
7	3.00	1.00	0.0100	0.532	6.5	28.0	5.8	2.35	1.596	0.040	0.014	0.182	1.832	10.96	167.2	87.1	89.6	78.0	6006	1.88	0.342	23.0	72.0	0.400	0.594
8	3.00	1.00	0.0170	0.532	6.2	25.0	6.5	2.65	1.596	0.068	0.017	0.155	1.836	10.96	167.5	86.9	86.5	75.2	5798	3.20	0.291	36.0	93.0	0.400	0.615
9	3.00	1.00	0.0150	0.556	6.0	32.5	5.5	2.2	1.668	0.060	0.012	0.195	1.935	11.46	168.8	86.2	88.3	76.1	5919	2.70	0.351	30.0	93.0	0.400	0.630
10	3.00	1.40	0.012	0.630	6.5	36.5	5.5	2.2	1.890	0.053	0.012	0.277	2.192	12.98	168.9	85.2	91.8	79.1	6153	1.90	0.376	21.0	89.0	0.450	0.686
11	3.00	1.50	0.0102	0.660	7.2	38.5	5.5	2.2	1.980	0.046	0.012	0.237	2.315	13.60	170.2	86.5	93.0	79.5	6234	1.55	0.420	18.0	93.0	0.450	0.710
12	2.50	1.66	0.0100	0.590	6.8	34.0	5.6	2.3	1.475	0.042	0.013	0.231	1.761	11.10	158.6	83.8	92.5	77.5	5659	1.69	0.392	18.0	90.0	0.400	0.638
13	2.50	2.00	0.0100	0.602	7.6	40.0	5.6	2.3	1.505	0.045	0.013	0.304	1.867	11.33	164.8	80.6	97.1	78.3	5941	1.66	0.505	8.0	98.0	0.400	0.620
14	2.50	2.00	0.0084	0.410	9.0	43.5	5.6	2.3	1.025	0.038	0.013	0.392	1.468	7.71	190.4	69.8	98.1	68.5	6002	2.05	0.956	4.0	62.0	0.300	0.418
15	2.50	2.00	0.0070	0.432	7.6	33.0	5.6	2.3	1.080	0.032	0.013	0.321	1.376	8.13	169.2	78.5	98.4	77.2	6020	1.62	0.881	4.0	78.0	0.300	0.439
16	2.05	1.70	0.0060	0.355	6.5	17.5	5.6	2.3	0.728	0.023	0.013	0.114	0.878	6.05	145.1	82.9	92.0	76.3	5099	1.69	0.321	14.0	62.0	0.250	0.386
17	1.50	1.43	0.0050	0.300	6.4	16.5	5.6	2.3	0.450	0.015	0.013	0.106	0.584	4.37	133.6	77.1	90.6	69.9	4295	1.66	0.353	16.0	67.0	0.200	0.331
18	1.00	1.73	0.0050	0.272	6.5	15.0	5.6	2.3	0.272	0.014	0.013	0.098	0.197	3.24	122.5	68.5	92.5	63.4	3580	1.84	0.360	14.0	90.0	0.150	0.294
19	1.00	2.20	0.0080	0.385	6.4	20.0	5.6	2.3	0.385	0.026	0.013	0.128	0.552	4.58	120.5	69.7	85.6	59.7	3313	2.08	0.332	18.0	87.0	0.250	0.450
20	1.00	2.40	0.0155	0.428	6.0	26.0	5.6	2.3	0.428	0.033	0.013	0.156	0.650	5.09	127.7	65.8	87.0	57.2	3367	3.62	0.364	34.0	102.0	0.300	0.492
21	0.60	2.52	0.0112	0.305	6.5	20.0	5.6	2.3	0.183	0.035	0.013	0.130	0.361	2.81	128.5	50.7	90.8	46.0	2722	3.67	0.426	17.0	74.0	0.200	0.336
22	0.60	2.40	0.0070	0.190	6.5	13.5	5.6	2.3	0.114	0.018	0.013	0.088	0.233	1.75	133.1	48.9	88.4	43.2	2650	3.68	0.463	16.0	79.0	0.100	0.215
23	0.60	2.43	0.0110	0.395	6.2	22.0	5.6	2.3	0.237	0.033	0.013	0.136	0.419	3.64	115.1	56.6	89.0	50.4	2668	2.78	0.344	22.0	87.0	0.250	0.444
24	1.50	1.50	0.0075	0.373	6.4	21.0	5.6	2.3	0.559	0.023	0.013	0.135	0.730	5.44	134.2	76.6	89.1	69.0	4272	2.01	0.359	19.0	83.0	0.250	0.410
25	1.50	1.80	0.0115	0.408	6.2	24.0	5.6	2.3	0.612	0.038	0.013	0.149	0.812	5.95	136.5	73.4	86.1	64.9	4082	2.81	0.365	33.0	87.0	0.300	0.474
26	2.05	2.00	0.0165	0.390	5.9	21.5	5.6	2.3	0.800	0.067	0.013	0.127	1.007	6.65	151.4	79.4	93.1	79.4	5160	4.23	0.326	16.0	65.0	0.300	0.419
27	2.05	2.00	0.0078	0.505	6.6	29.0	5.6	2.3	1.035	0.032	0.013	0.192	1.272	8.61	147.7	81.4	93.7	76.3	5193	1.54	0.379	16.0	65.0	0.400	0.539
28	2.05	2.05	0.0138	0.570	6.2	33.5	5.6	2.3	1.169	0.057	0.013	0.208	1.447	9.71	149.0	80.8	91.5	73.9	5071	2.42	0.365	26.0	109.0	0.400	0.623
29	2.50	2.05	0.0130	0.670	6.8	40.0	5.6	2.3	1.675	0.059	0.013	0.272	2.019	12.61	160.1	83.0	94.2	78.2	5763	1.94	0.406	18.0	92.0	0.500	0.711
30	3.00	2.00	0.0160	0.850	7.7	52.5	5.6	2.3	2.550	0.080	0.013	0.404	3.047	17.52	173.9	83.7	96.6	80.9	6475	1.88	0.475	17.0	74.0	0.750	0.880
31	1.21	2.82	0.0120	0.550	6.6	29.5	5.5	2.2	0.666	0.048	0.012	0.195	0.921	7.20	127.9	72.3	81.5	58.9	3469	2.18	0.355	10.0	18.0	0.450	0.675
32	1.21	2.85	0.0100	0.510	6.8	29.5	5.5	2.2	0.617	0.041	0.012	0.201	0.871	6.68	130.4	70.8	87.5	62.0	3725	1.96	0.394	6.0	15.0	0.400	0.583
33	1.25	2.88	0.0093	0.505	6.6	27.5	5.5	2.2	0.631	0.038	0.012	0.182	0.863	6.72	128.4	73.1	86.0	62.9	3721	1.84	0.360	7.0	16.0	0.400	0.587
34	1.30	2.85	0.0083	0.493	6.8	29.0	5.5	2.2	0.641	0.034	0.012	0.197	0.884	6.69	132.1	72.5	91.3	66.2	4028	1.68	0.400	5.0	15.0	0.400	0.540
35	1.30	2.85	0.0086	0.485	6.8	28.0	5.5	2.2	0.631	0.036	0.012	0.190	0.869	6.58	132.1	72.6	88.3	64.1	3896	1.77	0.392	6.0	14.0	0.400	0.549
36	1.30	3.00	0.0082	0.489	6.8	28.0	5.5	2.2	0.636	0.035	0.012	0.190	0.873	6.63	131.7	72.9	89.2	65.0	3935	1.68	0.389	6.0	15.0	0.400	0.548
37	1.30	3.00	0.0090	0.487	6.6	26.2	5.5	2.2	0.633	0.039	0.012	0.173	0.857	6.61	129.7	73.9	88.2	65.2	3891	1.85	0.355	6.0	14.0	0.400	0.552
38	1.80	2.30	0.0070	0.437	6.6	26.0	5.5	2.2	0.823	0.029	0.012	0.172	1.036	7.30	141.9	79.4	93.8	74.5	4872	1.53	0.376	4.0	25.0	0.300	0.487
39	2.60	1.40	0.0054	0.437	6.6	24.5	5.5	2.2	1.136	0.022	0.012	0.162	1.332	8.38	158.9	85.3	90.5	77.2	5645	1.24	0.371	5.0	20.0	0.300	0.483
40	2.80	1.80	0.0110	0.650	6.8	28.0	5.5	2.2	1.820	0.051	0.012	0.190	2.073	12.94	160.2	87.8	92.9	81.6	6015	1.69	0.292	5.5	22.0	0.500	0.700
41	3.70	0.50	0.0050	0.440	6.7	25.2	5.5	2.2	1.628	0.021	0.012	0.169	1.830	10.07	181.7	89.0	93.0	82.8	6925	1.14	0.384	15.0	79.0	0.300	0.473
42	2.60	1.5	0.0056	0.412	6.6	26.0	5.5	2.2	1.071	0.023	0.012	0.172	1.278	7.90	161.7	83.8	93.2	78.1	5814	1.36	0.417	4.0	19.0	0.300	0.442



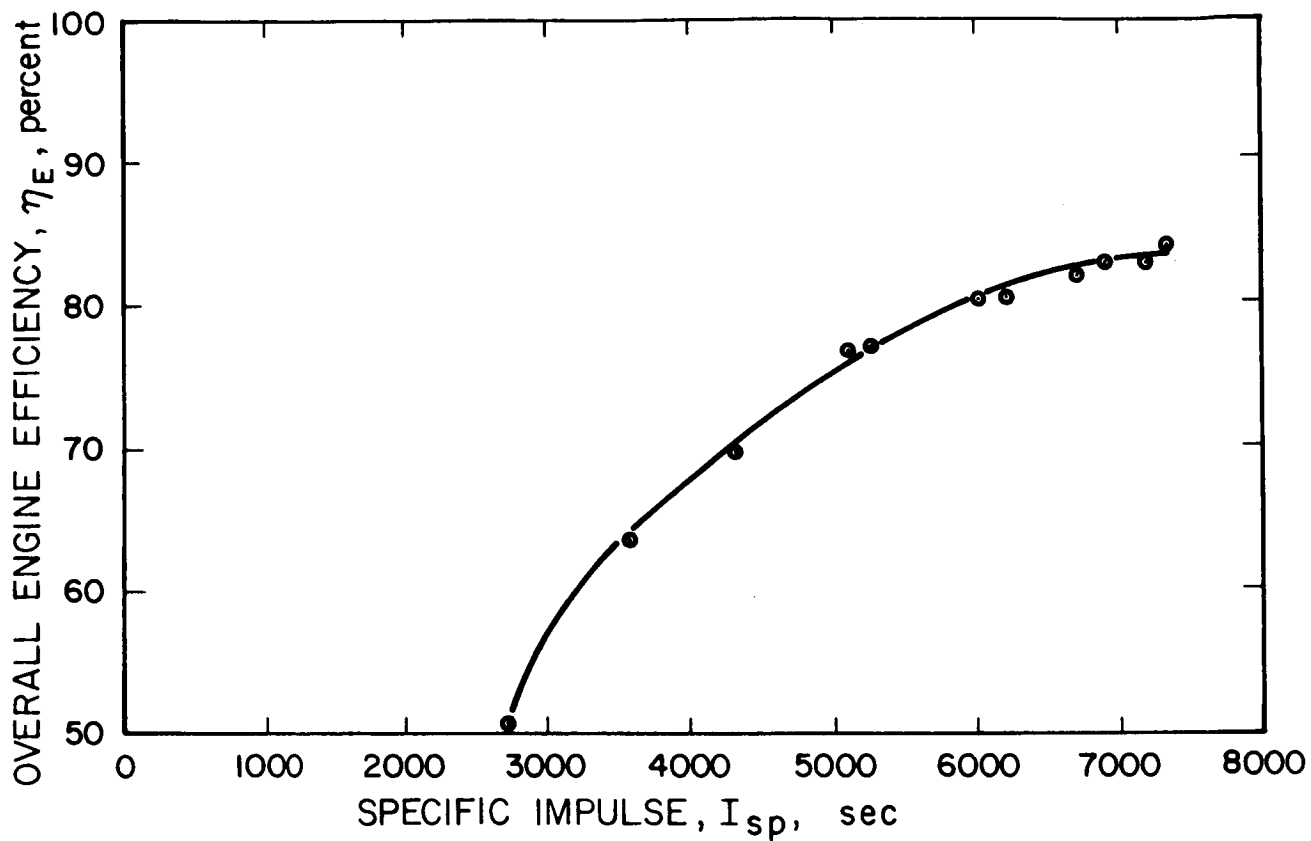


FIG. 63 DF-1 ENGINE OVERALL EFFICIENCY VERSUS SPECIFIC IMPULSE

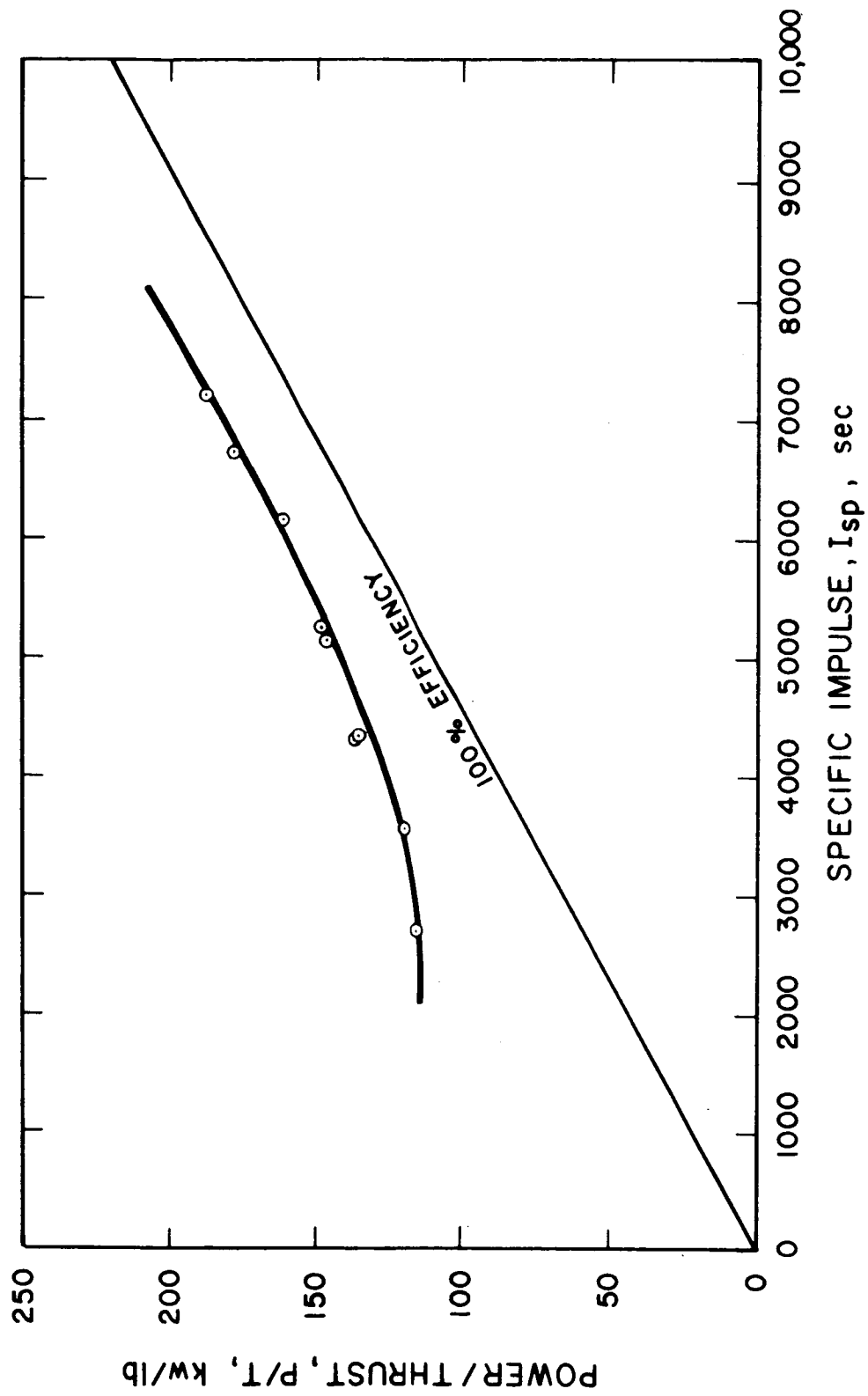


FIG. 64 POWER-TO-THRUST RATIO VERSUS SPECIFIC IMPULSE FOR DF ENGINE

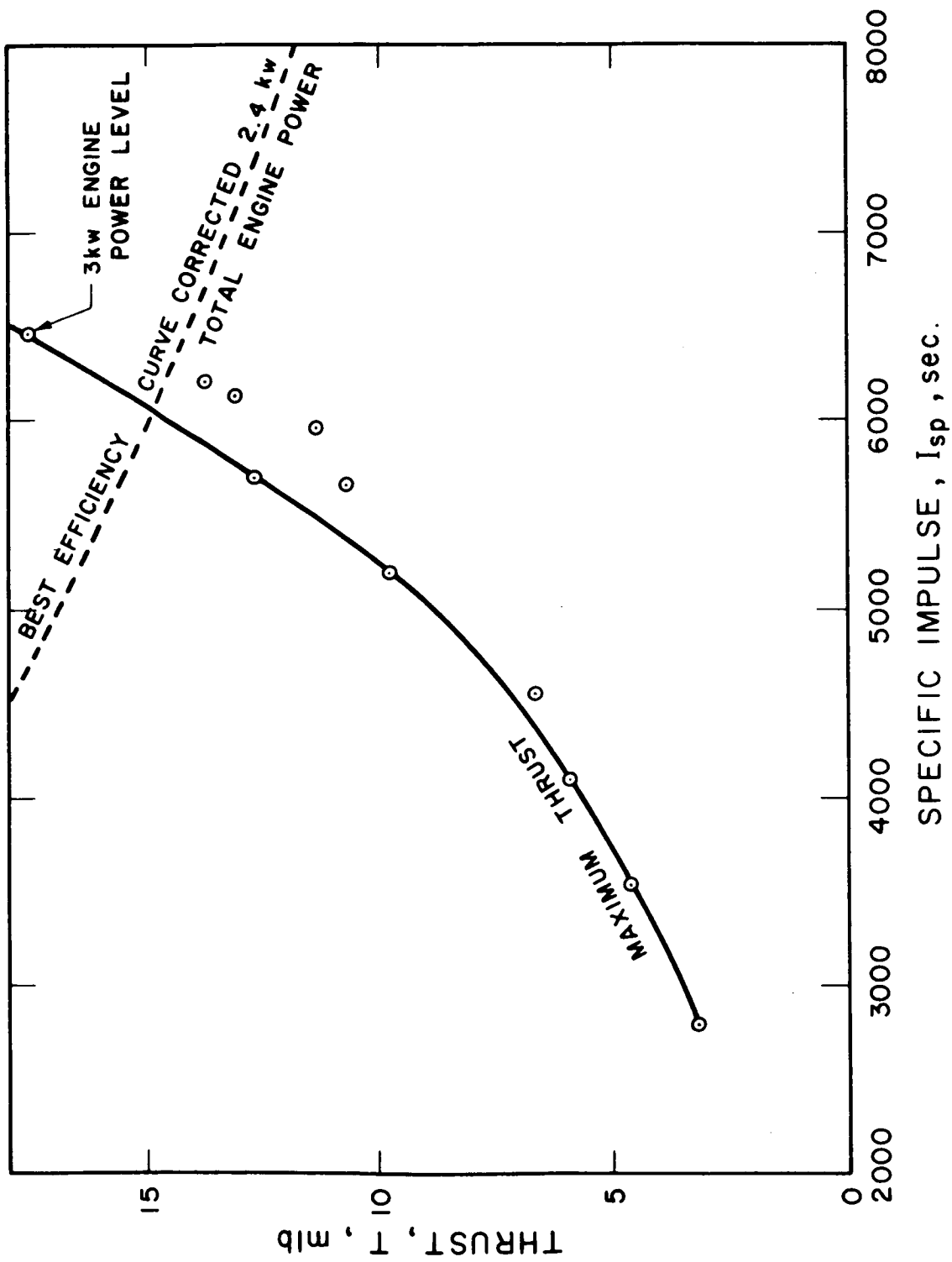


FIG. 65 DF ENGINE THRUST VERSUS SPECIFIC IMPULSE

### 3.3.1 Operating Level

The requirements of the 750-hour test were:

1. Run time of 750 hours or longer
2. Thrust level of 10 mlb or higher
3. A specific impulse in the range of 4000 to 7000 seconds
4. Total power to engine and feed system of 2.4 kilowatts or less

The 750-hour feed system was loaded with 2158 gms of cesium. Deducting the 38 gms calculated for performance mapping and estimating that 20 gms of cesium (less than one percent of the initial load) will remain trapped in the porous wick, 2100 grams of cesium should be available for the run. This would allow a flowrate of 513 mA for 825 hours (10 percent margin). At a mass efficiency of 93 percent, 10 mlb could be obtained at about 6350 seconds. This set a lower limit on the test specific impulse.

The performance mapping data were reviewed by the NASA Project Manager and EOS project personnel. The operating point was jointly chosen to optimize overall efficiency while meeting contractual requirements. The data of Table X were taken after the engine system had been operating continuously for 82 hours. For this operating point it was anticipated that the lifetime should be very long.

### 3.3.2 878-Hour Test

The first test was started on 28 December 1964. Termination of the run occurred 3 February 1965 after a total operating time of 878 hours. Termination was due to exhaustion of the cesium supply.

The system accumulated 771 hours of continuous operating time at the performance point presented in Subsection 3.3.1. Variations of all recorded operating parameters from their initial levels during the 771 hour period were extremely small. Beam current and accelerating voltages were maintained constant during the run.

TABLE X  
OPERATING POINT FOR FIRST LONG TEST

Positive High Voltage, $V_+$ (kv)	3.7
Negative High Voltage, $V_-$ (kv)	0.49
Negative HV Current, $I_-$ (amp)	0.0047
Beam Current, $I_B$ (amp)	0.440
Arc Voltage, $V_A$ (volt)	6.7
Arc Current, $I_A$ (amp)	25.5
Magnet Voltage, $V_M$ (volt)	5.4
Magnet Current, $I_M$ (amp)	2.2
Beam Power, $P_B$ (kw)	1.627
Drain Power, $P_D$ (kw)	0.0197
Magnet Power, $P_M$ (kw)	0.0119
Arc Power, $P_A$ (kw)	0.171
Total Power, $P_T$ (kw)	1.8296
Thrust, T (mlb)	10.05
Power-to-Thrust Ratio, P/T (kw/lb)	182
Power Efficiency, $\eta_p$ (%)	89
Mass Efficiency, $\eta_M$ (%)	~ 93*
Overall Engine Efficiency, $\eta_E$ (%)	82.7
Specific Impulse, $I_{sp}$ (sec)	6923
Ratio of Drain Current to Beam Current, $I_-/I_B$ (%)	1.07
Source Energy per Ion, $P_A/I_B$ (kev/ion)	0.389

\* Taken at time zero

At 771 hours a residual gas analysis was performed on the vacuum chamber. During the assembly of the analysis apparatus to the chamber, the backing line to the main diffusion pump was accidentally opened to atmosphere. This caused a pressure failure which resulted in an engine shutdown for approximately 45 minutes until normal pressure was restored. At that time, the engine was returned to operation at the original beam level. Immediately after restart it was clear that changes in the emissivity of the engine surfaces has taken place. However, after 16 additional hours of operation, operating parameters returned to the original levels. A 30 percent increase in the arc impedance was also noted after restart. The arc recovered its original impedance during the following 16 hours.

During the measurement of the residual gasses in the vacuum chamber a total pressure of  $7 \times 10^{-8}$  torr and a partial pressure of oxygen of less than  $3 \times 10^{-11}$  torr were measured. At this low partial pressure the arrival rate of oxygen on the aluminum accelerator is too low to have any significant effect on surfaces which are being sputtered.

Including performance mapping prior to start of the long test, the engine was operated a total of about 892 hours of which 878 hours were at the operating conditions chosen for the test. Analysis of 146 data points (four per day) taken during the 878-hour run give the average test parameters presented in Table XI. All of the basic power data are averages over the 878 hours. The mass utilization efficiency was determined by measurement of the amount of cesium consumed and is in good agreement with neutral detector data taken during performance mapping and at times during the extended test.

Upon removal from the vacuum system, the engine was found to be in excellent condition. Figures 66, 67, and 68 are photographs of the engine taken shortly after its removal from the test chamber. As in earlier tests with DE engines, the only apparent erosion was in the form of pits between apertures on the downstream

TABLE XI

DF ENGINE OPERATING PARAMETERS  
AVERAGED OVER 878-HOUR TEST

Positive High Voltage, $V_+$ (kV)	3.7
Negative High Voltage, $V_-$ (kV)	0.5
Negative HV Current, $I_-$ (amp)	0.0048
Beam Current, $I_B$ (amp)	0.440
Beam Power, $P_B$ (kW)	1.628
Drain Power, $P_D$ (kW)	0.020
Magnet Power, $P_M$ (kW)	0.012
Arc Power, $P_A$ (kW)	0.173
Total Power, $P_T$ (kW)	1.833
Thrust, T (mlb)	10.08
Power-to-Thrust Ratio, P/T (kW/lb)	181.8
Power Efficiency, $\eta_p$ (%)	88.8
Mass Efficiency, $\eta_M$ (%)	93.2
Overall Engine Efficiency, $\eta_E$ (%)	82.8
Specific Impulse, $I_{sp}$ (sec)	<u>6940</u>
Ratio of Drain Current to Beam Current, $I_-/I_B$ (%)	1.1
Source Energy per Ion, $P_A/I_B$ (keV/ion)	0.394
Total Cesium Flowrate, $I_O$ (amp)	0.472
Total Cesium Flowrate, (gm/hr)	2.35

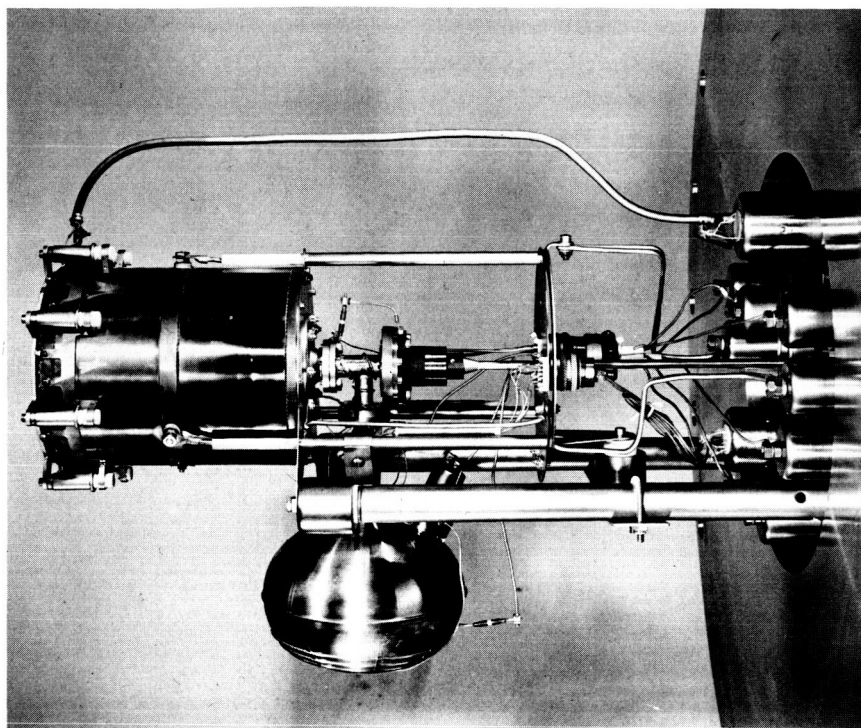


FIG. 66 DF ENGINE AND FEED SYSTEM AFTER 878-HOUR TEST



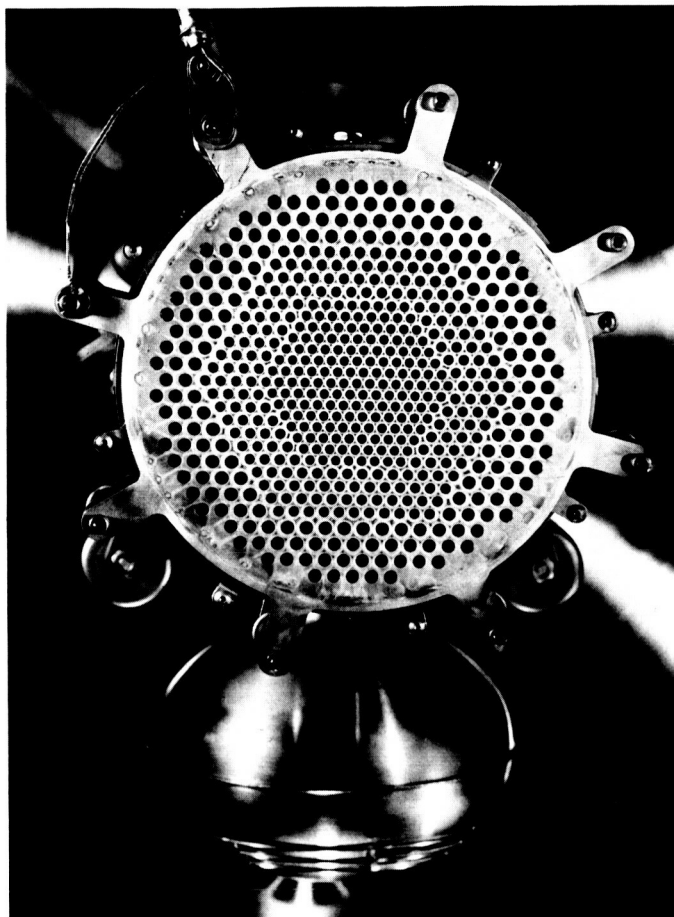


FIG. 67 DF ENGINE AND FEED SYSTEM AFTER  
878-HOUR TEST

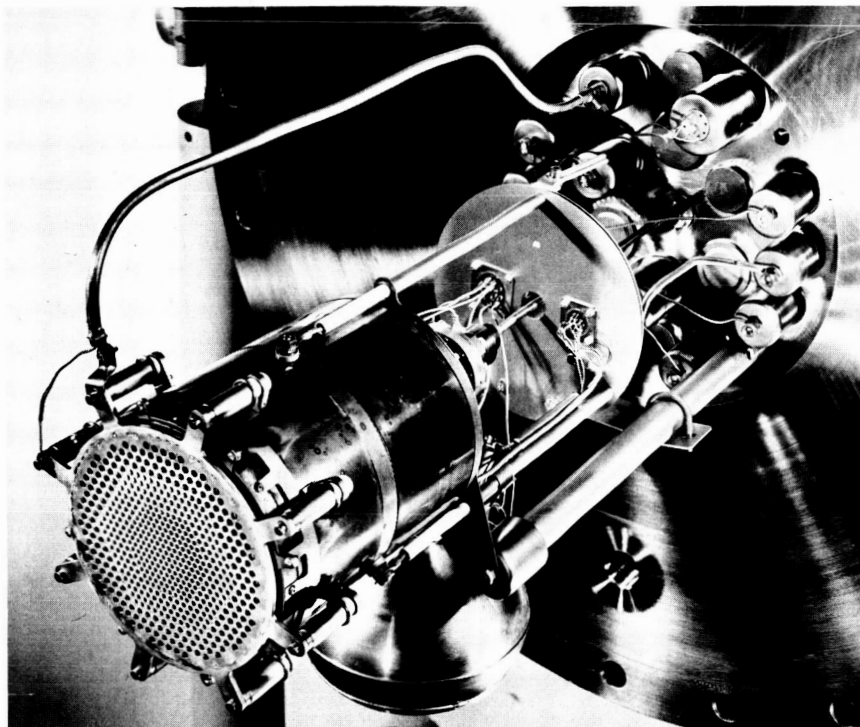


FIG. 68 DF ENGINE AND FEED SYSTEM AFTER 878-HOUR TEST

side of the accelerating electrode. The deepest pits occurred in the webs located between apertures of different sizes and were about 0.020- to 0.025-inch deep. The electrode was 0.125-inch thick so the pits had progressed through about 20 percent of the electrode.

### 3.3.3 880-Hour Test

Because of the excellent condition of the DF engine after the 878-hour test, it was decided by the NASA-Lewis Project Manager and EOS project personnel to retest the engine.

Prior to the second test, a minimum of cleaning was done on the engine. The electrode system was placed on the alignment jig and the accelerator electrode was removed. The gap side of the screen electrode was brushed to remove copper peelings and the accelerator plate was replaced. The electrode gap remained at 0.069 inch. Three small insulators at the rear of the engine support system which insulate the anode leads from cathode potential were cleaned before the system was rerun. No other engine components were cleaned.

The porous rod in the feed system was replaced. In addition, the diaphragm of the manual valve was replaced. This component had developed a leak, apparently during handling after the 878-hour run.

While the vacuum system was being cleaned, the engine was stored in a hot vacuum oven in an attempt to prevent contamination. Repeated openings of this facility to atmosphere, however, caused oxidation of sensitive engine surfaces (cathode emitter and accelerator electrode) which was not apparent until the engine was restarted.

The first attempt to start the second test failed because of an intermittent short between the accelerator electrode and the ground shield. Improper placement of one of the baffles in the vacuum system forced the ground shield against the engine. After 3 hours of operation the run was terminated due to this problem. The system was removed from the facility, the baffle was relocated, and the engine was reinstalled. The long test was restarted and the engine reached full beam at 8 PM on 10 March 1965.

Initially, the arc impedance was approximately 25 percent higher than at the end of the previous run. After approximately 150 hours of operation this impedance was within 8 percent of the normal value and was continuing to drop.

After 100 hours of operation, the frequency of high voltage overload cycling went up to about 2 cycles per hour, apparently due to electrode contamination. It was decided to reduce the operating level from 438 mA beam to 402 mA. This was done for approximately 20 hours and the cycling rate dropped to once every 5 hours. At this time, the original beam level was reestablished and was maintained for the remainder of the test. High voltage overload cycling was almost nonexistent at 500 hours into the run. Cleanup of the electrodes had apparently been completed.

The second DF-1 engine test was terminated due to exhaustion of cesium on 16 April, 1965. Total engine operating time for this test was 880 hours. The cumulative operating time at termination of the second test was 1772 hours.

Engine operation was normal at the end of the second test. The last data recorded prior to running out of cesium are presented in Table XII.

Figures 69, 70, and 71 are photographs of the DF-1 engine system taken upon its removal from the facility. Little increase of deterioration was noted upon inspection.

The electrode system had not been realigned exactly as it had been on the first test. The charge exchange pits on the downstream side of the accelerating electrode were coincident with those of the first test in only one small area of the electrode. Where the erosion was superimposed over that encountered in the previous test, the deepest pits were measured to be 0.033 to 0.037 inch deep. They were 0.020 to 0.025 inch deep after the first test, so it appeared that, as expected, the rate of penetration decreases as the pits deepen. Over other areas of the electrode, the new pits were displaced from the

TABLE XII

DF-1 ENGINE PERFORMANCE SHORTLY BEFORE  
TERMINATION OF SECOND LONG TEST

Positive High Voltage, $V_+$ (kv)	3.7
Negative High Voltage, $V_-$ (kv)	0.38
Negative HV Current, $I_-$ (amp)	0.0058
Beam Current, $I_B$ (amp)	0.439
Beam Power, $P_B$ (kw)	1.624
Drain Power, $P_D$ (kw)	0.024
Magnet Power, $P_M$ (kw)	0.012
Arc Power, $P_A$ (kw)	0.178
Total Power, $P_T$ (kw)	1.838
Thrust, T (mlb)	10.05
Power-to-Thrust Ratio, P/T (kw/lb)	182.8
Power Efficiency, $\eta_p$ (%)	88.4
Mass Efficiency, $\eta_M$ (%)	~ 92.0
Overall Engine Efficiency, $\eta_E$ (%)	~ 81.3
Specific Impulse, $I_{sp}$ (sec)	6850
Ratio of Drain Current to Beam Current $I_-/I_B$ (%)	1.3
Source Energy per Ion, $P_A/I_B$ (kev/ion)	0.406
Total Cesium Flowrate, $I_o$ (amps)	0.477
Total Cesium Flowrate, (gm/hr)	2.38

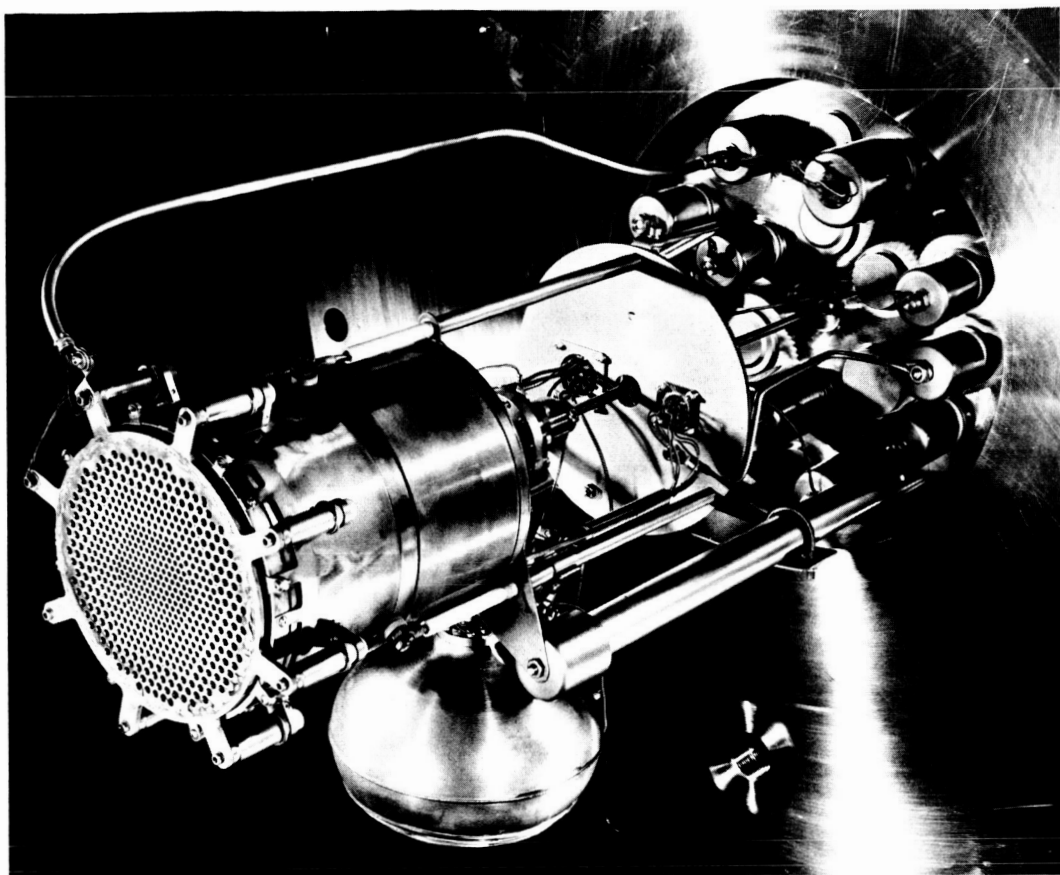


FIG. 69 DF-1 ENGINE SYSTEM AFTER 1,772 HOURS CUMULATIVE OPERATION

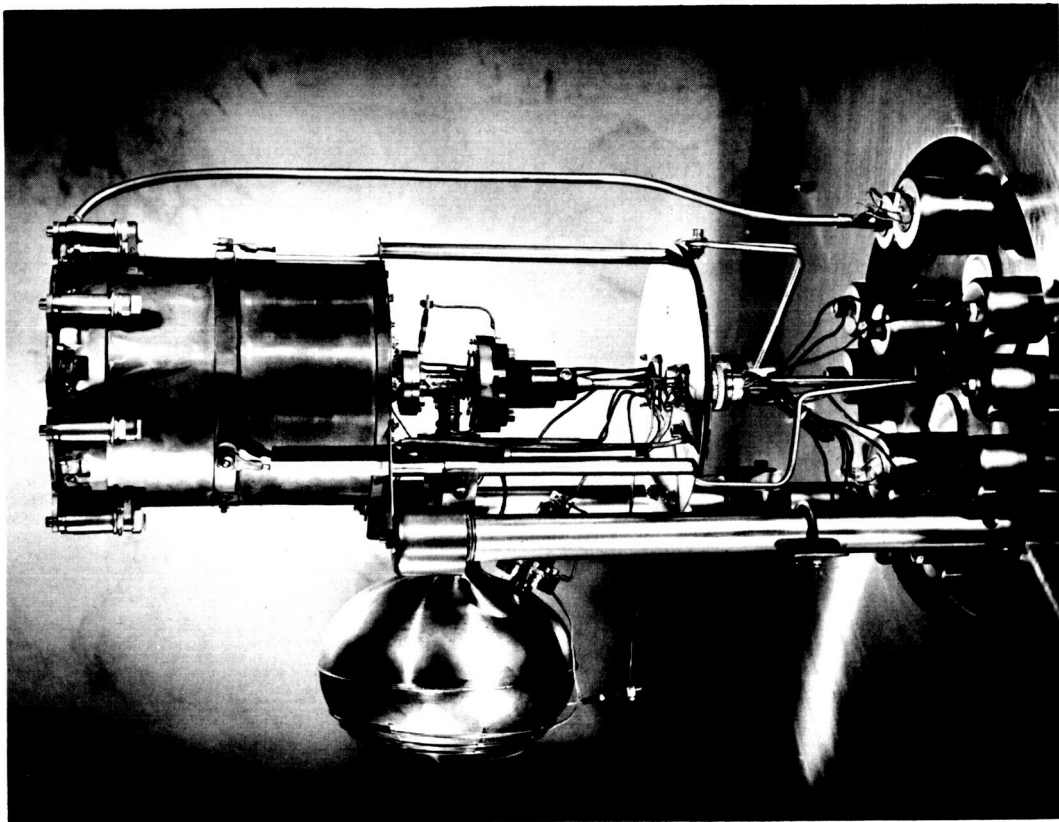


FIG. 70 DF-1 ENGINE SYSTEM AFTER 1,772 HOURS CUMULATIVE OPERATION

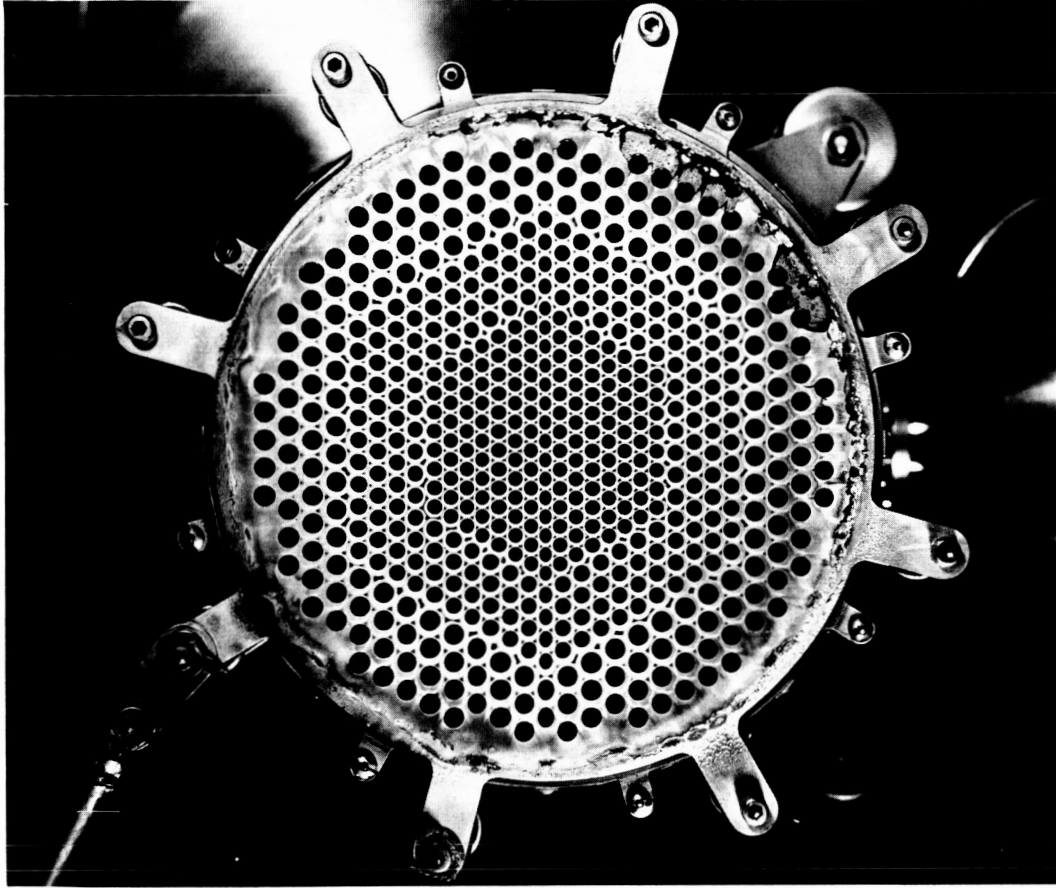


FIG. 71 DF-1 ENGINE SYSTEM AFTER 1,772 HOURS CUMULATIVE OPERATION



earlier ones made by several thousandths of an inch and were of approximately the same depth (0.020 to 0.025 inch deep).

Analysis of the deposits on the cathode orifice plate and screen electrode disclosed that the main constituents were copper and aluminum as in the first test (EOS Report 4920-ML-12)<sup>4</sup>. Both the downstream and upstream sides of the accelerating electrode had copper on them. The copper deposited on the gap side is assumed to have been reevaporated from the cathode orifice plate. In addition, most of the deposits showed the presence of small but significant amounts of titanium, assumed to have been sputtered back from the titanium hood (which extended in front of the engine) used as part of the ground screen system which surrounded the engine in the facility.

#### 3.3.4 838-Hour Test

It was decided by the NASA Project Manager and EOS project personnel to retest the engine system since it was still in excellent condition. The engine system was disassembled and parts cleaned of flaky or crumbly deposits as necessary. The accelerator electrode insulators were removed from the electrode system and the screen electrode and support were cleaned. The gap side of the accelerator electrode was cleaned by wiping with a dilute solution of nitric and sulfuric acid. The electrode was then rinsed in distilled water and dried; the downstream side was not cleaned. The electrode insulators were not cleaned. The electrode system was reassembled and the gap set at 0.070 inch as before.

It was discovered that the cathode heater terminal (external to cathode) had been fused and was open-circuited. The cathode heater was operating normally during a cleanup cycle at the termination of the second test and the incident is not understood. A new heater terminal was attached and the same cathode was reinstalled on the engine.

The engine was completely assembled, the feed system reloaded, and the engine system installed in the facility, which had been cleaned and refurbished where necessary.

During pump-down of the vacuum facility and feed system conditioning, one of the windows on the vacuum chamber cracked. Attempts to control the pressure and protect the cesium reservoir, which was being pumped out, failed. As a result, some cesium was expelled into the engine chamber and facility during the startup procedure.

Attempts to thermally cycle the engine and clean out the cesium resulted in the flaking of copper deposits on the inside of the arc chamber. Anode-to-cathode shorts due to this material forced the removal of the engine. A check of the electrode system revealed it to be in good condition and it was only necessary to clean the anode and arc chamber. No cesium was added to the reservoir as only a small percentage of the supply was lost.

The engine was reinstalled in the chamber and started satisfactorily on 28 April 1965. This run was terminated on 4 June 1965, at 838 hours, by the exhaustion of the cesium supply. This engine had accumulated 1772 hours of operation during its two previous long-term runs and periods of performance mapping. Thus, the DF-1 engine system had a cumulative operating time of 2610 hours.

During the greater portion of the third test, the DF engine was operated at the performance points shown in Table XIII. This point was somewhat lower than that at which the previous tests were run but was selected because stable operation of the feed loop could be maintained there. The performance points listed also represent the average conditions over the entire run.

Failures of support equipment resulted in a total of 60 hours during which the DF engine was not producing thrust. These failures were mostly in the high voltage supply control and alarm circuits.

After approximately 60 hours of operation, failure of the positive high-voltage supply to come on after a high-voltage arc resulted in about 2-1/2 hours of zero-beam condition during which

TABLE XIII

DF-1 ENGINE AVERAGED PERFORMANCE  
DURING THIRD EXTENDED TEST

Positive High Voltage, $V_+$ (kv)	3.65
Negative High Voltage, $V_-$ (kv)	0.32
Negative HV Current, $I_-$ (amp)	0.008
Beam Current, $I_B$ (amp)	0.434
Beam Power, $P_B$ (kw)	1.584
Drain Power, $P_D$ (kw)	0.032
Magnet Power, $P_M$ (kw)	0.012
Arc Power, $P_A$ (kw)	0.177
Total Power, $P_T$ (kw)	1.805
Thrust, T (mlb)	9.85
Power-to-Thrust-Ratio, P/T (kw/lb)	183
Power Efficiency, $\eta_p$ (%)	87.4
Mass Efficiency, $\eta_M$ (%)	~ 92.0
Overall Engine Efficiency, $\eta_E$ (%)	~ 80.4
Specific Impulse, $I_{sp}$ (sec)	6805
Ratio of Drain Current to Beam Current, $I_-/I_B$ (%)	1.84
Source Energy per Ion $P_A/I_B$ (kev/ion)	0.408
Total Cesium Flowrate, $I_o$ (amps)	0.472
Total Cesium Flowrate, (gm/hr)	2.36

the vaporizer stayed on and operated at its maximum output. The amount of cesium expended during this period was equivalent to that used during 35 to 40 hours of normal engine operation.

At approximately 350 hours, a change in the vaporizer characteristic was noted. This change was evidenced by the higher vaporizer power and consequent higher vaporizer temperature necessary to maintain the proper level of cesium input to the engine. The total variation in the vaporizer characteristic, which took place over a period of several days, resulted in a vaporizer power of about 21 watts or 7 watts higher than normal. The corresponding vaporizer temperature change was from about 275°C to about 350°C. At these powers and temperatures, the heating or flow increase response of the vaporizer was very sluggish and the cooling or flow decrease response was very rapid. Because of the highly nonlinear response, the feed system control loop was unable to function correctly and oscillations in the cesium feed-rate caused wide excursions of the beam level from its steady-state operating point.

The cause of the change in vaporizer characteristic was thought to be either an occlusion of the feed line in the valve or cathode, or a defective vaporizer rod. Assuming the former cause, efforts were made to clear the blockage by applying additional power to the valve heater and by closing and reopening the manual valve. These attempts were unsuccessful and it was necessary to alter the feed control loop to compensate for the erratic feed.

At approximately 600 hours, a change in the arc characteristic was noted. The arc impedance increased about 6 percent. The cathode heater appeared to have deteriorated and caused the engine to go into an unstable arc mode. Arc voltage was increased until the arc stabilized, and then reset at approximately its original value. At this time, it was also noted that the cathode heater appeared to be short-circuited. Since the cathode heater is used only for startup of a "cold" engine, this did not prevent continuation of the test.

After the third test, photographs were taken of the engine with the feed system removed (Figs. 72, 73, and 74). It can be seen that the engine was still in excellent condition.

Figure 75 shows the high voltage rest cycles, facility pressure, and accelerator electrode drain current versus time for the 2610 hours of operation of the DF-1 engine. The curve of rest cycles shows the cleanup which occurred during each test as the electrodes cleaned up.

The pressure profile shows the tank cleanup, the occurrence of the vacuum failure at 771 hours, and the breaks in vacuum for reloading the feed system between tests.

The accelerator electrode drain current shows some wear-in during early portions of the second and third tests and an increase from test to test due to insulator leakage and, during the third test, due to erratic operation caused by power supply failures.

### 3.4 Analysis of Components

The feed system was carefully inspected and analyzed after each test, since reloading required a complete system cleaning and replacement of the porous rod. Detailed analyses of engine components were made after completion of the third test.

#### 3.4.1 Feed System

The feed system was run for a total of 896 hours during performance mapping and the first long duration engine run. At the end of the run, the system was weighed and 13.4 grams of cesium were found to remain. This amount was held entirely by the porous rod and the reservoir itself was completely empty.

During disassembly of the feed system in the dry box two deposits of an unknown substance were found. These deposits were on the manual valve diaphragm and plunger. A spectrographic analysis was made with the results shown in Table XIV. Sample SN4-9 was from the plunger and SN4-10 from the diaphragm. The major constituent was cesium.

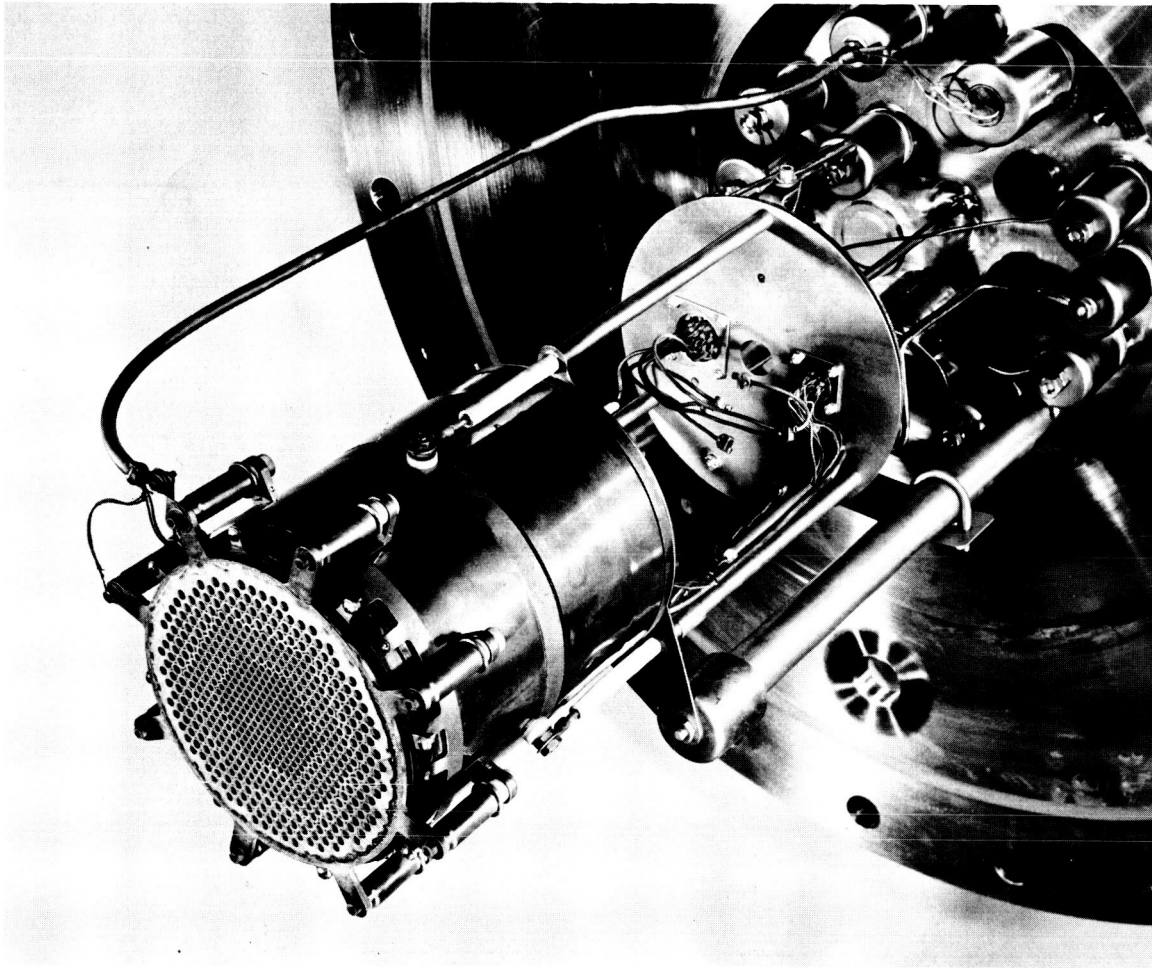


FIG. 72 DF-1 ENGINE AFTER 2610 HOURS CUMULATIVE OPERATION WITH FEED SYSTEM REMOVED

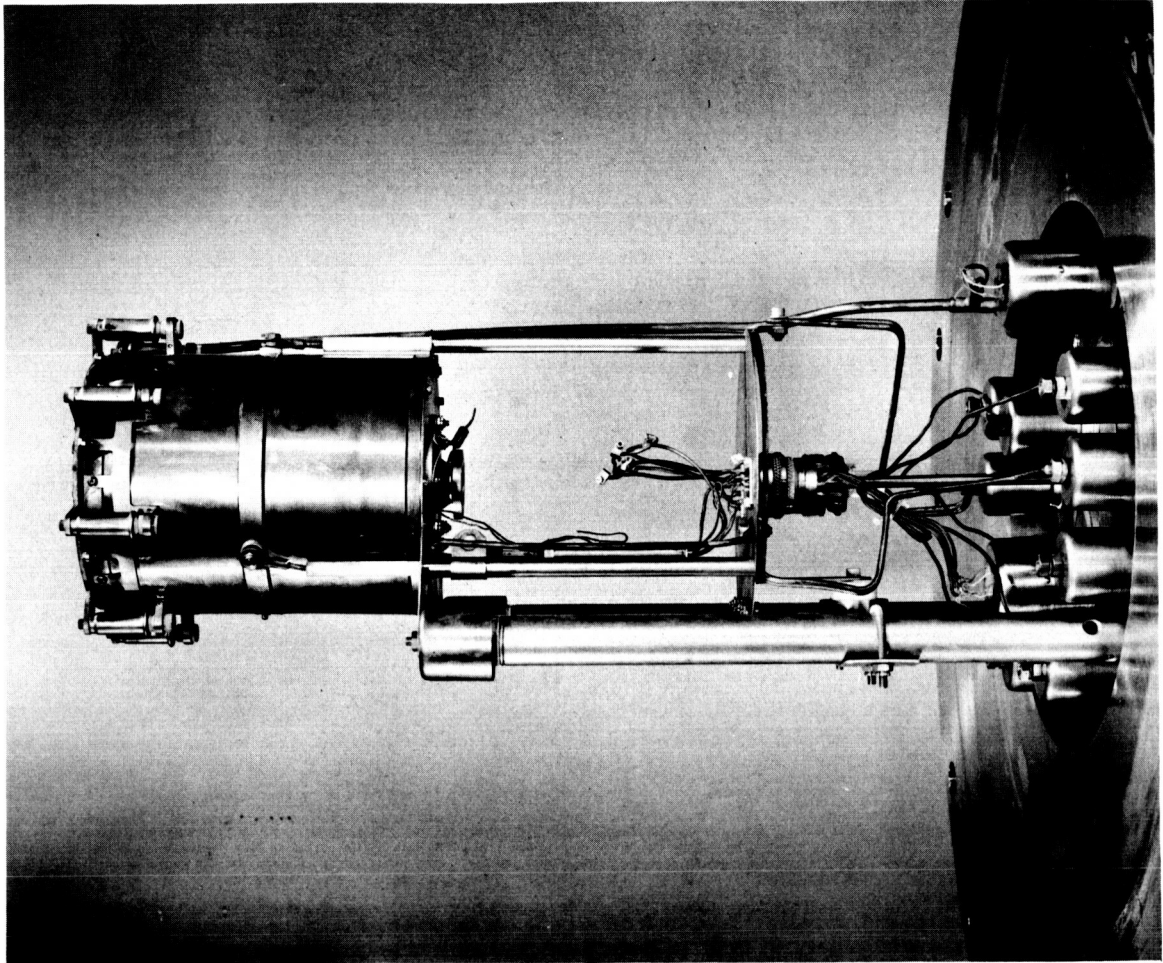


FIG. 73 DF-1 ENGINE AFTER 2610 HOURS CUMULATIVE OPERATION WITH FEED SYSTEM REMOVED

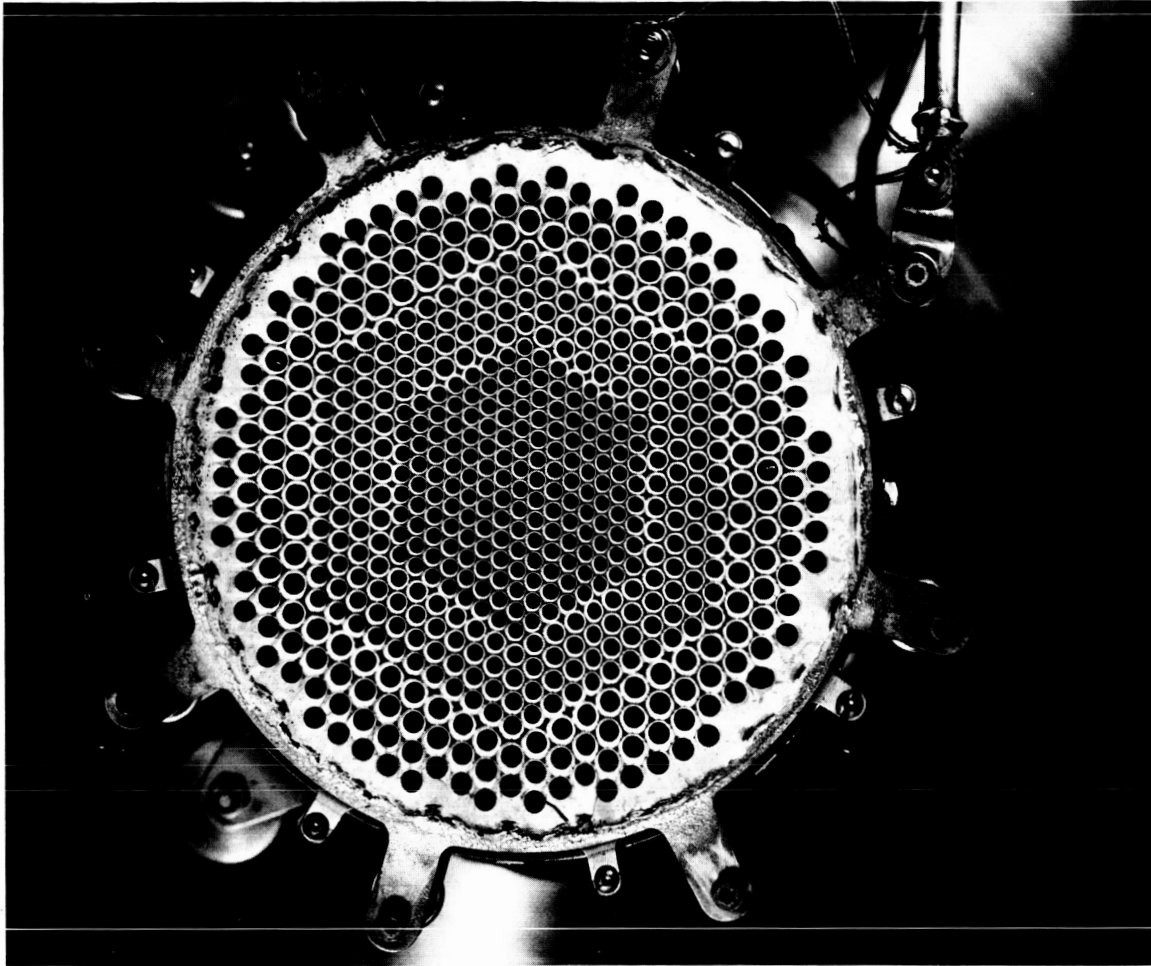


FIG. 74 DF-1 ENGINE AFTER 2610 HOURS CUMULATIVE OPERATION WITH FEED SYSTEM REMOVED



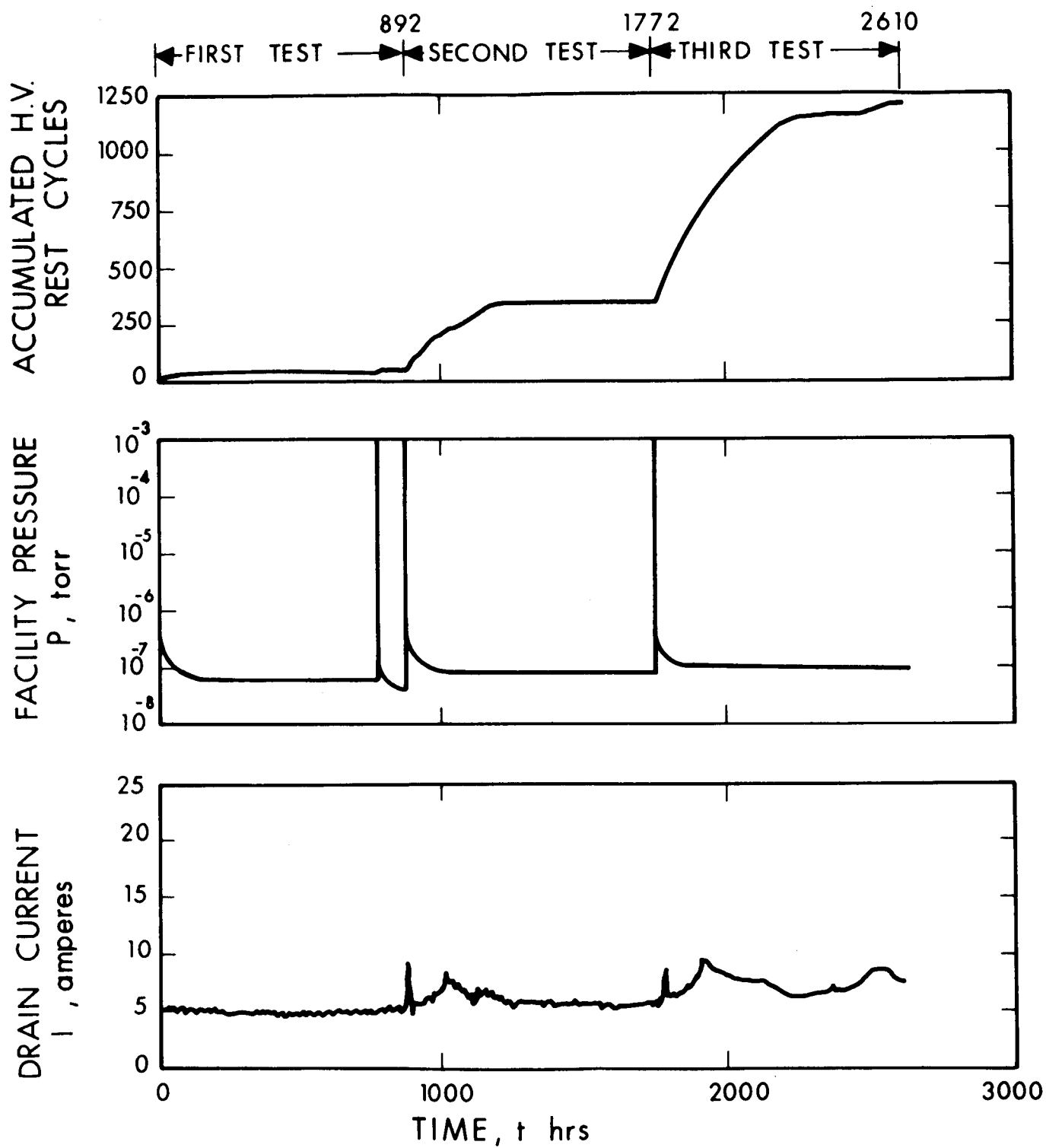


FIG. 75 TIME DEPENDENT FUNCTIONS FROM 2610-HOUR TEST

**TABLE XIV**  
**ANALYSIS OF DEPOSITS IN VALVE**

	<u>SN 4-9</u>	<u>SN 4-10</u>
Cesium-	Major constituent - - -	
Iron-	0.070%	0.26%
Silicon-	1.8	0.011
Sodium-	0.67	0.022
Magnesium-	0.0035	0.00044
Manganese-	0.0068	0.014
Boron-	0.093	not detected less than 0.005
Chromium-	0.026	0.059
Aluminum-	0.0028	0.0023
Copper-	0.0031	0.0013
Calcium-	0.0018	0.0012

Five samples of the porous rod were taken as shown in Fig. 76. Table XV gives the results of the spectrographic analysis of these samples. Sample SN4-2 is of a sample removed from the rod during initial assembly of the feed system. Due to the dry condition of the reservoir, a cesium sample could not be taken for spectrographic analysis.

After removing the feed system from the dry box, all parts were cleaned with stainless cleaner, washed in distilled water, dried, and weighed. The changes in weight are tabulated in Table XVI.

Near the conclusion of the first engine run (when the cesium was depleted), the vaporizer power had increased and excessively heated the end of the vaporizer rod. All cesium was evaporated from the rod for a distance of approximately 3/4 inch. Because of this, the vaporizer surface condition could not be visually evaluated.

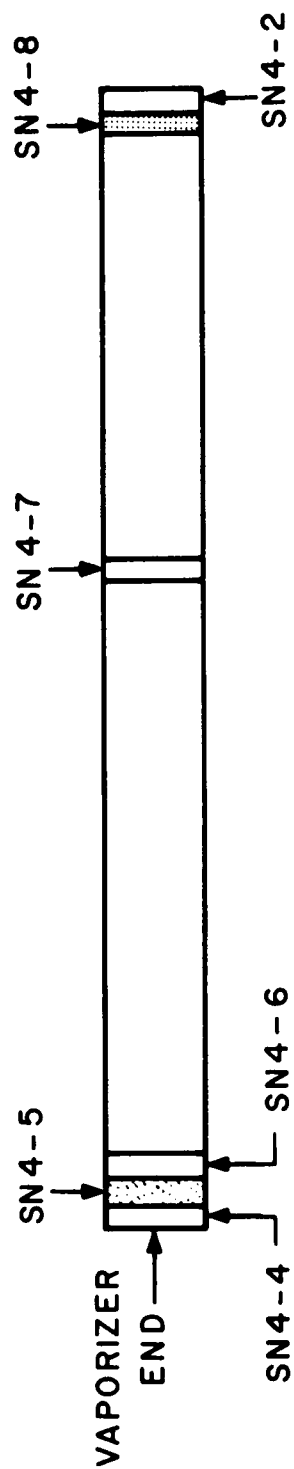


FIG. 76 POSITION OF SAMPLES TAKEN FROM POROUS ROD

TABLE XV  
ANALYSIS OF SECTIONS OF POROUS ROD

LAB. NOS.	33782-4-1	33782-4-2	33782-4-3	33782-4-4	33782-4-5	33782-4-6
SAMPLE NOS.	4SN4	4SN5	4SN6	4SN7	4SN8	SN4-2
Nickel	Rem.	Rem.	Rem.	Rem.	Rem.	Rem.
Iron	.47%	.17%	.40%	.18%	.16%	.17%
Chromium	.15 - .25%*	.03%	.06%	.005%	.03%	.02%
Cobalt	.08%	.08%	.08%	.08%	.09%	.08%
Copper	.06%	.04%	.03%	.03%	.07%	.03%
Manganese	.025%	.02%	.025%	.01%	.01%	.01%
Silicon	.45%	.08%	.08%	.09%	.61%	.05%
Titanium	.003%**	.003%**	.003%**	.003%**	.003%**	.003%**
Aluminum	.007%	.004%	.005%	.004%	.005%	.007%
Magnesium	.003%**	.003%**	.003%**	.003%**	.003%**	.003%**

\*The range of concentration is an estimate, as it fell outside the range of standards

\*\*Less than

TABLE XVI

## WEIGHT CHANGES DURING AND AFTER 2610-HOUR TESTS

Weights	Before	After Run 1 $\Delta$ Weight	After Run 2 $\Delta$ Weight	After Run 3 Weight	After Run 3 $\Delta$ Weight	Total $\Delta$ Weight
Control Fin	5.7461	-	-	5.57105	-	-0.17505/-3%
Fin Assembly	441.552	-	-	420.6429	-	-20.9091/-4.6%
Port Valve Fl.	33.66685	-0.0009/-0.0028%	-	33.6552	-	-0.01165/-0.03%
Port Seal	1.7251	+0.0007/-0.041%	+0.00285/+0.12%	-	+0.0001/0%	-
Res.	959.000	-5.5544/-0.058%	-	946.6406	-	-12.3594/-1.29%
Res. Seal	1.73405	+0.0003/+0.017%	+0.00257/+0.0145%	-	+0.0021/+0.12%	-
Heater	90.2374	-0.047/-0.052%	-	90.0674	-	-0.17/-0.19%
Heater Seal	1.7407	+0.0011/-0.063%	+0.0014/+0.079%	-	+0.00125/+0.072%	-
Valve Body	231.7584	-	-	231.2126	-	-0.5458/-0.23%
Valve Seal	5.12815	+0.0076/+0.15%	-0.0699/-1.35%	-	+0.0015/+0.03%	-
Valve Diaphragm	666.54740	-0.0152/-0.023%	-	* 59.9379	-0.03565/-0.06%	-
Valve Tip	4.53910	-0.02165/-0.48%	+0.001/+0.02%	* 4.70915	+0.0022/+0.048%	-
Valve-Eng. Seal	1.74510	-	-	-	+0.00175/+0.10%	-

\* Replaced during tests

Further analysis of the reservoir was not performed as it was decided to replace the porous rod and reload the feed system for further testing with the DF engine. When assembling the manual valve, a leak was discovered in the diaphragm assembly which was then replaced.

#### Second Test

The feed system was run for a total of 880 hours during the second long duration engine run. At the end of the run, the system was weighed and 12.0 grams of cesium remained. This amount was held entirely by the porous rod. The reservoir itself was completely empty.

Five samples of the porous rod were taken as before. Table XVII lists the results of the spectrographic analysis made on these samples. Sample SN4-11 is of a sample removed from the rod during initial assembly of the feed system. Due to the dry condition of the reservoir, a cesium sample could not be taken for spectrographic analysis.

After removing the feed system from the dry box, all parts were cleaned with a stainless steel cleaner, washed in distilled water, dried, and weighed. The changes in weight are tabulated in Table XVI.

As in test 1, at the conclusion of the engine run (when the cesium was depleted), the vaporizer power had increased and excessively heated the end of the vaporizer rod. All cesium was evaporated from the rod for a distance of approximately 3/4 inch. Because of this, the vaporizer surface could not be visually compared with previous runs.

Further analysis of the reservoir was not performed as it was decided to replace the porous rod and reload the feed system for further testing with the DF engine.

TABLE XVII  
ANALYSIS OF POROUS ROD AFTER SECOND TEST

<u>Element</u>	Control Sample <u>SN1-13</u>	<u>SN1-14</u>	<u>SN1-15</u>	<u>SN1-16</u>	<u>SN1-17</u>	<u>SN1-11</u>
Manganese	0.11%	0.10%	0.10%	0.10%	0.14%	0.01%
Iron	0.70%	0.49%	0.78%	0.48%	0.61%	0.019%
Silicon	0.13%	0.09%	0.17%	0.12%	0.20%	0.04%
Copper	0.11%	0.08%	0.14%	0.12%	0.22%	0.04%
Cobalt	0.17%	0.15%	0.15%	0.17%	0.22%	0.11%
Titanium	0.01%*	0.01%*	0.01%	0.01%*	0.01%*	0.003%*
Nickel	rem	rem	rem	rem	rem	rem
Chrome	0.1-0.5%	0.06%	0.07%	0.02%*	0.02%*	0.003%*

\*Less than

### Third Test

The feed system was run for a total of 838 hours during the third long duration run. At approximately 350 hours, a change in the vaporizer characteristic was noted. The cause of this change in vaporizer characteristic was thought to be either an occlusion of the feed line in the valve or cathode or a defective vaporizer rod.

Because of this change in the vaporizer, it was necessary to disassemble the feed system and engine with great care to determine where any occlusion may have developed. Therefore, all parts were disassembled in the dry box. All feed system surfaces were as they had been after previous tests. No obstructions were noted.

The feed system was weighed and 17.4 grams of cesium remained. This amount was held entirely by the porous rod and the reservoir itself was completely empty. Due to the dry condition of the reservoir, a cesium sample could not be taken for spectrographic analysis.

When the porous rod was removed from the reservoir, a surface area of approximately the reservoir height by  $1/4$  the rod circumference was found to have not been wetted by the cesium.

Five samples of the porous rod were taken as shown in Fig. 76. Table XVIII lists the results of the spectrographic analysis made on these samples. Sample SN4-18 is of a sample removed from the rod during initial assembly of the feed system.

After removing the feed system from the dry box, all parts were cleaned with stainless cleaner, washed in distilled water, dried, and weighed. The changes in weight are tabulated in Table XVI.

As part of the analysis, photomicrographs were made of the control fin before and after the run, and of a weld section taken from the reservoir. There was no evidence of cesium attack in either instance.

Not only did the feed system far surpass its design life of 750 hours, but these analyses indicated an operating capability at least several times the accumulated operational total of 2610 hours.



TABLE XVIII  
ANALYSIS OF POROUS ROD AFTER THIRD TEST

<u>Element</u>	Control Sample <u>SN1-21</u>	<u>SN1-22</u>	<u>SN1-23</u>	<u>SN1-24</u>	<u>SN1-25</u>	<u>SN1-18</u>
Manganese	0.05%*	0.05%*	0.05%*	0.05%*	0.05%*	0.06%
Iron	0.34%	0.51%	0.39%	0.24%	0.16%	0.18%
Silicon	0.30%	0.07%	0.08%	0.09%	0.07%	0.10%
Copper	0.035%	0.06%	0.065%	0.065%	0.07%	0.02%
Cobalt	0.085%	0.14%	0.14%	0.17%	0.085%	0.32%
Titanium	0.018%	0.005%*	0.005%*	0.005%*	0.005%	0.01%
Magnesium	0.007%	0.003%	0.004%	0.004%	0.004%	0.004%*
Nickel	rem	rem	rem	rem	rem	rem
Aluminum	0.49%	0.02%	0.03%	0.03%	0.03%	-

\*Less than

### 3.4.2 Engine Components

The engine was disassembled in a vacuum drybox and its components carefully examined. The accelerating electrode, cathode mounting plate, and cathode orifice plate were coated with back-sputtered copper.

#### Cathode

The cathode heater was covered with a white flaky substance. This substance appeared to be hygroscopic and was water soluble and was, therefore, presumed to be an oxide of cesium. The tantalum sheath on the cathode heater wire showed visible deterioration. Figure 77 shows the little cathode after cleaning.

Figure 78a is a cross-section view of the cathode emitter used in the 2610-hour test. The outer ring of white material is the tantalum sheath, while the inner white circle is the tantalum heater wire. The outer diameter of the wire is 0.074 inch. Figure 78b is a cross-section view of an unused sample of the same type of heater wire. The unused sample is from a different lot of wire, however, hence the discrepancy in the thickness of the outer sheath. The sheath of the cathode heater after 2610 hours of engine operation shows evidence of only slight intergranular attack. There is no evidence of any considerable loss of material from the sheath due to sputtering. Future engines will, however, incorporate an external cathode heater and the emitting surface will be of solid tantalum wire.

#### Contamination

Most of the anode surfaces were covered with a sooty substance. This was probably carbon left by decomposition of stray organic contaminants.

The engine components were removed from the drybox and small samples for spectrographic analysis were taken from the cathode heater, orifice plate, anode, the downstream side of the screen, and both sides of the accelerator. Results of these analyses are shown in Table XIX.

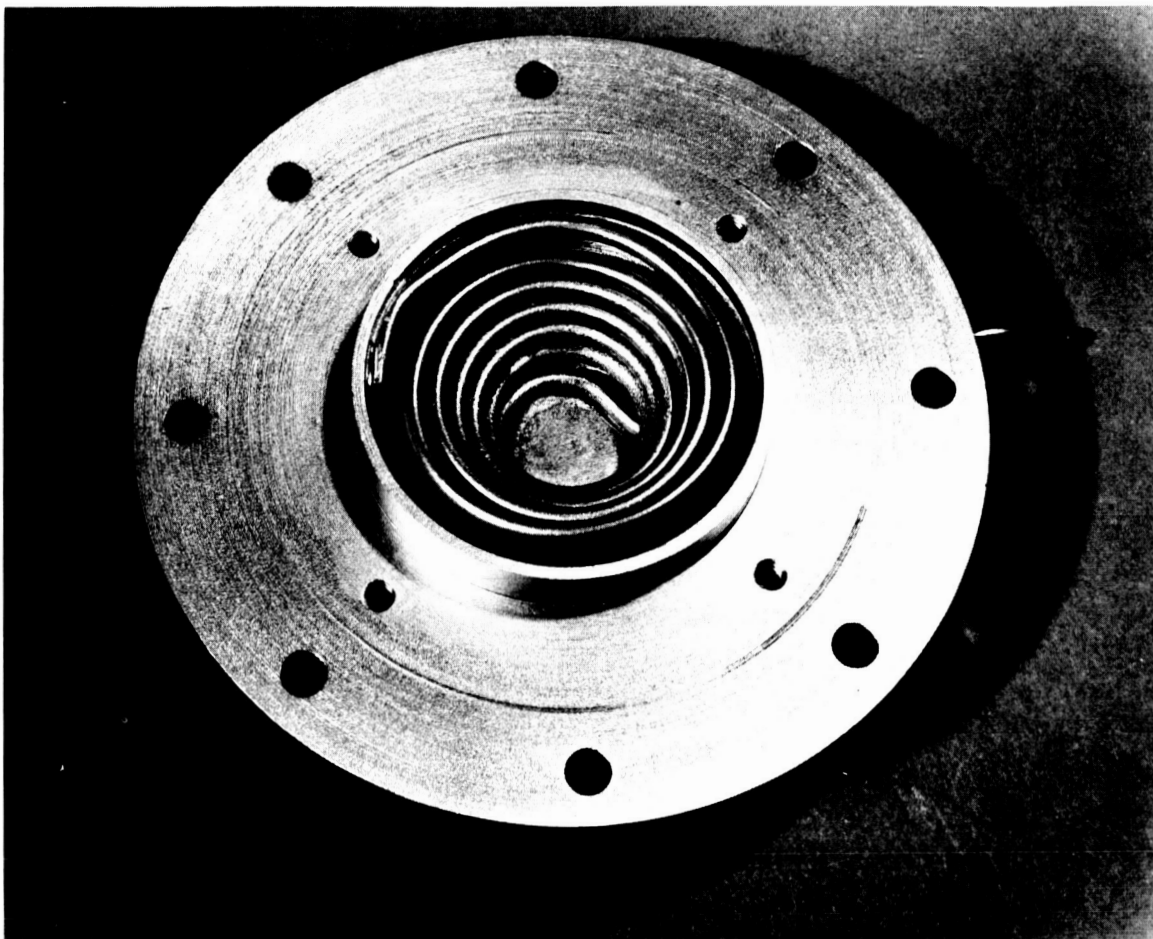


FIG. 77 DF-1 CATHODE AFTER 2610 HOURS CUMULATIVE OPERATION



FIG. 78a CROSS SECTION OF DF-1 CATHODE EMITTER

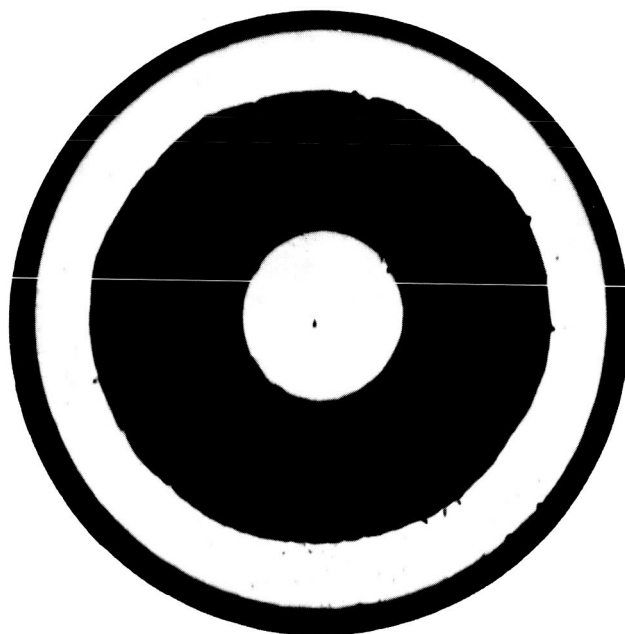


FIG. 78b CONTROL SAMPLE

TABLE XIX  
SPECTROGRAPHIC ANALYSIS OF ENGINE COMPONENTS

<u>Component</u>	<u>Base Material</u>	<u>Major Contaminant</u>	<u>Other Significant Contaminants</u>
Accelerating Electrode (downstream)	Aluminum	Copper	Titanium
Accelerating Electrode (upstream)	Aluminum	Copper	Titanium Molybdenum
Screen Electrode (downstream)	Molybdenum	Aluminum	Copper
Anode (inside front)	Copper	Aluminum	Titanium
Cathode Orifice Plate (downstream)	Molybdenum	Copper	Aluminum
Cathode Heater	Tantalum	Copper	Aluminum

The copper is back-sputtered from the vacuum system liner and collector, and aluminum is sputtered from the accelerator electrode. Titanium came from the ground shield. The molybdenum found on the accelerator came from the screen or cathode.

Small samples of the back-sputtered copper were removed from the downstream side of the accelerator and from the ground screen. The average thickness of the coating from each area was measured and samples of known area were carefully weighed to determine the density per unit area of the back-sputtered copper. The average thicknesses were found to be 0.0052 inch and 0.0038 inch for the material from the ground screen and accelerator, respectively. The densities were 45.5 milligrams/square centimeter on the ground screen and 40.9 milligrams/square centimeter on the accelerator.

#### Accelerator Erosion

The accelerating electrode was then examined under a binocular microscope and the deepest pits due to charge-exchange erosion were plotted and measured. The maximum depth found was, as expected, in the web area between the small innermost holes and the next larger size. The deepest pit, i.e., the point where the charge-exchange erosion was coincident during all three long runs, was 0.043 inch deep. A section of the accelerator containing this pit was cut out, sectioned, and photomicrographed.

Figures 79a and 79b are cross-sectional views of the deepest pit found on the downstream side of the accelerator. They are taken at magnifications of 75X and 16X respectively. The depth of the pit, measured prior to sectioning of the electrode, was  $0.043 \pm 0.002$  inch. Figure 79a was taken with a calibrated ocular; each scale division on the photo corresponds to 0.00075 inch. The overall depth of the pit measured in this manner is 0.026 inch. The discrepancy between the measurement before sectioning and the measurement given by the calibrated ocular is due to the removal of some of the copper deposits on the downstream side of the accelerator between measurements, and failure to section the pit cross section at its maximum depth.

Small displacements of the electrode alignment between the three long-term runs caused the axis of the sputtered pit to shift progressively to the right in the photographs. Evidence of this is shown by the left profile of the pit cross section which exhibits the pit minima from the first two long-term tests. The light area on the upper half of the left side of the pit profile is back-sputtered copper from the collector.

Figure 80 shows a cross-sectional view of one of the accelerator apertures. The downstream portion of the aperture was widened due to loss of material from the wall surfaces caused by sputtering by poorly focused ions. Plating from back-sputtered copper has narrowed the upstream end of the aperture. The two processes, sputtering of the downstream wall areas and plating of the upstream areas, combine to yield a nozzle-like configuration for the accelerator aperture. The ridges around the downstream opening are also caused by plating due to back-sputtered copper. The aperture pictured is from the intermediate (0.1130-inch diameter) aperture pattern, but the behavior described above is qualitatively characteristic of all apertures.



FIG. 79a CROSS SECTION OF THE DEEPEST PIT (X75)

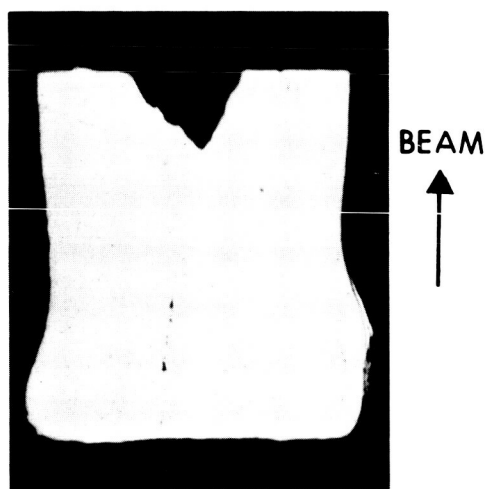


FIG. 79b CROSS SECTION OF THE DEEPEST PIT (X16)



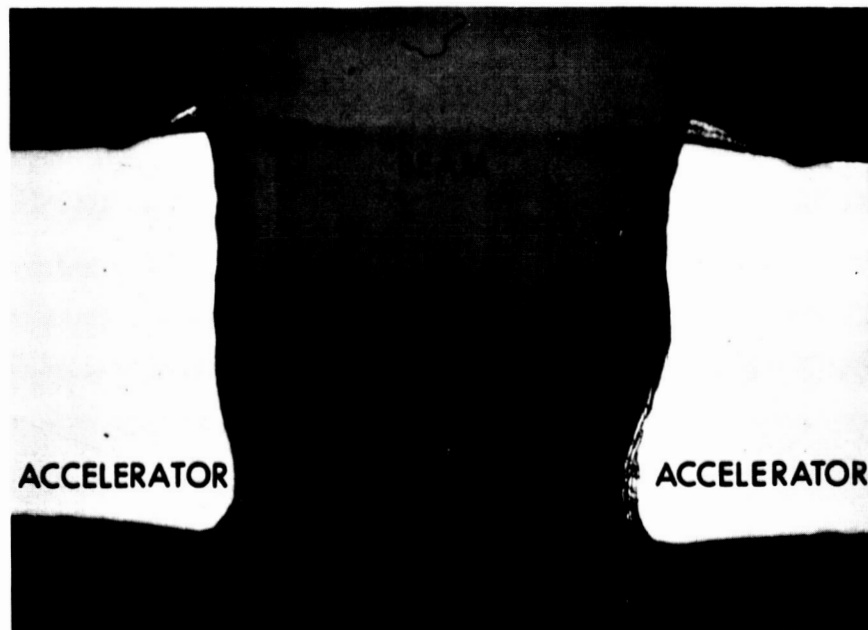


FIG. 80 ACCELERATOR-ELECTRODE APERTURE CROSS SECTION

### Weight Losses

All critical parts were weighed dirty as they came from the vacuum chamber, then, with the exception of the shell assembly, rinsed thoroughly with hot water and reweighed. No significant weight changes were found. Table XX shows these weights, together with those recorded prior to the start of the first long duration run.

TABLE XX  
ENGINE WEIGHTS

	<u>Prior to 1st Run</u>	<u>After 2610 Hours</u>	
		<u>Dirty</u>	<u>Clean</u>
Shell Assembly	763.5010 gms	763.3331	—
Screen Electrode	72.6507	73.1186	73.0972
Accelerating Electrode	102.5819	104.4586	102.4337
Electrode Support Ring	37.2278	37.2264	37.2264
Cathode Housing	180.8132	181.5842	179.7513
Cathode Orifice Plate	28.5255	29.2780	28.4706
Anode	232.8220	234.1534	233.5408

### 3.5 Conclusions

#### 3.5.1 Performance

The following conclusions may be drawn from the performance mapping data:

1. For a given specific impulse, optimum overall engine efficiency is consistent with long lifetime. Optimum overall performance generally occurs with minimum accelerator potential and drain current, which in turn result in minimum accelerator electrode sputtering, the only known lifetime limiting factor.

2. Maximum overall efficiency is not necessarily obtained at maximum thrust. This is true especially at the lower specific impulses.
3. Thrust levels of 10 mlb or greater may be obtained at optimum efficiency and long lifetime for specific impulses above 6000 seconds.
4. Below 6000 seconds specific impulse, the thrust level must be reduced to obtain optimum efficiency and long lifetime. At 5000 seconds, for example, one can obtain a thrust of nearly 10 mlb but both efficiency and lifetime will be reduced. The efficiency and lifetime could be improved for higher thrusts at low specific impulses by using an electrode system more suitable for operation with lower source and accelerator potentials; the DF electrode system was designed for optimum operation at 7000 seconds specific impulse.
5. For higher specific impulses, overall engine efficiency is obtained with higher mass efficiency and source energy expenditures in ev/ion. The power efficiency is approximately given by the ratio of positive high voltage,  $V_+$ , to  $V_+$  plus the ev/ion expended in the source. As  $V_+$  is reduced to reduce the specific impulse, the power efficiency becomes the predominant factor in overall efficiency. At lower specific impulses, it therefore becomes desirable to reduce both the source ev/ion and mass efficiency to increase the power efficiency and obtain the maximum overall engine efficiency.

#### 3.5.2 Engine Lifetime Limitations

Although a 2 percent degradation of engine performance was experienced during 2610 hours of operation, there was nothing to indicate an operational life of less than 10,000 hours. Further, the slight performance degradation noted was undoubtedly influenced to a significant extent by removal of the engine from the vacuum system between tests.

Analysis of the DF-1 engine, at conclusion of 2610 hours of operation, disclosed electrode erosion to be the only predictable factor which could limit its operational life. Extrapolation of data from the three long tests on pit depth as a function of time indicates a breakthrough time of approximately 20,000 hours. Figures 81, 82, and 83 show extrapolations made on linear, semilog, and log-log graphs.

Subsequently, a test was conducted to determine whether breakthrough of the pits to the upstream side of the accelerator electrode would cause a catastrophic failure. Sixty-six of the deeper pit locations were drilled through a DF accelerating electrode as shown in Fig. 84. The 66 large holes were chosen to simulate a more severe pitting condition than would be anticipated under normal, long-term operation.

The engine was then operated for four hours. The accelerator drain current was only slightly higher than normal and no abnormal erosion could be detected. Table XXI lists the operating parameters obtained.

It was concluded that catastrophic failure will not occur even when the accelerator pits have eroded through to the upstream side. Consequently, failure of the electrode should not occur until its structural integrity is destroyed. Extrapolation of data to that point would be difficult, but estimates yield operational life expectancies of well over 20,000 hours.

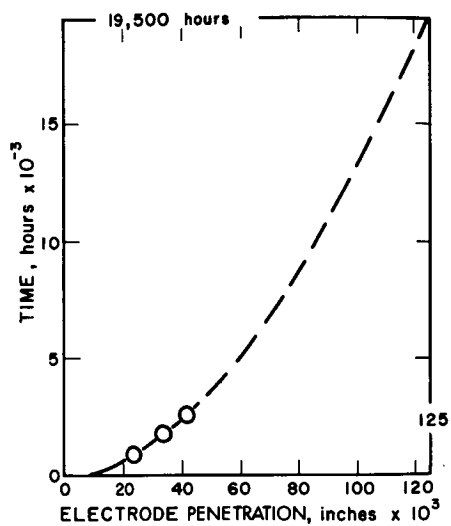


FIG. 81

EXTRAPOLATIONS OF EROSION  
PIT BREAKTHROUGH

FIG. 82

EXTRAPOLATIONS OF EROSION  
PIT BREAKTHROUGH

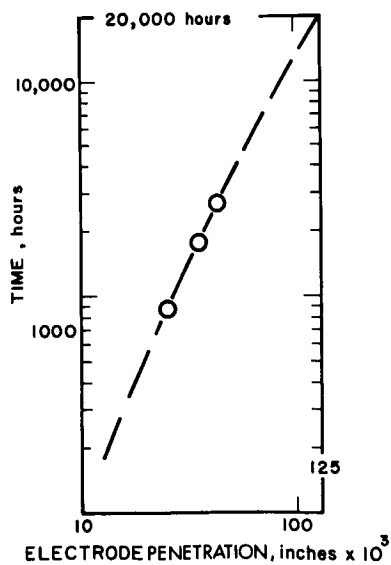
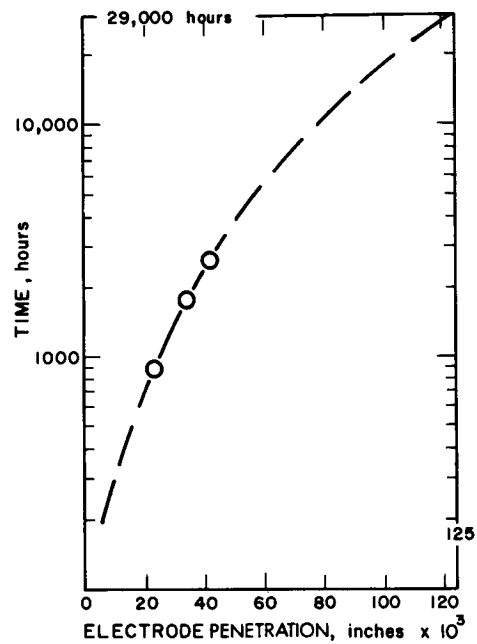


FIG. 83

EXTRAPOLATIONS OF EROSION  
PIT BREAKTHROUGH

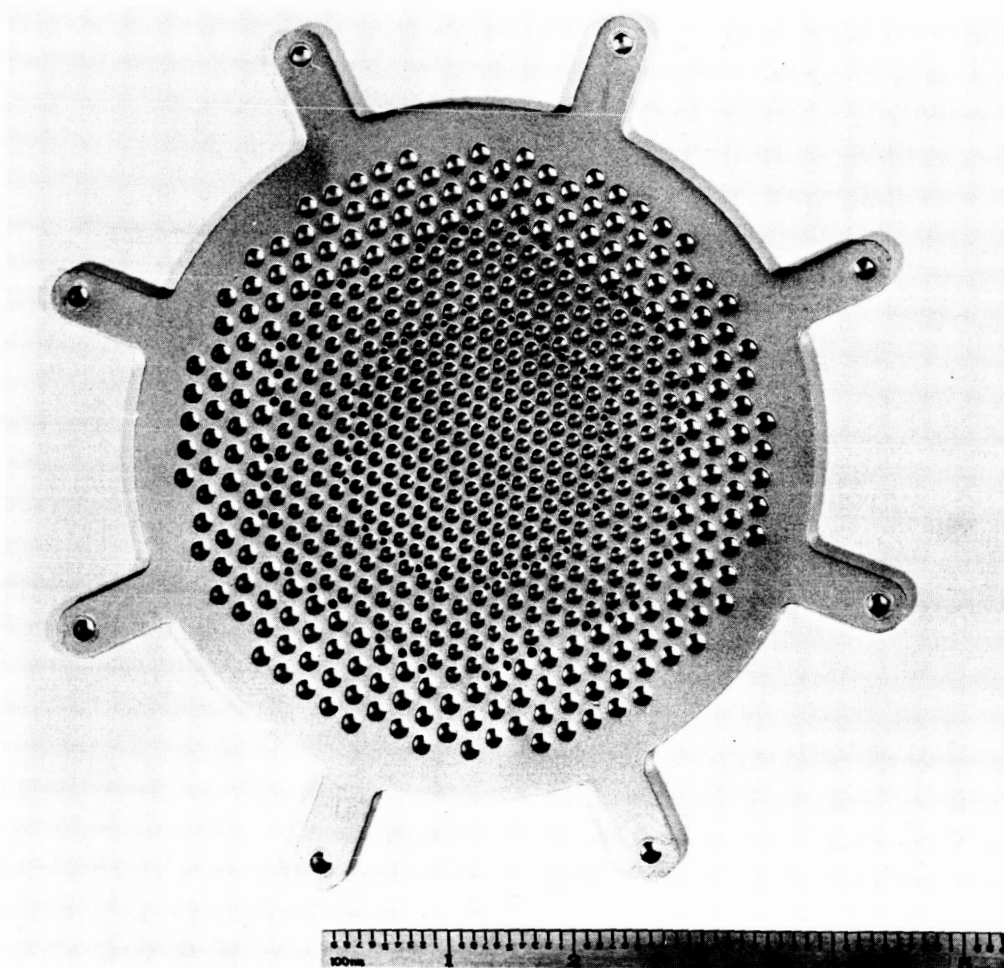


FIG. 84 DF ACCELERATOR ELECTRODE WITH HOLES DRILLED THROUGH  
AT EROSION PIT LOCATIONS

TABLE XXI  
ENGINE PERFORMANCE WITH ACCELERATOR  
EROSION PITS DRILLED THROUGH

$V_+$ (kv)	3.7
$V_-$ (kv)	0.7
$I_-$ (amp)	0.0074
$I_B$ (amp)	0.440
$V_A$ (volt)	7.2
$I_A$ (amp)	24.5
$P_B$ (kw)	1.628
$P_D$ (kw)	0.033
$P_M$ (kw)	0.012
$P_A$ (kw)	0.176
$P_T$ (kw)	1.849
T (mlb)	10.1
P/T (kw/lb)	183
$\eta_p$ (%)	88.0
$\eta_M$ (%)	92.5
$\eta_E$ (%)	81.4
$I_{sp}$ (sec)	6990

#### 4. APPLIED RESEARCH

##### 4.1 Plasma Distribution Studies

The plasma distribution studies were undertaken to improve engine performance through investigation of the discharge characteristics. The effort included ion and neutral efflux distribution measurements and tests of engine design modifications.

##### 4.1.1 Ion and Neutral Efflux Distributions

Faraday cup ion collectors and neutral cesium detectors were mounted on an electromechanical probe drive and used to determine spatial distributions of the ion and neutral cesium atom effluxes from the engine.

##### Off-Axis Neutral Probe

This detector was located at an angle of 45 degrees to the beam axis and could be moved in such a way as to scan across a diameter of the engine. A schematic of the experimental setup is shown in Fig. 85.

An electrical readout from the detector positioning mechanism allowed the measured efflux to be plotted as a function of detector position directly on an X-Y recorder. A shutter was provided to allow determination of background signal levels from the neutral detector.

Initial tests made with a DE engine gave uncertain results due to higher collimation of neutrals by the smaller apertures in the center of the electrodes than by the larger apertures near the periphery. A set of uniform geometry electrodes from the DD engine (EOS Report 3670-Final)<sup>1</sup> was adapted to the DE engine to obtain more straightforward results.



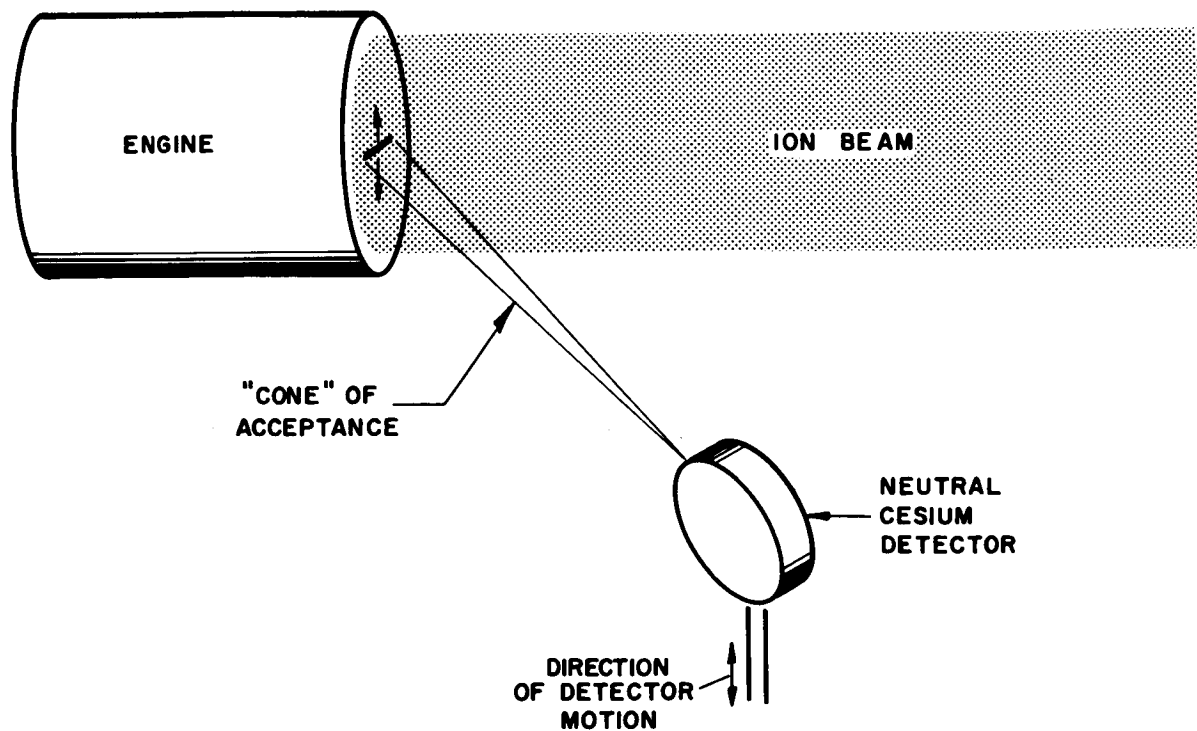


FIG. 85 SCHEMATIC OF SCANNING NEUTRAL DETECTOR EXPERIMENT

Figure 86 presents data taken for operation with a 4 kv, 300 mA beam with 91 percent mass utilization. With a beam being extracted, there was a distinct dip in the neutral efflux from the center of the source. With the high voltage turned off but the arc left on, the plasma extrudes through the electrodes and the distribution is as shown in the middle curve of the figure. The detector signal is, of course, much larger in this case. With the feedrate maintained but the arc extinguished, the third distribution was obtained.

#### Magnetic Field Effects

Figure 87 shows the effect of the magnetic field on the neutral efflux distribution. The lower total efflux at higher fields somewhat obscures the fact that the dip in the center is more pronounced at higher magnetic fields. At zero magnetic field there was no dip and the neutral efflux distribution appeared to be quite similar to that for the case where the arc is extinguished. These results are consistent with theoretical considerations of the effect of the magnetic field on the plasma density distribution; for higher fields, the plasma density is more peaked at the center and the probability of a neutral atom being ionized is therefore higher.

The acceptance angle was then reduced on the neutral detector to provide higher resolution in the neutral efflux distribution, and a Faraday cup collector was mounted alongside the neutral detector but extending into the center of the beam. A set of beam density profiles for a constant beam current of 300 mA at different values of magnet current appears in Fig. 88. The peaking effect of the magnetic field is clearly shown. The large acceptance angle of this Faraday probe and the distance (about 5 inches) from the engine made it somewhat insensitive to changes in engine operation.

Figure 89 shows neutral efflux profiles obtained at the same time as the beam profiles of Fig. 88. A neutral detector mounted in the tank at a greater distance and with a larger acceptance

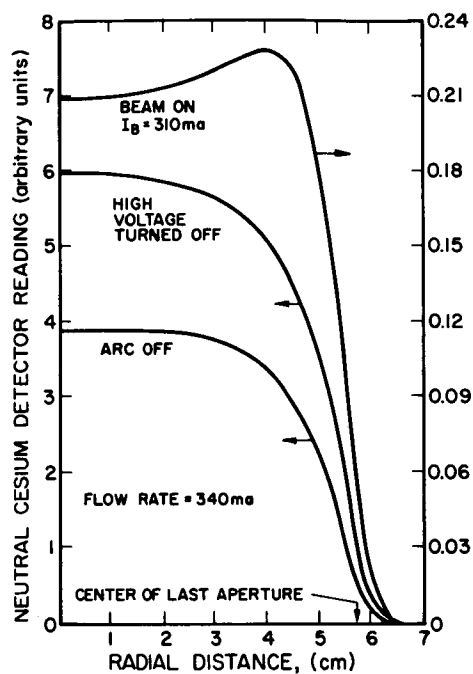


FIG. 86

VARIATION OF NEUTRAL EFFLUX DISTRIBUTION WITH BEAM ON, BEAM OFF, AND ARC OFF CONDITIONS

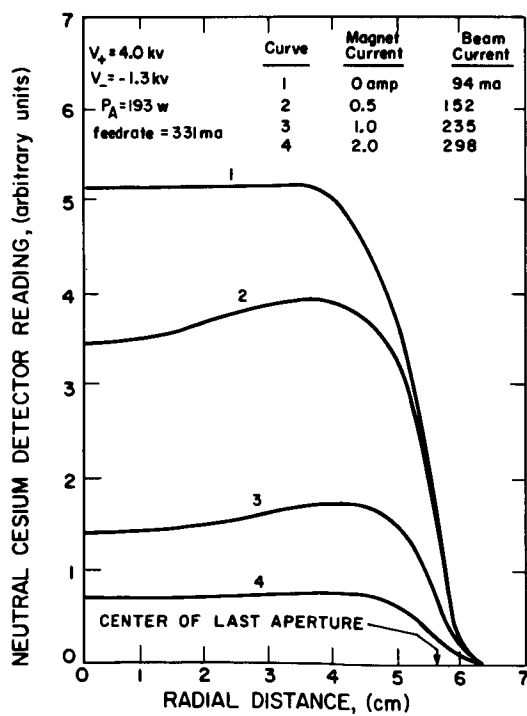


FIG. 87

NEUTRAL EFFLUX DISTRIBUTION WITH VARIED MAGNETIC FIELD

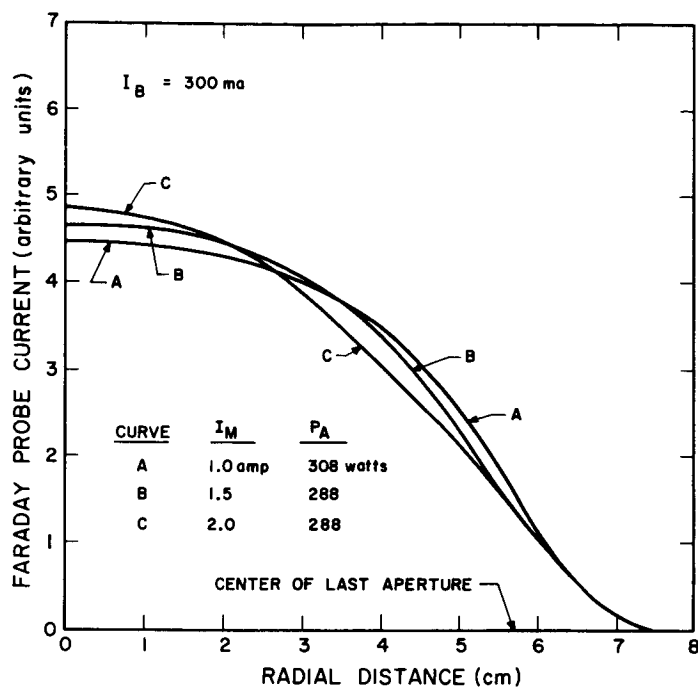


FIG. 88  
BEAM DENSITY DISTRIBUTION  
VARIATIONS WITH MAGNETIC  
FIELD

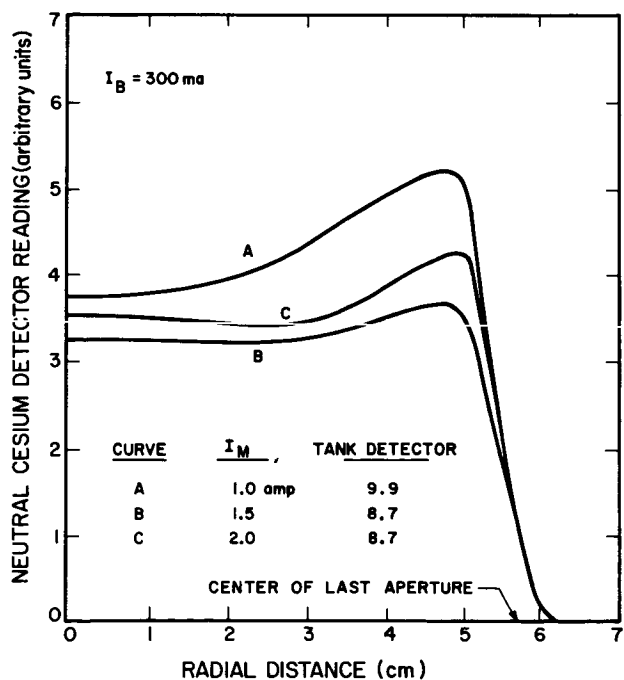


FIG. 89  
NEUTRAL EFFLUX DISTRIBUTION  
VARIATION WITH MAGNETIC FIELD

angle gave the relative readings shown while these curves were taken. At high magnetic fields the peak in neutral efflux from the periphery of the engine becomes more pronounced. This peak may be due, in part, to evaporation of cesium from the anode in addition to the reduced probability of ionizing collisions relative to that at the axis of the discharge.

#### Cathode Orifice Geometry Effects

Figure 90 shows neutral efflux distributions obtained with three different cathode orifice configurations. These curves were taken with the same values of magnet current, beam current, and source potential. The arc power supply setting was held constant but arc power varied due to changes in arc impedance caused by the orifice changes.

Curve A (Fig. 90) was obtained with the standard orifice. Curved B was obtained with an orifice plate which had eight apertures equally spaced on a 1-3/4 inch diameter circle. The object of this test was to inject the electrons and cesium into the arc chamber in such a way as to increase the ion density near the periphery of the electrodes. Beam density profiles obtained showed questionable differences but the shape of Curve B indicates an increase in the neutral density towards the edge of the chamber.

To obtain Curve C, the original orifice was spaced away from the cathode to allow neutrals to enter the chamber radially. The effective cross-sectional area of the resultant gap was approximately equal to the area of the central orifice. Here again a slight increase in neutral efflux distribution towards the periphery was noted but no change in the beam density distribution was found.

#### Collimated Faraday Cup Probe

Ion efflux distributions were measured with the standard Faraday probe for the permanent magnet modification (paragraph 4.4) and electromagnetic versions of the DE engine. These

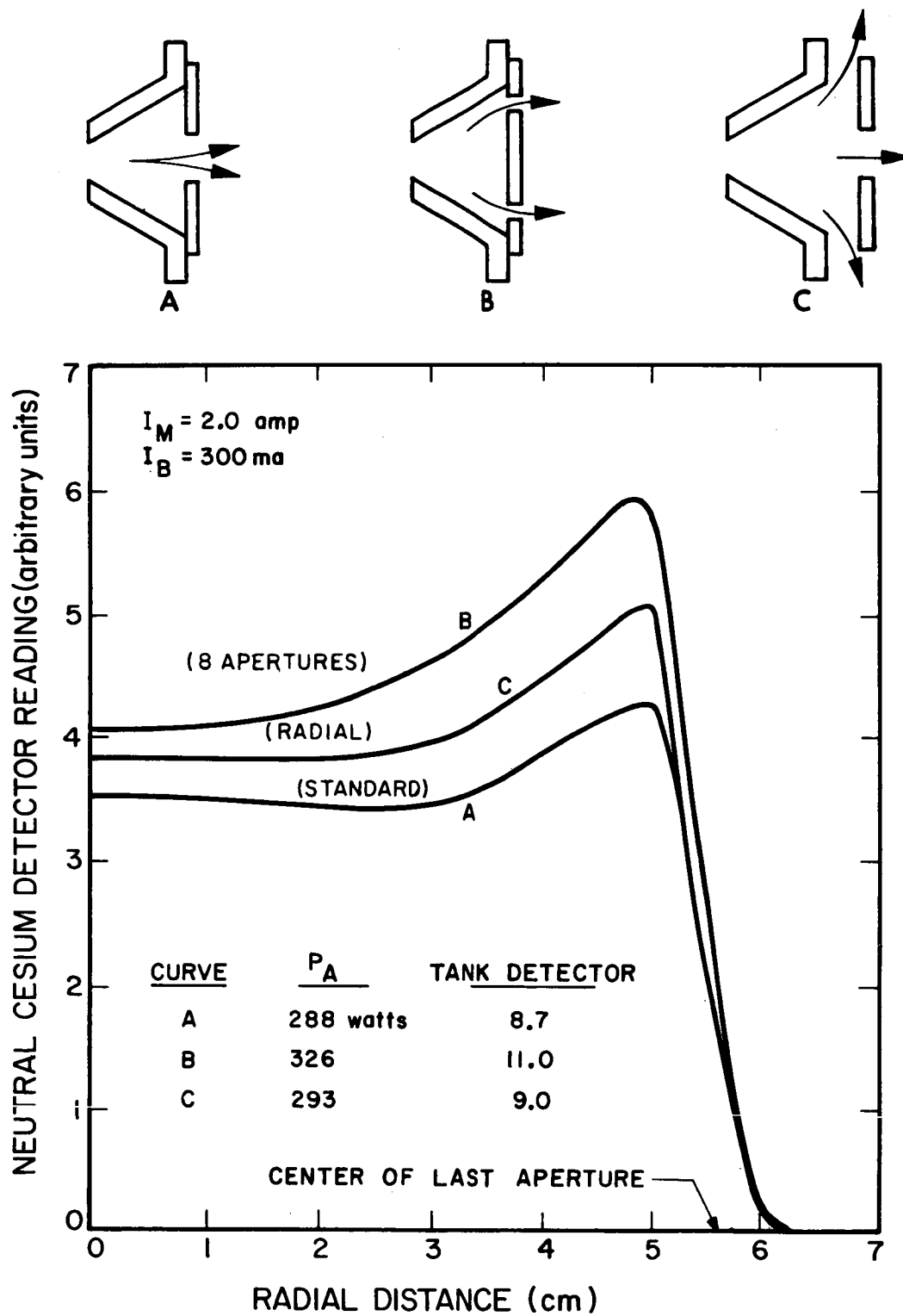


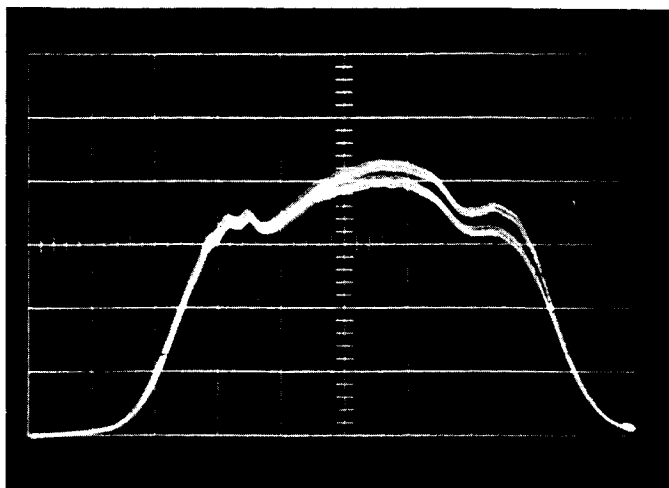
FIG. 90 NEUTRAL EFFLUX DISTRIBUTIONS WITH DIFFERENT CATHODE ORIFICE CONFIGURATIONS

are shown in Figs. 91a and 91b respectively. These figures are photographs of oscilloscope traces with the vertical deflection proportional to the probe signal and the horizontal deflection proportional to the probe position. The dip near the edge of the curves is caused, in part, by the small, aperture-free area at the radius where aperture sizes are changed. The primary cause of the dip appears to be the change in focussing and collimation of the ion efflux across the aperture size transition region. The dip in the center of the distribution of Fig. 91b was due to masking of a radial row of screen electrode apertures to allow thermocouple measurements of accelerator electrode temperatures. With this exception, the two profiles are quite similar.

Figure 91c is an ion efflux distribution measured from the DE engine using a collimated Faraday probe. Collimation was obtained by adding an additional aperture to the probe. This probe measured only those ions which were exhausted along the axis of the probe and has a very small angular acceptance ( $\sim 2$  degrees). The integral of the observed distribution over the area of the engine is therefore a fraction (about 20 percent) of the total ion beam. Information obtained with this probe is strongly dependent upon focussing as can be seen in the curves of Figs. 92, 93, and 94. These curves were obtained in the same manner as those of Fig. 91c, using the collimated probe. The two sides of the curves were averaged to eliminate a slight skew which was present due to probe misalignment.

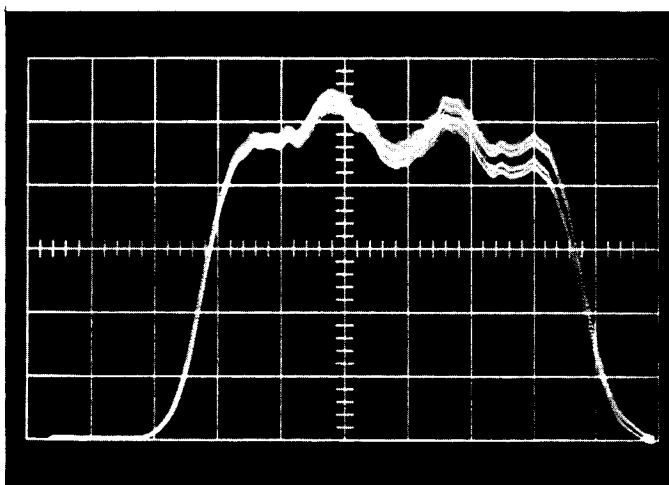
#### Effects of Positive and Negative High Voltages

Figures 92 and 93 show the effect of variations in source potential and accelerator electrode potential respectively. The three curves of Fig. 92 show that higher source potentials improve focussing. High source potential, however, tends to make the change in ion optics more apparent across the transition between the two hole size patterns used. Figure 93 indicates that lower accelerator



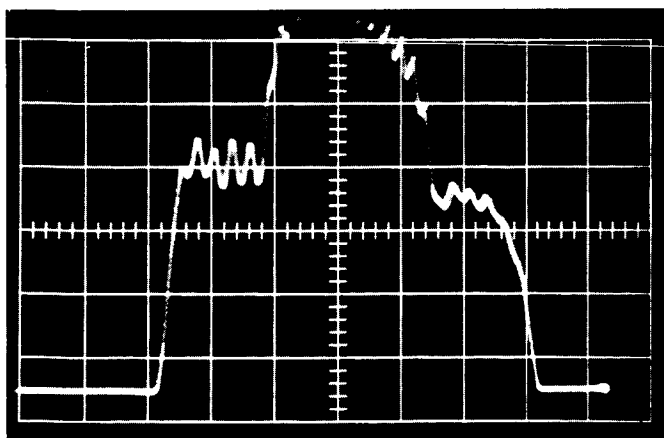
$V_+ = 3.5 \text{ kv}$   
 $V_- = -1.0 \text{ kv}$   
 $I_B = 400 \text{ ma}$   
 $P_A = 292 \text{ watts}$

(a) DE Engine with permanent magnets



$V_+ = 3.8 \text{ kv}$   
 $V_- = -1.1 \text{ kv}$   
 $I_B = 420 \text{ ma}$   
 $P_A = 300 \text{ watts}$   
 $I_M = 1.9 \text{ amps}$

(b) DE Engine

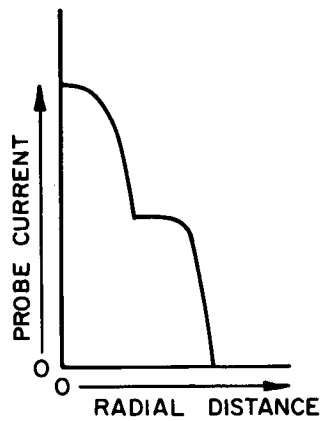


$V_+ = 3.0 \text{ kv}$   
 $V_- = -1.2 \text{ kv}$   
 $I_B = 365 \text{ ma}$   
 $P_A = 336 \text{ watts}$   
 $I_M = 1.9 \text{ amps}$   
 Collimated Probe

(c) DE Engine

FIG. 91 ION BEAM CURRENT DENSITY DISTRIBUTIONS

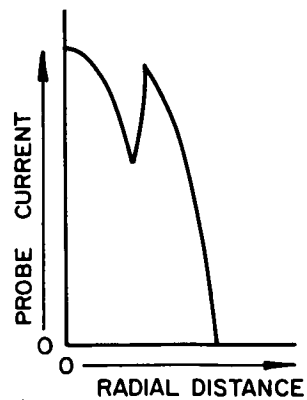




$V_+ = 3.0$  kv  
 $V_- = -1.2$  kv  
 $P_A = 336$  watts  
 $I_B = 365$  ma  
 $I_M = 1.9$  amps  
 (a)

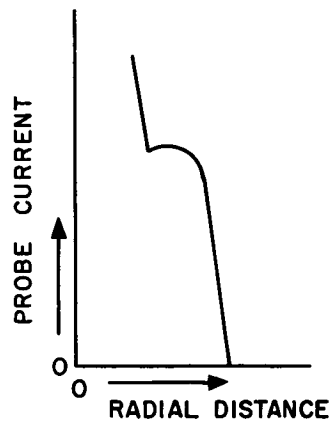


$V_+ = 3.5$  kv  
 $V_- = -1.2$  kv  
 $P_A = 336$  watts  
 $I_B = 375$  ma  
 $I_M = 1.9$  amps  
 (b)

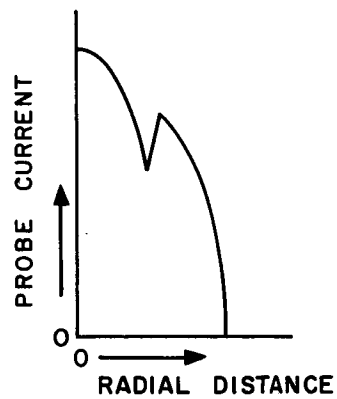


$V_+ = 4.0$  kv  
 $V_- = -1.2$  kv  
 $P_A = 328$  watts  
 $I_B = 370$  ma  
 $I_M = 1.9$  amps  
 (c)

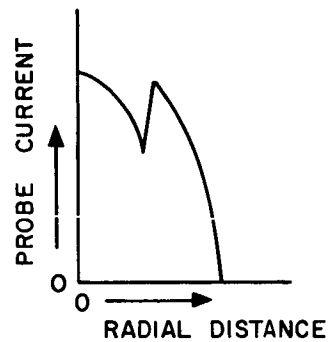
FIG. 92 VARIATION OF ION CURRENT DENSITY DISTRIBUTION WITH SOURCE POTENTIAL



$V_+ = 3.5 \text{ kv}$   
 $V_- = -0.9 \text{ kv}$   
 $P_A = 328 \text{ watts}$   
 $I_B = 370 \text{ ma}$   
 $I_M = 1.9 \text{ amps}$   
 (a)

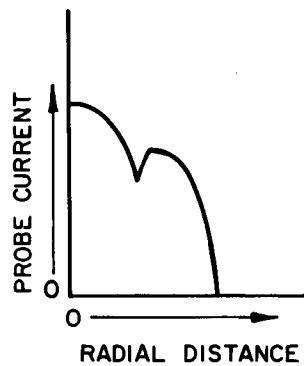


$V_+ = 3.5 \text{ kv}$   
 $V_- = -1.2 \text{ kv}$   
 $P_A = 336 \text{ watts}$   
 $I_B = 375 \text{ ma}$   
 $I_M = 1.9 \text{ amps}$   
 (b)

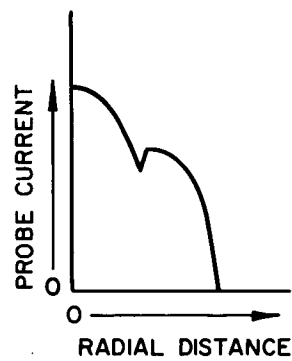


$V_+ = 3.5 \text{ kv}$   
 $V_- = -1.5 \text{ kv}$   
 $P_A = 328 \text{ watts}$   
 $I_B = 370 \text{ ma}$   
 $I_M = 1.9 \text{ amps}$   
 (c)

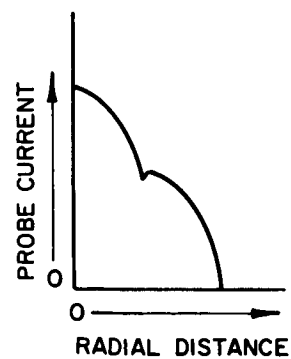
FIG. 93 VARIATION OF ION CURRENT DENSITY  
 DISTRIBUTION WITH ACCELERATOR  
 POTENTIAL



$V_+ = 3.5 \text{ kv}$   
 $V_- = -1.2 \text{ kv}$   
 $P_A = 364 \text{ watts}$   
 $I_B = 380 \text{ ma}$   
 $I_M = 1.7 \text{ amps}$   
 (a)



$V_+ = 3.5 \text{ kv}$   
 $V_- = -1.2 \text{ kv}$   
 $P_A = 372 \text{ watts}$   
 $I_B = 380 \text{ ma}$   
 $I_M = 1.9 \text{ amps}$   
 (b)



$V_+ = 3.5 \text{ kv}$   
 $V_- = -1.2 \text{ kv}$   
 $P_A = 366 \text{ watts}$   
 $I_B = 380 \text{ ma}$   
 $I_M = 2.1 \text{ amps}$   
 (c)

FIG. 94 VARIATION OF ION CURRENT DENSITY DISTRIBUTION WITH MAGNETIC FIELD

electrode potentials improve the focussing. This is to be expected since the decelerating region downstream from the accelerator electrode slows the exhausted ions in the axial direction but does not greatly affect transverse velocities. Thus, for a given trajectory to the accelerator (constant current and accelerating gap potential) higher decelerating potential drops will increase the angle between the exhausted ion and the engine axis.

#### Magnetic Field Effect

Figure 94 shows ion efflux profiles obtained with different values of magnet current. As shown before, the higher magnetic fields cause the distribution to peak at the center.

#### Liquid-Nitrogen-Cooled Neutral Cesium Detector

Since an uncertainty existed as to the angular variations in neutral efflux, a neutral detector was designed to work in the beam.

This detector had a more effective sweep system than other detectors (longer sweep length and improved venting) and used  $\text{LN}_2$  cooling to condense cesium out of the filament housing. A schematic of this neutral detector is shown in Fig. 95. Ions entering the front aperture see a transverse electric field which deflects them up through the grid and out of the detector. Two apertures are used after the sweep electrodes so that reevaporated cesium from the sweep area will not be measured. The entire detector is liquid-nitrogen cooled to capture stray cesium atoms on the walls of the device, thus preventing a cesium pressure buildup. Neutral cesium atoms arriving at the hot tungsten filament are ionized by surface ionization and repelled from the filament, which is biased positive with respect to the detector walls. A portion of these ions are intercepted by the collector and measured. The detector was mounted on the probe drive used for the previous tests so that neutral efflux measurements as a function of radial position could be obtained. The collimated

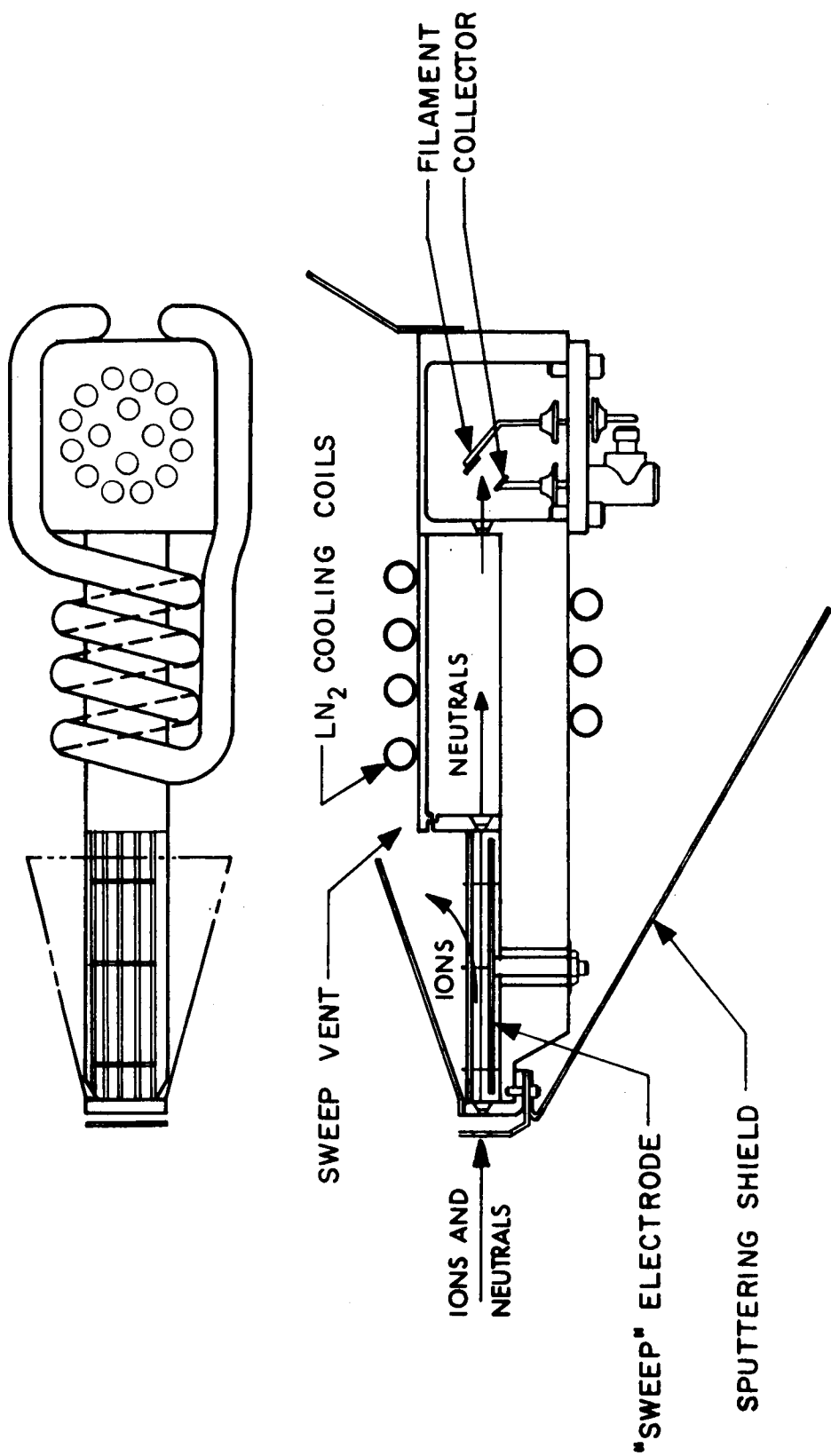


FIG. 95 LIQUID-NITROGEN-COOLED NEUTRAL DETECTOR

Faraday probe was also mounted with the cooled neutral detector to allow simultaneous scanning of both ion and neutral efflux distributions. The  $\text{LN}_2$ -cooled neutral cesium detector is shown mounted in the vacuum facility in Fig. 96. The entire detector was housed in a shield to prevent contamination by sputtered copper and excessive heating when passed through the ion beam. The collimated Faraday probe can be seen protruding from the shield directly above the front aperture of the neutral detector.

#### Detector Operation

The initial operation of the neutral detector was intended to verify the effectiveness of the sweep electrode and cooling in reducing the beam interference and background level. Figure 97 shows the detector output as a function of the potential applied to the sweep electrode. With ion energies of 2.5 kev, a potential of only 50 volts was required to deflect the ions out of the detector line of sight. At 5 kev ion energies, 100 volts was adequate. Normal operation, at 300 volts, should allow no ions to pass the sweep area at any reasonable specific impulse for the DE engine.

The effect of cooling on the background was satisfactory. When the detector was operated at  $25^\circ\text{C}$ , the background level increased with each successive pass through the ion beam. Cooling to  $-30^\circ\text{C}$  or lower allowed repeated passes through the beam with no residual increase in the background level, which was only a few percent of the signal level.

#### Neutral Efflux Distributions

The engine was mounted in the vacuum tank so that when the detector support shaft was rotated the detector remained aimed at the center of the accelerator electrode. The support shaft was rotated to the desired view angle and then swept vertically through the beam. The detector output was then plotted as a function of the vertical position of the support shaft. A set of these distributions taken at different angles from the beam axis appear in Fig. 98.

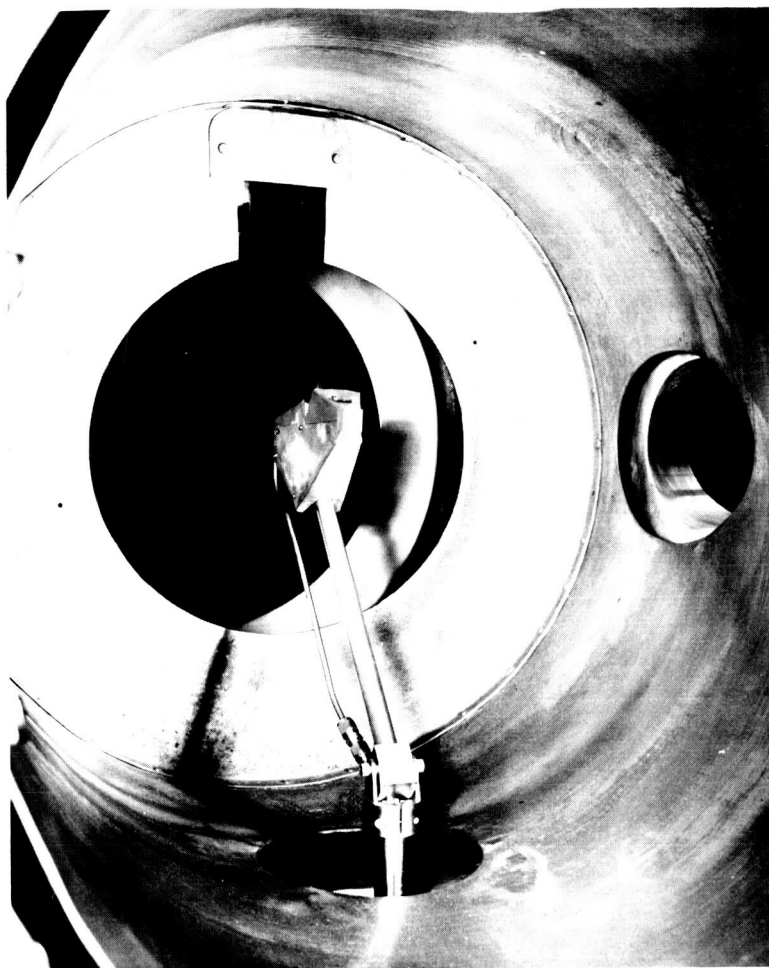


FIG. 96 LIQUID-NITROGEN-COOLED SCANNING NEUTRAL DETECTOR

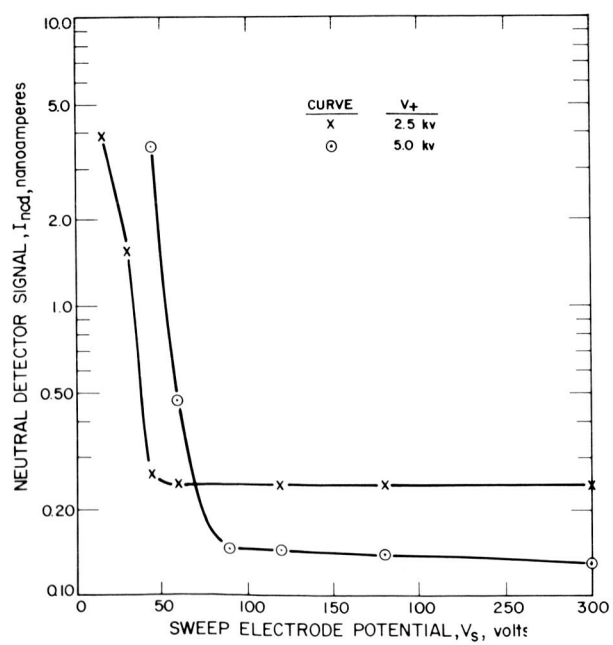


FIG. 97  
EFFECT OF SWEEP ELECTRODE  
POTENTIAL VARIATION

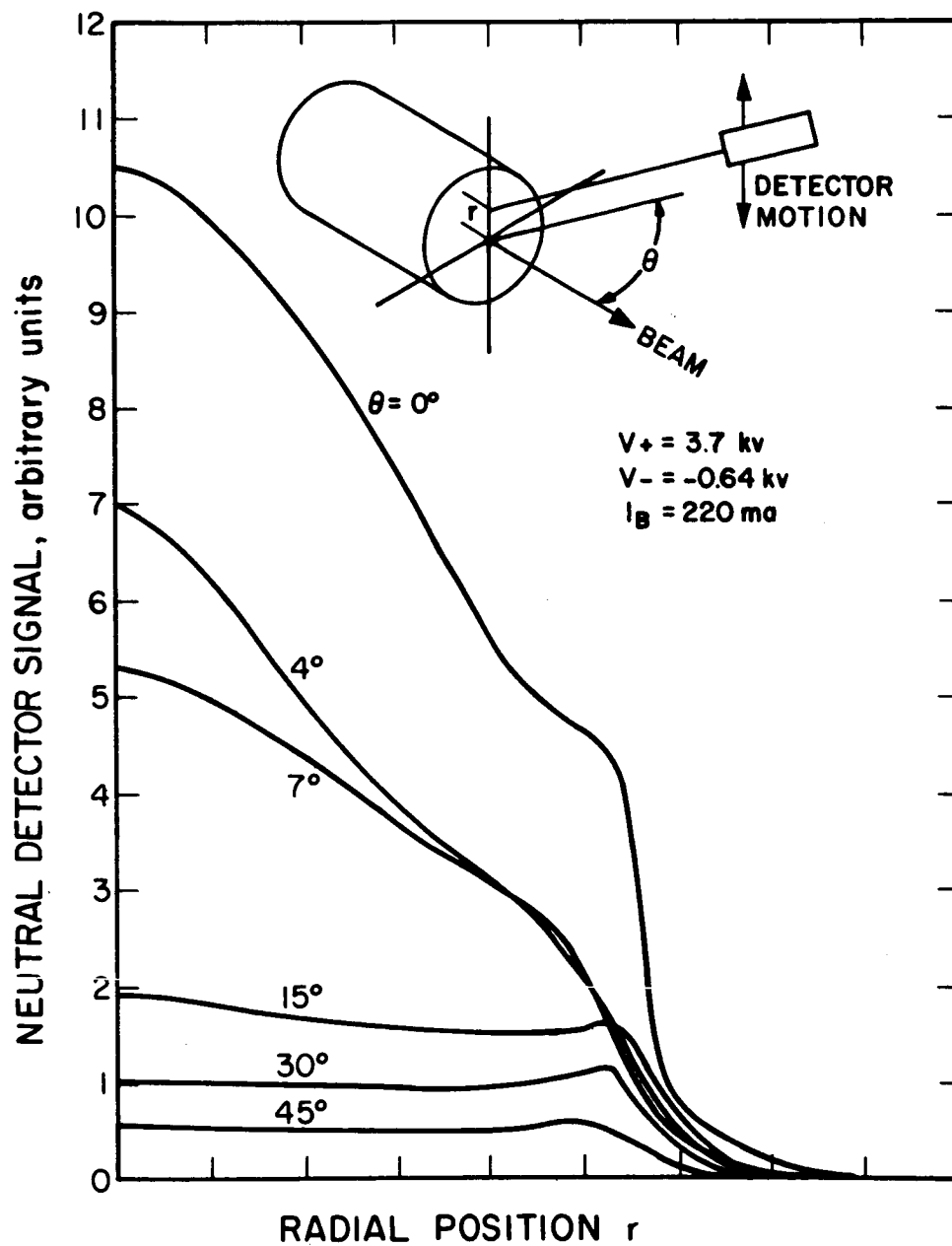


FIG. 98 NEUTRAL EFFLUX DISTRIBUTIONS



The distributions were obtained using a DE engine with a set of uniform geometry electrodes. At a detector to beam angle of 45 degrees, the distribution obtained compares well with those obtained with the off-axis detector taken at the same angle. The intensity of the neutral efflux along the engine axis was attributed to neutrals formed by charge exchange of the highly directed beam ions.

As a check on the effect of charge exchange on the neutral efflux distribution, the axially directed ion and neutral effluxes were measured at two different values of positive high voltage. Since the beam current and feedrate were maintained constant, the only change was in the accelerating and focusing fields. The distribution of the axial component of the neutral efflux changed in the same manner as the ion efflux indicating that charge exchange of beam ions was significant in determining the nature of the neutral efflux distribution.

#### 4.1.2 Electrode Redesign

Since the transition between the two regions of different aperture sizes was so noticeable in beam profile measurements on the DE engine, a new electrode system was designed for use on the permanent magnet engine. The principal change was the addition of a third hole size region between the central and peripheral areas. The screen electrode was made of iron in order to complete the permanent magnet circuit. Copper was used for the accelerator electrode to allow ease of fabrication. The variable gap was obtained by warping the screen electrode during fabrication.

The PM engine electrodes were mounted on a DE engine for design verification tests. The first observation made during operation of the PM electrodes was that the drain current as a function of gap potential with constant beam current displayed a very distinct minimum. At low gap potentials, of course, the plasma tends to extrude.

At higher potentials the plasma sheath is forced away from the screen, defocusing the beams and causing high drains. At typical operating voltages and beam currents the minimum drains were between 0.5 and 1.0 percent of the beam current. This corresponded to a reduction by a factor of 2, in some cases, over the DE electrode drains. The perveance of the PM electrode system also obeyed a  $V^{3/2}$  dependence much more closely than did the perveance of the DE electrodes. This indicated that a closer match to the plasma distribution was obtained through the addition of the intermediate hole pattern. Finally, the magnetic field required for optimum performance varied from 6 gauss to a beam level of 250 mA to over 9 gauss at a beam level of 785 mA. This variation was necessary to maintain the shape of the plasma density distribution. A change in magnet current, however, was not required for good performance.

#### 4.1.3 Inverted Engine

Since the potential gradients within the discharge chamber tend to increase the ion density at the center of the chamber, and since attempts to inject the cesium into the chamber at about a 1-inch radius had not changed this distribution significantly, an engine was designed with the anode on the axis and with autocathodes at the periphery of the chamber. In addition, the engine was designed to feed the cesium through the autocathodes, injecting it toward the rear of the discharge chamber. The inversion of the anode and cathode was expected to provide a potential distribution which would tend to increase the ion density toward the periphery of the source as compared with the DE engine.

The design is shown in Fig. 99. A heated feed tube assembly was used to bring cesium to the cathodes mounted at the screen end of the chamber. The engine shell was a DE shell with an extension at the screen end to provide for mounting the cathodes. The cathodes had heated tantalum emitters similar to those of the DE cathode but smaller in size. This device was operated but no distribution data

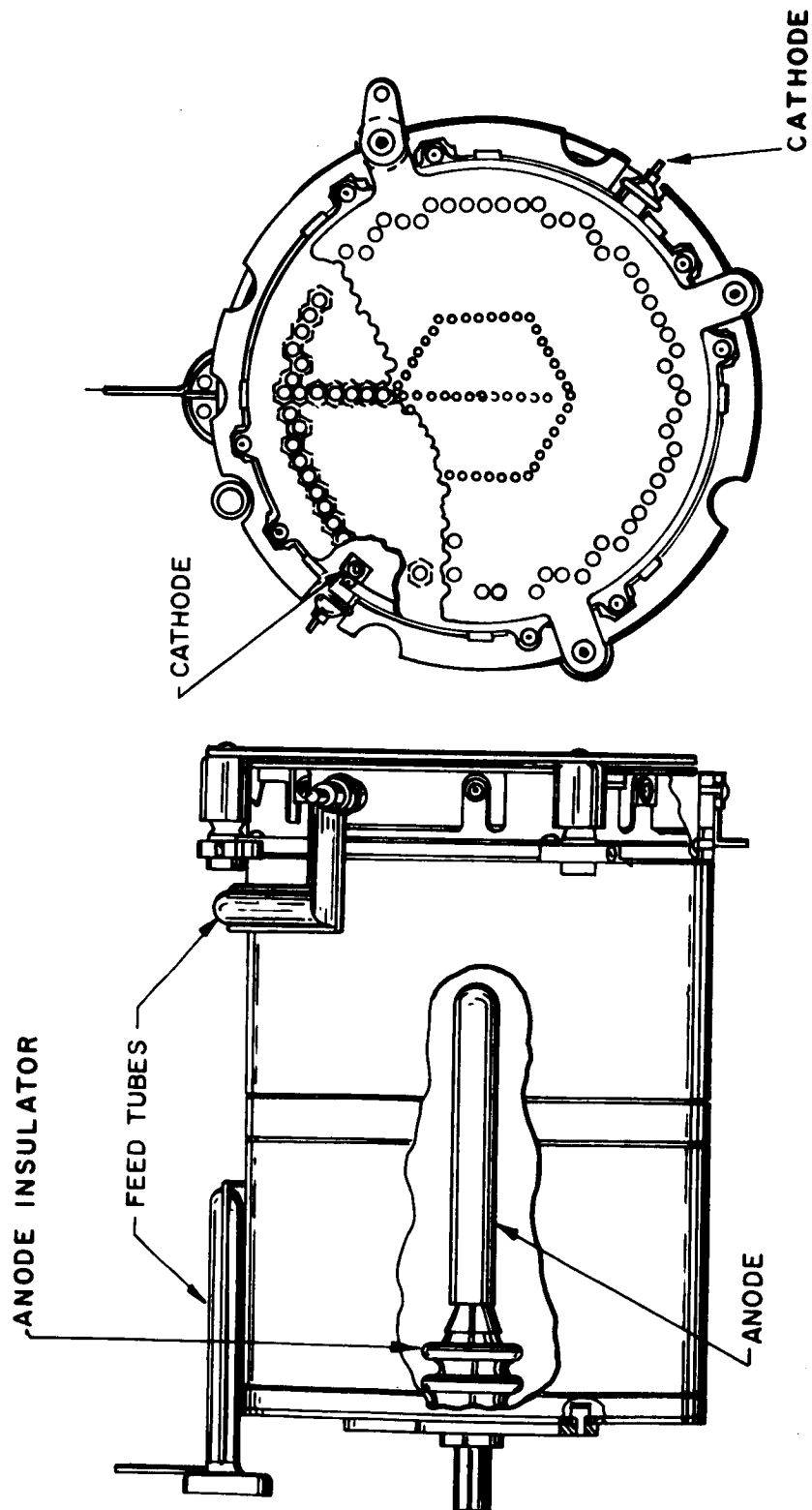


FIG. 99 INVERTED ENGINE DESIGN

were obtained. Some observations on the initial operation of this engine are discussed below.

The arc impedance was not consistent as with the DE engine. Arc impedances of from 0.1 to 5 ohms were observed. The auto-cathodes overheated considerably, apparently causing the emitter surfaces to operate in the negative slope region of the emission-versus-temperature curves. Although the arc started very smoothly, both cathodes did not always start together. The discharge operated steadily on either or both of the cathodes.

Cesium leaks around the cathode feed lines caused high-voltage breakdowns but beam currents of 300 mA were obtained with 4-percent drain currents and an arc power of 450 watts.

The inverted engine was rebuilt with larger cathodes and retested with the following results:

1. The cathodes did not overheat.
2. Many modes of arc operation were observed, most of which were unstable.
3. The only stable mode of operation was with zero magnetic field and high arc voltages. In this mode a beam current of 250 mA was obtained at a source energy expenditure of 1800 ev per ion.
4. The arc was difficult to initiate.
5. Increased anode dissipation due to high arc voltages and the small area of the axial anode caused the anode temperature to exceed 1000°C which destroyed the engine.

#### 4.1.4 Magnetic Field Modification

The increased performance of the PM engines appeared to be due, in part, to the divergent magnetic field which exerted a downstream force on electrons. This set up a potential gradient which accelerated ions toward the screen electrode. Operation at high mass utilization efficiency was then possible with a lower degree of ionization in the discharge chamber. Efficient operation is then obtained

with reduced arc power. This effect had been noted by Reader (Ref. 5) but attempts to improve DE engine performance in this manner had failed.

#### Modified DE Field Tests

The objective of these tests was to obtain more efficient operation with an electromagnet engine by duplicating the field of the PM engine. The magnetic fields on the axis of PM-1 and PM-2 are shown in Fig. 100. As a first step, the number of turns on the rear coil of a DE engine was increased by fifty percent by adding a rear coil over the original winding. This produced an axial field as shown in Fig. 101, curve B. This engine operated with an overall efficiency about three percent higher than normal for DE engines.

To reduce the drop-off at the screen, a second coil was added at the front of the engine. This coil was ten inches in diameter and positioned in the plane of the screen electrode. The shape of the field obtained is shown by curve C in Fig. 101. The overall efficiency of the engine was not increased but a further reduction in arc power was found. This reduction in arc power was offset by increased drains.

A distributed coil was then wound on a DE shell in such a manner as to approximate the field obtained with the additional front and rear coils. The spacing between turns was varied to shape the field. Close-spaced winding was used near each end and near the center structural ring on the shell. The result was a reduction in the drop-off at the ends and the dip in the center of the engine. The field obtained is compared with that of the DE engine in Figs. 101 and 102.

The engine with the distributed coil was operated and the performance obtained is shown by the circled data points in Fig. 103. Performance was about four percent above the DE level. The electrodes for the 750-hour test engine with the three aperture sizes were then placed on this engine to obtain a better match to the plasma distribution. Subsequent operation was found to be 8 percent more efficient than the DE engine as shown by the X data points in Fig. 103.

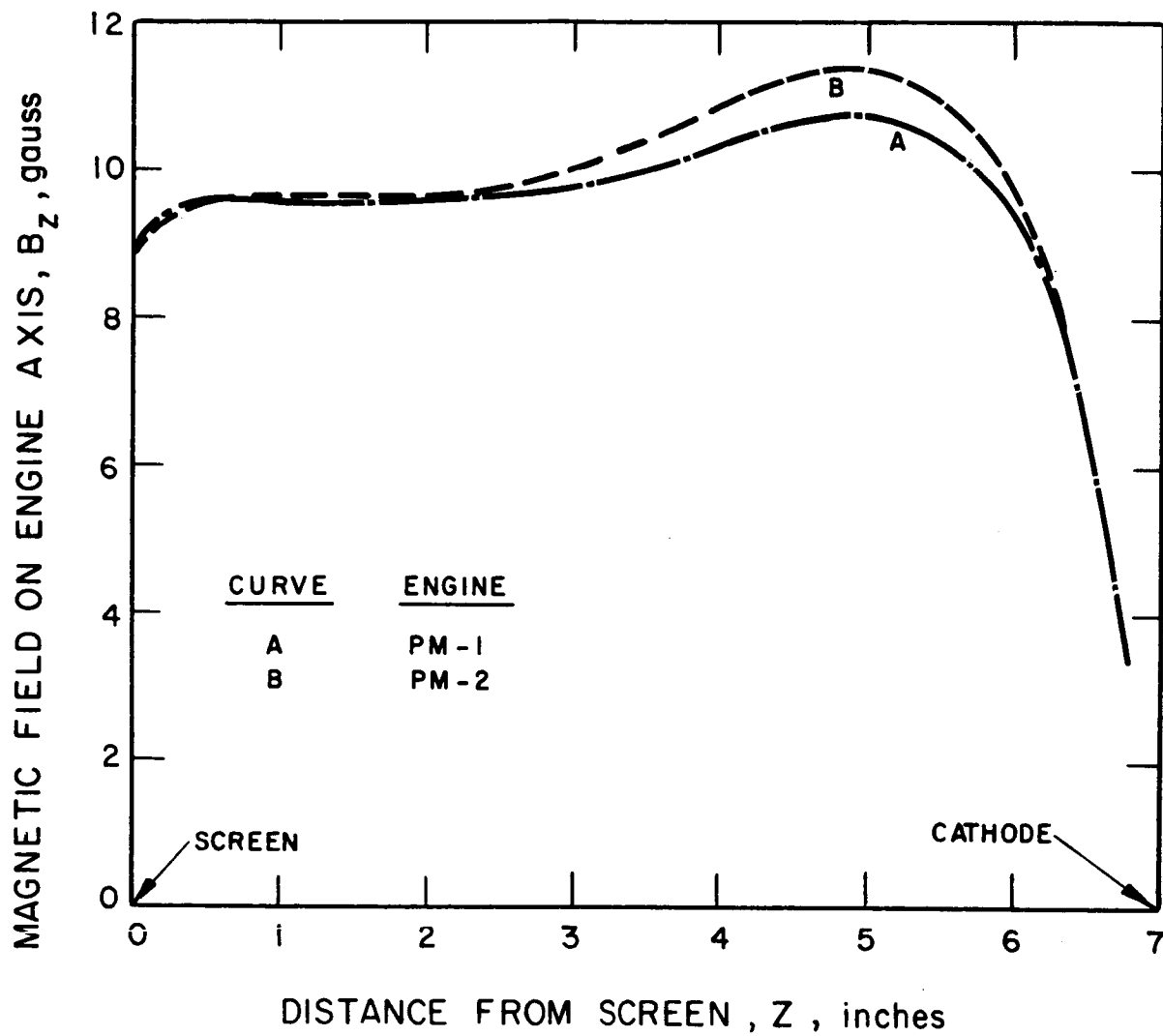


FIG. 100 PM ENGINE FIELD CONFIGURATIONS

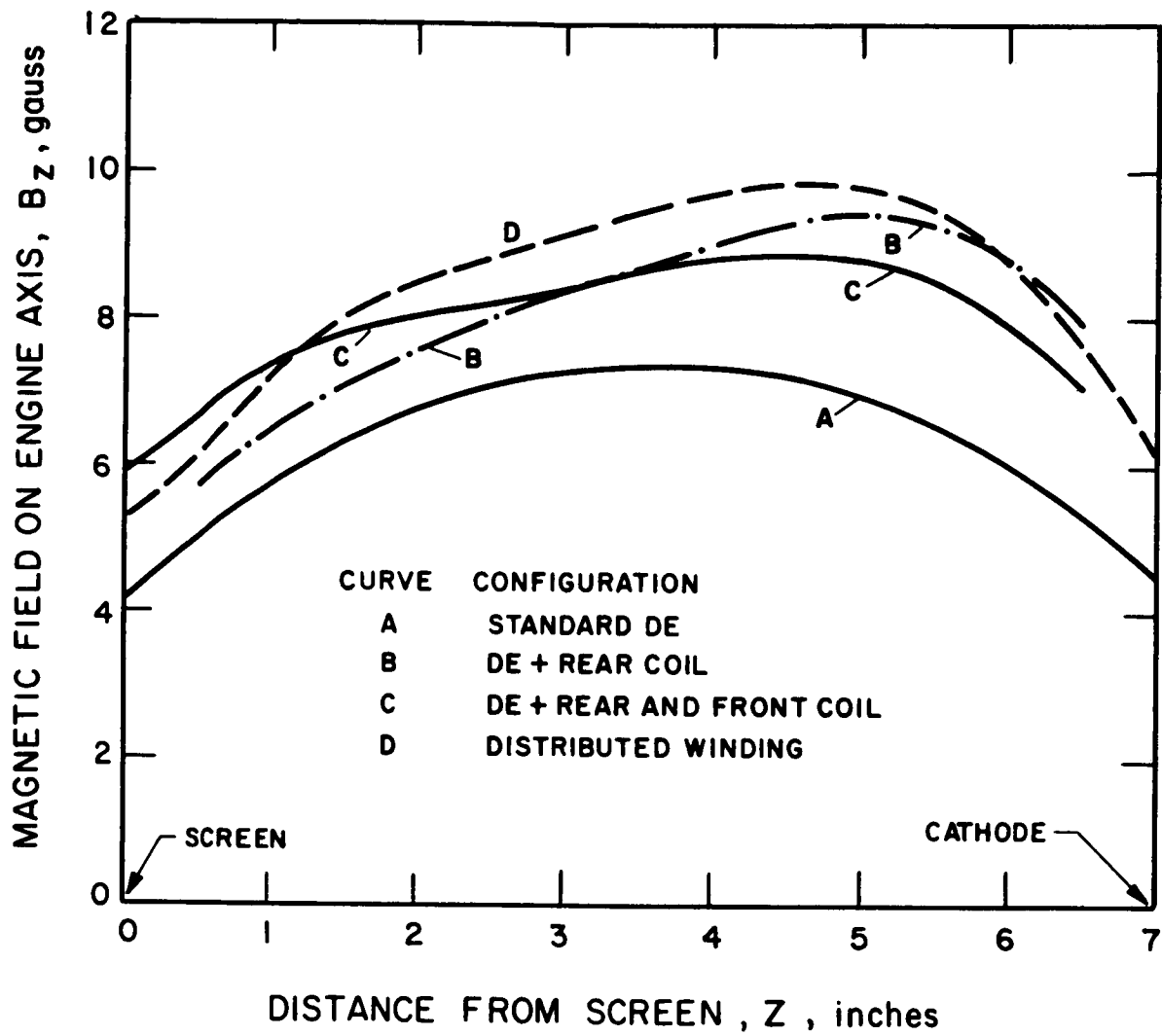


FIG. 101 ELECTROMAGNET FIELD CONFIGURATIONS

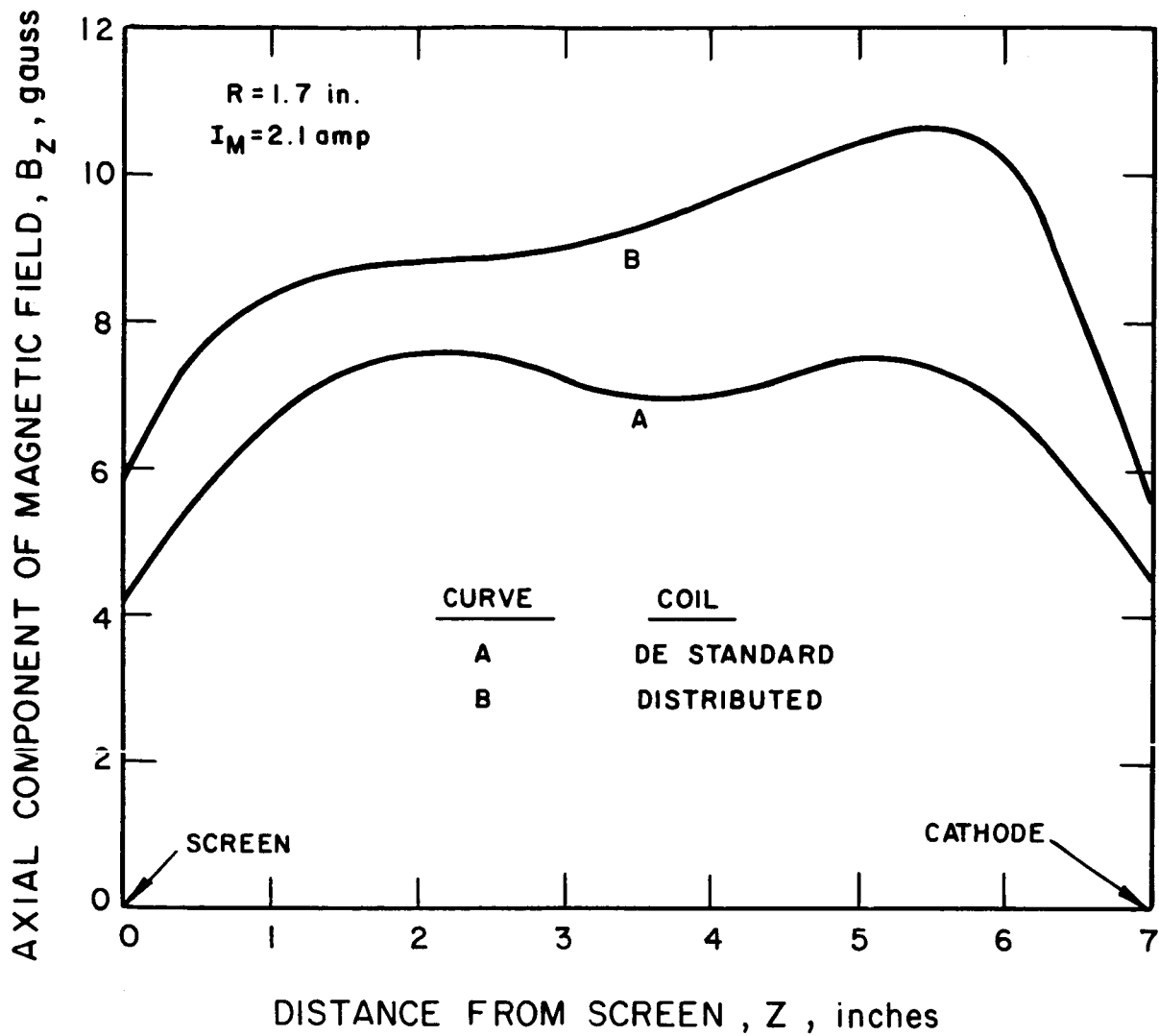


FIG. 102 DE AND DISTRIBUTED COIL FIELDS OFF-AXIS



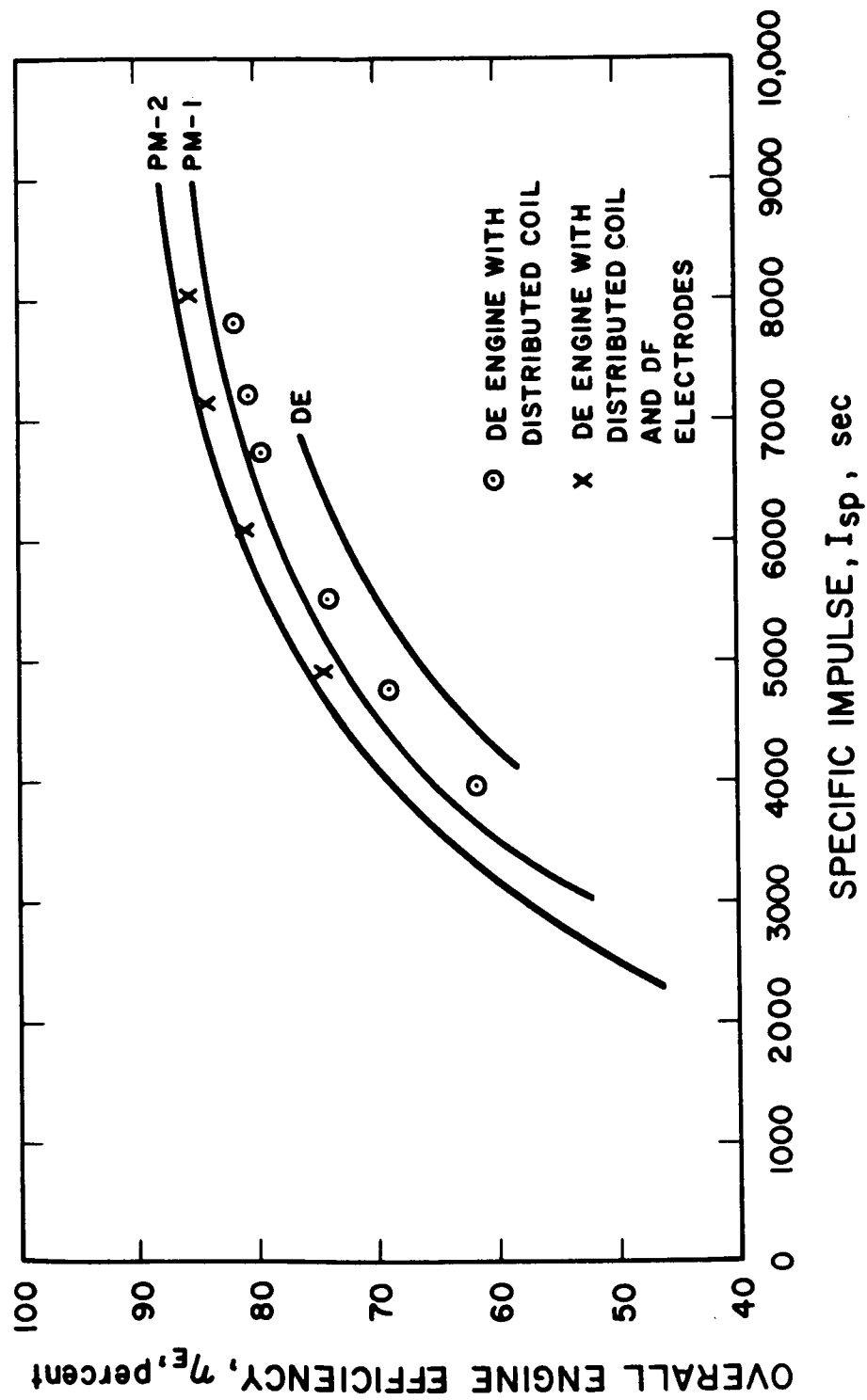


FIG. 103 DISTRIBUTED COIL ENGINE EFFICIENCIES

### Repeatability

A second engine was wound in the same manner as the first distributed coil engine. The second field was identical with the first within  $\pm 0.2$  gauss per ampere which was within measurement accuracies.

### Further Tests

To allow further evaluation of the effects of magnetic field gradients on the engine, a pair of Helmholtz coils with a diameter of approximately 3-1/2 times that of the engine was constructed. These coils were operated both as Helmholtz coils and with unequal currents as required to produce magnetic field gradients within the volume of a DE engine. The coils were wired so the divergence and magnitude of the field could be varied independently. It was found that very linear magnetic fields were obtained when the center of the rear coil was 1 inch behind the cathode plate, and the center of the screen coil was mounted 1 inch forward of the screen electrode. Any reasonable linear field divergence, defined here as  $\Delta B_z / B_z \text{ max}$ , could be produced by these coils.

For these tests a DE engine with DF electrodes was used. The total magnetic field was adjusted to give optimum engine performance after the divergence was set. Difficulties with the neutral detector readings prevented good mass efficiency measurements, but operating points were established at a constant feedrate of about 460 mA equivalent current. The beam current was then measured as a function of arc power for four field divergences.

Figure 104 shows the beam current plotted against the ratio of the arc power to the beam current,  $P_A / I_B$ , for a uniform field, and 9.7, 20, and 24 percent field divergences. This graph shows better performance at higher field divergences. At lower mass utilization, as would be used at low specific impulse, the 20-percent divergence appears to give better results than the 24-percent divergence. No more quantitative data were obtained.

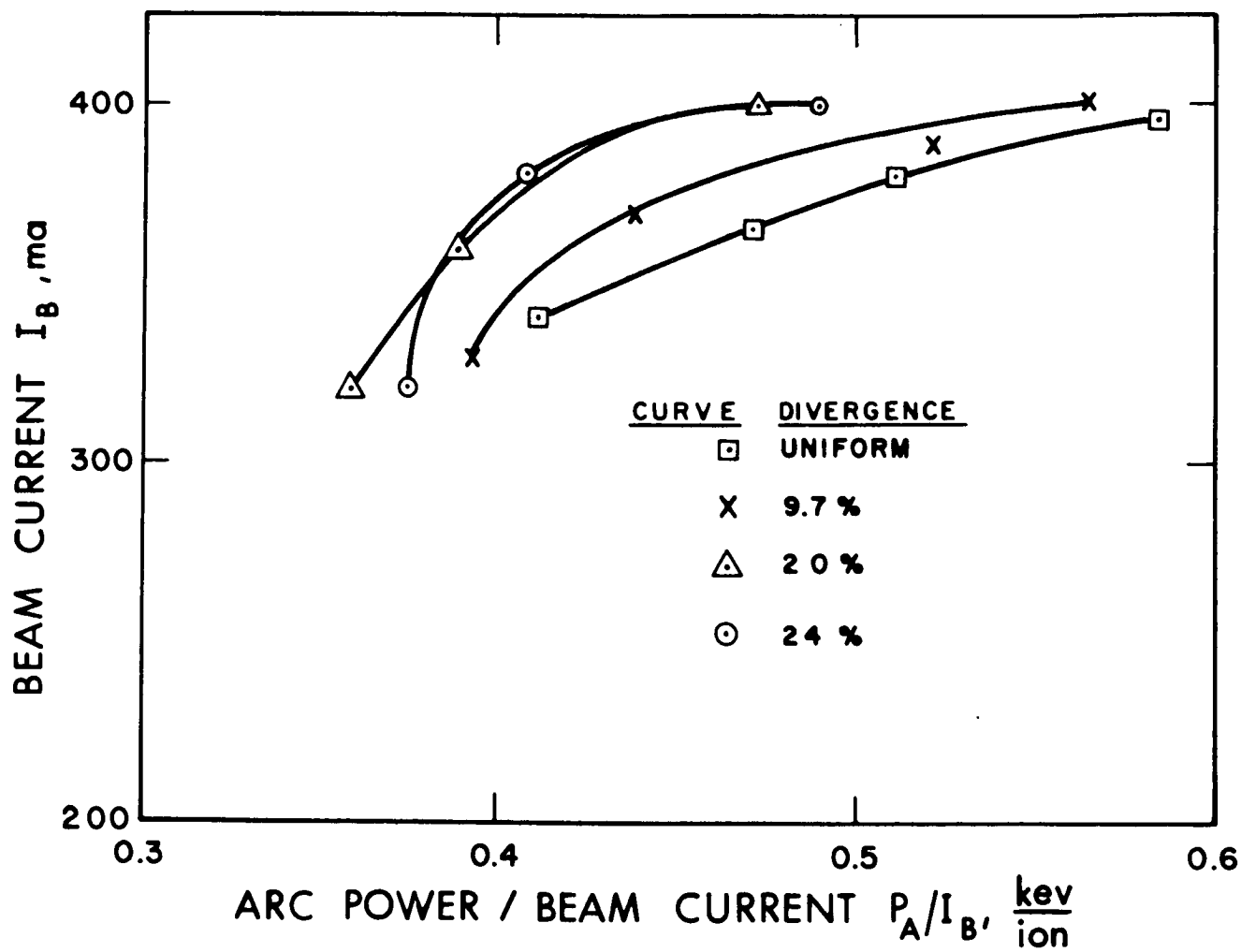


FIG. 104 SOURCE EFFICIENCY VARIATIONS WITH MAGNETIC FIELD DIVERGENCE

## 4.2 Conceptual Design of Large Engine

The objective of this task was a conceptual design of a 30-kilowatt cesium electron-bombardment ion engine. A more specific goal was to achieve a thrust of 0.1 pound at a specific impulse of 5000 seconds to produce a design consistent with the limits imposed by mission requirements and existing or practicable power source systems. A 20 cm Kaufman engine (Ref. 6) was provided by the NASA Program Manager, making possible a number of supporting tests, upon which the conceptual design is, in part, based.

### 4.2.1 Scaling Requirements

Analysis of a three-dimensionally-scaled DF engine and its predicted performance leads to design restraints for engine scaling and the delineation of areas in which development is required to obtain good scaling.

#### Three-Dimensional Scaling

The DF engine could be scaled by increasing all existing dimensions by some scale factor. The results of such scaling of a DF engine by a factor of 4 are shown in Table XXII.

Since the electrode gap would be increased by a factor of 4, it would sustain 4 times the positive high voltage. This would result in an increase in specific impulse from 5000 to 10,000 seconds. Since the number of apertures would remain constant and the perveance per aperture (current per aperture divided by the three-halves power of the source potential) would not be changed, the beam current would be increased by the three-halves power of the scaling factor from 300 mA for the DF engine to 2.4 amperes for the scaled engine. This would result in an increase in thrust from 5 mlb to 80 mlb. The power-to-thrust ratio, assuming no net change in engine efficiency, would increase with specific impulse from 150 kw/lb to 250 kw/lb and the total power would increase from 0.75 kw to 20 kw. Maintenance of the high source efficiency of the DF engine would not be guaranteed, however, because the ion beam current density would be

TABLE XXII  
SCALING OF DF ENGINES

Scaling		3 Dimen- sional	2 Dimen- sional	Design
Scale Factor	x1	x4	x4	x4
Positive High Voltage, V+ (kv)	2	8	2	2
Specific Impulse, $I_{sp}$ (sec)	5,000	10,000	5,000	5,000
Beam Current, $I_B$ (amp)	0.3	2.4	4.8	6.0
Thrust, T (mlb)	5	80	80	100
Power-to-Thrust Ratio, P/T (kw/lb)	150	250	150	150
Power, P (kw)	0.75	20	12	15
Beam Current Density, $j_B$ (mA/cm <sup>2</sup> )	2.5	1.25	2.5	3.1
Thruster Weight, W (lb)	3.5	224	56	50
Thruster Specific Weight, W/P (lb/kw)	4.7	11.2	4.7	3.3

reduced by a factor of 2. The DF engine operated at 5000 seconds is already below its optimum current density of approximately 3.5 mA/cm<sup>2</sup> over the electrode area. Therefore, while a savings in engine weight in terms of weight per kilowatt of beam power would be made, it would be at the expense of source efficiency and high power-to-thrust ratios caused by the high specific impulse.

#### Two-Dimensional Scaling

To maintain the specific impulse at 5000 seconds and the ion beam current density at even the low level of 2.5 mA/cm<sup>2</sup>, the electrode gap and aperture diameters would have to be held constant. The third column in Table XXII shows the result of a two-dimensional scaling of the DF engine. Since the number of apertures would now be increased by the square of the scaling factor, a proportionate increase in beam current would be obtained. This engine would produce 80 mlb of thrust at a total power of 12 kw. The specific weight (pounds per kilowatt) of the engine would be the same as that of the DF engine.

Difficulties would be encountered in maintaining the shape of the plasma density distribution if the length of the chamber were held constant as the diameter increased. This suggests the use of multiple feed points and/or multiple autocathodes in the scaled engine, or an increase in the chamber length if the single autocathode were used. This would increase the specific weight of the scaled engine slightly.

A second problem created by a two-dimensionally-scaled engine design is that of maintaining the electrode gap within limits which afford stable operation. As suggested by Reader (Ref. 7) an upper limit exists for the ratio of electrode diameter to electrode gap for flat electrode systems. A number of solutions may be suggested for this problem.

1. The electrodes could be bowed to take the shape of portions of concentric spheres so that the thermomechanical distortion would be reduced over that of a flat plate. This would produce a slight beam divergence and would probably tend to restrict the operating range of the engine.
2. The electrodes could be reinforced using a rib structure. This, however, would reduce the electrode area available for beam current extraction.
3. A third, and more promising solution, would be the addition of electrode gap spacers distributed across the area of the electrodes. If such an insulating spacer system could be used, the gap could be kept small for even very-large-diameter electrodes.

#### Optimum Scaling

To operate the cesium discharge at slightly higher densities and efficiencies, a scaling as shown by the last column of Table XXII would be used. The electrode gap could be reduced slightly with respect to the gap of the DF engine and the aperture diameters decreased. This would yield a 5000-second specific impulse engine which

would produce 100 mlb of thrust at a total engine power of 15 kw. Assuming that the thicknesses of the electrodes and the cathode plate were not changed, the engine would be scaled with no net increase in the weight-to-thrust ratio. As the engine is scaled, it would be unnecessary to increase the shell thickness above that used on the DF engine. The DF shell thickness would provide adequate structural strength for the scaled engine, and holding the thickness constant would result in further specific weight reductions. As shown in paragraph 4.4, the magnet weight for this engine should scale in direct proportion to the engine electrode area.

#### 4.2.2 Supporting Tests

A twenty-centimeter Kaufman mercury bombardment engine provided by the NASA Lewis Research Center was modified for use with cesium. The mercury diffusor plates and the cathode were removed and the supporting holes sealed. The steel anode was replaced with a copper anode to conduct the higher current anticipated with cesium. A DE engine cathode and orifice plate were mounted to the chamber on the axis. The magnetic field was measured. Figure 105 shows a comparison of the fields of the twenty-centimeter engine and the DF engine. The field configuration was considered to be adequate so no modifications were made to the magnet windings.

The electrodes supplied with the engine were tested first. The electrode support system was changed to resemble that used on the DE engine and the electrode gap was set at 0.080 inch. This small gap was chosen since a distortion in the electrodes existed which would cause the electrode gap to increase as the electrodes distorted during engine operation. The engine was tested using a 750-hour zero-g feed system identical to that used with the DE and DF engines.

#### Results

Startup was smooth and operation was stable. The feed system was adequate at the thrust level run and appeared to be adequate for much higher levels.

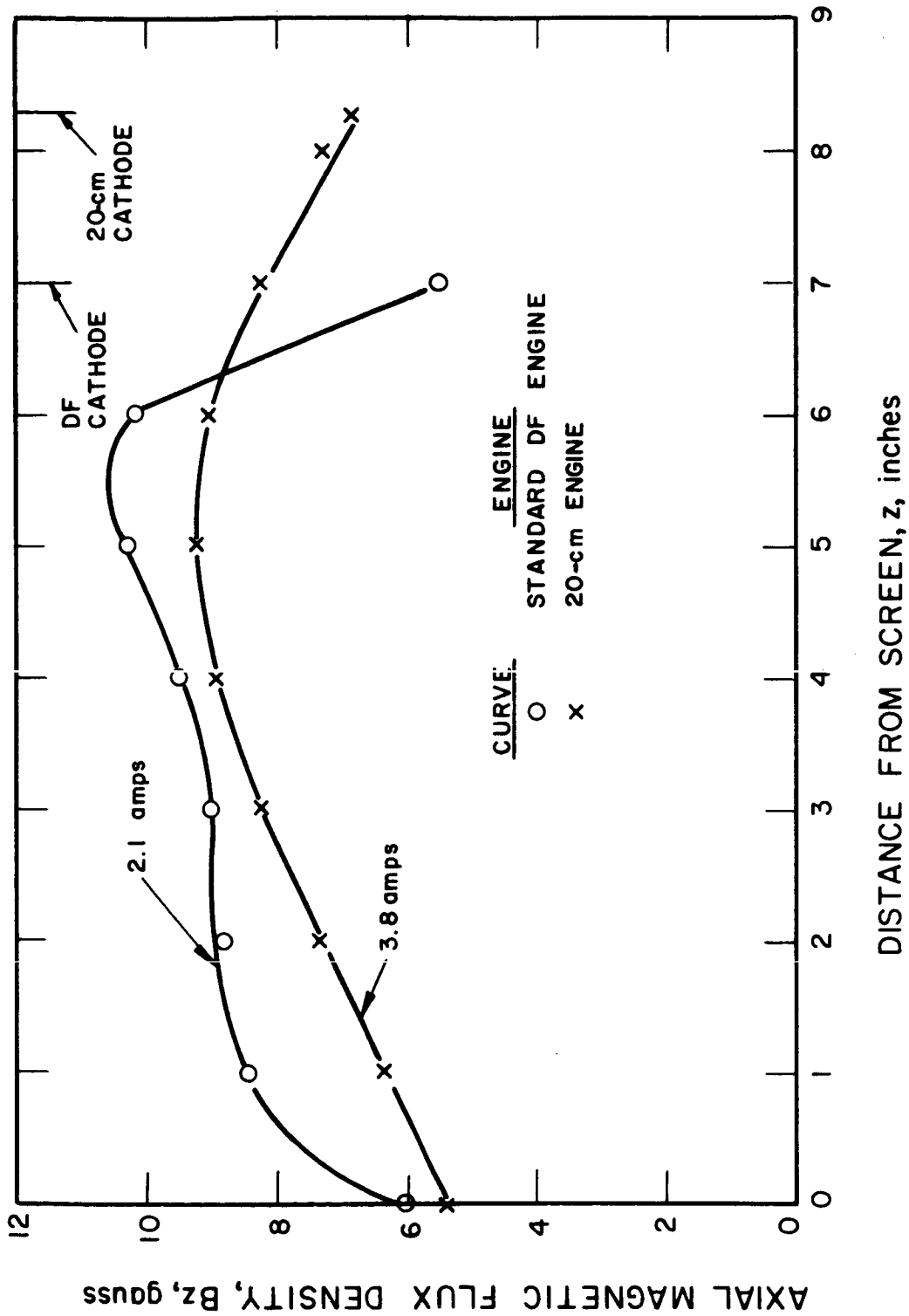


FIG. 105 AXIAL MAGNETIC FIELD COMPONENTS OF DF AND 20-cm ENGINE



Performance at the specific impulses near 8000 seconds was comparable to that of the DE source but fell below as specific impulse was lowered; the large apertures and thick screen electrode supplied with the 20-cm engine were more suited to higher electrode voltages.

Inspection of the accelerator electrode after the run revealed that most of the charge exchange ions were striking near the center of the electrode, indicating a very peaked plasma distribution. This, together with the electrode design, prevented large current extraction. The maximum current obtainable at 3.5 kv (~6200 sec) was 700 mA.

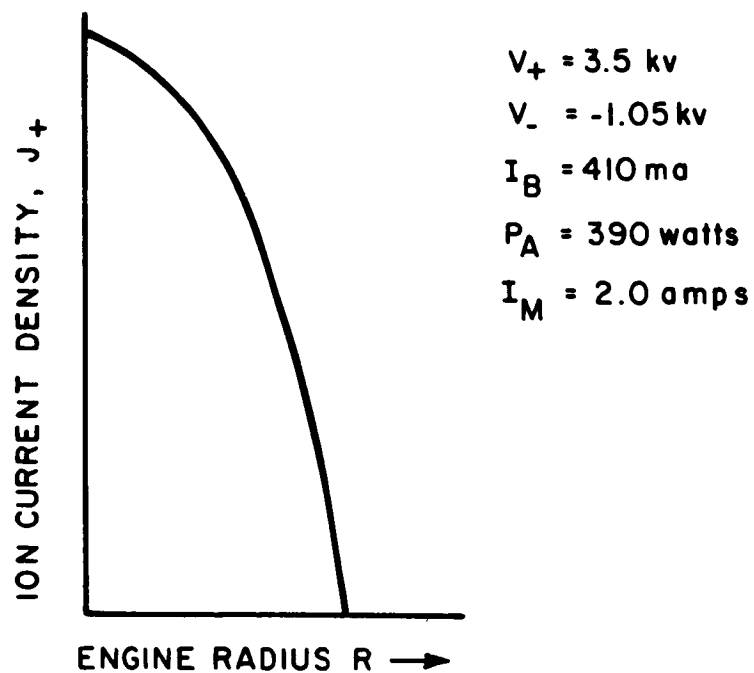
#### Ion Efflux Distributions From 20-cm Engine

The engine was further tested and ion efflux distributions were obtained. The beam profile was quite peaked as shown in Fig. 106a. A 3-inch diameter baffle was then placed about 2-1/2 inches in front of the cathode orifice and beam profile measurements were repeated. Results are shown in Fig. 106b. The baffle clearly improved the distribution but at the expense of considerably higher arc power.

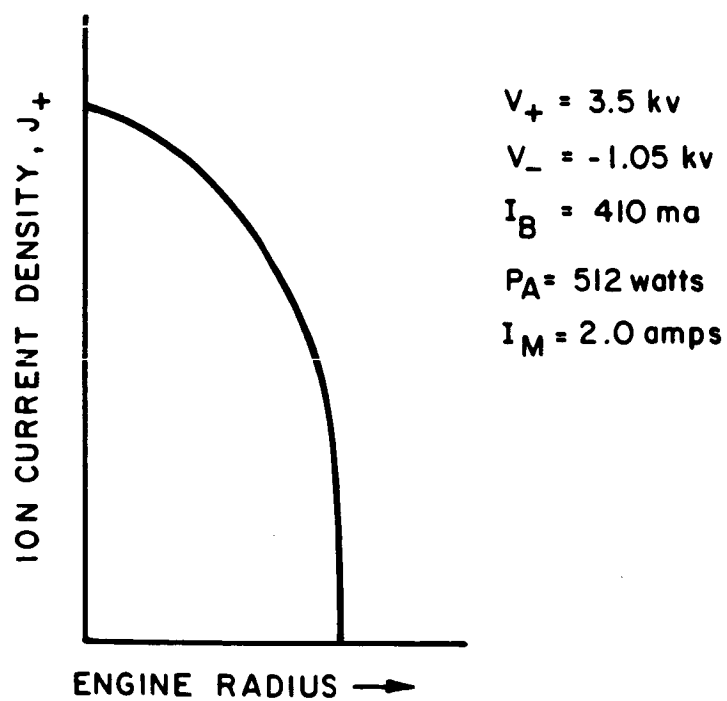
It was concluded that with the single axial cathode, the neutral cesium flow distribution into the arc chamber was not favorable for this short chamber. Without the baffle, performance was a few percent more efficient than that of the DE engine, presumably due to the divergent magnetic field. With the baffle, performance was about the same as that of the DE engine. Changes in the cesium flow distribution as well as improved electrode geometry appeared necessary to approach DF engine performance.

#### Electrode Design

For a scaled-up cesium electron-bombardment ion engine the overall size of the electrode system will depend on the design thrust level and specific impulse. The ion density as a function of the normalized radius  $r/a$  ( $a$  = anode radius) should not change significantly. A satisfactory match between electrode perveance per unit area and ion density may then be obtained by increasing the number



a. 20-cm ENGINE WITHOUT BAFFLE



b. 20-cm ENGINE WITH BAFFLE

FIG. 106 ION CURRENT DISTRIBUTIONS FOR 20-cm ENGINE

of apertures while retaining the aperture diameters and spacings of the DF electrodes. The same relative areas of the electrodes would be occupied by each of the three basic aperture geometries.

To better evaluate electrode scaling, a set of distributed geometry electrodes was made for the 20-cm source. These electrodes are shown in Fig. 107. The uniform geometry electrodes are also shown for comparison.

Performance with this set of electrodes was comparable to that obtained with the uniform geometry electrodes but, as expected, higher beam levels were obtained. It was difficult to maintain high performance levels for any appreciable length of time because thermal expansion caused the electrodes to bow toward each other, resulting in high-voltage breakdown. This difficulty, a consequence of the large diameter of the electrodes, was expected. To solve the problem of maintaining a close gap with large-area electrodes, an electrode gap spacer was designed.

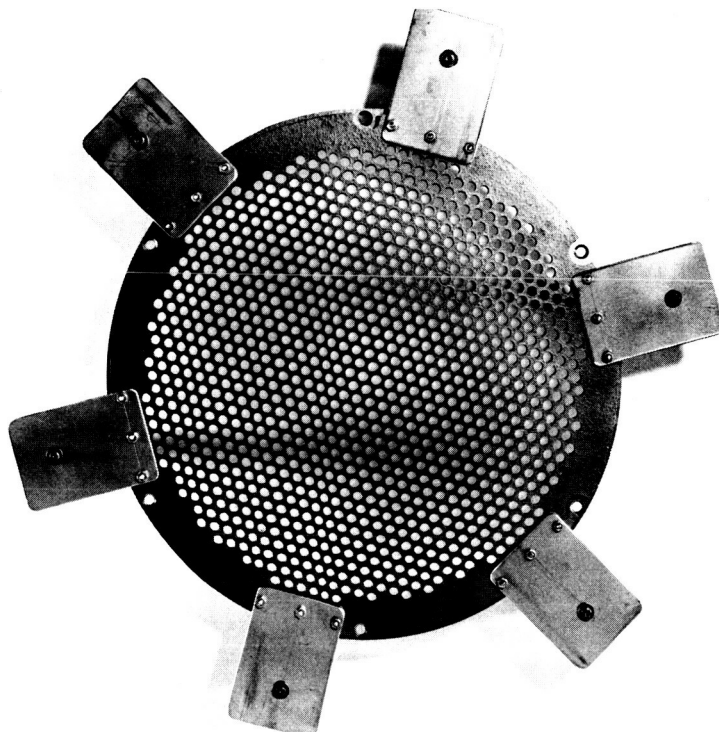
#### Electrode Gap Spacer

The electrode gap spacer consisted of a Supramica insulator protected from cesium contamination by two nesting stainless steel shields. A schematic of this insulator is shown in Fig. 108. The spacer was installed in the center of a set of DF electrodes and the electrode gap set at 0.050 inch. The electrodes were tested on a standard DF engine. Engine performance was identical to that obtained with an electrode system without the electrode gap spacer. The engine was operated for 7 hours with no residual accelerator electrode drain increase.

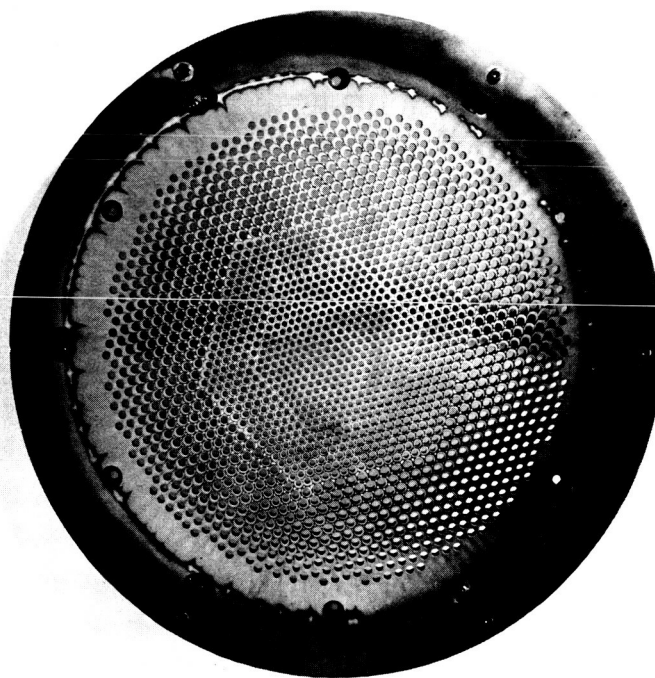
It was concluded that electron bombardment ion engine electrodes may be increased in diameter without difficulty if they are provided with such properly shielded interelectrode spacers.

#### 4.2.3 Conceptual Design

Fig. 109 shows the conceptual design. The chamber length has been increased over that of the DF engine but a length-to-



a. UNIFORM GEOMETRY ELECTRODES



b. DISTRIBUTED GEOMETRY ELECTRODE

FIG. 107 20-CM SOURCE ELECTRODE SYSTEMS

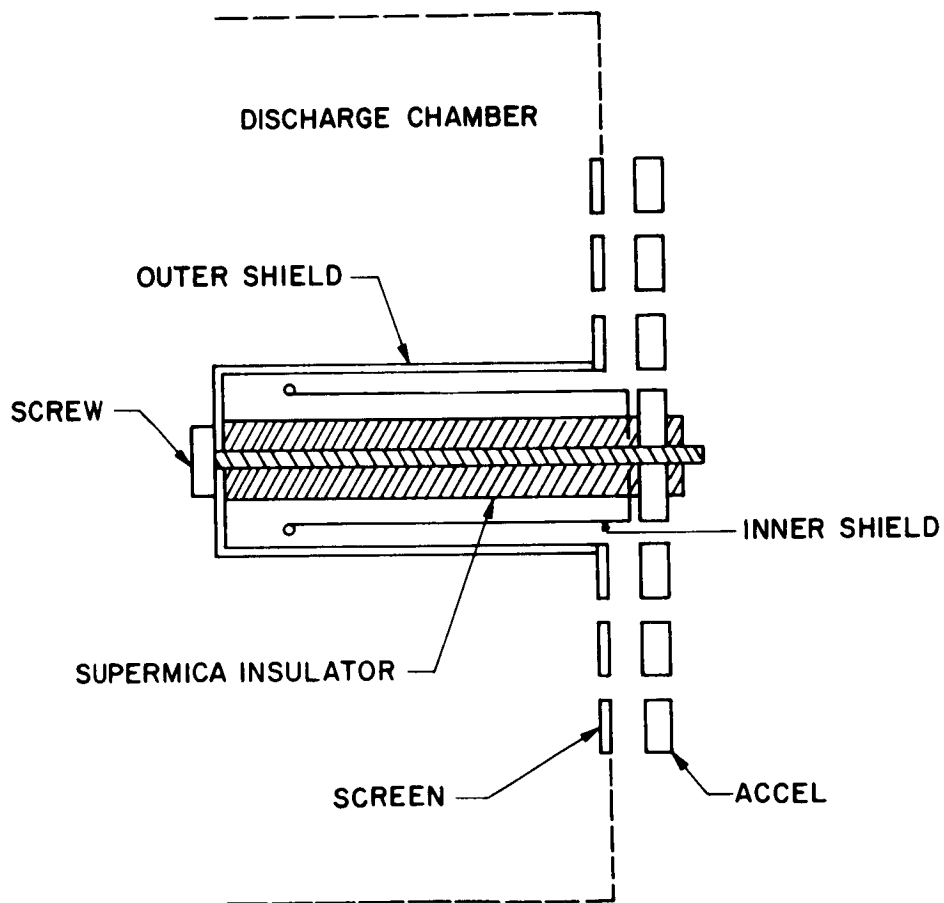


FIG. 108 SCHEMATIC OF INTERELECTRODE GAP SPACER

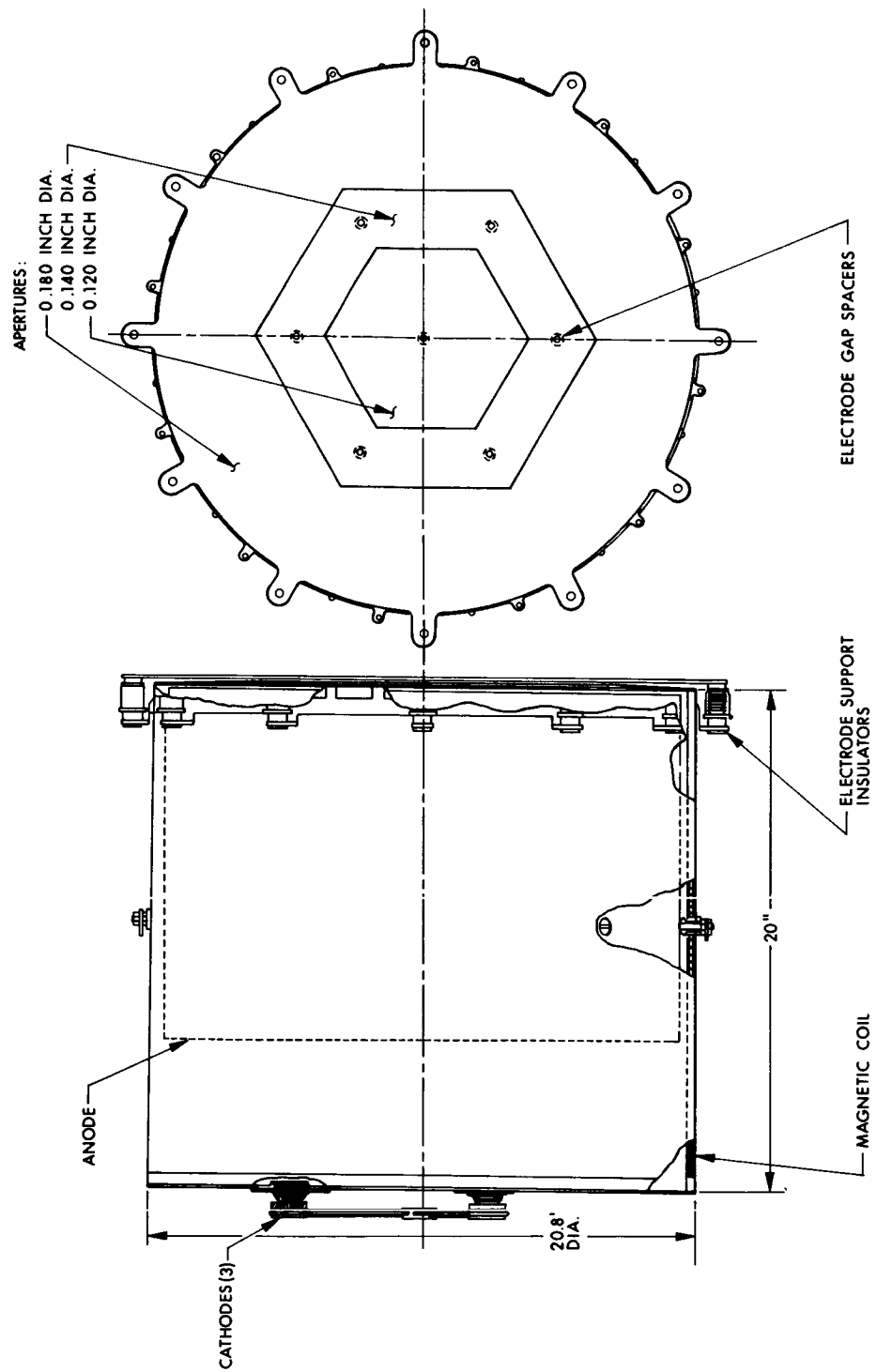


FIG. 109 30 KW ION ENGINE

diameter ratio of 1 has been used rather than 1.4 for the DF engine. Multiple autocathodes are used to provide a more uniform plasma density distribution. Interelectrode gap spacers would be employed at seven points as shown.

Stability of the multiple autocathodes would have to be investigated. For this design, a parallel feed tube impedance has been employed to help maintain flow stability between the three cathodes. Results of operation of two cathodes in the inverted engine. (Paragraph 4.1 of this report) suggest that the multiple cathodes could indeed be made stable. Component weights for this design are shown in Table XXIII. The total thruster weight is approximately 50 pounds. Table XXIV shows projected performance at both 5000 and 7000 seconds for the large engine and at 5000 seconds for the DF engine.

The use of such a scaled-up engine would provide a lower thruster specific weight and simplify the propulsion system for large-thrust missions. It must be pointed out, however, that this thruster design is conceptual in nature and can only be proved through a research, development, and testing program.

TABLE XXIII  
COMPONENT WEIGHTS FOR CONCEPTUAL  
DESIGN 100 mlb ENGINE

<u>Component</u>	<u>Weight, lbs.</u>
Engine Shell	14.0
Magnet	4.4
Anode	15.5
Cathode Plate	5.7
Screen Electrode	2.5
Accelerator	2.5
Cathodes (3)	1.3
Shields, Insulators, etc.	4.2
Total Engine Weight	50.1

TABLE XXIV  
PROJECTED PERFORMANCE

	<u>DF</u>	<u>Large Engine</u>	
	5000	5000	7000
Specific Impulse $I_{sp}$ (seconds)			
Positive High Voltage, $V_+$ (kv)	2.0	2.0	3.8
Beam Current $I_B$ (amp)	0.3	6.0	8.0
Thrust T (mlb)	5.0	100	185
Beam Power $P_B$ (kw)	0.600	12.00	30.40
Arc Power $P_A$ (kw)	0.110	2.30	3.00
Drain Power $P_D$ (kw)	0.017	0.26	0.43
Magnet Power $P_M$ (kw)	0.010	0.16	0.16
Total Power $P_T$ (kw)	0.737	14.72	34.09
Power-to-Thrust Ratio P/T (kw/lb)	147.4	147.2	184.2



#### 4.3 Autocathode Studies

The autocathode of the DE engine required 90 watts for about 20 minutes to preheat to operating temperature. Objectives of this portion of the program were to reduce the starting power requirement, eliminate the need for the separate cathode preheat power supply, simplify the cathode design, and to improve, if possible, the cathode performance.

The cesium autocathode, shown in Fig. 110, consists of a cathode chamber enclosing a heated tantalum emitter through which the cesium is passed to the discharge chamber. An orifice between the cathode and discharge chambers increases the cesium pressure and plasma densities in the cathode. The hot cesiated tantalum emitter is capable of electron emission current densities of 1 to 10 amp/cm<sup>2</sup>. Ion bombardment delivers sufficient energy to the emitter to maintain the required operating temperature. After initiation of the discharge, the cathode heater is turned off and autocathode operation commences. Bombarding ion energies (7 to 9 volt cathode drop) are below sputtering thresholds so only negligible sputtering damage occurs.

##### 4.3.1 Autocathode Starting Characteristics

To determine the minimum cathode temperature to initiate a discharge, an external heater was added to a DE cathode housing. With the heat source on the outside of the cathode, the internal temperature could be approximated by the housing wall temperature. Initial operation indicated that the arc could be started by maintaining the housing at a temperature high enough to prevent cesium condensation. It appears that under these conditions enough cesium is delivered into the discharge chamber to initiate a glow discharge, which develops into the full arc mode with autocathode operation.

Figure 111 shows a temperature time profile for a cold cathode startup. The internal cathode heater was not used. A power of 90 watts was applied through the external heater on the

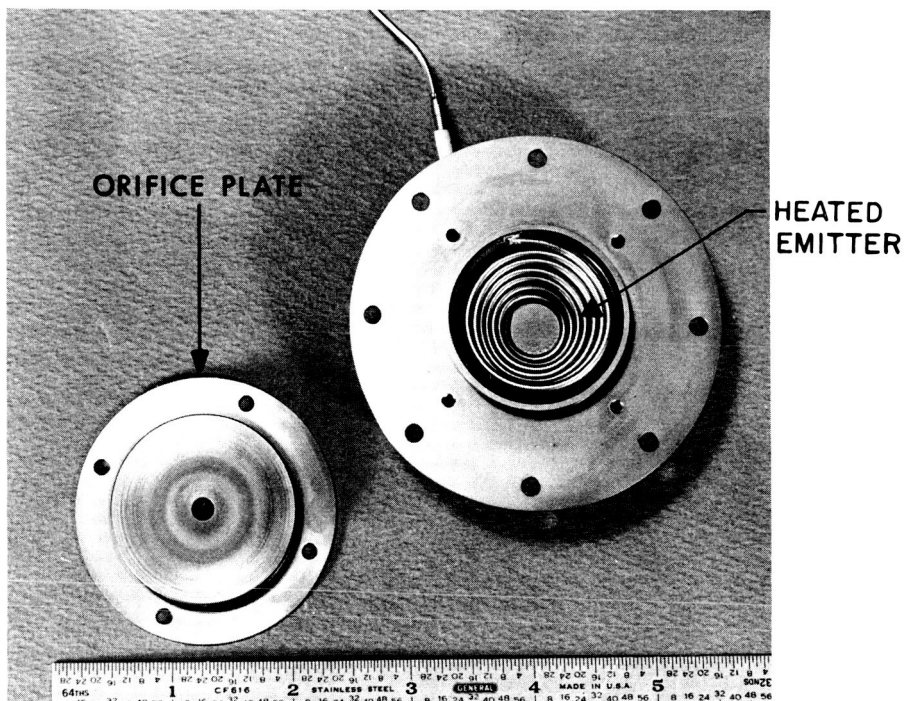


FIG. 110 INTERNALLY-HEATED DE CATHODE WITH  
ORIFICE PLATE REMOVED

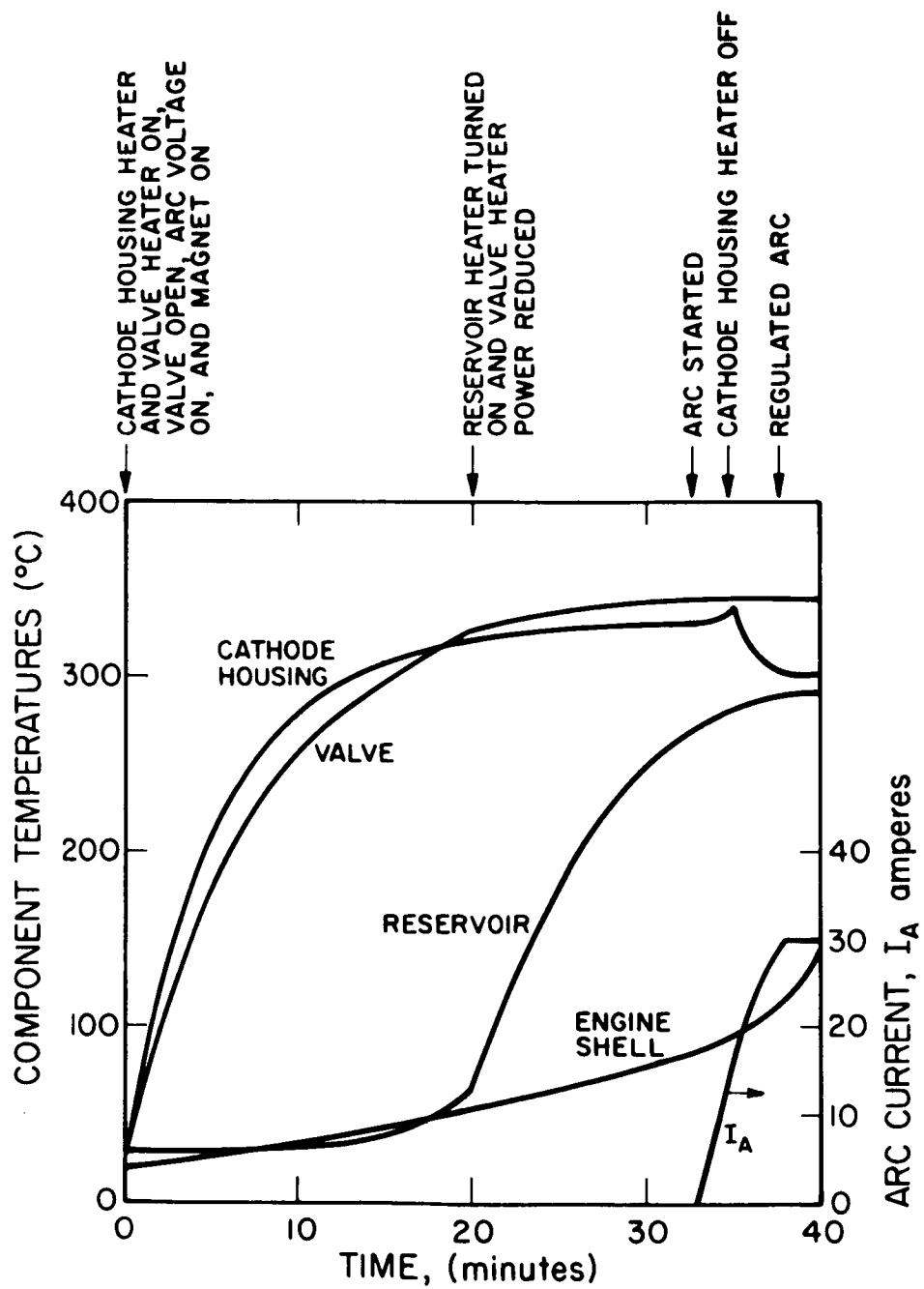


FIG. 111 COLD CATHODE START-UP PROFILE

cathode housing until the arc was initiated. All cathode tests were made with a laboratory reservoir which has higher temperature and power requirements and longer response times than the "zero-gravity" type feed system.

For the first 20 minutes, the valve and cathode housings were brought to operating temperatures. No power was fed to the reservoir but some increase in reservoir temperature was observed due to heat conduction from the valve. At the end of the first heating phase the reservoir power was turned on, and after about 9 minutes traces of cesium flow from the engine were observed with the neutral cesium detector in the vacuum tank. Three minutes later the arc started and the reservoir power was regulated to maintain an arc current of 30 amperes. During the first two minutes of arc operation, the external heater was left on. When the arc current reached 20 amperes, the heater was turned off and the cathode housing cooled to 300°C.

The thermocouple used to measure the cathode housing temperature was moved to obtain more accurate temperature readings and the test was repeated. The minimum temperature for reliable starting was found to be 340 to 350°C.

Using the internal heater, it was possible to start consistently with a power of 25 watts for the normal orifice. During these starts, the housing reached a temperature of 240°C. The cathode emitter obviously attained higher temperatures.

Initiation of the discharge is enhanced by increasing the orifice diameter. This, however, reduces source efficiency because higher flow rates must be used to maintain adequate cesium coverage.

#### 4.3.2 Operating Characteristics

The effects of orifice diameter, emitter structure, and magnetic field were investigated and the emitter temperature was measured in an operating engine.

### Orifice Diameter

To investigate the effect of the cathode orifice, a series of orifice plates with varying aperture diameters was prepared. Three of these orifices were operated in a DE engine with the following results.

The first or control orifice had the standard 0.189-inch diameter. The data on source efficiency obtained with this orifice are shown by the circled points in Fig. 112. These data are within 1 percent of those found previously with the DE engines.

The second orifice tested had a diameter of 0.128 inch. Source efficiency was about 2 to 3 percent below that of the control as indicated by the triangles in Fig. 112. This restricted cathode orifice made the arc more difficult to start. The cathode temperature had to be slightly raised to initiate the discharge. The arc impedance was increased slightly and the orifice plate operated hot enough to cause an apparent recrystallization of the titanium around the orifice.

The third orifice tested had a diameter of 0.284 inch. This also reduced source efficiency by 2 to 3 percent. Starting characteristics were enhanced slightly (smoother turn-on) and the orifice ran cooler than the control orifice as evidenced by an accumulation of copper backsputtered from the vacuum system around the orifice. This orifice also appeared to reduce the arc impedance as compared with the control. Arc instabilities were found whenever arc voltages above 9 volts were used during the engine heating phase of the turn-on sequence.

### Emitter Structure Tests

A new cathode was designed for the DE engine which used only an external heater (Fig. 113). The cathode was supported by the orifice plate to reduce conductive cooling to the engine body. External surface area and thermal mass were reduced but the volume and emitter area approximated those of the DE cathode. The emitter was formed from tantalum and was replaceable.

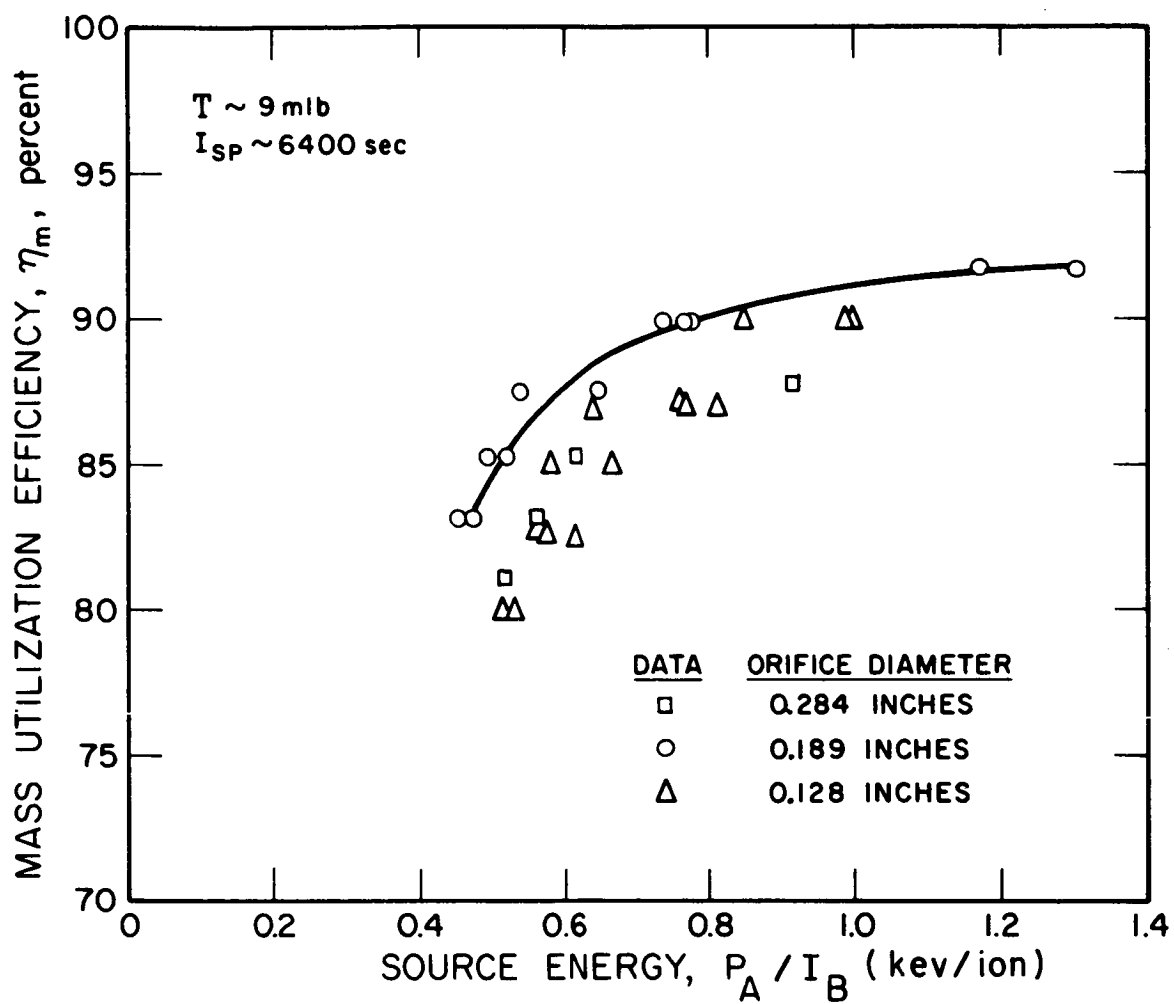


FIG. 112 EFFECT OF ORIFICE DIAMETER ON SOURCE EFFICIENCY

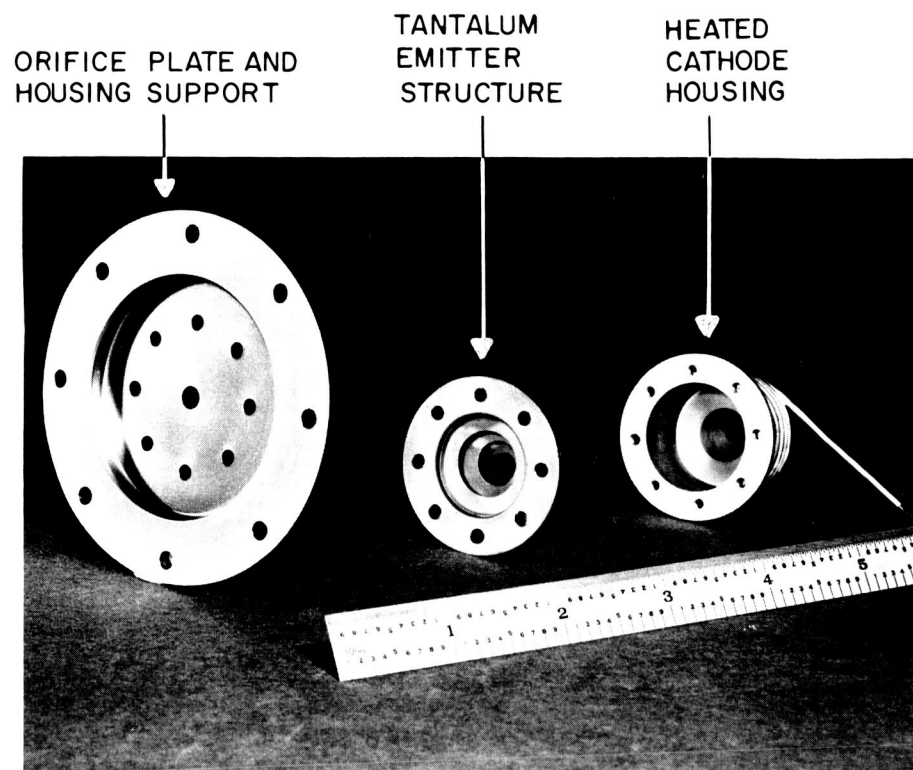


FIG. 113 EXTERNALLY HEATED CATHODE

The arc was extremely difficult to start with this cathode. Once in operation, however, engine performance appeared normal. The emitter was mounted between the cathode housing and the orifice plate. During preheating, the orifice plate acted as a heat sink, causing the emitter to operate at a lower temperature than the housing. To increase emitter temperature during preheating, a corrugated tantalum cylinder was inserted between the emitter and the housing. Subsequent starts with 52 watts of heater power and a housing temperature of  $410^{\circ}\text{C}$  were successful. The housing ran hotter during autocathode operation, however, and the source efficiency was reduced.

A series of emitter structures, supported only by the housing walls, was then fabricated. These emitters were helixes of tantalum strip fastened to the housing at both ends. The cross section and number of turns were varied to obtain different thermal and electrical impedances from the emitter to the housing. Four of these emitters were tested in a DE engine. The main difference in operating parameters which could be observed was in overall source efficiency as shown by the data in Table XXV. As indicated, the second and third emitters were superior. These two cathodes also started more smoothly.

The externally heated autocathode with the four-turn, 0.010-inch thick emitter was tested further. Operating data appear in Table XXVI. The arc started smoothly with 50 watts of preheat power and operation at the levels shown was very stable. The operation at high beam levels was similar to that with the DE cathode but mass efficiency at lower levels was reduced.

A tantalum wire emitter was then tested. This cathode operated with higher mass efficiency at low (200 to 400 mA) beam levels than was obtained with previous emitters. Starting characteristics were not noticeably changed.



TABLE XXV  
SOURCE EFFICIENCY WITH  
EXTERNAL HEATER CATHODES

<u>Emitter Number</u>	<u>1</u>	<u>2</u>	<u>3</u>	<u>4</u>
Thickness (inches)	0.010	0.010	0.010	0.005
Width (inches)	0.5	0.25	0.125	0.125
Number of turns	1	2	4	4
Flow rate (amp)	0.452	0.425	0.435	0.430
Mass Efficiency	81.5	89	87.4	84.5
Source Energy per Beam Ion (kev/ion)	0.658	0.675	0.624	0.989

#### Effect of Magnetic Field

To determine the extent that cathode operation was affected by magnetic field changes, a coil was placed around the cathode of a DE engine. The engine was then tested with various coil currents. No significant changes in cathode operation or arc characteristics were observed. The source efficiency was typical of the DE engine configuration.

#### Emitter Temperature

A DE cathode was modified to allow measurement of the emitter temperature. The original emitter was replaced with a tubular tantalum coil. Thermocouples were placed inside the emitter near the center and at one end. A heater was attached to the outside of the cathode housing for starting purposes. This cathode was then operated with a DE engine with the following results.

The temperature near the center was about 10°C below that of the support end during preheat. As expected, a slight lag in response to external power was also noted at the center.

While operating a 15-volt, 30-ampere arc, the temperature was approximately 980°K at the center and 920°K near the end. (The end cools by conduction to the housing.)

TABLE XXVI  
ENGINE PERFORMANCE WITH EXTERNAL HEATER AUTOCATHODE  
(Four-Turn 0.010-inch Thick Emitter)

	<u>1</u>	<u>2</u>	<u>3</u>	<u>4</u>
$V_+$ (kv)	3.5	3.5	5.0	6.0
$V_-$ (kv)	1.0	1.0	0.8	0.9
$I_-$ (amp)	0.005	0.007	0.009	0.016
$I_B$ (amp)	0.385	0.467	0.635	0.750
$V_A$ (volt)	7.8	9.0	7.6	7.4
$I_A$ (amp)	39.0	56.0	55.0	59.0
$P_R$ (kw)	1.349	1.633	3.175	4.500
$P_D$ (kw)	0.020	0.032	0.055	0.114
$P_M$ (kw)	0.007	0.008	0.010	0.011
$P_A$ (kw)	0.304	0.504	0.418	0.437
$P_T$ (kw)	1.680	2.177	3.658	5.062
$T$ (mlb)	8.56	10.4	16.9	21.9
$P/T$ (kw/lb)	196.0	209.0	216.0	231.0
$\eta_p$ (%)	80.3	75.1	86.8	88.9
$\eta_M$ (%)	72.4	85.0	90.0	90.0
$\eta_E$ (%)	58.8	63.8	80.0	80.9
$I_{sp}$ (sec)	5250.0	6160.0	7900.0	8530.0
$I_-/I_B$ (%)	1.2	1.5	1.5	2.2
$P_A/I_B$ (kev/ion)	0.790	1.080	0.658	0.583

During operation at beam levels of 350-400 mA, the temperature of the emitter dropped to 890°K at the center. Estimates of the cesium arrival rate at the emitter surface are from  $10^{20}$  to  $10^{21}$  atoms/cm<sup>2</sup>/sec for which emission currents of 1 to 5 amp/cm<sup>2</sup> can be obtained. This was in agreement with the arc current of 38 amperes which corresponds to 1.5 amp/cm<sup>2</sup>. This demonstrated that the DE cathode operated in the positive slope region of the emission versus temperature curves for cesiated tantalum, as it was designed to do.

#### 4.3.3 Improved Cathode

Based on the above test results, a new cathode was designed, built, and tested. This cathode, shown in cross section in Fig. 114, incorporates the following features:

1. Increased volume for a larger emitter.
2. External heater distributed to offset loss of heat to the cathode plate during warmup.
3. High-impedance heater for operation from the arc power supply.
4. Hemispherical emitter structure of solid tantalum construction.

The emitter shape and size were determined empirically since only rough criteria for design of the internal cathode structure were determined. Figure 115 shows the new cathode.

#### Starting Power Requirements

The heater impedance of 13.4 ohms allowed operation of the heater directly from the arc power supply. About 28 volts were used for starting the arc. At this voltage, 60 watts were dissipated in the heater. This brought the cathode starting temperature to about 350°C. After the arc was established and the arc voltage reduced to the normal 7 to 8 volts, the heater dissipation dropped to less than 5 watts. The heater was disconnected with no change in engine performance.

The cathode was operated in a DE engine and mass efficiency of 92.6 percent obtained at an energy expenditure of

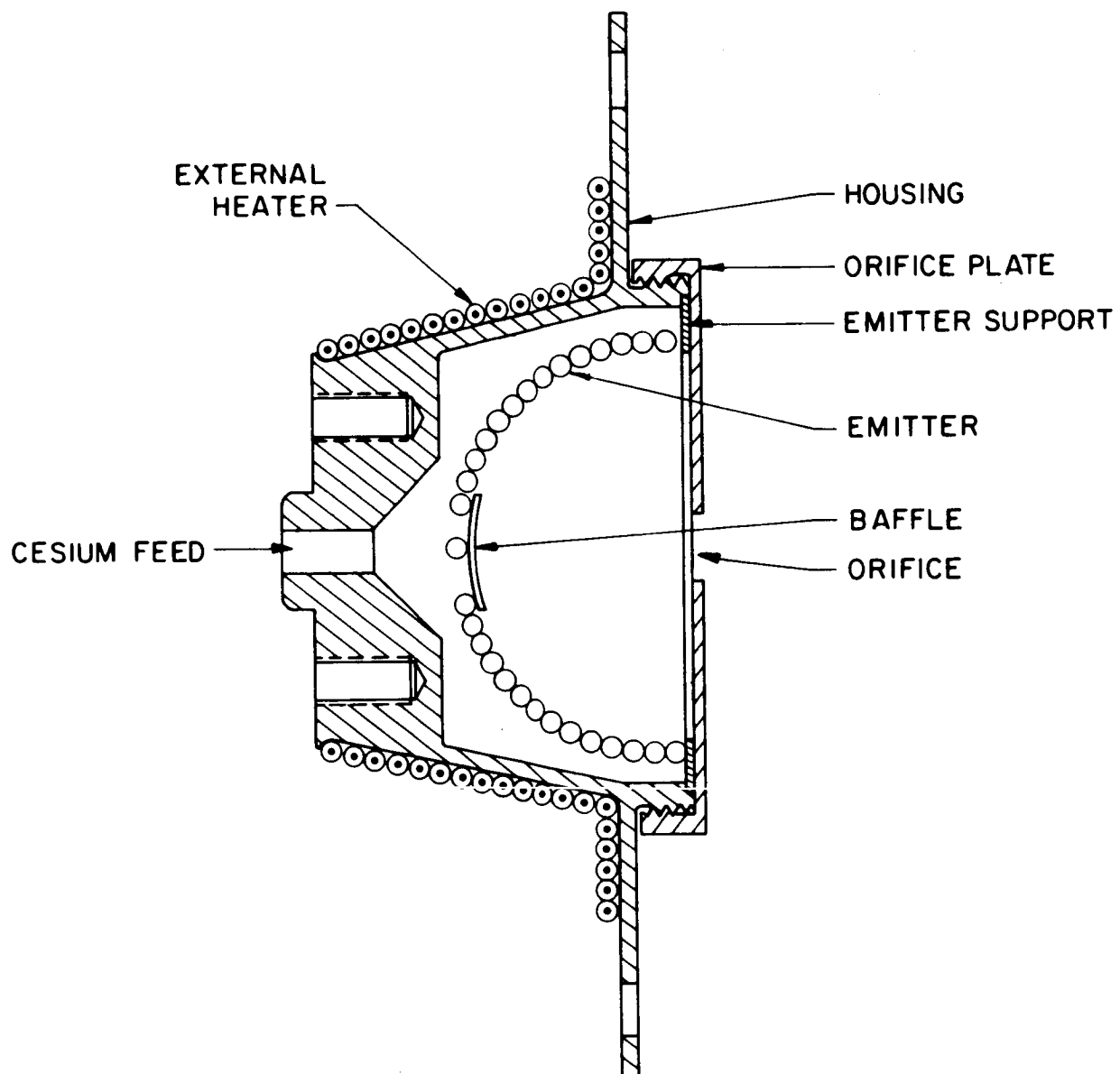


FIG. 114 EXTERNAL HEATER AUTOCATHODE DESIGN

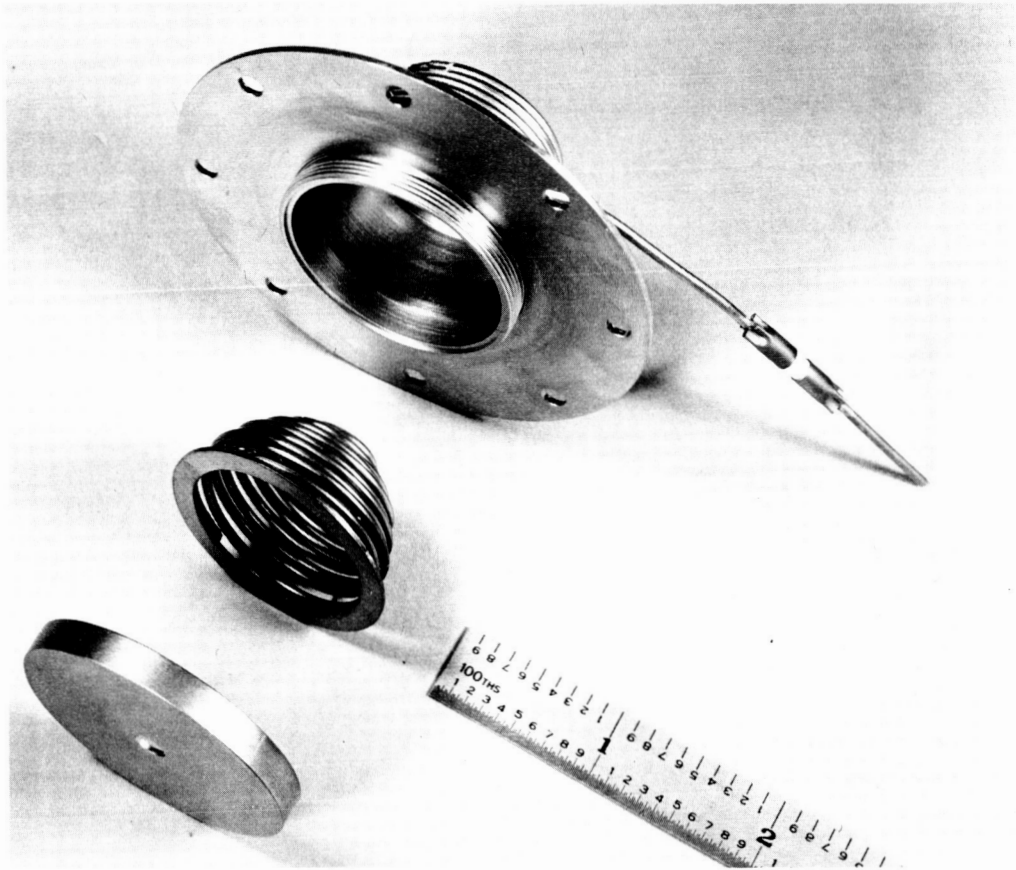


FIG. 115 EXTERNAL HEATER AUTOCATHODE

773 ev/ion in the arc. This was equivalent to the performance obtained with DE cathodes. The cathode was then tested on the PM-1 engine. Operation was successful and the PM-1 engine performance was not altered.

### Conclusions

A simple autocathode was developed which used an external heater for increased reliability. The heater could be operated directly from the arc power supply, thereby eliminating the need for the cathode heater supply. Operation of the cathode was equally as efficient as the DE cathode. This cathode was not used on the long life testing portion of the contract because it was developed too late in the program.

#### 4.4 Permanent Magnet Engines

The permanent magnet studies were undertaken to determine the feasibility of replacing the electromagnet of the DE engine with a permanent magnet circuit. Analysis of the field requirements showed that while the power and weight requirements of the electromagnet for the cesium electron bombardment ion engine were not severe, a savings in weight could be effected over the weight of the DE engine, in addition to the savings of magnet power losses. A permanent magnet modification of a DE engine was designed, fabricated, and tested. The satisfactory results obtained led to the decision to design a complete new engine using a permanent magnet shell. This engine performed with unexpectedly high efficiency. The cause of the increased efficiency was determined to be a divergent magnetic field toward the screen electrode in addition to the use of a new electrode geometry.

The results of these studies, together with the improved electrode system described in paragraph 4.1, led to development of the DF engine.

#### 4.4.1 Magnetic Field Requirements

The magnetic field requirements were developed in terms of the effect of the field on engine performance, weight and power requirements for an electromagnet, and weight requirements for a permanent magnet system.

##### Magnetic Field Functions and Configuration

Optimization of engine operation has always occurred when the magnetic field was two to three times that required to prevent primary electrons from reaching the anode of the engine. In the 6.5, 10, and 12.5 cm sources the product of anode radius and optimum magnetic field strength has remained constant at about 55 gauss-cm. This is in agreement with developed theory which maintains that the field must be strong enough to allow primary electrons to thermalize with the Maxwellian distribution before reaching the anode and to restrain the electrons in the high-energy tail of the distribution. Thermalization occurs rapidly in the cesium discharge in comparison with the time required before an ionizing collision. This may be compared to sources operated on mercury which require fields about five times as great when the primary electron energies are five times those of a cesium engine of the same size. The fields required to constrain these electrons should only be  $\sqrt{5}$  times those of the cesium engines. The difference between the operation of the two sources is that the mercury atoms are ionized by primary electrons and the cesium atoms are ionized by the electrons in the high-energy tail of the Maxwellian distribution.

Experiments conducted under contract NAS3-2516 suggested that the field of the cesium bombardment engine was not critical in configuration, i.e., that divergence or convergence toward the screen electrode did not improve performance. A uniform or solenoidal field configuration was considered the goal of this portion of the program.

##### Power and Weight Requirements

Analysis of the power and weight requirements of electromagnets for the cesium bombardment engine was based on the

assumption of equivalence of the magnet to a single-turn coil of anode diameter and of negligible length.

For a single-turn coil, the field at the center is given by

$$B_o = I/r$$

where I is the loop current and r is the loop radius. The power is given by

$$P_M = I^2 R$$

where R is the loop resistance which is given by

$$R = 2\pi r / \gamma A$$

where A is the cross-sectional area of the loop and  $\gamma$  is the conductivity of the loop material. The power dissipated may then be expressed as

$$P_M = r^2 B_o^2 2\pi r / \gamma A$$

The weight of the loop may be expressed as

$$W = 2\pi r A \rho$$

where  $\rho$  is the density of the loop material. Taking the product of power and weight eliminates A. Thus,

$$PW_M = 4\pi^2 r^4 B_o^2 \rho / \gamma$$

Since it has been found that the field required is proportional to the reciprocal of anode radius it may be stated that



for a given type of engine, the power-weight product is proportional to the source area and the square of the field strength. Inasmuch as the thrust level should follow engine area, the penalty paid for the magnetic field should be independent of thruster size, in terms of power-to-thrust and weight-to-thrust ratios, and dependent only on the type of propellant used. In practice, a slight savings has been found with larger sources since the coil radius is not anode radius but rather anode radius plus some constant.

#### Permanent Magnet System Configurations

Several possible configurations for a permanent magnet system which would provide the required field are shown in Fig. 116. The first system shown has the advantage of simplicity. For most feasible ion engines, however, this system does not take advantage of the maximum energy product of available materials in that the field is determined by the maximum flux density alone and the full coercive force of the magnetic material is not utilized. It is also not a minimum weight system. The second configuration utilizes the maximum energy product available in the magnetic material. This is offset by the additional weight required for the magnet extensions which must have about as high a cross section as the magnets, and by the additional leakage which is incurred by shortening the magnets.

The third scheme, shown in Fig. 116c, has an advantage over discrete magnet systems in that the area of the screen electrode and cathode plate need not be larger than the discharge chamber to prevent severe leakage and consequent field distortion.

#### Permanent Magnet Weight

Assuming a configuration is shown in Fig. 116c, the quantity of magnetic material required would be:

$$V_M = \ell A_m = \ell B_A K/B_R$$

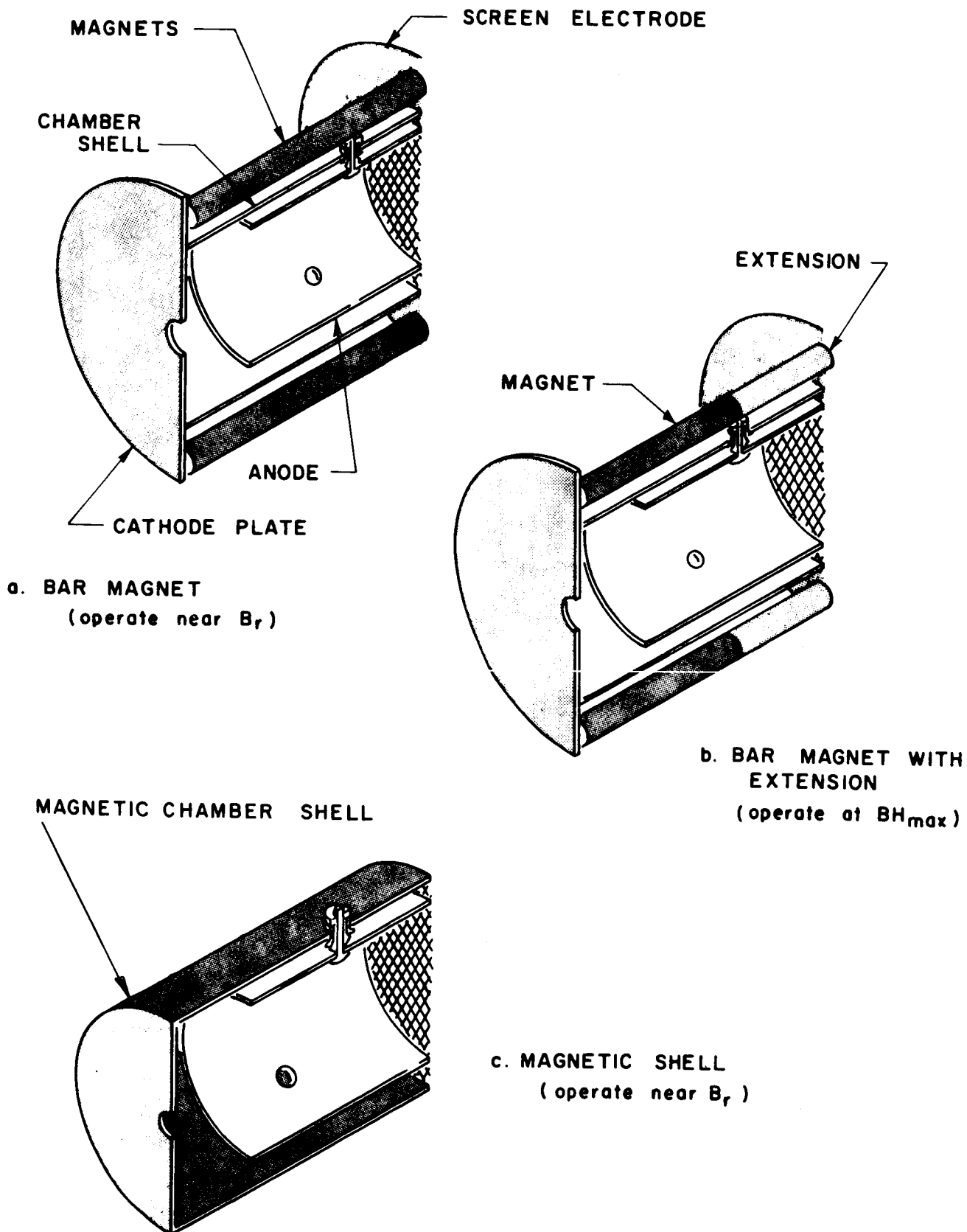


FIG. 116 PERMANENT MAGNET ENGINE CONFIGURATIONS

where  $v_M$  is the volume of the magnetic material,  $l$  is the length of the magnetic cylinder,  $B$  is the field strength in the engine in gauss,  $A_g$  is the area of the engine,  $K$  is a form factor (approximately 4 for the cesium engine), and  $B_R$  is the maximum residual flux density of the permanent magnet material. For a material such as Vicalloy ( $0.3 \text{ lb/in}^3$ ,  $B_R \approx 12,000$  gauss) the weight of the permanent magnet material required is about 0.15 lb for a DE type engine. This is considerably less than the existing weight of the DE engine shell and electromagnet (1.65 lb).

An analysis similar to that performed on the electromagnet again showed the weight of the required magnetic material to be proportional to the thrust level and square of the basic field strength requirement.

Two subtle areas of difficulty are present in the design of a permanent magnet ion engine.\* First, the junction between the permanent magnets and the end plates of the engine must be made in such a way as to prevent a high reluctance. This may be done by "immersing" the ends of the permanent magnet material in the end plates. Secondly, the web area between apertures on the screen electrode must be sufficiently large to prevent magnetic saturation.

#### 4.4.2 Permanent Magnet Modification of a DE Engine

Modification of a DE engine, to make use of a permanent magnet, first required the mapping of the magnetic field of a DE engine. The plot of axial field strength in gauss/ampere at three radial distances including the axis is shown in Fig. 117a. The radial field was also measured and the data reduced to yield the magnetic field plot of Fig. 117b. As expected, the field was solenoidal and was used as a design reference for the permanent magnet field.

A permanent magnet version of the basic DE engine was then designed and built. No effort was made to minimize either size or weight of the modified engine. Only the electromagnets, screen electrode and cathode plate were modified for the first test. Pure iron was used as the permeable material for the screen and cathode plate.

---

\*P. D. Reader, Personal Communication, 24 March 1964.

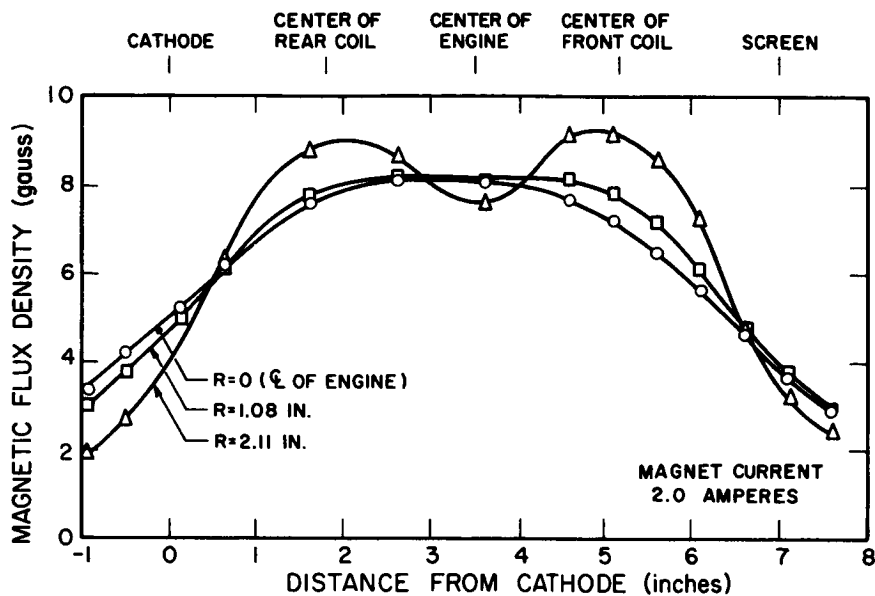


FIG. 117a AXIAL COMPONENT OF MAGNETIC FIELD OF DE ENGINE WITH ELECTROMAGNETS

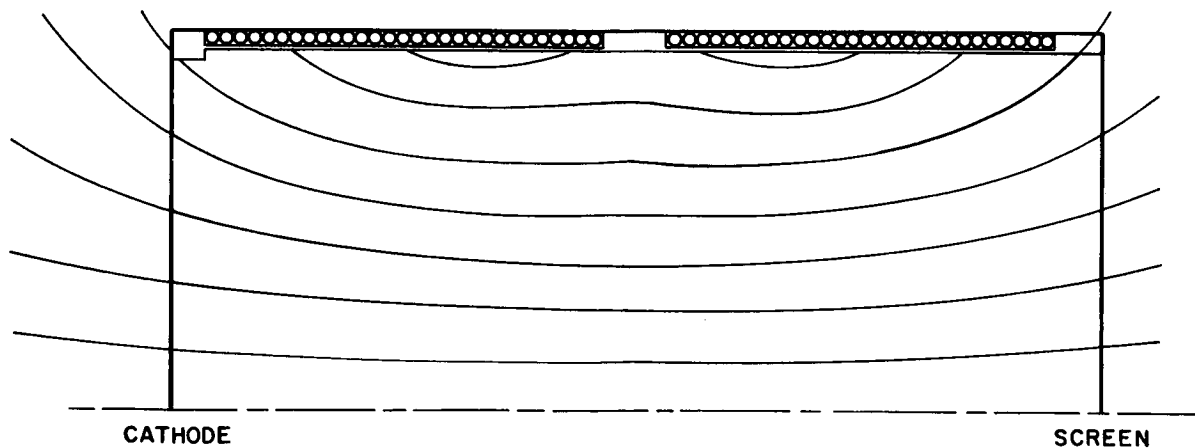


FIG. 117b PLOT OF MAGNETIC FIELD LINES FOR DE ENGINE WITH ELECTROMAGNETS

The modification was designed for operation with a number of rod-shaped Alnico V permanent magnets. This was done to allow adjustment of the total cross section of the permanent magnet material by adding or removing magnets to obtain the desired field strength; the demagnetizing force exerted on the magnets in this configuration was only 10 oersteds at the desired field strength in the engine, which was not enough to reduce the flux in the Alnico magnets appreciably below  $B_R$ . A square cathode plate design was used for mounting convenience and a round screen electrode was designed. Thickness of the cathode plate was maintained far above the required minimum and pole pieces were provided to insure good magnetic coupling between the magnets and end plates.

#### Engine Tests

The field within the modified engine was measured and the number and size of the magnets adjusted to obtain a field similar to that of the DE engine. Data on the axial component of the permanent magnet field are shown in Fig. 118. A clearer understanding of the differences may be obtained from Figs. 117b and 118b. The convergence toward the screen electrode indicated in Figs. 118a and 118b was due to the 15-percent-larger area of the square cathode plate.

The permanent magnet modified DE engine is shown in Fig. 119. The engine, as modified, weighed two pounds more than the electromagnet version. Two thirds of this extra weight was in the cathode plate which was twice as thick as the screen electrode.

This modified engine was operated with the following results:

1. Autocathode operation was satisfactory.
2. Some long period (several seconds) instabilities occurred at beam levels between 300 and 400 milliamperes. Beam fluctuations of 50 milliamperes were observed.
3. The modified screen electrode (Armco magnet iron) bowed toward the accelerating electrode enough to reduce the maximum voltage across the gap to 3.5 kilovolts during early operation.

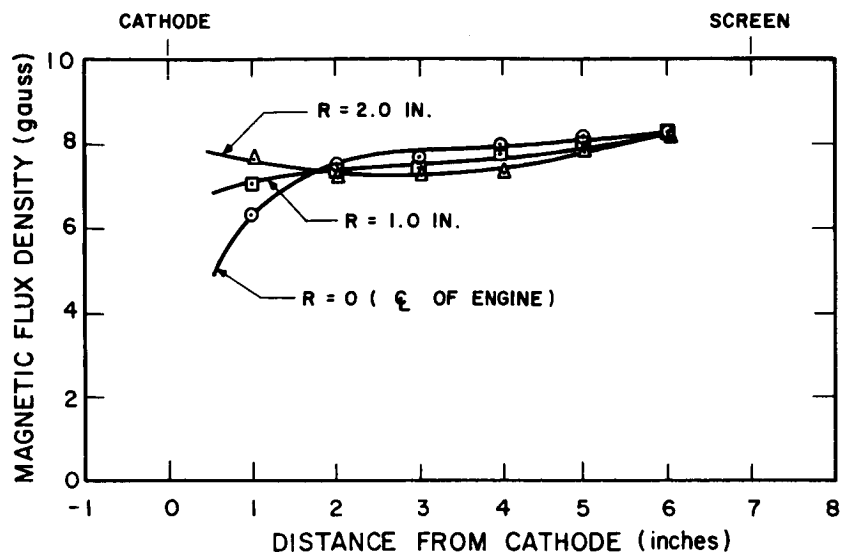


FIG. 118a AXIAL COMPONENT OF MAGNETIC FIELD OF DE ENGINE WITH PERMANENT MAGNETS

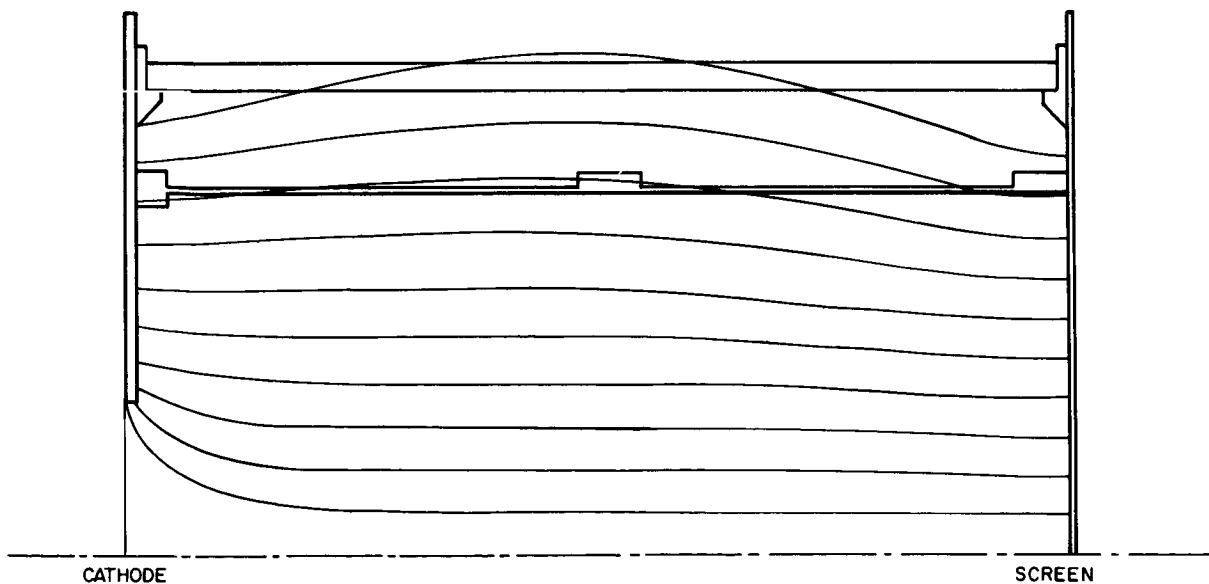


FIG. 118b PLOT OF MAGNETIC FIELD LINES FOR DE ENGINE WITH PERMANENT MAGNETS

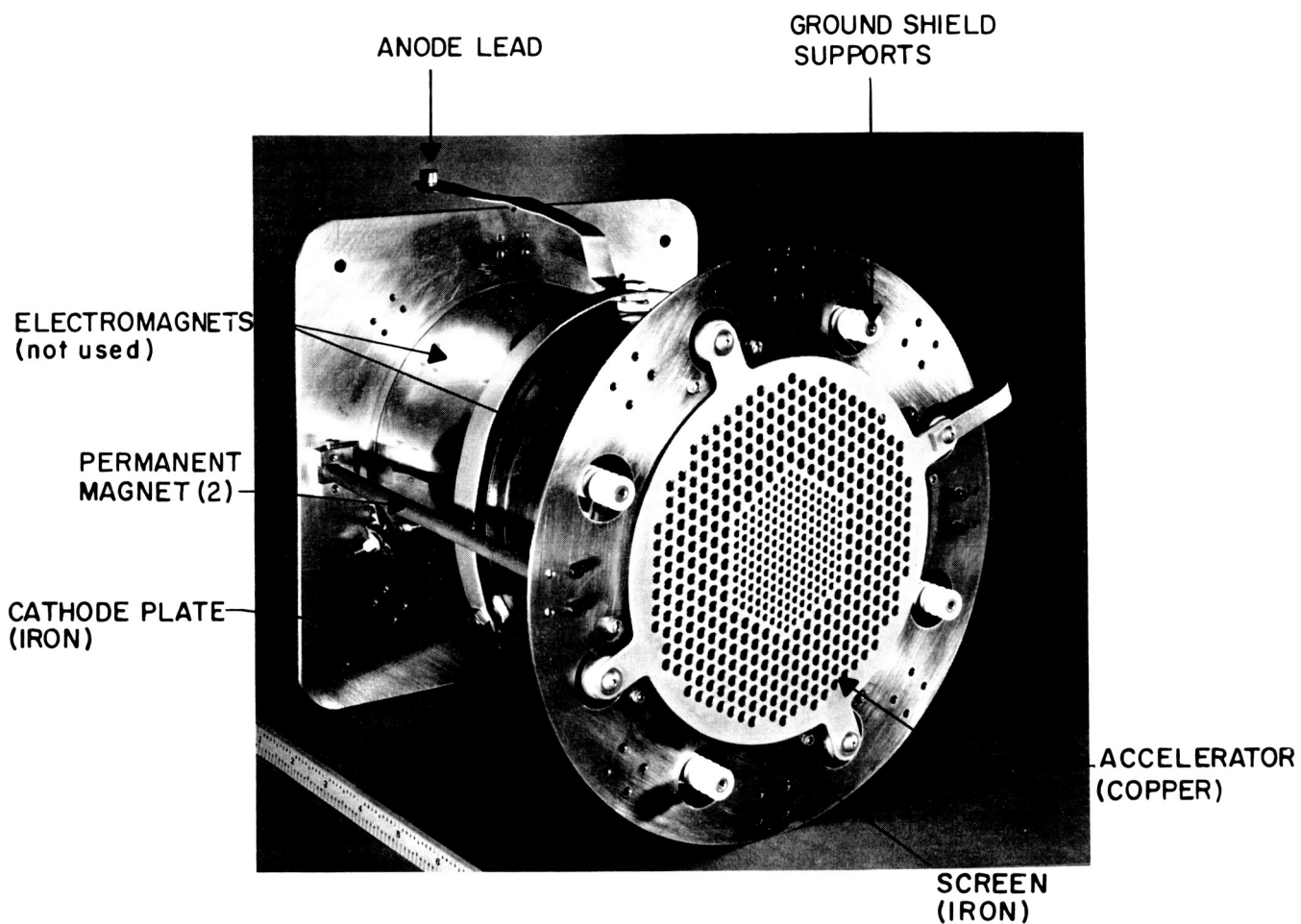


FIG. 119 DE ENGINE WITH PERMANENT MAGNET MODIFICATION

4. Higher voltages could be sustained after preliminary operation.
5. Data taken at a 500-milliampere beam level are shown in Table XXVII with similar data taken with the normal DE engine. The performance was comparable to that of the DE engine with the electromagnet configuration.

At low power levels the iron screen electrode bowed toward the accelerating electrode, reducing the gap and voltage capability of the accelerator system. At intermediate power levels of engine operation, the copper accelerating electrode bowed out also but then cooled and repositioned. The long period instabilities noted are believed to have been due to thermomechanical bowing and relaxation of the electrode. At higher engine power levels, the electrode bowing was apparently stabilized with the gap near normal.

#### 4.4.3 Permanent Magnet Engine

With the feasibility of using permanent magnets on an electron-bombardment cesium ion engine established, a new engine was designed to test the practicability of the magnetic circuit of Fig. 116c, and to take advantage of its inherent advantages. Since a low (about 9 gauss) field was required for this engine a workable magnetic material was desired; a coercive force of about 10 oersteds was the minimum requirement for the magnetic material. Availability dictated the use of 0.016-inch thick Vicalloy for the engine shell rather than the design minimum of about 0.007 inch. The new electrode (three aperture sizes) design developed under the Plasma Distribution Studies was used. Pure iron rims were designed for each end of the Vicalloy shell to act as cathode plate and screen electrode support locations and as pole pieces.

The cathode and anode were similar to those of the DE design. The accelerator support insulators were mounted further from the electrode gap and attached to the front rim of the shell by flexures which allowed free radial displacement. Fig. 120 shows the PM engine design. The cylinder of the PM engine was rolled from



TABLE XXVII  
COMPARISON OF DE ENGINE PERFORMANCE WITH  
ELECTROMAGNETS AND PERMANENT MAGNETS

	<u>Electromagnets</u>		<u>Permanent Magnets</u>
$V_+$ (kv)	3.5	3.6	3.5
$V_-$ (kv)	1.0	0.8	1.0
$I_-$ (amp)	0.010	0.0065	0.0065
$I_B$ (amp)	0.565	0.425	0.500
$V_A$ (volt)	7.4	7.25	7.6
$I_A$ (amp)	47.0	38.0	46.0
$P_B$ (kw)	1.980	1.530	1.750
$P_D$ (kw)	0.045	0.029	0.029
$P_M$ (kw)	0.006	0.008	0.0
$P_A$ (kw)	0.348	0.276	0.350
$P_T$ (kw)	2.379	1.843	2.129
$T$ (mlb)	12.6	9.6	11.1
$P/T$ (kw/lb)	189.0	192.0	191.0
$\eta_p$ (%)	83.0	83.0	82.2
$\eta_m$ (%)	90.0	91.0	92.0
$\eta_e$ (%)	75.0	75.5	75.6
$I_{sp}$ (sec)	6550.0	6700.0	6670.0
$I_-/I_B$ (%)	1.7	1.5	1.3
$P_A/I_B$ (kev/ion)	0.614	0.649	0.700

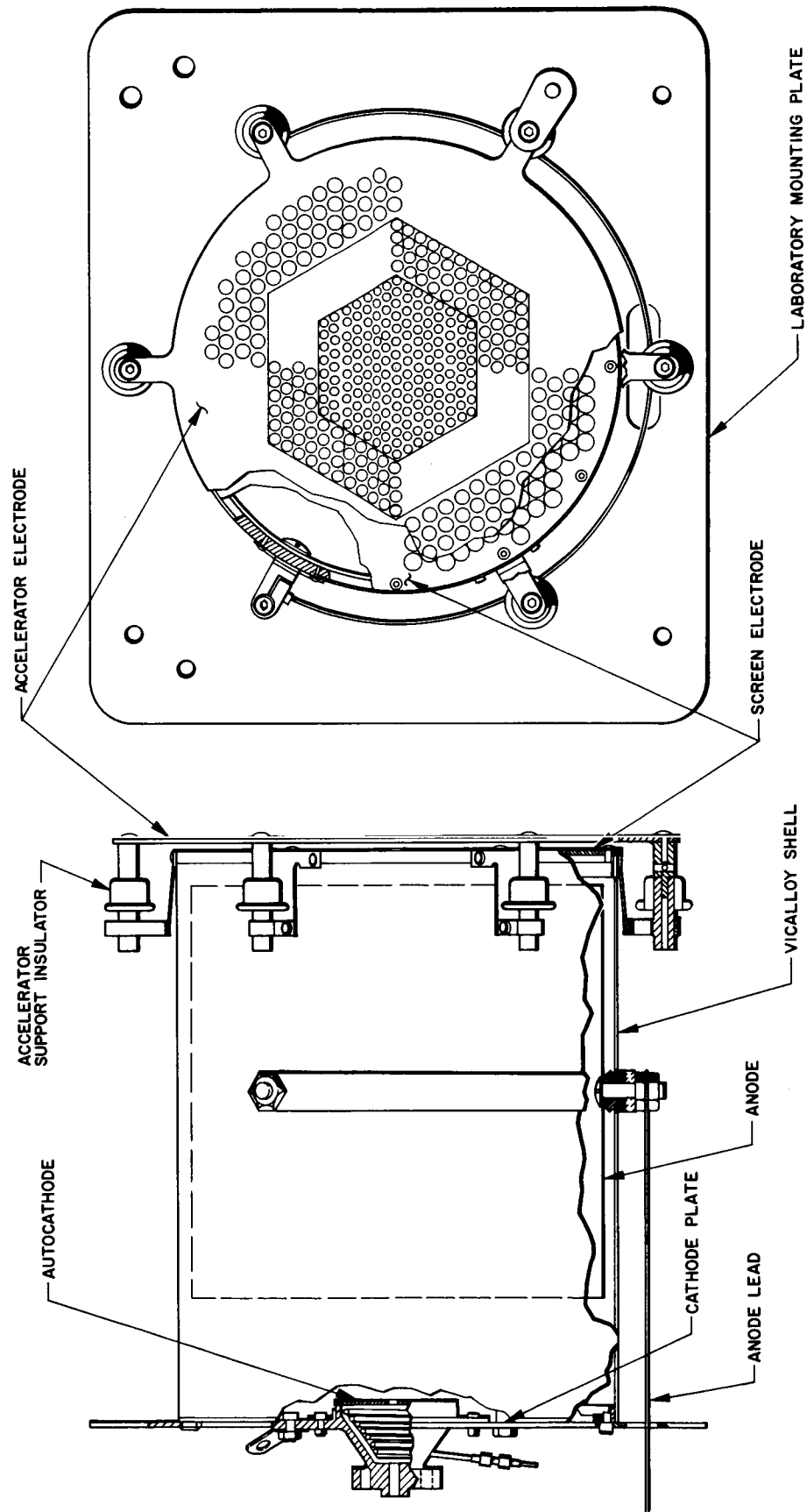


FIG. 120 PERMANENT MAGNET ENGINE DESIGN

0.016-inch thick Vicalloy sheet and electron-beam welded to the two iron rims. The cylinder was then heat treated to develop its magnetic properties.

#### Initial Tests

The permanent magnet engine is shown in Fig. 121. A copper accelerating electrode was used for the first tests. The cylinder was fully magnetized and then demagnetized to a field of approximately 8 gauss. The engine operated at a mass efficiency of only 84 percent compared with about 91 percent for the DE engine. Higher mass efficiencies could be obtained but only at the expense of arc power. The arc current for a given flowrate and arc voltage was about 25 percent higher than experienced with the DE engine. These factors indicated that the magnetic field was too low.

The electrode gap was then reduced and the operation of the engine was reevaluated. Overall efficiency of the permanent magnet engine was about ten percent below that obtained with the DE engine.

The magnetic field within the engine was then mapped with the results shown in Fig. 122. This figure shows the axial component of the magnetic field along three parallel lines including the axis. As can be seen, the field was far from uniform throughout the chamber. The desired field of 8 gauss existed only at the center of the engine where it was measured during the charging and stabilization process. Passing the shell through a weak alternating field region to stabilize the shell had apparently affected the intensity of the magnetization more at the ends of the shell. Near the screen electrode, the field was down to 3 gauss and varied by 50 percent for two points 180° apart at a 1.6-inch radius. Further magnetization tests were then undertaken.

An electromagnet was placed inside the engine with pole pieces which fit the support rings on both ends of the shell. Attempts to magnetize the shell with this magnet resulted in a number

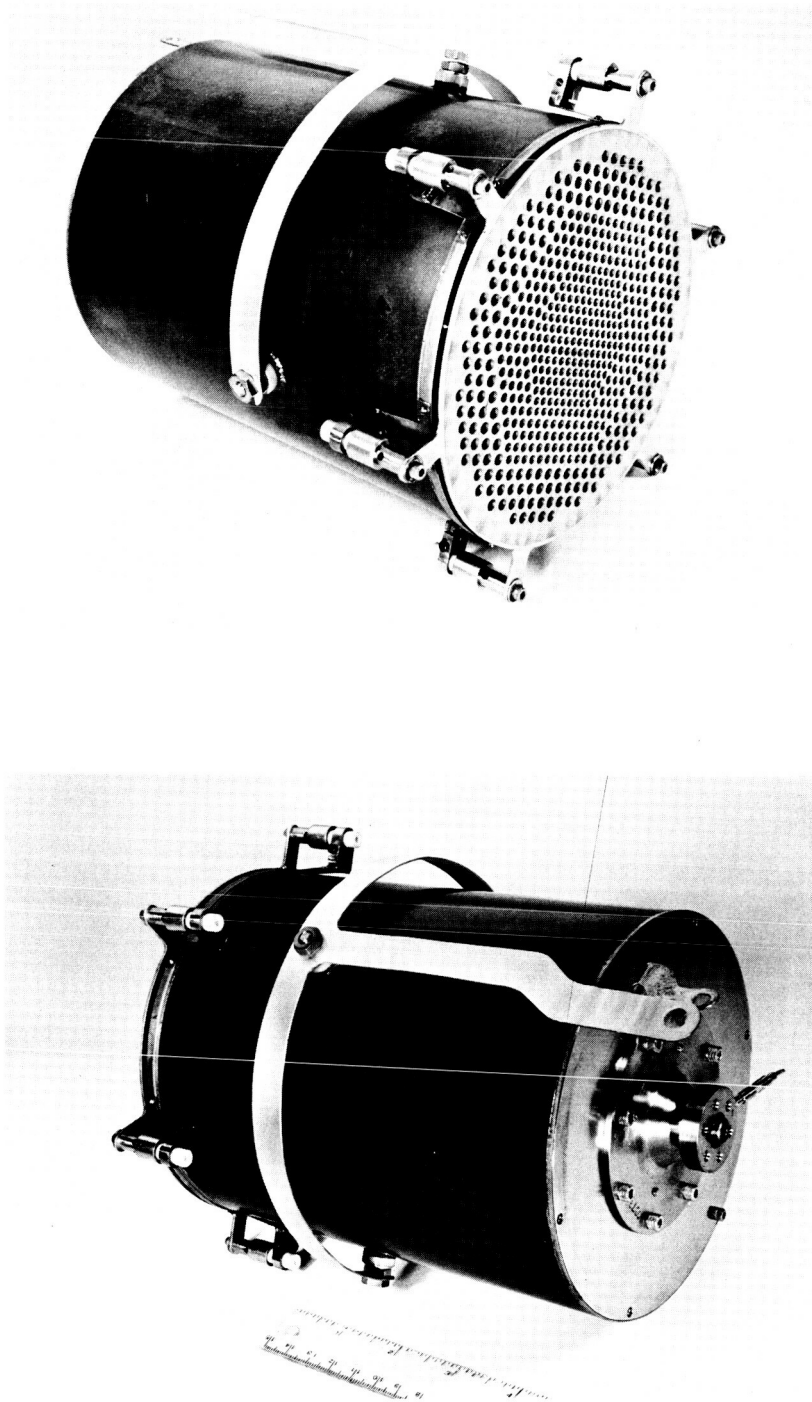


FIG. 121 PERMANENT MAGNET ENGINE

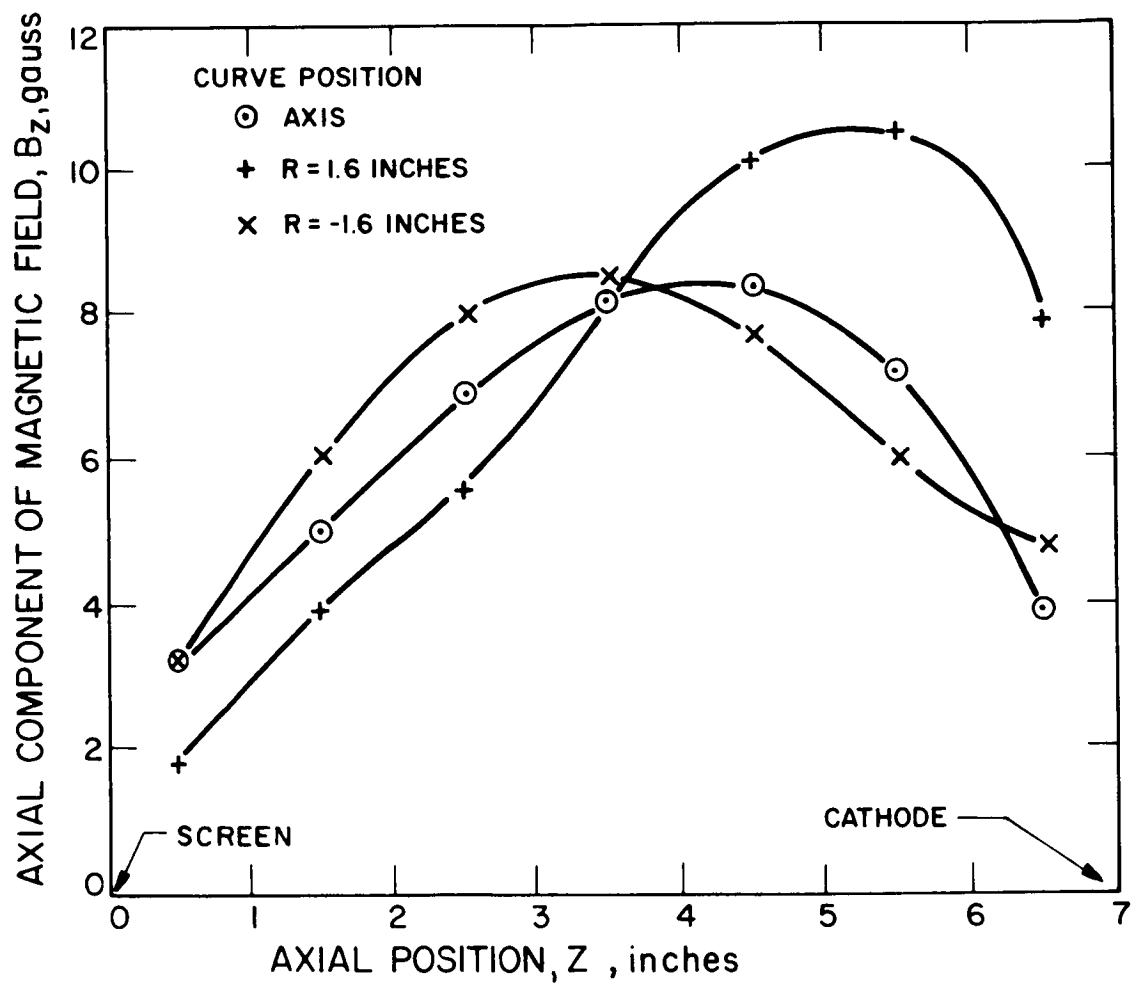


FIG. 122 PERMANENT MAGNET ENGINE MAGNETIC FIELD

of varied magnetic field configurations. While the fields obtained were far from desirable they showed the possibility of obtaining any desired field by proper adjustment of the charging field.

Since the magnetization process was found to require close control, a magnetizing coil was fabricated which provided a uniform field over a volume large enough to accommodate the engine shell.

Tests with an unmagnetized shell then revealed that the iron rims at both ends of the shell converge the charging field causing significantly higher magnetization at the ends of the shell than in the middle. It was found necessary to magnetize to the point where the center of the shell was properly magnetized and then reverse the field to demagnetize the ends slightly. A forward field of 135 oersteds followed by a reversed field of 75 oersteds left the shell uniformly magnetized. A field within the engine of about 10 gauss was obtained with a divergence toward the screen electrode of about 15 percent.

#### 4.4.4 Performance

After successful magnetization of the shell, the PM-1 engine was assembled and operated. Instabilities in the arc were noted at arc voltages between 7 and 8 volts. Operation was much steadier at 6.5 volts than above the instability range but the beam current was not reduced. Although the arc impedance was not unlike that of the DE engine, the mass efficiency of the PM engine was much higher.

After a few hours of operation to verify the mass utilization efficiency determinations, the engine was operated over a range of specific impulses from 3000 to 9000 seconds. A total operating time of 15 hours was recorded during three consecutive days. Performance data for the engine are presented in Table XXVIII. The most significant difference between the operation of the PM-1 engine and the DE engine was the reduction in the arc power required for a given mass utilization efficiency as shown in Fig. 123. The elimination of the magnet power and a reduction of the drain power due to the improved extraction optics also improved the overall performance. The operating parameters listed in Table XXVIII are representative of over 50 operating

TABLE XXVIII  
PM-1 ENGINE PERFORMANCE

Run	<u>1</u>	<u>2</u>	<u>3</u>	<u>4</u>	<u>5</u>
Positive High Voltage, $V_+$ (kv)	0.9	1.2	1.95	2.5	3.0
Negative High Voltage, $V_-$ (kv)	2.6	2.2	1.6	1.5	1.0
Negative HV Current, $I_-$ (amp)	0.0116	0.0045	0.0036	0.0039	0.0039
Beam Current, $I_B$ (amp)	0.437	0.323	0.293	0.380	0.420
Arc Voltage, $V_A$ (volt)	6.0	6.4	6.6	6.5	6.5
Arc Current, $I_A$ (amp)	30.7	21.5	18.0	25.5	32.0
Beam Power, $P_B$ (kw)	0.393	0.387	0.571	0.950	1.260
Drain Power, $P_D$ (kw)	0.040	0.015	0.012	0.016	0.016
Arc Power, $P_A$ (kw)	0.184	0.137	0.118	0.166	0.208
Total Power, $P_T$ (kw)	0.617	0.539	0.701	1.132	1.484
Thrust, T (mlb)	4.93	4.21	4.87	7.15	8.65
Power to Thrust, P/T (kw/lb)	125.0	128.3	144.0	158.5	171.8
Power Efficiency, $\eta_p$ (%)	63.7	71.7	81.4	84.1	84.9
Mass Efficiency, $\eta_M$ (%)	80.3	85.4	87.4	91.8	92.3
Overall Engine Efficiency, $\eta_E$ (%)	51.2	61.2	71.2	77.2	78.4
Specific Impulse, $I_{sp}$ (sec)	2950.0	3620.0	4730.0	5617.0	6187.0
Ratio of Drain Current to Beam Current, $I_-/I_B$ (%)	2.7	1.4	1.2	1.0	0.93
Source Energy per Ion, $P_A/I_B$ (kev/ion)	0.422	0.424	0.403	0.437	0.495

TABLE XXVIII (contd)  
PM-1 ENGINE PERFORMANCE

Run	<u>6</u>	<u>7</u>	<u>8</u>	<u>9</u>	<u>10</u>	<u>11</u>	<u>12</u>
V <sub>+</sub> (kv)	3.5	3.5	4.35	4.95	5.65	6.25	6.25
V <sub>-</sub> (kv)	0.8	0.8	1.2	0.8	0.8	0.8	1.0
I <sub>-</sub> (amp)	0.0035	0.0035	0.0050	0.0044	0.0054	0.0073	0.0066
I <sub>B</sub> (amp)	0.431	0.437	0.572	0.540	0.504	0.485	0.649
V <sub>A</sub> (volt)	6.4	6.5	6.2	6.5	6.5	6.9	6.2
I <sub>A</sub> (amp)	31.5	32.5	38.5	37.0	35.0	40.0	41.5
P <sub>B</sub> (kw)	1.509	1.530	2.488	2.673	2.847	3.031	4.056
P <sub>D</sub> (kw)	0.015	0.015	0.028	0.025	0.034	0.051	0.047
P <sub>A</sub> (kw)	0.202	0.211	0.239	0.240	0.228	0.276	0.257
P <sub>T</sub> (kw)	1.726	1.756	2.755	2.938	3.109	3.358	4.360
T (mlb)	9.58	9.73	14.2	14.3	14.3	14.4	19.3
P/T (kw/lb)	179.7	174.9	196.0	204.8	217.0	233.2	225.7
$\eta_p$ (%)	87.4	87.1	90.3	91.0	91.6	90.3	93.0
$\eta_M$ (%)	92.4	93.3	91.5	93.0	92.8	94.5	90.9
$\eta_E$ (%)	80.8	81.3	82.6	84.7	85.0	85.3	84.0
I <sub>sp</sub> (sec)	6690.0	6756.0	7400.0	8010.0	8550.0	9160.0	8810.0
I <sub>-</sub> /I <sub>B</sub> (%)	0.81	0.80	0.87	0.82	1.1	1.5	1.0
P <sub>A</sub> /I <sub>B</sub> (kev/ion)	0.469	0.483	0.418	0.444	0.452	0.570	0.396



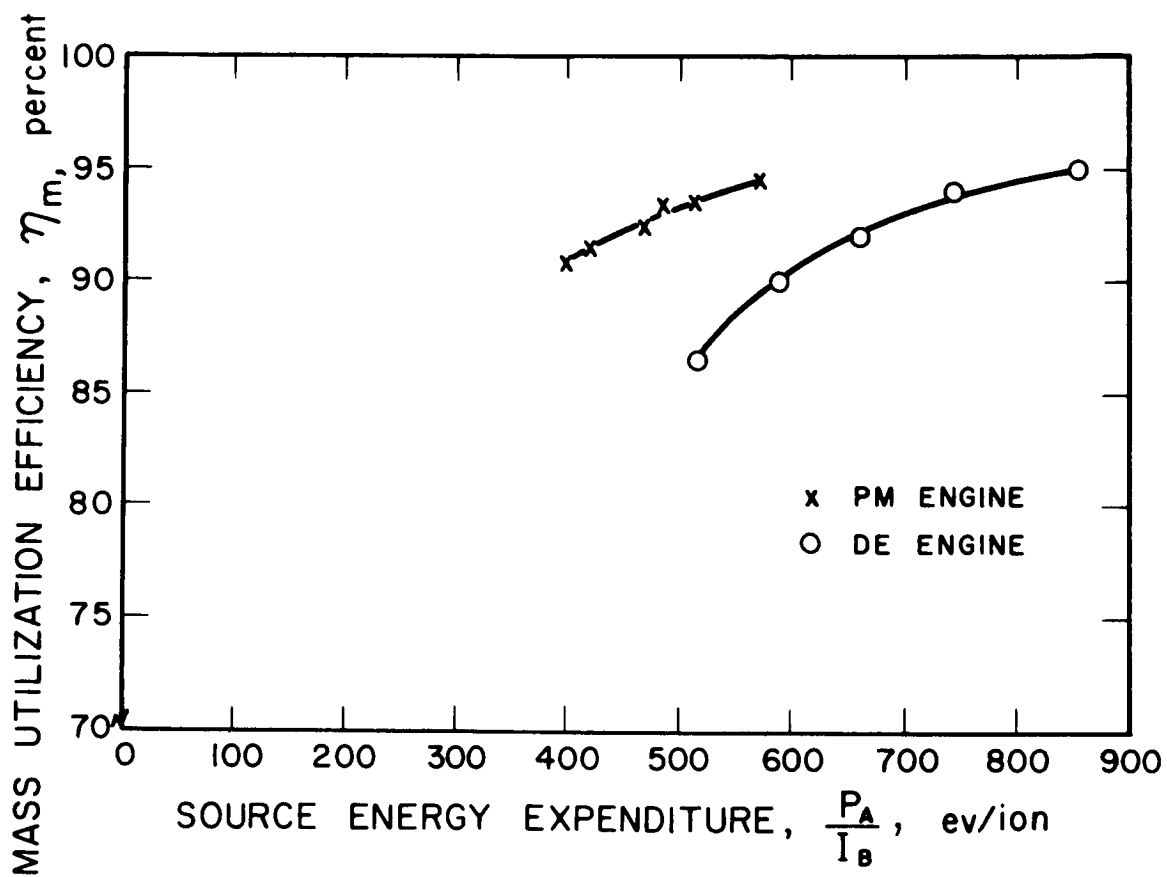


FIG. 123 MASS UTILIZATION EFFICIENCIES OF PM-1 AND DE ENGINES

points where the engine was run for at least ten minutes prior to recording data. Points 6 and 7 were taken an hour apart during steady operation.

This portion of the program had been successfully concluded with the performance mapping of the PM engine. It was decided, however, to extend the studies and a second permanent magnet engine shell was assembled.

The second permanent magnet engine shell was assembled with the DE cathode, iron screen, and the copper accelerating electrode used on the first PM engine. The magnetic field was measured along the axis and was highly convergent toward the screen. The mass efficiency at comparable source energies per ion was found to be substantially lower than in PM-1. To obtain a mass efficiency of 92.7 percent required 785 ev/ion. The magnetization of the shell was then changed to resemble the field of the first engine but with slightly more divergence toward the screen electrode.

The operation of the second engine was then mapped over a range of specific impulses from 2260 to 8840 seconds with the results shown in Table XXIX. The overall engine efficiency and power-to-thrust ratios for the two PM engines and the DE engine are shown as a function of specific impulse in Figs. 124 and 125. As the data show, the PM-2 engine was more efficient than PM-1.

A comparison of weights between the DE engine and PM engine is made in Table XXX. The greatest savings in weight was in the engine shell. Additional weight reductions were made in the anode and the screen (iron rather than molybdenum) as well as the cathode plate which did not have the mounting "ears" of the DE engine. Weight could be further reduced by using thinner material for the Vicalloy cylinder.

#### Conclusions

A lighter, simpler, and more efficient engine was developed under this portion of the program. Disadvantages apparent in the PM engine are:

TABLE XXIX  
PM-2 ENGINE PERFORMANCE

Run	<u>1</u>	<u>2</u>	<u>3</u>	<u>4</u>	<u>5</u>
Positive High Voltage, $V_+$ (kv)	0.6	0.8	1.0	1.2	1.6
Negative High Voltage, $V_-$ (kv)	2.0	1.9	1.8	1.6	1.3
Negative HV Current, $I_-$ (amp)	0.0055	0.0046	0.0037	0.0032	0.0027
Beam Current, $I_B$ (amp)	0.250	0.250	0.250	0.253	0.255
Arc Voltage, $V_A$ (volt)	5.9	5.9	6.0	6.0	6.0
Arc Current, $I_A$ (amp)	14.0	13.5	13.5	13.5	15.0
Beam Power, $P_B$ (kw)	0.150	0.200	0.250	0.304	0.408
Drain Power, $P_D$ (kw)	0.014	0.012	0.010	0.009	0.008
Arc Power, $P_A$ (kw)	0.083	0.080	0.081	0.081	0.090
Total Power, $P_T$ (kw)	0.247	0.292	0.341	0.394	0.506
Thrust, T (mlb)	2.30	2.66	2.98	3.29	3.85
Power to Thrust, P/G (kw/lb)	107.0	110.0	115.0	119.0	132.0
Power Efficiency, $\eta_p$ (%)	60.7	68.5	73.3	77.2	80.6
Mass Efficiency, $\eta_M$ (%)	75.5	78.1	82.3	85.1	88.3
Overall Engine Efficiency, $\eta_E$ (%)	45.8	54.2	60.3	65.6	72.0
Specific Impulse, $I_{sp}$ (sec)	2260.0	2710.0	3190.0	3610.0	4330.0
Ratio of Drain Current to Beam Current, $I_-/I_B$ (%)	2.20	1.84	1.48	1.26	1.06
Source Energy per Ion, $P_A/I_B$ (kev/ion)	0.330	0.320	0.324	0.320	0.353

TABLE XXIX (contd)  
PM-2 ENGINE PERFORMANCE

Run	<u>6</u>	<u>7</u>	<u>8</u>	<u>9</u>	<u>10</u>	<u>11</u>
$V_+$ (kv)	2.0	2.5	3.0	3.75	4.5	6.0
$V_-$ (kv)	1.2	1.1	1.2	1.0	0.8	0.7
$I_-$ (amp)	0.0036	0.0028	0.0035	0.0036	0.0031	0.0034
$I_B$ (amp)	0.345	0.340	0.450	0.500	0.500	0.560
$V_A$ (volt)	6.3	6.2	6.5	6.4	6.5	6.4
$I_A$ (amp)	20.0	18.5	26.0	28.0	27.0	28.5
$P_B$ (kw)	0.690	0.850	1.350	1.875	2.250	3.360
$P_D$ (kw)	0.012	0.010	0.014	0.017	0.016	0.023
$P_A$ (kw)	0.126	0.115	0.169	0.179	0.176	0.182
$P_T$ (kw)	0.828	0.975	1.533	2.071	2.442	3.565
$T$ (mlb)	5.8	6.4	9.3	11.5	12.6	16.3
$P/T$ (kw/lb)	143.0	152.0	165.0	180.0	194.0	219.0
$\eta_p$ (%)	83.4	87.2	88.1	90.5	92.2	94.3
$\eta_M$ (%)	90.6	90.7	93.0	93.1	93.5	93.2
$\eta_E$ (%)	75.6	79.1	81.9	84.3	86.2	87.9
$I_{sp}$ (sec)	4960.0	5560.0	6240.0	6990.0	7680.0	8840.0
$I_-/I_B$ (%)	1.04	0.82	0.78	0.72	0.62	0.61
$P_A/I_B$ (kev/ion)	0.365	0.338	0.376	0.358	0.350	0.325

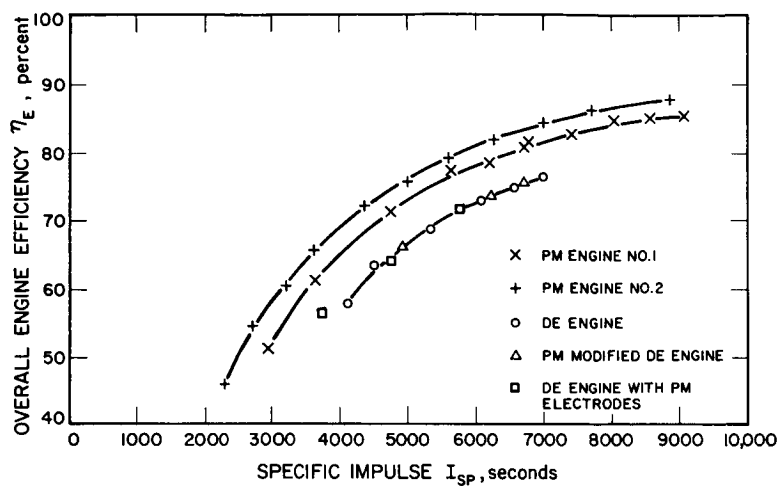


FIG. 124

PM-1, PM-2, AND DE ENGINE OVERALL EFFICIENCIES

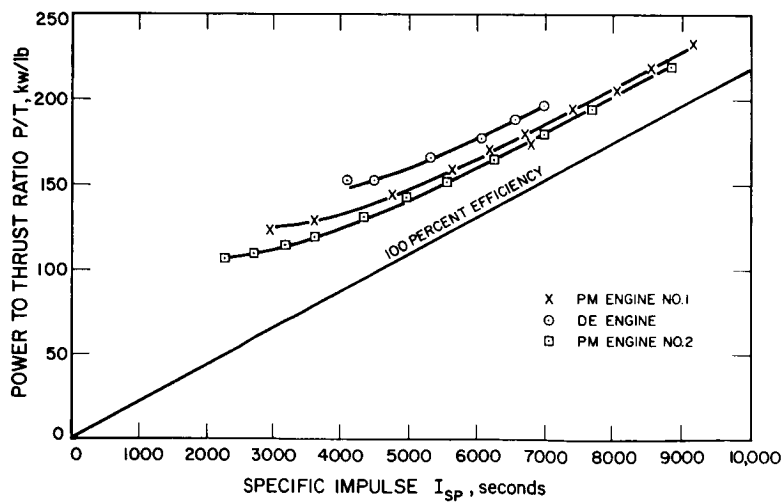


FIG. 125

PM-1, PM-2, AND DE ENGINE POWER-TO-THRUST RATIOS

TABLE XXX  
DE AND PERMANENT MAGNET ENGINE WEIGHTS

<u>Component</u>	<u>Weight (grams)</u>	
	<u>DE Engine</u>	<u>PM Engine</u>
Shell Assembly	745	364
Anode	360	245
Cathode Assembly	98	98
Cathode Plate	136	57
Screen Electrode	118	38
Accelerator Electrode (Cu)	141	160
Assembled Engine (includes anode and electrode supports)	1956	1112

1. Its performance reproducibility (PM-1 and PM-2 engine performances were not identical).
2. The reliability of this engine has not been proven.
3. The magnetic materials used may be subject to effects of an adverse radiation environment.

This program did lead to a very significant improvement in engine performance.

#### 4.5 Advanced Neutralizers

The DF engine systems were operated without a neutralizer since an efficient, long-lived neutralizer was unavailable. Near the end of the program a very promising device was developed and ion beam neutralization tests were initiated.

A "Plasma Bridge" neutralizer similar to those developed at Electro-Optical Systems, Inc. under Air Force Contract AF 33(615)-1530 and described in Ref. 8 was operated with a PM engine. This neutralizer utilizes a cesium plasma to couple the neutralizer to the beam. This coupling significantly reduces the neutralizer-to-beam perveance. The neutralizer tested is shown schematically in Fig. 126. It is an externally heated cesiated cathode similar to the cesium bombardment engine cathode.

Cesium is supplied, by a small laboratory feed system, to a discharge chamber. The chamber is heated to about 600°C by a sheathed external heater. A small orifice in the chamber (typically 0.006 inch) faces toward the ion engine beam. A discharge is established between the cathode and the ion beam, which floats to a positive potential. From this discharge the ion beam acquires all the electrons it needs for neutralization. The hot cesiated tantalum surface, with appropriate geometry, can put out 100 times as many electrons as neutral cesium atoms and makes an efficient emitter. In addition, the discharge supplies slow ions which overcome space charge problems.

The PM-1 engine was operated for 5 hours at a thrust of 10 millipounds, a specific impulse of 6770 seconds, and a power-to-thrust

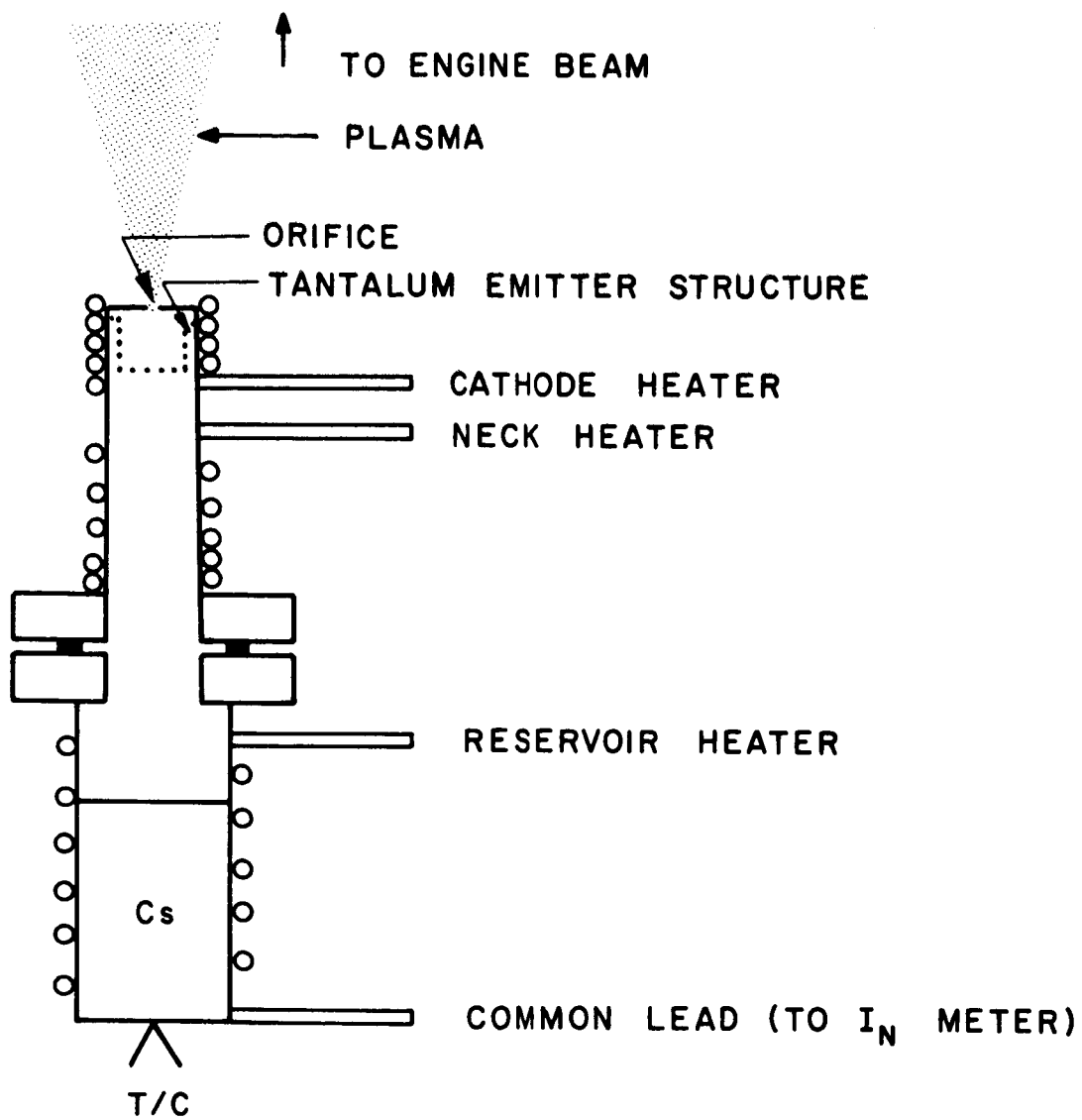


FIG. 126 SCHEMATIC OF PLASMA BRIDGE NEUTRALIZER



ratio including neutralizer of 187.4 kilowatts per pound. The test was performed using the electrical system of Fig. 127. The penalties paid for neutralization with this device are both power and weight loss penalties. The power losses include cathode power, cesium feed tube power, reservoir power, and a power corresponding to the product of beam current times beam potential with respect to ground. During these tests the cesiated tantalum cathode used 5.7 watts, the feed tube 8.8 watts, and the reservoir power was 15 watts. The beam potential, as measured by floating the vacuum system liner and collector, was 9 volts. The beam current was 438 milliamperes, so the power lost due to nonzero beam potential was 4 watts. The total power was 33.5 watts or approximately 2 percent of the total system power.

The cesium flowrate as determined by weight loss of the neutralizer reservoir was equivalent to 16 milliamperes or 3.4 percent of the engine flowrate of 476 milliamperes. The effect of the cesium expenditure is to lower the total system specific impulse, requiring a higher positive high voltage to maintain the power-to-thrust ratio of the engine. In this case the increase in power-to-thrust ratio due to a theoretical increase in positive high voltage to allow the system to operate at 6950 seconds would have been 3.7 kw per pound. Thus converting the penalty entirely to terms of power-to-thrust losses, the net loss was 7 kw per pound.

At the end of the 5-hour run the reservoir power was reduced and satisfactory operation was maintained down to a flowrate estimated to be 20 to 25 percent of the test flowrate. Further tests were conducted to optimize overall performance of this particular device.

The neutralizer was retested with the PM-1 engine. The operating point shown in Table XXXI was held for 7 hours. Power to the neutralizer reservoir was adjusted to maintain the neutralizer-to-beam potential (vacuum system collector potential) at about 9 volts. Lower potentials could be obtained but only at the expense of increased neutralizer cesium flowrates. The flowrate of the neutralizer was determined, by weight loss to be 0.84 percent of the engine flowrate.

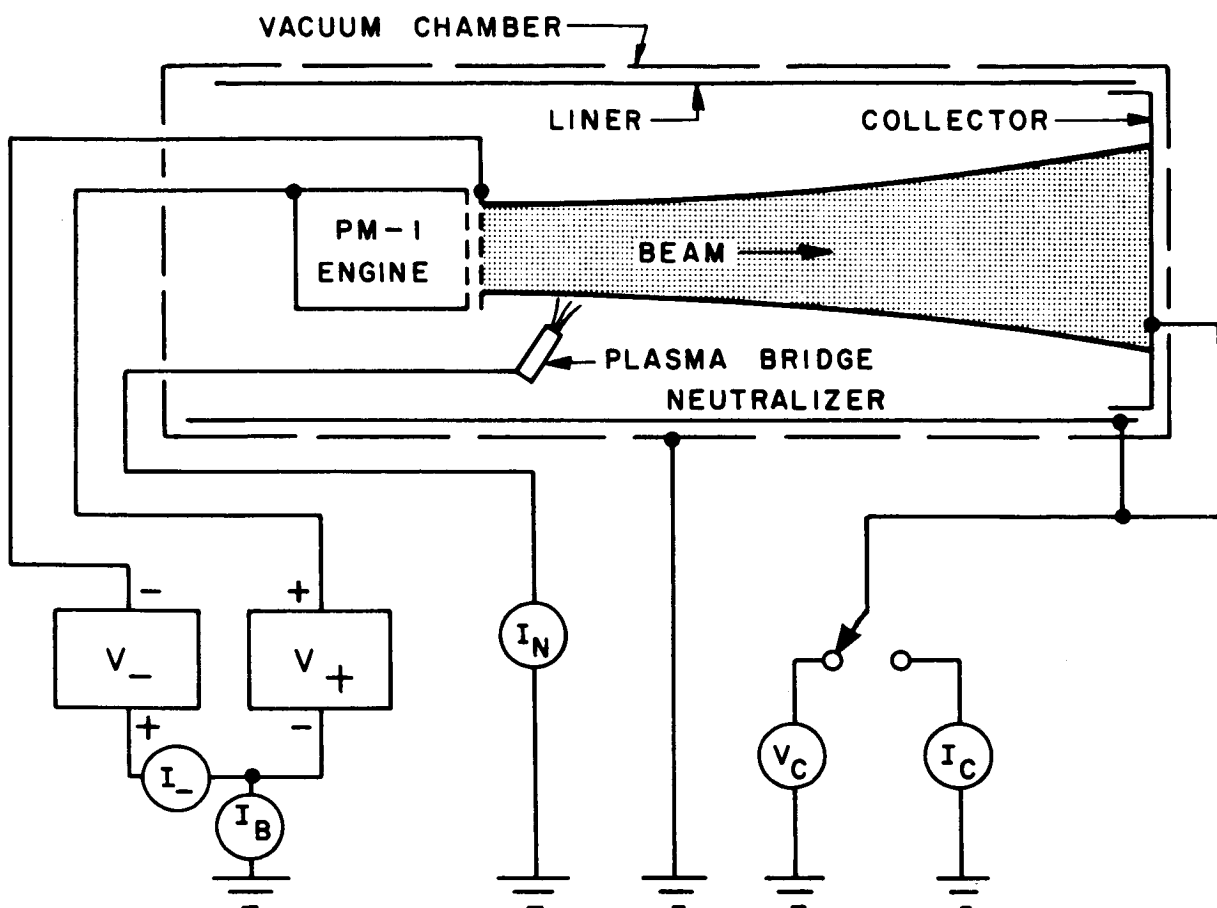


FIG. 127 ELECTRICAL SCHEMATIC FOR NEUTRALIZER TESTS

TABLE XXXI  
PM-1 ENGINE PERFORMANCE WITH NEUTRALIZER

<u>Run</u>	<u>1</u>
Positive High Voltage, $V_+$ (kv)	3.8
Negative High Voltage, $V_-$ (kv)	0.8
Negative HV Current, $I_-$ (amp)	0.005
Beam Current, $I_B$ (amp)	0.435
Arc Voltage, $V_A$ (volt)	6.6
Arc Current, $I_A$ (amp)	26.0
Beam Power, $P_B$ (kw)	1.653
Drain Power, $P_D$ (kw)	0.023
Arc Power, $P_A$ (kw)	0.172
Total Engine Power, $P_T$ (kw)	1.848
Thrust, $T$ (mlb)	10.1
Engine Power-Thrust Ratio, $P/T$ (kw/lb)	183.0
Engine Specific Impulse, $I_{sp}$ (sec)	7000.0
Neutralizer Heater Power (watts)	28.4
Perveance Power, $V_B \times I_B$ (watts)	3.9
Specific Impulse Loss (equivalent watts)	12.0
Total Equivalent Neutralizer Power, (watts)	44.3
$\Delta P/T$ for Neutralization (kw/lb)	4.4

The penalty for neutralization during this run was 4.4 kw/lb including reservoir, feed tube, and cathode heater powers, perveance loss ( $V_B \times I_B$ ), and the equivalent loss for the reduction in specific impulse. This was only two-thirds the penalty previously obtained. It was concluded that the discharge neutralizer could solve the problems previously encountered in engine neutralization and that this device promised not only high efficiency, but long lifetime.

One remaining problem was to verify that the low level of accelerator potential did, indeed, prevent backstreaming of electrons from the neutralized beam to the engine. The only metering system which can guarantee accurate measurement of the beam current would be an ion collector system with appropriate electron traps.

Operation was usually verified by making a step-wise reduction in the accelerator potential and observing the resultant effect on the beam current. Any increase in beam current was taken to be due to backstreaming electrons. If such a result was obtained, the negative electron-trap potential of the accelerator was increased until the above test was successful. A plot of measured beam current as a function of accelerator potential is shown in Fig. 128. As the data show, an accelerator potential of only 200 volts was required to prevent backstreaming of electrons. In the run for which these data were taken, the accelerator potential was maintained at 300 to 400 volts. This potential was found to yield minimum accelerator electrode drain current. The cause of the beam current increase with accelerator potentials greater than 300 volts was the increase in plasma sheath area as the sheath was forced away from the screen electrode. This characteristic is typical of high perveance electrodes.

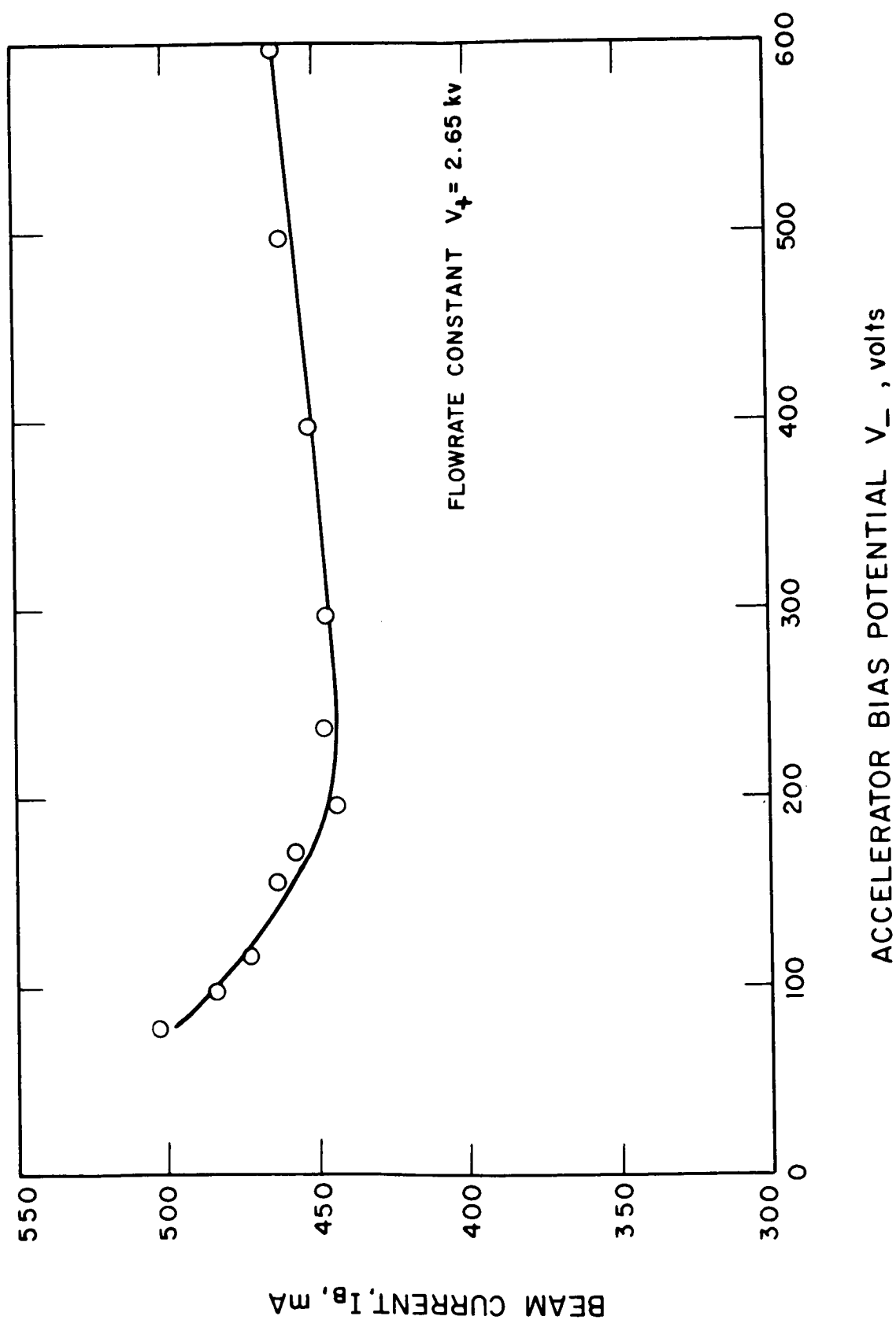


FIG. 128 BEAM CURRENT VERSUS ACCELERATOR BIAS

## REFERENCES

1. Electro-Optical Systems, Inc., Ion Rocket Engine System Research and Development, by R. C. Speiser, R. M. Worlock, F. A. Barcatta, G. C. Reid, and G. Sohl, EOS Report 3670-Final (NASA CR-54067), Pasadena, California, 28 June 1964
2. Electro-Optical Systems, Inc., Applied Research on Contact Ionization Thrustor, EOS Report 3830-Final (APL TDR 64-52), Pasadena, California, May 1964
3. Electro-Optical Systems, Inc., Ion Rocket System Research and Development, by R. C. Speiser, EOS Report 4920-ML-8, Pasadena, California, 10 November 1964
4. Electro-Optical Systems, Inc., Ion Rocket System Research and Development, by R. C. Speiser, EOS Report 4920-ML-12, Pasadena, California, 10 March 1965
5. P. D. Reader, Investigation of a 10-Centimeter-Diameter Electron-Bombardment Ion Rocket, NASA TN D-1163
6. P. D. Reader, Experimental Effects on Propellant Introductory Mode on Electron-Bombardment Ion Rocket Performance, NASA TN D-2587
7. P. D. Reader, "Scale Effects on Ion Rocket Performance," ARS Journal, Vol. 32, No. 5, March 1962, pp. 711-714
8. Electro-Optical Systems, Inc., Program for the Exploratory Development of a Contact Ionization Thrustor, EOS Report 4800-Final, Technical Report, (AFAPL-TR-65-68), Pasadena, California, May 1965

## APPENDIX A

### QUALITY ASSURANCE

The quality assurance system employed to service the needs of NASA-Lewis Contract NAS3-5250 evolved during the early phases of NASA-Lewis Contract NAS3-2516. Close cooperation between technical and product assurance personnel resulted in a flexible, efficient system for providing program support.

The basic system may be described as a shop traveller scheme. Quality information pertaining to fabricated articles and assemblies is entered on the traveller while work is in process. The traveller is ultimately placed in a permanent file as a record of actual detail part history. Supplementing shop traveller information are laboratory log books containing test data, log books containing calibration records, and material certification files at receiving inspection. The shop travellers are instrumental in establishing quality criteria. Engineering drawings, test procedures, material and process specifications, and their respective revisions are prepared with the aid of the quality information on hand.

#### A.1 Quality Assurance Program Requirements

Detailed quality assurance program requirements were specified in NASA-Lewis Document QA-1a, "Quality Assurance Program Provisions for Research, Test, and Development Projects," dated 13 July 1962, in EOS Report, 3670-QAP-2, "Quality Assurance Plan - Revised," dated 22 January 1963, and in the clarifications noted under Task VI of the work statement for Contract NAS3-5250. A quality program plan meeting these provisions was generated at the beginning of the program. This plan (EOS Report 4920-QAP-1, "Inspection and Test Plan," dated

24 February 1964) provided the planning function for inspections and tests conducted during the contract effort. Included in the test plan were the equipment log and failure report formats used.

#### A.2 Quality Assurance Program Functions

Quality assurance program functions pertained to the overall project activity and were not intended to be accomplished by any one department or group. Specific quality obligations were imposed on organizational elements other than the EOS Product Assurance Group which retained responsibility for the execution of product assurance policies and programs. A representative from Product Assurance was assigned to the project to work together with these other organizational elements. The representative assisted these groups in performing their quality assurance assignments. In this manner project and quality activity were continuously integrated.

Appendix A of NASA-Lewis Report CR-54067, "Ion Rocket Engine System Research and Development," dated 28 June 1964, describes these quality assurance program functions in detail.

#### A.3 Quality Assurance Program Information

Equipment logs were prepared and maintained for each of the following:

- DE-1 engine
- DER-1 engine
- DER-2 engine
- DF-1 engine
- DF-2 engine
- 4923 S/N 1 feed system
- 4923 S/N 2 feed system
- 4923 S/N 3 feed system
- 4923 S/N 4 feed system

Over three hundred shop travellers were processed during the contract period. Quality information contained on completed



travellers was reviewed. Engine and feed system vellums were revised in accordance with pertinent red-marks contained on the travellers.

Calibration data were recorded in a separate bound laboratory log book. Test data were recorded directly in the equipment logs.

Special processing instructions were issued for vacuum brazing of tantalum to molybdenum with palladium-cobalt filler material.

Test procedure 4922-1, "Reliability Engine Component Weights," was released.

Test procedure revision 3670-3B, "Magnet Coil Check, Air," was released.

"EOS Ion Physics Electrical Laboratory Calibration Procedures," revision C.P. 3670A was released.

Section III.1, "Procedure for Installation of Zero-G Feed System Equipped Gas Discharge Engine in Vacuum Facility" of "Assembly Cleaning and Operating Procedures for DE Engine System," was revised and released.

#### A.4 Failure Reports

Ten failures were reported during the contract period. Of these, four were failures of vacuum or electronic equipment not subject to the quality assurance system. The remaining six failures and corrective actions taken are summarized below.

##### (a) Orifice Plate

Continuous arcs between DER-1 engine electrodes were observed after 1/2 hour run time on 24 May 1964. A flaky, black substance was found in the electrode gap, the bottom of the anode, and the cryogenic test chamber liner below the electrode gap. Sample analysis of this substance indicated high titanium alloy content. Engine inspection after test showed erosion on the cathode orifice plate. This plate was machined from Ti-6AL-4V alloy per AMS 4928.

Drawing 703727 revision A was released specifying molybdenum orifice plate material.

(b) Accelerating Electrode

DER-1 engine drain currents increased to 23 ma on 26 May 1964 after 23 hours operation. Similarly, drain currents increased to 15 ma on 6 June 1964 17-1/2 hours run time, and to 22 ma on 18 June 1964 after 20-1/2 hours run time.

Changing accelerating electrode material to copper led to 200 hours continuous operation with no increase in drain current.

(c) Lead Wire Connector

A DER-1 engine cathode to anode short circuit was observed on 11 July 1964 after 58 hours operating time. The short circuit was between the anode and cathode pins in Deutsch connector DM5606-37-3P-644.

Drawing 703762 revision B was released deleting anode and cathode terminals in the connector.

(d) Magnet Terminal Connection

Arc fluctuations (make and break condition) were observed with DER-1 engine on 25 July 1964. The copper lead wire was loose inside the Alite ceramic tube feedthrough magnet terminal.

Drawing 703708 revision D was released requiring the lead wire to be crimped to the feedthrough terminal.

(e) Port Valve

Liquid cesium from the reservoir was forced into the anode cavity during vacuum chamber roughing with DER-2 engine and 4923 S/N 2 feed system on 12 October 1964. Upon its removal from the chamber, the port valve was found clogged with cesium. The same thing was observed again with DER-1 engine and 4923 S/N 2 feed system on 30 October 1964.

Drawing 703649 revision F was released substituting the 704513 port valve for the 703924-1 valve. The 704513 valve has a larger bore, thereby minimizing clogging potential.

(f) Reservoir Pumpdown

Liquid cesium from the reservoir was forced into the anode cavity with DER-2 engine and 4923 S/N 3 feed system on 13 November 1964. The failure probably resulted from gas pockets which were trapped in the solid cesium during vacuum chamber roughdown.

Section III.1, "Procedure for Installation of Zero-G Feed System Equipped Gas Discharge Engine in Vacuum Facility," of "Assembly Cleaning and Operating Procedures for DE Engine System" was revised and released.

REPORT DISTRIBUTION LIST FOR  
CONTRACT NAS3-5250

NASA Headquarters (1)  
FOB - 10B  
600 Independence Avenue, S.W.  
Washington, D. C. 20546  
Attn: RNT/James Lazar

NASA-Lewis Research Center (1)  
21000 Brookpark Road  
Cleveland, Ohio 44135  
Attn: Spacecraft Technology Procurement  
Section (M.S. 54-2)

NASA-Lewis Research Center (1)  
21000 Brookpark Road  
Cleveland, Ohio 44135  
Attn: Technology Utilization Office (M.S. 3-19)

NASA-Lewis Research Center (1)  
21000 Brookpark Road  
Cleveland, Ohio 44135  
Attn: Technical Information Division (M.S. 5-5)

NASA-Lewis Research Center (2)  
21000 Brookpark Road  
Cleveland, Ohio 44135  
Attn: Library (M.S. 3-7)

NASA-Lewis Research Center (1)  
21000 Brookpark Road  
Cleveland, Ohio 44135  
Attn: Spacecraft Technology Division  
J. H. Childs (M.S. 54-1)

NASA-Lewis Research Center (2)  
21000 Brookpark Road  
Cleveland, Ohio 44135  
Attn: Spacecraft Technology Division  
D. L. Lockwood (M.S. 54-3)

NASA-Lewis Research Center (1)  
21000 Brookpark Road  
Cleveland, Ohio 44135  
Attn: Spacecraft Technology Division  
R. R. Nicholls (M.S. 54-3)

NASA-Lewis Research Center (1)  
21000 Brookpark Road  
Cleveland, Ohio 44135  
Attn: Spacecraft Technology Division  
S. G. Jones (M.S. 54-3)

NASA-Lewis Research Center (1)  
21000 Brookpark Road  
Cleveland, Ohio 44135  
Attn: Spacecraft Technology Division  
F. E. Kavanagh (M.S. 54-3)

NASA-Lewis Research Center (13)  
21000 Brookpark Road  
Cleveland, Ohio 44135  
Attn: Spacecraft Technology Division  
J. A. Wolters (M.S. 54-3)

NASA-Lewis Research Center (1)  
21000 Brookpark Road  
Cleveland, Ohio 44135  
Attn: Electric Propulsion Laboratory  
W. Moeckel (M.S. 301-1)

NASA-Lewis Research Center (1)  
21000 Brookpark Road  
Cleveland, Ohio 44135  
Attn: Electric Propulsion Laboratory  
H. R. Kaufman (M.S. 301-1)

NASA-Lewis Research Center (1)  
21000 Brookpark Road  
Cleveland, Ohio 44135  
Attn: Report Control Office (M.S. 5-5)

NASA Scientific & Technical Information Facility (6)  
P. O. Box 33  
College Park, Maryland 20740  
Attn: NASA Representative RQT-2448

NASA Marshall Space Flight Center (1)  
Huntsville, Alabama 35812  
Attn: Ernest Stuhlinger (M-RP-DIR)

Research and Technology Division (1)  
Wright-Patterson AFB, Ohio 45433  
Attn: AFAPL (APIE-2)/R. F. Cooper

AFWL (1)  
Kirtland AFB, New Mexico  
Attn: WLPC/Capt. C. F. Ellis

Aerospace Corporation (1)  
P. O. Box 95085  
Los Angeles, California 90045  
Attn: Library Technical Documents Group

Jet Propulsion Laboratory (1)  
4800 Oak Grove Drive  
Pasadena, California 91103  
Attn: J. W. Stearns

Hughes Research Laboratories (1)  
3011 Malibu Canyon Road  
Malibu, California 90265  
Attn: G. R. Brewer

Hughes Research Laboratories (1)  
3011 Malibu Canyon Road  
Malibu, California 90265  
Attn: H. J. King

Ion Physics Corporation (1)  
South Bedford Street  
Burlington, Massachusetts  
Attn: Sam Nablo

TRW Systems Group (1)  
TRW Inc.  
One Space Park  
Redondo Beach, California 90278  
Attn: D. B. Langmuir

Westinghouse Astronuclear Laboratories (1)  
Electric Propulsion Laboratory  
Pittsburgh, Pennsylvania 15234  
Attn: H. W. Szymanowski

TRW Equipment Laboratories (1)  
TRW Inc.  
23555 Euclid Avenue  
Cleveland, Ohio 44117  
Attn: R. T. Craig

General Electric Space Flight Propulsion  
Laboratory (1)  
Cincinnati, Ohio 45215  
Attn: M. L. Bromberg

Field Emission Corporation (1)  
Melrose Avenue at Linke Street  
McMinnville, Oregon 97128  
Attn: L. W. Swanson

University of California (1)  
Space Science Laboratory  
Berkeley 4, California  
Attn: H. P. Smith

United Aircraft Corporation (1)  
Research Laboratories  
East Hartford, Connecticut 06108  
Attn: R. G. Meyerand, Jr.

Aerospace Power Division (1)  
Wright-Patterson AFB, Ohio 45433  
Attn: Jack W. Geis-AFAPL/APIT